

When planets get too hot: exploration of the runaway greenhouse with 1-D and 3-D climate models

Guillaume Chaverot

▶ **To cite this version:**

Guillaume Chaverot. When planets get too hot: exploration of the runaway greenhouse with 1-D and 3-D climate models. Astrophysics [astro-ph]. Université de Genève (Genève, Suisse). Faculté des sciences, 2023. English. ⟨NNT : ⟩. ⟨tel-04875116⟩

HAL Id: tel-04875116

https://hal.science/tel-04875116v1

Submitted on 8 Jan 2025

HAL is a multi-disciplinary open access archive for the deposit and dissemination of scientific research documents, whether they are published or not. The documents may come from teaching and research institutions in France or abroad, or from public or private research centers.

L'archive ouverte pluridisciplinaire **HAL**, est destinée au dépôt et à la diffusion de documents scientifiques de niveau recherche, publiés ou non, émanant des établissements d'enseignement et de recherche français ou étrangers, des laboratoires publics ou privés.



HAL Authorization

UNIVERSITÉ DE GENÈVE
Département d'Astronomie

FACULTÉ DES SCIENCES
Pr. Emeline Bolmont & Dr. Martin Turbet

When planets get too hot: exploration of the runaway greenhouse with 1-D and 3-D climate models

THÈSE

présentée à la Faculté des sciences de l'Université de Genève
pour obtenir le grade de Docteur ès sciences,
mention Astronomie et Astrophysique

par

Guillaume CHAVEROT

de

Belfort (France)

Thèse N^{o} 5774

GENÈVE
Observatoire Astronomique de l'Université de Genève
2023

UNIVERSITÉ DE GENÈVE
FACULTÉ DES SCIENCES

DOCTORAT ÈS SCIENCES, MENTION ASTRONOMIE ET ASTROPHYSIQUE

Thèse de Monsieur Guillaume CHAVEROT

intitulée :

«When Planets Get Too Hot: Exploration of the Runaway Greenhouse with 1-D and 3-D Climate Models»

La Faculté des sciences, sur le préavis de Madame E. BOLMONT, professeure assistante et directrice de thèse (Département d'astronomie), Monsieur M. TURBET, docteur et codirecteur de thèse (Laboratoire de Météorologie Dynamique (LMD), Institut Pierre et Simon Laplace (IPSL), Université de la Sorbonne, Paris, France), Monsieur C. LOVIS, professeur associé (Département d'astronomie), Madame M. BRUNETTI, docteure (Section de physique) et Monsieur N. MAYNE, professeur (Department of Physics and Astronomy, University of Exeter, United Kingdom), autorise l'impression de la présente thèse, sans exprimer d'opinion sur les propositions qui y sont énoncées.

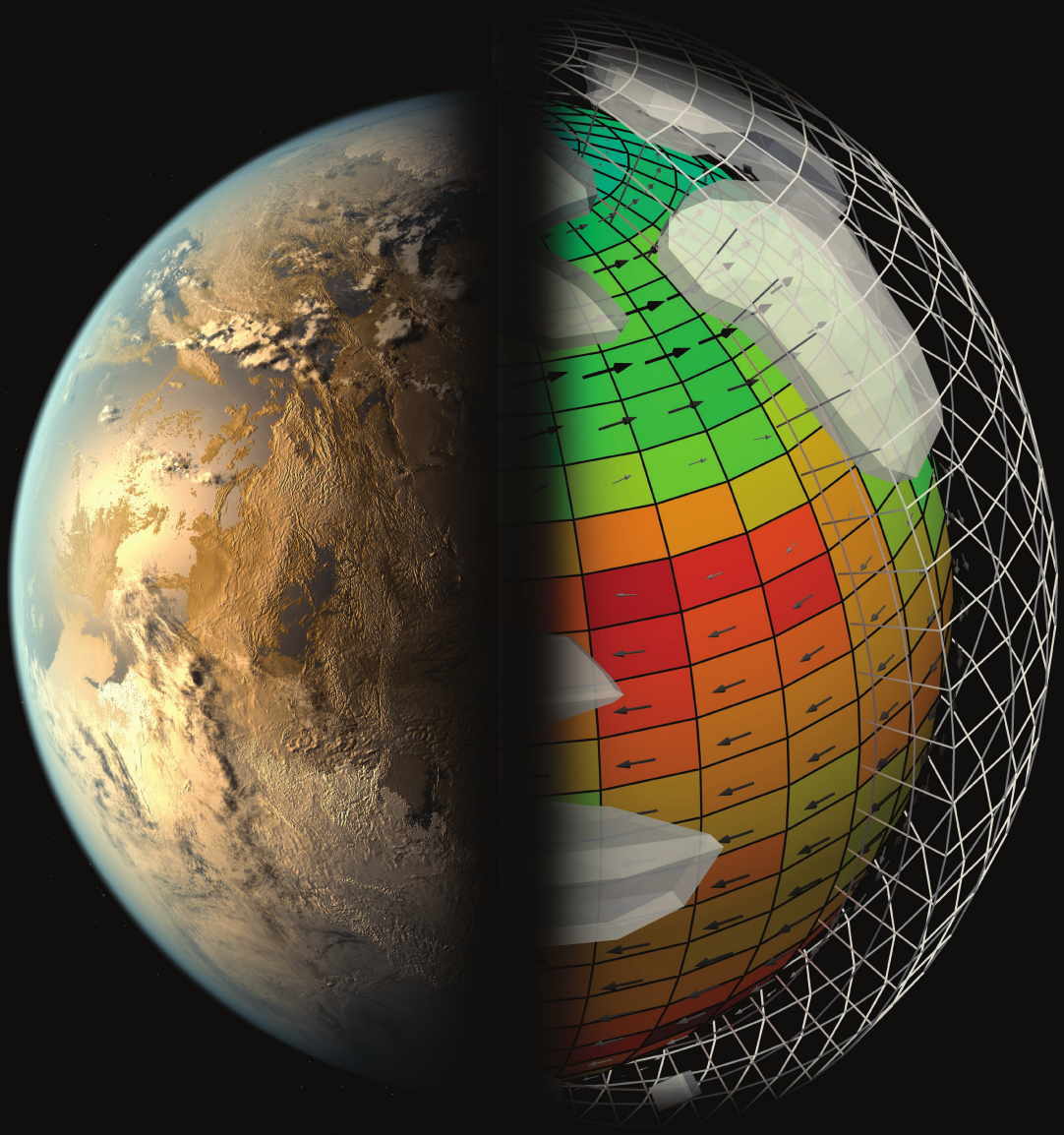
Genève, le 23 octobre 2023

Thèse - 5774 -

Le Décanat

N.B. - La thèse doit porter la déclaration précédente et remplir les conditions énumérées dans les "Informations relatives aux thèses de doctorat à l'Université de Genève".

Ce travail de thèse a donné lieu à des publications dont la liste se trouve à la page 137.



Courtesy of Emeline Bolmont & Siddharth Bhatnagar

Abstract

Since the dawn of humanity, one question that has animated philosophers is that of life. The debate about its origins, and its uniqueness on Earth, is at the heart of almost all religions. Ancient philosophers tried to answer this question with the limited technical means at their disposal. Nowadays, the development of technology allows us to observe the Universe with unprecedented precision. Since the detection of the first extra-solar planet orbiting a solar-type star named Pegasi 51b, in 1995, an impressive number of planets with various characteristics have been discovered. Some are similar to Jupiter but with extreme temperatures (so-called Hot-Jupiter), while others are similar in size and mass to our Earth. The study of these small, rocky planets raises questions about their habitability. Are they really Earth-like ? Or more like Venus ? Or even Mars ? Can they have liquid water on their surface ? This is an essential condition for life as we know it.

This is the context of my PhD work. Using different 1-D and 3-D numerical climate models, I have studied the major processes, particularly the runaway greenhouse effect, which can turn a habitable planet into a totally uninhabitable planet. Or should I say, removing any possibility of water in liquid phase on the surface of these planets. The conditions governing the existence of a "habitable" climate are multiple and induce climate multistability. Therefore, I also studied the possible transition between these states, via a perturbation induced by a stochastic event. However, climate modelling is not an isolated science. The atmosphere interacts with the rocky interior of the planet, as well as with its host star. Climate is therefore influenced by numerous external processes, which must be understood in order to model reality as accurately as possible. Moreover, the atmospheric composition is absolutely pivotal to the study of climate. As we can see, the Earth's climate change is induced by an increase in anthropogenic CO_2, modifying the climatic response. Therefore, I have also studied in detail the molecular spectroscopy needed to produce the data essential for climate models. This is an important preliminary step to guarantee the robustness and accuracy of the models we use to describe exoplanets.

Finally, the aim to better understand the processes governing the climate of small, temperate, rocky planets is part of a broader effort to strengthen our knowledge for promising future observational missions. The quantity and precision of the expected data will require high-performance tools for analysis. Climate models will certainly play a key role in this process.

Résumé

Depuis l'aube de l'humanité, une question qui anime les penseurs est celle de la vie. Le débat de ses origines, et de son unicité Terrestre est au cœur de presque toutes les religions. Les philosophes de l'antiquité ont tenté de répondre à cette question avec les moyens techniques limités dont ils disposaient. Le développement des technologies permet de nos jours d'observer l'Univers avec une précision inégalée. Depuis la détection de la première planète extra-solaire orbitant autour d'une étoile similaire au Soleil en 1995, Pegasi 51b, un nombre impressionnant de planètes aux caractéristiques variées ont été découvertes. Certaines sont semblables à Jupiter mais avec des températures extrêmes (les bien nommées Jupiter-chaudes), d'autres sont de taille et de masse similaires à notre Terre. L'étude de ces petites planètes rocheuses stimule le questionnement sur l'habitabilité. Sont-elles réellement similaires à la Terre ? Ou plutôt semblables à Vénus ? Ou même à Mars ? Peuvent-elles avoir de l'eau liquide à leur surface ? Ceci étant une condition indispensable à la vie telle qu'on la connaît.

C'est dans ce contexte que se place mon travail de thèse. À l'aide de différents modèles numériques de climat 1-D et 3-D, j'ai étudié les processus majeurs, notamment le processus d'emballement de l'effet de serre, pouvant rendre une planète habitable totalement inhabitable. Ou devrais-je dire plutôt, éliminant toute possibilité d'eau en phase liquide à la surface de ces planètes. Les conditions régissant l'existence d'un climat dit "habitable" sont multiples et induisent une multistabilité climatique. J'ai donc également étudié la transition possible entre ces états, via une perturbation induite par un processus stochastique. Par ailleurs, la modélisation du climat n'est pas une science isolée. L'atmosphère est en interaction avec l'intérieur rocheux de la planète ainsi qu'avec son étoile. Le climat est donc influencé par de nombreux processus externes qu'il faut connaître afin de tendre à modéliser la réalité de la manière la plus exacte possible. De plus, la composition atmosphérique est un élément absolument central dans l'étude du climat. Nous le voyons avec le changement climatique terrestre induit par l'augmentation anthropique de CO_2. J'ai donc par ailleurs étudié en détail la spectroscopie moléculaire nécessaire à la production de données essentielles aux modèles de climat. Ceci est une étape préliminaire importante afin de garantir la robustesse et la précision des modèles que l'on utilise pour décrire les exoplanètes.

Finalement, la volonté de mieux comprendre les processus régissant le climat des petites planètes rocheuses tempérées s'inscrit dans une optique plus large, de renforcement de nos connaissances en vue de futures missions d'observation prometteuses. La quantité et la précision des données attendues vont nécessiter des outils performants pour être analysées. Dans ce processus, les modèles de climats vont certainement jouer un rôle clef.

Notation

Acronyms	
GCM	Global Climate Model
EBM	Energy Balanced Model
HZ	Habitable Zone
ISR	Incoming Stellar Radiation
ASR	Absorbed Stellar Radiation
OTR	Outgoing Thermal Radiation (a.k.a Outgoing Longwave Radiation, OLR)
IR	Infrared
UV	Ultraviolet
CIA	Collision Induced Absorption

Physical constants	
$c = 2.99792458 \times 10^{8}$ m.s^{-1}	Speed of light
$h = 6.62607015 \times 10^{-34}$ J.s	Planck constant
$\hbar = 1.054571818 \times 10^{-34}$ J.s	Reduced Planck constant (a.k.a. Dirac constant)
$k_B = 1.380649 \times 10^{-23}$ J.K^{-1}	Boltzmann constant
$N_a = 6.02214076 \times 10^{23}$ mol^{-1}	Avogadro constant

Remerciements

Je tiens en premier lieu à remercier ceux sans qui tout ceci n'aurait pas été possible : Emeline et Martin. Merci pour votre patience, votre gentillesse, votre rigueur et votre bienveillance. Merci de m'avoir montré que la science se fait avec les gens et non pas dans la compétition ou l'arrogance. Pendant ces quatre ans, vous m'avez poussé à donner le meilleur de moi-même, à toujours me questionner pour comprendre les choses en profondeur, à écouter, bref à faire de la science. Je chéris cette rigueur et cette curiosité que vous portez en vous et que vous avez su me communiquer. J'espère pouvoir encore longtemps marcher à vos côtés pour en apprendre toujours plus. Merci.
Thank you to all the jury members for your time, your relevant questions and useful comments. It has been a pleasure to present my work to you, and I hope you enjoyed reading this manuscript.

Merci à mes collègues de bureau qui ont toujours essayé de répondre à mes nombreuses questions, pas toujours pertinentes. Merci à ceux qui ont déployé leurs ailes pour voir si l'herbe est plus verte ailleurs et avec qui j'ai partagé un café, une discussion ou un simple bonjour. Merci à tous les gens de l'équipe que j'ai côtoyé et à tout le personnel de l'observatoire pour leur gentillesse et leur bienveillance. Un sourire au détour d'un couloir est bien plus qu'un simple sourire. Cet environnement de travail est incroyable parce que vous le définissez.

Merci tout spécialement à la team qui m'a accompagné toutes ces années et sans qui la vie n'aurait pas eu cette saveur. Dany, Mathilde K., Yassin, Marion, Alex, Léna, Mathilde H., Omar, Yann, Siddharth, William, Lucile et tous les autres. Vous m'avez donné la force de ne rien lâcher dans les moments difficiles, et vous étiez là pour en profiter dans les moments heureux. J'espère vous avoir rendu ne serait-ce que le dixième de ce que vous m'avez donné.
Je suis heureux de voir que le groupe s'agrandit avec des petits nouveaux au potentiel certain ! Léna, Mathilde, Sidd, Yanou, je suis très confiant quant à votre capacité à faire des journées de qualité et des nuits de folie. Il y a tant à dire et pourtant si peu de mots.
Mon cher Dany, te voilà le senior de ce groupe (malgré ta jeunesse indéniable !), je suis heureux d'avoir pu te côtoyer dès les débuts. Merci Omar pour toutes ces discussions, tu m'as énormément appris sur des sujets aussi divers que variés. Marion, les pauses caf' n'auraient pas eu cette gaieté sans ce petit accent chantant, c'est certain. Léna, tu as égayé ce bureau dès ton arrivée avec ton énergie et ta bonne humeur. Siddharth, I enjoyed all our discussions (even when you were a young Master student) and the beers we drank together. Petite Mathilde, ton impressionnante énergie semble ne pas avoir de limite ! De ton dernier jus à ta première bière, que de chemin parcouru. Camarade Alex, camarade William, je vous

salue et vous dis un profond merci pour toutes ces discussions enflammées, et ces tintements de verre. Lucile, tu es la dernière d'une série de très belles rencontres. Tu as su trouver les mots justes au moment où j'en avais le plus besoin et je t'en remercie. Mention spéciale au trio incroyable, le K, le D et le Y pour toute cette puff ridée, tous ces excès de fromage et pour ces fous rires. Le temps fut bref, mais il en fut d'autant plus intense.

Je souhaite aussi m'incliner devant ces gens brillants que j'ai eu la chance de rencontrer, et avec qui n'importe quelle question complexe semble déroutante de simplicité. Jérémy, François, Franck, Ehouarn et tant d'autres ; chaque discussion avec vous fut pour moi aussi intense que révélatrice. J'ai finalement une pensée à tous ces gens que j'ai pu croiser en conférence et ailleurs, au détour d'un café ou d'une bière, et dont j'oublie le nom. Merci pour toutes ces discussions, professionnelles ou non, qui m'ont tant apporté. On dit que la science se fait bien plus autour d'un café que devant un ordinateur. Je n'aurais jamais cru cet adage aussi vrai ! La science est fascinante grâce aux gens passionnés qui en parlent et qui la font vivre. J'espère pouvoir encore longtemps vous côtoyer, vous écouter et vous applaudir.

Bien évidemment, je remercie toute ma famille pour leur soutien indéfectible et leur amour. Bien que les pages de ce manuscrit soient peut-être quelque peu obscures à vos yeux, vous m'avez toujours poussé à continuer dans cette voie, et vous avez su trouver les mots pour apaiser mes doutes et mes frustrations. Mon cœur déborde tout spécialement d'affection pour mes deux grands-mères qui n'ont pas hésité à braver la route pour m'écouter parler dans une langue inconnue pendant des heures.

J'aimerais conclure ceci par quelques mots pour ceux à qui, par deux fois, je dois la vie. A leur soutien, à leur sourire, à toutes ces discussions, à ces silences lourds de sens, à ces regards, à ces cris et à ces pleurs. À mes parents tout simplement. Vous qui m'avez toujours soutenu, poussé en avant, relevé, stimulé et aimé sans retenue. Je ne serai pas là sans vous et pour cela je souhaite vous dédier les quelques pages qui suivent, et tout particulièrement les joies, les doutes et surtout le plaisir d'apprendre qu'elles renferment.

Contents

List of Figures **xviii**

List of Tables **xix**

1 Introduction **1**

1.1 Detection and characterization of exoplanets . . . 3
1.1.1 Detection techniques . . . 3
1.1.1.1 The radial velocity technique . . . 3
1.1.1.2 The planetary transit technique . . . 4
1.1.2 Atmospheric characterization . . . 5
1.1.2.1 Characterizing transiting planets . . . 5
1.1.2.2 Out-of-transit characterization . . . 6
1.2 Habitability . . . 6
1.2.1 Definition of habitability . . . 6
1.2.2 The habitable zone - main definition . . . 8
1.2.2.1 The inner edge . . . 10
1.2.2.2 The outer edge . . . 12
1.2.3 Alternative definitions of the habitable zone . . . 12
1.3 The runaway greenhouse transition: a deeper insight into the mechanisms involved . . . 13
1.4 Climate models . . . 14
1.4.1 1-D inverse radiative-convective models . . . 15
1.4.2 Energy balance models . . . 16
1.4.3 The Generic-PCM . . . 17
1.5 Toward a complete understanding of terrestrial planets . . . 19
1.5.1 Atmosphere-interior interactions . . . 20
1.5.2 Atmospheric escape . . . 20
1.6 Organization of the manuscript . . . 22

I Absorption spectroscopy **23**

2 Absorption spectroscopy for climate modeling **25**

2.1 Fundamental notions of spectroscopy . . . 26

2.2 State-of-the-art . . . 26

2.2.1 Line intensity . . . 26

2.2.2 Line broadening . . . 27

2.2.3 Shape of the absorption lines . . . 28

2.2.3.1 Line-center . . . 28

2.2.3.2 Farwings and χ factors . . . 29

2.2.4 Collision induced absorption and dimers . . . 31

2.2.5 The challenge of gas mixtures . . . 32

2.3 From high resolution spectra to opacity data . . . 33

2.3.1 Mean-Rosseland and gray calculation . . . 33

2.3.2 The correlated-*k* approach . . . 34

3 SpeCT: SPEctra for Correlated-k Tables **37**

3.1 Motivation: From lab experiments to climate modeling . . . 38

3.1.1 Focus on CO_2 . . . 38

3.2 Technical description of SpeCT . . . 39

3.2.1 Computation of line-centers & continua . . . 40

3.2.2 Data limitations . . . 41

3.3 Databases & line-lists . . . 43

3.4 Discussion and prospects . . . 43

II The runaway greenhouse **45**

4 The onset of the runaway greenhouse **47**

4.1 Motivation: The importance of subtle spectroscopic effects . . . 48

4.1.1 A detailed description of 1-D inverse radiative convective models . . . 48

4.1.1.1 Computation of the pressure-temperature profile . . . 48

4.1.1.2 Radiative transfer . . . 49

4.2 How does the background atmosphere affect the onset of the runaway greenhouse ? . . . 51

4.3 The onset of the runaway greenhouse for atmospheres with CO_2 . . . 72

4.4 Evolution of planetary albedo . . . 74

4.5 Limits for dense atmospheres 77

5 The entire transition of the runaway greenhouse 79

5.1 Motivation: from habitable to uninhabitable 80
5.2 First exploration of the entire runaway greenhouse transition with a GCM 81
5.3 Observability of temperate and post-runaway states 97
5.4 Long-term evolution of post-runaway states 100
5.5 Reversibility of the runaway greenhouse 101

III Climate multistability of small terrestrial planets 103

6 Resilience of the snowball state 105

6.1 Motivation: The concept of climate multistability 106
6.2 Resilience of the snowball Earth 109
6.3 Implications for exoplanets 127
6.3.1 S-tipping: an inefficient way to deglaciate a planet 127
6.3.2 Toward a more complex definition of the habitable zone 127

IV Conclusions and prospects 131

7 Conclusions 133

7.1 Conclusions 134
7.2 Prospects 135

A Publication list 137

A.1 Peer-reviewed research articles 137
A.2 Peer-reviewed contributions through on-site and remote observations 138
A.3 Other contributions 138

Bibliography 139

List of Figures

1.1 First radial velocity measurement of 51 Pegasi 4
1.2 Schematic view of the transit light curve of an exoplanet 5
1.3 Schematic view of the phase curve of an exoplanet 7
1.4 Artist's view of the three phases of water as a function of the distance to the star 8
1.5 Overview of the inner edge of the HZ computed with 1-D and 3-D climate modeling . . 11
1.6 Schematic view of an EBM 17
1.7 Scheme of the main physical processes of the Generic-PCM 18

2.1 Absorption spectrum of a pure CO_2 gas with and without χ factor corrections 30
2.2 Absorption spectrum of a pure CO_2 gas at 300 K and 1 bar 32
2.3 Grey and mean-Rosseland opacities of a pure H_2O gas at 300 K and 1 bar 34
2.4 Absorption coefficient as a function of wavenumber and cumulative probability 35

3.1 Scheme of ro-vibrationnal modes of CO_2 39
3.2 Scheme of the three IR absorption bands of CO_2 39
3.3 Main absorption bands of CO_2 41

4.1 Schematic view of a 1-D radiative-convective model 50
4.2 OTR as a function of the global surface temperature for H_2O+CO_2 mixtures 72
4.3 Absorption spectra for a H_2O+CO_2 mixture with various H_2O pressures 73
4.4 Albedo as a function of the surface temperature for a H_2O+N_2 atmosphere 75
4.5 Evolution of the ASR and OTR for a H_2O+N_2 atmosphere 76
4.6 Temperature profiles of pure water vapor atmospheres 78

5.1 Schematic overview of the phase curve configurations 97
5.2 Transmittance maps along the runaway greenhouse transition 98
5.3 Transmission spectra along the runaway greenhouse transition 99
5.4 Cloud pattern of temperate and post-runaway states 102

6.1 The multiple climate states of a temperate planet 107
6.2 Hysteresis cycles induced by the ice-albedo and the cloud feedback 107
6.3 Scheme of B-tipping and S-tipping 108
6.4 Overview of the inner edges of the HZ computed with 1-D and 3-D climate models . . . 128

List of Tables

1.1 Advantages and disadvantages of 1-D radiative-convective models 15
1.2 Advantages and disadvantages of 1-D EBMs 17
1.3 Advantages and disadvantages of GCMs 19

3.1 References for the continua and CIAs used in SpeCT 41
3.2 Spectroscopic data available in HITRAN 42
3.3 Definition domain of the CIA with their extrapolation temperature threshold 42

Chapter 1

Introduction

Contents

1.1 Detection and characterization of exoplanets 3

1.1.1 Detection techniques 3

1.1.2 Atmospheric characterization 5

1.2 Habitability 6

1.2.1 Definition of habitability 6

1.2.2 The habitable zone - main definition 8

1.2.3 Alternative definitions of the habitable zone 12

1.3 The runaway greenhouse transition: a deeper insight into the mechanisms involved 13

1.4 Climate models 14

1.4.1 1-D inverse radiative-convective models 15

1.4.2 Energy balance models 16

1.4.3 The Generic-PCM 17

1.5 Toward a complete understanding of terrestrial planets 19

1.5.1 Atmosphere-interior interactions 20

1.5.2 Atmospheric escape 20

1.6 Organization of the manuscript 22

The first exoplanet orbiting a Sun-like star was discovered in 1995 (Mayor & Queloz 1995), three years after the discovery of the very first exoplanet, which was orbiting a pulsar (Wolszczan & Frail 1992). However, is 1995 the actual beginning of the exoplanet field ?

> *"Furthermore, there are infinite worlds both like and unlike this world of ours. For the atoms being infinite in number, as was proved already, are borne on far out into space. For those atoms, which are of such nature that a world could be created out of them or made by them, have not been used up either on one world or on a limited number of worlds, nor again on all the worlds which are alike, or on those which are different from these. So that there nowhere exists an obstacle to the infinite number of the worlds."*[1]
>
> Letter to Herodotus, Epicurus

In the continuity of atomists such as Democritus, Epicurus (341 - 270 BC) formulated a theory of infinite worlds, based on the infinite number of atoms existing in the universe. This was of course a thought experiment. Indeed, the lack of technical instruments at that time made it impossible to validate/invalidate this theory. Later on, during the 17th century, the development of new technologies and scientific instruments created a stimulating context for philosophers to imagine the most accurate way to understand the Universe. One of the most famous scientist of that time, Galileo Galilei fought in favor of rationality rather than faith, highlighting the role of mathematics in all areas of study. Simultaneously, Francis Bacon proposed the formulation of a modern scientific method[2], still used nowadays. The iterative process is the following:

1. Formulation of a **question** potentially motivated by an observation.
2. **Theory** or hypothesis developed in order to answer the question.
3. **Prediction** made in the context of the theory proposed.
4. **Testing** of the prediction made by the theory. This can be, for example, an experiment or an observation.
5. **Analysis** of the testing. If the test is in accordance with the prediction, the theory is considered true *within the framework of current knowledge*. If not, another theory is formulated to answer the question.

Therefore, this is a cyclic method, allowing the possibility to correct a theory to make it more general, in other words to make it more universal. Moreover, the key point making this method as "scientific" in the modern meaning of this word is that any theory can be invalidated by a counter-example. This was a real novelty in the attempt to understand the Universe, compared with the dominant spirit of previous centuries. All the modern science, including everything discussed in this manuscript, is based on this

[1] Traduction from Steve Naragon website, University of Manchester, `https://users.manchester.edu/Facstaff/SSNaragon/Online/texts/316/Epicurus,LetterHerodotus.pdf`

[2] see Bacon, F. (1620) Novum Organum

iterative scheme proposed 400 years ago. Finally, the evolution of techniques and instruments allowed, by the end of the 20th century, the testing of the 2000 year-old plurality of worlds theory. The analysis of the results obtained by observing the star named Pegasi-51 (and by the numerous other works done in the next following few months) initiated a great enthusiasm for "planet hunting". This manuscript is thus only a very small additional step in this infinite journey, and what an exciting journey, fuelled by curiosity and enriching encounters.

Of course this shortcut in the history of science forgets many names of women and men who contributed step-by-step to a more complex understanding of the Universe, allowing scientists to imagine and accept the possibility of other planets. There is no great discoveries without a scientific context helping the correct analysis of an experiment, or of an observation. It is then the smartness of some people which makes the difference to see the right solution among all the other inaccurate possibilities, creating new fields at the same time.

1.1 Detection and characterization of exoplanets

As written above, science aims to answer questions to try to understand a bit more the Universe. To try to understand planets outside our solar system (and maybe our planet at the same time), we first need to observe them. The historical method used to observe the first exoplanets is the radial velocity technique (Sect. 1.1.1.1). Slightly later, with the improvement of instruments and motivated by the first detection, another method named planetary transit was developed (Sect. 1.1.1.2). They are the two main methods to detect exoplanets. However, other techniques exist such as direct imaging (e.g., Marois et al. 2010) or micro-lensing (e.g., Bond et al. 2004) but they are not discussed in this manuscript.

1.1.1 Detection techniques

1.1.1.1 The radial velocity technique

The historical method used to find the first exoplanet (Mayor & Queloz 1995), and a lot of others after it, is named radial velocity technique. When a planet is orbiting a star, the couple rotates around the common center of gravity. If the orbital plane is not purely perpendicular to the line-of-sight, the projected movement of the star along this line-of-sight will be a back and forth movement towards and away from the observer. This back-and-forth movement induces an alternating red and blue shift of the coming light. By observing such star with a spectrograph, it is possible to measure this periodic shift of the different emission lines in the spectrum. In other words, the idea is to measure the relative position of an emission line from a stellar spectrum over time. If the position varies with a constant period, that could mean that a planet orbits the star. The aim of the radial velocity method is to use multiple emission lines to quantify, as precisely as possible, the Doppler shift of the star as a function of its orbital phase, as shown by Fig. 1.1. Then, it is possible to infer the minimal mass of the planet and its distance to the host star with the amplitude and the period of the radial velocity variation. To infer the actual mass of the planet, additional methods such as the transit technique are needed. For multi-planetary systems or

eccentric planetary orbits, the signal is not purely sinusoidal and requires advanced numerical techniques to compute the planetary parameters (e.g., Hara & Ford 2023).

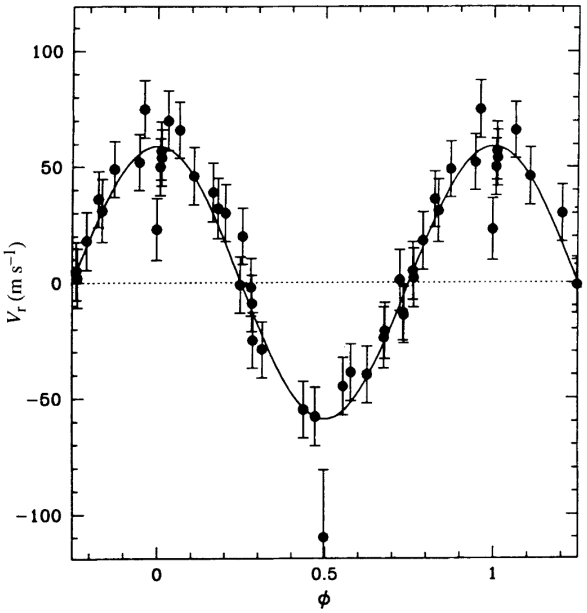


Figure 1.1: Doppler shift of 51 Pegasi as a function of the orbital period Φ. Black dots are the observational measurements taken over four different nights. Figure from Mayor & Queloz (1995).

1.1.1.2 The planetary transit technique

The first transit detected with this method was in 2000 (Charbonneau et al. 2000) looking at the star HD208458, around which a planetary-mass object had been detected with radial velocity. The idea is very simple: if a planet passes in front of a star, it blocks a part of the light, as shown by Fig. 1.2. Knowing this, the aim is to search for a periodic decrease of the stellar light, meaning that a planet is probably passing between the observer and the star. This was the aim of CoRoT (Baglin et al. 2006), the first spacecraft dedicated to the detection of transiting exoplanets. Then, the Kepler space telescope (Borucki et al. 2010) allowed the detection of more than 2700 exoplanets. In total in 2023, more than 4100 exoplanets[3] (about 75% of the known exoplanets) were discovered thanks to this method.

The light drop is proportional to $(R_p/R_s)^2$ where R_p is the radius of the planet and R_s the radius of the star. That means that the larger the planet, the deeper the transit. Therefore, is it possible to infer the radius of the planets by knowing the characteristics of the star. By combining the transit method giving the radius with a radial velocity measurement giving a mass (or at least a minimal mass) it becomes possible to study the density of the planet. This opens an entire area of research focused on the modeling of the composition of the interior of the planet (e.g., Wang et al. 2022). The main issue is that the planet needs to transit between the observer and the star, meaning that the orbital plane needs to be aligned with the line of sight. This very specific configuration limits the number of planets detectable through this

[3] according to `https://exoplanetarchive.ipac.caltech.edu/index.html`

method. As this transit probability is low, the strategy is to look at a lot of stars (for instance, the Kepler sample had more than 100'000 stars). This ensures to be able to detect a reasonable number of transits. And when a planet transits, we can actually do much more than just detect it, we can characterize its atmosphere too.

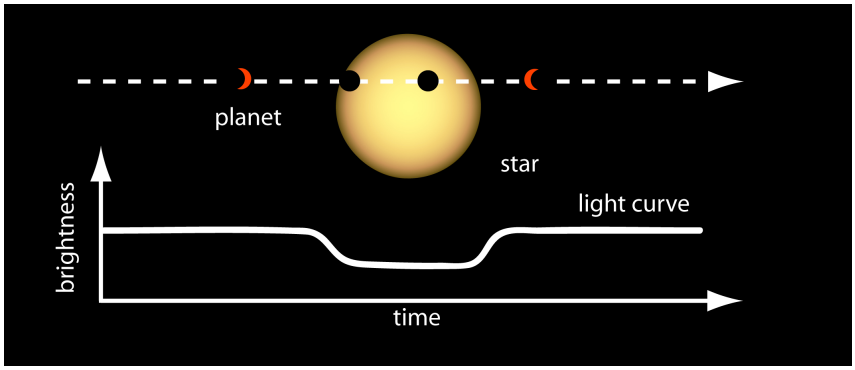


Figure 1.2: Schematic view of the transit light curve of an exoplanet. The top scheme represents the illumination of the planet along its orbit. The bottom scheme is the received flux from the system compared to the flux of the star. Credit: NASA Ames

1.1.2 Atmospheric characterization

1.1.2.1 Characterizing transiting planets

For a planetary system in a transiting configuration, it is possible to characterize the atmosphere of the planet. Indeed, when the planet transits, a part of the stellar light is passing through the planetary atmosphere (if there is one). Molecules in the atmosphere absorb a part of the light at very specific wavelengths, depending on their spectral signature. The differences between the stellar spectrum outside the transit and during the transit give an information on the composition of the atmosphere. By doing such measurement in multiple wavelengths, it could be possible to infer the composition of the top part of the atmosphere. Knowing the composition of the atmosphere of a planet is absolutely key to be able to model its atmosphere and constrain further its properties (e.g., temperature profile).

It is easier to characterize large and hot planets such as Hot-Jupiter[4] thanks to their large radii and puffed atmosphere. Observations of these planets have shown a great diversity (e.g., Sing et al. 2016). However, the last generation of observatories such as the James Webb Space Telescope (JWST, e.g. Rieke et al. 2015 ; Birkmann et al. 2022) or the CHaracterising ExOPlanet Satellite (CHEOPS, Benz et al. 2021), are able to measure very tiny variations of light intensity of few tens of ppm. Therefore, it becomes possible to characterize the atmosphere of small rocky exoplanets such as the TRAPPIST-1 system (e.g., Morley et al. 2017 ; Lustig-Yaeger et al. 2019 ; Wunderlich et al. 2019 ; Fauchez et al. 2019). However, probing the atmosphere of a planet with transit spectroscopy can be tricky if the star is very active (e.g., Rackham et al. 2018). Still using the fact that the planet transits, another observation

[4]Planets similar to Jupiter in terms of size and composition but highly irradiated, thus very hot, due to their proximity to the host star.

is possible by measuring the secondary eclipse depth, happening when the planet passes behind the star. This is explained is the following subsection. This method is not as sensitive to the star as transit spectroscopy and also allows having information on the atmosphere and its capacity to transport heat from the day-side to the night-side (Greene et al. 2023 ; Zieba et al. 2023).

1.1.2.2 Out-of-transit characterization

As written in the previous section, the transmission spectroscopy method is only possible if the planet transits. However, it is not the only way to characterize the atmosphere of the planet. Even if the planetary orbit is not aligned with the line of sight, some flux coming from the star can be reflected by the planet, as shown by Fig. 1.3. In this configuration, by measuring the light coming from the system during an entire planetary orbit, it is possible to construct the phase curve of the system (see Fig. 1.3). The amount of stellar light reflected by the planet gives an estimation of its Bond albedo (i.e., the albedo at the top of the atmosphere), which is a function of the characteristics of the atmosphere if there is one (clouds, hazes, gas composition). Moreover, if the planet is hot enough it could emit enough IR radiations to be detected, also contributing to the total flux budget coming from the system. Detecting these very tiny variations of light could give precious information about extra-solar planets, especially on their composition and structure.

The next generation of instruments such as RISTRETTO@VLT (Lovis et al. 2022) or ANDES@E-ELT (Marconi et al. 2022) aim to walk this way by combining different advanced techniques in order to reach the precision required to probe directly the light coming from the planet. More precisely, their objective is to detect the light reflected by the planet to try to probe them down to the surface, which is not possible with transit spectroscopy. Long term projects, such as the Large Interferometer For Exoplanets (LIFE, see Quanz 2019), aim to reach the precision required to measure the thermal emission of small temperate planets. As an example, the contrast ratio between the flux from the star and that from the planet, needed to observe Proxima-b with such technique, is of the order of 10^{-7}.

Thanks to transmission spectroscopy and reflected light methods, we start to characterize small rocky exoplanets.

In addition to the ongoing observations of the TRAPPIST-1 system with JWST (e.g., Greene et al. 2023 ; Zieba et al. 2023), instruments in preparation such as RISTRETTO@VLT and ANDES@E-ELT will allow characterizing, in a near future, temperate rocky exoplanets (e.g., Proxima-b). Therefore, there is a real interested to study the question of habitability to understand these worlds, and to select the most interesting targets.

1.2 Habitability

1.2.1 Definition of habitability

Following our knowledge in biology and pre-biotic chemistry, life as we know it is based on carbon and requires liquid water as a solvent to allow efficient and fast molecular interactions. Therefore, liquid

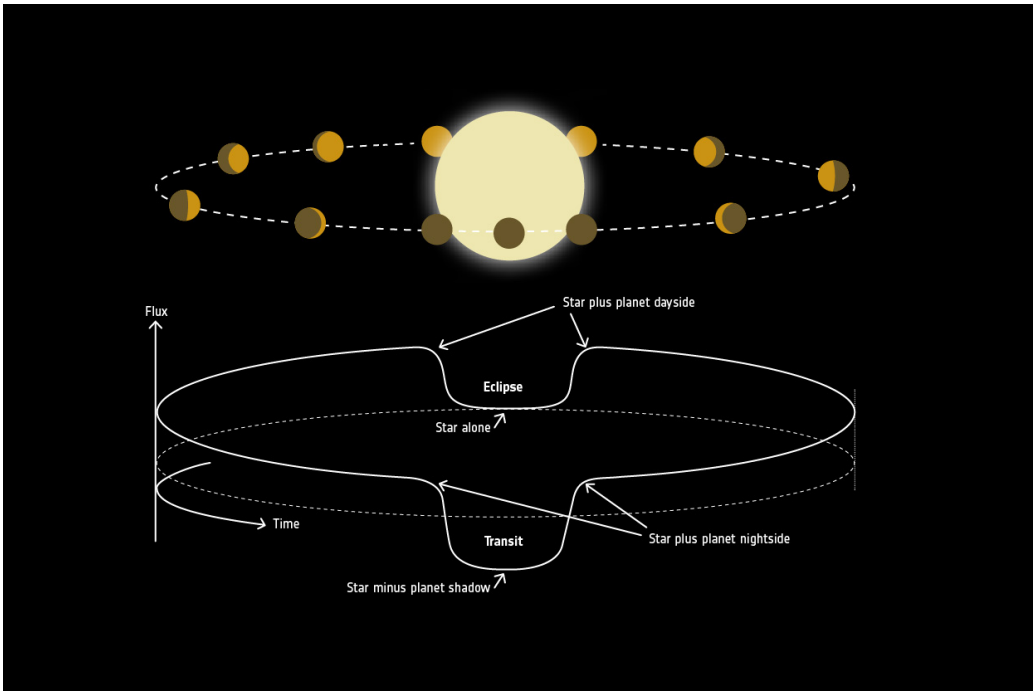


Figure 1.3: Schematic view of the phase curve of an exoplanet. The top scheme represents the illumination of the planet along its orbit. The bottom scheme is the received flux from the system compared to the flux of the star. Credit: ESA

water is a necessary but not sufficient condition for life to be sustained. The other known conditions are the presence of carbon, a stable surface and a source of energy.

Carbon is a very abundant element, able to form four molecular bonds with other atoms. It does not form too strong molecule bonds, allowing easy re-combinations through chemical reactions. Thanks to these characteristics, carbon chemistry is very rich and diverse, which is a good point to be able to produce a molecular complex with auto-reproduction capabilities[5]. A stable environment is also required in order to keep complex molecules intact over long enough timescales. That means that it is complicated to consider the emergence of life in water clouds, for example. Their strong variability and the short life-time of the droplets make them a priori as an inhospitable environment compared to the surface of a terrestrial planet. Finally, there is no chemical interactions without any energy source. On the Earth, the main provider of energy is the Sun through the emission of photons. However, hydrothermal vents are also considered as a good environment providing water, energy under the form of heat and a solid surface. Following this idea, there is a strong interest of the community for the icy moons of the solar system, especially the ones hosting a subsurface ocean such as Europa, Ganymede, Callisto or Enceladus. This motivated two major missions toward the outer solar system: the JUpiter ICy moons Explorer (JUICE, see Grasset et al. 2013) successfully launched in April 2023 and Europa Clipper (Howell & Pappalardo 2020) planned in 2024.

This question of the conditions for the emergence of life is terribly complex, this is one of the main focus of the astrobiology field. The usual simplification done is to search for exoplanets potentially

[5]This is the most conservative definition of a life form

hosting liquid water. This is also justified by the fact that for now we can receive information from the very top of the atmosphere of exoplanets. Probing the deeper part of the planet, and eventually the surface, is still very challenging but should be achievable with reflected light spectroscopy (RISTRETTO and ANDES). Therefore, the easiest detectable bio-markers could come from life form living at the surface of a planet and adding abiotic molecules in the atmospheres. The best example of this is the production of O_2 on the Earth through photosynthesis.

1.2.2 The habitable zone - main definition

The presence of liquid water at the surface of a planet is assumed to be a required condition in the presence of detectable life. Searching for water in the liquid phase implies the definitions of 3 different climate regimes for a terrestrial planet:

- **Snowball**: If a given planet with a given atmospheric composition is too far from the host star, all the potential water is frozen due to low insolation.
- **Hot**: If this planet is too close to the host star, all the potential water is evaporated due to high insolation.
- **Temperate**: There is a range of distance for which the insolation allows water in the liquid phase on the surface of the planet.

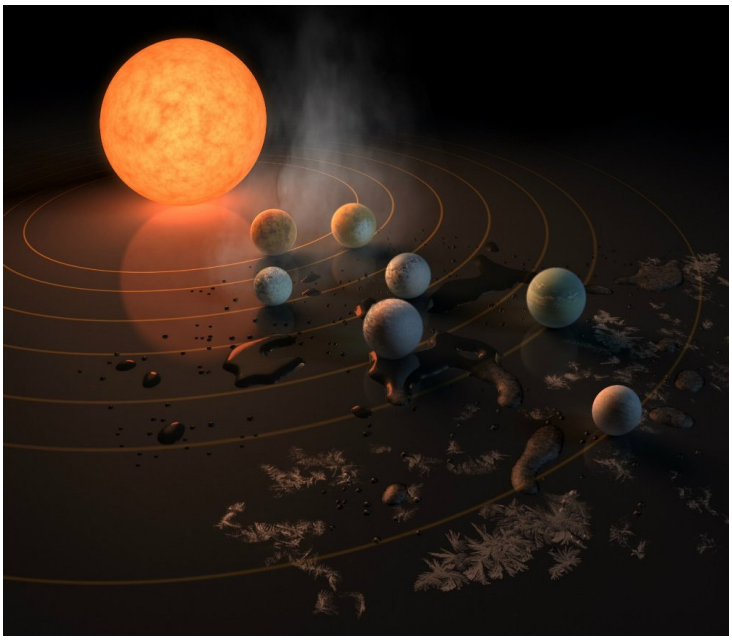


Figure 1.4: Artist's view of the TRAPPIST-1 system, illustrating the concept of HZ with the three phases of water as a function of the distance to the star. Credit: NASA/JPL-Caltech

This range of distances allowing for liquid water at the surface of the planet is called the Habitable Zone (HZ, Huang 1959 ; Hart 1978). To avoid any misinterpretation of this concept, a more neutral

denomination should be preferred, such as Temperate Zone. Indeed, the notion of habitability for exoplanets, especially when saying "habitable" could mean habitable for Earth's life. This could imply a possibility of expansion of humanity in the Universe (i.e., the possibility for life to go from a planetary system to another) which is unrealistic with technologies based on known physics. Even if life, in the sense of auto-reproducible complex molecules, could emerge, there is no planet B for Earth's life[6].

The capacity of a planet to sustain liquid water is a function of the insolation it receives, thus of the distance to its host star. The stellar type and the temperature of the star also affect the flux arriving at the top of the atmosphere (Kopparapu et al. 2013). The characteristics of the planet itself are of a great importance as well, especially the atmospheric composition (e.g., Abe et al. 2011 ; Goldblatt et al. 2013 ; Koll & Cronin 2019 ; Ramirez 2020). We see on the Earth that small variations of the CO_2 content, on the order of tens of part-per-million (ppm), strongly affect the climate (Pörtner et al. 2022). The mass of the planet also influences the global temperature by affecting the surface pressure (Kopparapu et al. 2014). On top of these three main parameters and effects, other parameters could influence the climate, thus the boundaries of the HZ. The rotation rate affects the redistribution of heat across the atmosphere (Yang et al. 2014 ; Kopparapu et al. 2017). The distribution of the continents as well as the properties of the clouds affect the Bond albedo of the planet, thus its radiative equilibrium. Last but not least, the tidal heating induced by strong gravitational forces happening in close-in planetary systems could create a forcing at the bottom of the atmosphere (e.g., Barnes et al. 2013 ; Bolmont 2018).

All these processes make a generic calculation of the HZ extremely complex. Moreover, some parameters, such as the Bond albedo of the planet, can affect the climate enough to allow different stable climate regimes at a given distance to the star. It has been shown that the Earth, at its current orbital distance, can sustain the three different climate regimes presented above: snowball, temperate and hot (e.g. Shields et al. 2014 ; Wolf & Toon 2014 ; Turbet et al. 2021). This is called climate multistability, and it is discussed more in detail in Chapter 6.

Let us consider a planet in the HZ with a liquid ocean at the surface. If this planet is virtually pushed away from the star, the polar caps will expand following the decrease of surface temperature. At some point, when the polar caps reach approximately 30° latitude (Pierrehumbert et al. 2011) a runaway glaciation is triggered by the difference of albedo between ice and liquid water. To find the outer edge of the habitable zone, so to push the runaway glaciation onset distance to larger distances, we add greenhouse gases in the atmosphere of the planet. Usually, we consider CO_2. This strong greenhouse gas seems common on terrestrial planets, as it is key on the Earth, Venus, and Mars. The outer edge of the HZ, called maximum greenhouse, is defined by the distance to the star for which the greenhouse effect of CO_2 is not sufficient to delay the runaway glaciation. Generally, this happens when the cooling due to the Rayleigh scattering of the CO_2 is stronger than the warming due to its greenhouse effect. According to Kopparapu et al. (2013), this happens at 1.67 AU for the Earth. The Rayleigh scattering is less efficient under M-dwarf irradiation, thus the maximum greenhouse is delayed for such systems (Ramirez 2018).

On the other side, if the temperate planet virtually drifts toward the star, its temperature increases. The ocean evaporates, and at some point the planet reaches a threshold for which there is enough water

[6]Courtesy of Michel Mayor

vapor in the atmosphere to absorb almost all the thermal flux from the surface. The planet is not able to cool down anymore and the temperature increases continuously, leading to the evaporation of the entire ocean. This is the runaway greenhouse process, discussed in detail in Sect. 1.3. According to Kopparapu et al. (2013), this happens at 0.95 AU for the Earth's atmosphere. These two processes are usually used to define the outer and inner edges of the HZ (Goldblatt & Watson 2012 ; Ramirez 2018) and I will expand on them in the following sections.

1.2.2.1 The inner edge

The runaway greenhouse

The inner edge of the HZ is historically studied to understand the difference between the Earth and Venus. Venus, sometimes considered as the uninhabitable sister of the Earth, has a similar mass (0.8 $M_\oplus$) and radius (0.95 $M_\oplus$) but a global temperature of about 750 K. This is due to a very thick CO_2 dominated atmosphere (90 bar) and an insolation 1.9 times higher than the one of Earth. However, in the past, the faint young Sun allowed a lower insolation on Venus, motivating studies to understand the difference of state between these two planets we observe now. The most commonly admitted scenario is that if Venus was in the HZ in the past, it underwent a runaway greenhouse process triggered by the increasing luminosity of the Sun, leading to the Venus we know (e.g., Ingersoll 1969 ; Kasting 1988). The current inner limit of the HZ is thus somewhere in between the Earth and Venus. In the continuity of these works, the first 1-D climate models allowed to compute estimates of the inner edge of the HZ of extra-solar systems (Kasting et al. 1993 ; Selsis et al. 2007 ; Kopparapu et al. 2013, 2014). More specifically, Kopparapu et al. (2013) propose a parameterized equation to easily compute the HZ boundaries as a function of the temperature of the star. A year after, Kopparapu et al. (2014) went further and explored the effect of varying the mass and gravity of the planet. The equation provided by Kopparapu et al. (2013, 2014) is largely used in the exoplanet community to statistically study habitability of large sample of planets, especially to compute the occurrence rate of detected exoplanets in the HZ (Dressing & Charbonneau 2015 ; Bryson et al. 2021 ; Bergsten et al. 2022 ; Hill et al. 2022 ; Chen et al. 2023).

Later on, more accurate estimates of the inner limit of the HZ were possible thanks to a continuous increase of climate model complexity. Indeed, 1-D climate models usually neglect the clouds and do not account properly for the global dynamics. More complex 3-D Global Climate Models (GCMs, see Sect. 1.4.3) include intrinsically 3-D processes, allowing a more accurate representation of the climate of a planet. More precisely, Leconte et al. (2013) show that the downward branch of the Hadley cells[7] reduces the humidity around the tropics. As there is less water vapor, there is less IR absorption and the planet cools down more efficiently (see also Chaverot et al. 2023 in Sect. 5.2). Consequently, the planet can host water in the liquid phase under a higher insolation than what is allowed with a 1D model, pushing the inner edge of the HZ closer to the star. This illustrates the shortcomings of using a 1D model.

The calculation of the inner edge of the HZ using a 1D model and considering the atmosphere of the Earth is presented in Fig. 1.5 by the red dashed line (Kopparapu et al. 2013). Other works studying

[7] On the Earth, there is a specific circulation named the Hadley circulation formed by a wet ascending branch at the equator and a dry descending branch at the tropics.

tidally locked planets with a GCM show an inner limit of the HZ much closer to the star (Yang et al. 2014 ; Kopparapu et al. 2016, 2017). Here the key mechanism is the cloud formation and not directly the dynamics. Indeed, for the specific case of tidally locked planets, the global circulation in the atmosphere is not the same as for fast rotators (e.g., the Earth). Some studies (Yang et al. 2013, 2014 ; Way et al. 2016 ; Kopparapu et al. 2016, 2017) showed that in this case, a thick cloud deck forms at the substellar point[8], increasing drastically the Bond albedo of the planet. This "cloud shield" delays the runaway greenhouse of tidally locked planets, pushing at the same time the inner edge of the HZ even closer to the star where the flux is higher (gray, blue, and red curves in Fig. 1.5).

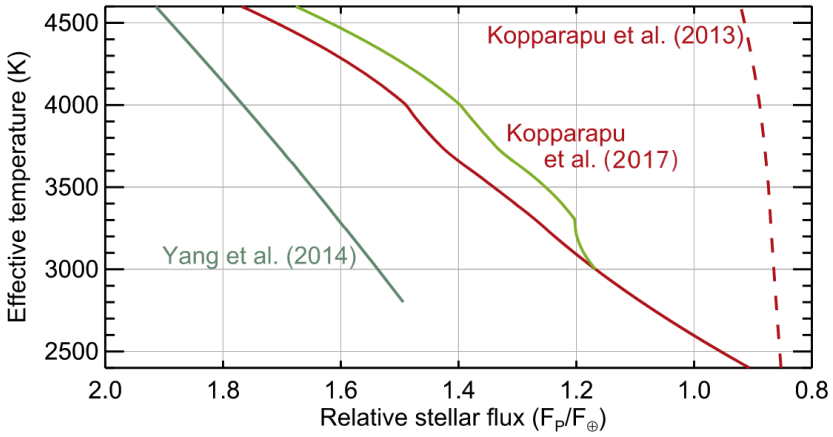


Figure 1.5: Inner limits of the HZ for different effective stellar temperature, as a function of the relative stellar flux received by the planet. The red dashed line is the inner edge estimated by using a 1-D radiative-convective model Kopparapu et al. (2013). Gray and red solid curves correspond to the inner edge of the HZ of a tidally locked planet, computed with a GCM (from Yang et al. 2014 and Kopparapu et al. 2017 respectively). The green curve corresponds to the moist state (Kopparapu et al. 2017). The figure is adapted from Kopparapu et al. (2017).

The moist greenhouse

When the ocean starts to evaporate, the high stratosphere is enriched in water vapor. The water molecules will be photo-dissociated under the effect of the X/UV stellar flux, stronger at the top of the atmosphere. Water molecules can break to produce atoms of oxygen and hydrogen. Thanks to their very light mass, hydrogen atoms can easily escape into space (see Sect. 1.5.2 for more details). The planet can lose its water through if experiencing this state named moist greenhouse (Kasting 1988). There is no consensus so far in the literature to know if this moist greenhouse is a transient state of the runaway greenhouse (with a water rich atmosphere and an evaporating ocean) or if it is a proper stable state with stable surface ocean. Some GCMs find a stable moist greenhouse preceding the runaway greenhouse (Wolf & Toon 2015 ; Popp et al. 2016), while others do not (Leconte et al. 2013). Some papers pointed out that difference in the computation of the specific humidity of the stratosphere could explain this difference (Kopparapu et al. 2017 ; Yang et al. 2019). Another possible answer is proposed by Popp et al. (2015) involving differences in the convective scheme of the models. Indeed, as the spatial resolution of GCMs is limited by the computation time, sub-grid parameterizations[9] are required to accurately

[8]Location on the planet where the flux from the star arrives perpendicularly to the surface

[9]Parameterization of the physical processes happening at a scale smaller than the minimal size of the numerical grid.

represent the small scale convection. These subtle differences could induce large differences between the models at larger scale (Yang et al. 2016).

1.2.2.2 The outer edge

The definition of the maximum greenhouse is based on the ability of greenhouse gases to delay the runaway glaciation. However, under very cold temperatures, even CO_2 is able to condense. If a part of the planet becomes cold enough to let CO_2 condense (at the poles or on the night-side of a tidally locked planet), a cold trap is formed, leading to the condensation of all the CO_2 and the complete glaciation of the planet. This can precipitate to a snowball state at a shorter distance than the maximum greenhouse (e.g., Turbet et al. 2017 ; Kadoya & Tajika 2019).

Other gases can also have a significant effect on the outer edge of the HZ. For example, Ramirez & Kaltenegger (2018) highlighted a complex effect of CH_4, delaying the maximum greenhouse for hot stars (hotter than 4500 K) and shrinking the HZ for cooler stars. Several studies showed that hydrogen can delay the maximum greenhouse thanks to spectroscopic effects, inducing an intense absorption in the infrared (Pierrehumbert & Gaidos 2011 ; Ramirez & Kaltenegger 2017). More precisely, while Kopparapu et al. (2013) estimate the outer edge of the HZ at 1.67 AU for the Earth's atmosphere, Pierrehumbert & Gaidos (2011) showed that it can be extended up to 10 AU for a Sun like star by assuming 40 bar of H_2. Ramirez & Kaltenegger (2017) computed an outer edge a 2.4 AU by considering more realistically a hydrogen pressure constrained by volcanism processes.

1.2.3 Alternative definitions of the habitable zone

The growing number of detected exoplanets[10] and the improvement of characterization methods allowed the emergence of a new field questioning the possibility of detecting extra-terrestrial life. By using knowledge of biology, chemistry and geology, one of the aim of the astrobiology field is to constrain the potential bio-markers we can detect on exoplanets. For an astronomer, such bio-markers would be a sign that there is life on a planet. For this to happen, this life must be sufficiently evolved and have colonized enough of the planet to have a significant impact on the composition/properties of the atmosphere. As one of the necessary ingredients to reach that state is the presence of liquid water, the quest for life is intimately linked with our capacity to identify planets susceptible to host surface liquid water, so to our definition of the HZ. Therefore, alternative - or additional - definitions are proposed in the literature to be more representative of the complexity of the question.

First of all, the key point of the main definition of the HZ is the presence of liquid water. This is a necessary but not sufficient condition for life to exist. Based on the radiation conditions required for photosynthesis to happen on the Earth, Hall et al. (2023) proposed to define a photosynthetic HZ. The idea is to define the virtual zone around a star for which water is in the liquid phase, and in which irradiation allows photosynthetic reactions. This condition is based on Earth's conditions, the only comparison point we have.

[10] 5,483 confirmed exoplanets on July 29th 2023, according to `https://exoplanetarchive.ipac.caltech.edu/`.

As explained in the previous section, the HZ depends on the stellar flux. The luminosity of main sequence F, J and K stars increases over time, thus the position of the HZ evolves over the lifetime of the star. Some works (e.g., Hart 1978 ; Kasting 1988 ; Underwood et al. 2003) studied this evolution, proposing the definition of a Continuous HZ (CHZ). It could be interesting to include this temporal evolution factor in the main definition of the HZ to account for the fact that life needs time to emerge.

As showed in Fig. 1.5, the position varies a lot by accounting for 3-D processes such as the clouds and the global dynamics. Using a GCM, Turbet et al. (2021) showed that for hot water-dominated planets, clouds tend to form preferentially on the night side, leaving the day-side completely cloud-free. This specific cloud pattern is optimal to keep the planet hot, with a low albedo on the day-side and a strong greenhouse effect on the clouds on the night-side. Consequently, a hot steam planet will require a very low insolation to be able to condense a surface ocean. Based on this conclusion, Turbet et al. (2023) proposed the definition of a Water Condensation Zone (WCZ), delimiting the distance to the star for which a planet can condense a water surface ocean. This is discussed more in detail in Sect. 6.3.2

As a last example of this non-exhaustive list, some studies (Gonzalez et al. 2001 ; Lineweaver et al. 2004) proposed to define a Galactic HZ (GHZ) by searching for areas in which stellar types and metallicity are favorable to host terrestrial planet. They also search for old enough stars to account for the time required by life to emerge. Based on these criteria, they constrain the GHZ to stars located between 4 and 12 kpc from the Galactic center and formed between 4 and 8 Gy ago (Lineweaver et al. 2004).

1.3 The runaway greenhouse transition: a deeper insight into the mechanisms involved

As introduced in the previous section, if a terrestrial planet with a water ocean is too close to its host star, the ocean evaporates and the global temperature increases because of the strong greenhouse effect of the water vapor. There is a threshold for which the bottom part of the atmosphere becomes optically thick enough to absorb entirely the infrared (IR) emission from the surface. In other words, there is a maximum of the thermal emission of the planet, which is named the Simpson-Nakajima limit (Simpson 1929 ; Nakajima et al. 1992). Once this threshold is reached, there is no radiative equilibrium possible anymore between the absorbed flux and the thermal emission from the planet. Consequently, the temperature increases as well as the evaporation, creating a runaway of the positive feedback which leads to the evaporation of the entire ocean. This is the so-called runaway greenhouse (Komabayasi 1967 ; Ingersoll 1969 ; Kasting 1988 ; Goldblatt & Watson 2012). It is an unstable transition characterized by a continuous radiative imbalance. When the entire ocean is evaporated, the global temperature reaches 1800 K approximately for an Earth's size ocean (Kopparapu et al. 2013 ; Goldblatt et al. 2013 ; Turbet et al. 2019 ; Boukrouche et al. 2021) and the planet starts to emit in the visible (Goldblatt et al. 2013 ; Boukrouche et al. 2021). Water vapor is optically thinner in these wavelengths, thus the thermal emission of the planet increases again, allowing a post-runaway steady state with a hot and steam atmosphere (e.g., Turbet et al. 2021).

From a general point of view, the runaway greenhouse separates two populations of planets with

very different characteristics: temperate worlds and hot post-runaway planets. Temperate planets could share similar properties with the Earth, for example by hosting a water surface ocean. Post-runaway planets have a puffed steam dominated atmosphere, increasing their visible size compared to the temperate ones (Turbet et al. 2019). Their temperature ranges are from few hundreds of Kelvin to few thousands, depending on their water vapor content (Hamano et al. 2013 ; Boukrouche et al. 2021 ; Turbet et al. 2019 ; Selsis et al. 2023). Due to these conditions, a thick cloud deck is formed on the night-side at the top of the atmosphere (Turbet et al. 2021).

Multiple studies estimated the conditions triggering the runaway greenhouse for small terrestrial planets using 1-D models (Kasting et al. 1993 ; Kopparapu et al. 2014, 2013 ; Goldblatt et al. 2013 ; Ramirez et al. 2014 ; Yang et al. 2016 ; Koll & Cronin 2019 ; Chaverot et al. 2022) or 3-D models (Yang et al. 2013 ; Leconte et al. 2013 ; Wolf & Toon 2014, 2015 ; Popp et al. 2016 ; Kopparapu et al. 2016, 2017). Estimating the precise insolation for which a planet goes in runaway for a specific atmospheric composition is highly relevant to determine the HZ inner limit for exoplanets but also in the context of the Earth. A question could be to know the pressure of CO_2 required to significantly change the inner edge of the HZ (e.g., Goldblatt et al. 2013 ; Ramirez et al. 2014). Or for a given quantity of CO_2 in the atmosphere, when will the Earth go in runaway[11] ? Subtle spectroscopic processes could be key to compute precisely the radiative balance near the onset of the runaway greenhouse (e.g., Chaverot et al. 2022). As shown by multiple studies (Leconte et al. 2013 ; Yang et al. 2013 ; Kopparapu et al. 2017), the clouds and the global dynamics largely affect both the thermal emission and the Bond albedo of a planet entering the runaway greenhouse. These processes cannot be neglected for a precise understanding of the onset of this radiative imbalance.

1.4 Climate models

All the questions related to habitability and detection of bio-signatures required a great understanding of the climate of the planets we target. A solution for this is to simulate virtually the climate of exoplanets, by using various numerical climate models. The aim of this section is to propose an overview of the main type of models existing in the literature, with a focus on the models I developed and used during my PhD.

To study the atmosphere of a planet, different types of numerical models were developed along the years following the evolution of computer power. Initially described by analytic equations (0-D models), our understanding of the atmospheric structure improved thanks to simple models as 1-D radiative-convective models (Sect. 1.4.1). Later, the young exoplanet field has benefited from the work and the tools developed to study the Earth, especially complex 3D models named Global Climate Models (GCMs) (Sect. 1.4.3). At the same time, other intermediate types of models (in terms of complexity) were developed, such as Energy Balanced Models (EBM) (Sect. 1.4.2). Many more types of models exist even if they are not presented in this work, such as 1-D time marching models, 1.5-D EBMs or 2-D EBMs. Even if there is a clear hierarchy of complexity, all the subtlety is to identify the right type of

[11] Knowing that the luminosity of the Sun increases during its main sequence.

model among all of them to answer the scientific question asked. Simple 1-D models are able to explore a large parameter space, while GCM can highlight complex 3-D effects of particular cases (i.e., tidally locked planets) or of global processes such as the runaway greenhouse. There are several GCMs in the literature, developed with different physical setups including, for example, a fully dynamical ocean or photochemistry. Taking advantage of this variety of models is necessary to build an accurate and complete understanding of exoplanets.

1.4.1 1-D inverse radiative-convective models

1-D inverse radiative-convective models are the historically first climate models (Manabe & Wetherald 1967) developed and used to study in detail planets and exoplanets (Kasting 1988). The assumption is that one single vertical column of atmosphere represents well the behavior of the entire atmosphere. The global 3-D circulation is neglected (or parameterized) and the temperature profile is supposed to be at the hydrostatic equilibrium. As cloud formation is driven by the global dynamics and by the inhomogeneous distribution of the humidity, their effects are usually neglected as well. It is possible to parameterize them in specific cases, but this makes the models less generic. For instance, a parameterization based on Earth cloud measurements is not necessarily valid for another terrestrial planet orbiting a M-dwarf such as TRAPPIST-1.

These models are made of two parts (see Sect. 4.1.1 for a detailed description). First, assuming boundary conditions at the surface (temperature, partial pressures of the gases), the temperature profile is computed following an adiabatic lapse rate, which defines how temperature depends on pressure. Second, knowing the atmospheric structure, a radiative transfer calculation is performed. To do so, opacity data for various pressure, temperature and mixing ratio conditions are required. From these data, it is possible to compute both the thermal emission of the planet, also known as Outgoing Thermal Radiation (OTR), and the incoming flux absorbed by the atmosphere, known as Absorbed Stellar Radiation (ASR) (see Sect. 4.1.1.2). There is no temporal evolution in 1-D inverse radiative-convective models, meaning that the OTR and the ASR are not necessary equal (i.e., the system is not at the equilibrium). These fluxes are determined by the surface temperature and pressure. The main advantages and disadvantages of this category of models is presented in Table 1.1. I developed and used this type of model as discussed in Chapter 4.

Table 1.1: Advantages and disadvantages of 1-D radiative-convective models

Pros	**Cons**
Easy to use and flexible	No global dynamics (No latitude/longitude)
Computationally inexpensive	No consistent calculation of the clouds
Adapted to explore a large parameter space	No temporal evolution
	Convective profile forced below the stratosphere

1.4.2 Energy balance models

There are different levels of complexity for energy balance models (EBM). The simplest EBMs use globally averaged quantities (0-D EBMs) while the more complex use a latitude/longitude grid (2D EBM). In between these two class of EBMs, 1-D EBMs which consider only the latitudinal dimension are a good compromise between accuracy and efficiency. Another intermediate level of complexity can be used by combining two 1-D EBMs, typically to represent the day-side and the night-side of a tidally locked planet, with a parameterization to account for the circulation between the two sides (1.5D EBMs).

In this section I focus on 1-D latitudinal EBMs where the planet is represented by a single latitude strip (see Fig. 1.6). Therefore, there is no vertical extent contrary to 1-D radiative-convective models presented previously. The assumption here is that for fast rotators (i.e., rotation rates similar to the one of the Earth), the longitudinal heat redistribution is efficient enough to be averaged. In other words, that means that the behavior of the entire atmosphere is well represented by a latitude strip, averaged over the longitude. The heat transport and the radiative balance are computed using Eq. (1.1) (Williams & Kasting 1997 ; Spiegel et al. 2008 ; Dressing et al. 2010):

$$C\frac{\delta T(x,t)}{\delta t} - \frac{\delta}{\delta x}\left(D_x(1-x^2)\frac{\delta T(x,t)}{\delta x}\right) + I(T) = S(1-A(T)), \tag{1.1}$$

where x is the latitudinal coordinates of the grid cell, t is the time, C is the effective heat capacity of the atmosphere (which includes also information about the ground), D_x the diffusion coefficient, I the thermal emission (OTR), S the incoming stellar radiation and A the albedo. The diffusion factor D_x is a key factor to adapt the model to different heat redistributions representative of different atmospheric compositions and different rotations (e.g., Pierrehumbert et al. 2011). As EBMs are focused on the study of the radiative balance of the atmosphere (similarly to 1-D radiative-convective models presented in Sect. 1.4.1), important adjustable parameters are the absorbed and emitted fluxes. The OTR (I in Eq. (1.1)) is here assumed to be only a function of the surface temperature. Usually, the absorbed flux is only function of the surface albedo, which can include a forcing due to the cloud coverage. That means that the radiative effect of the clouds (greenhouse effect in the IR and high albedo in the visible) is not consistently computed. Because of this, the parameterization of the OTR and ASR is a subtle adjustment that is one of the main sources of differences between the different models.

These models better represent the dynamics of the climate thanks to their latitudinal dimension, but this requires adjustment of the diffusion coefficient (D_x in Eq. (1.1)) to the different atmospheric compositions and planetary rotations studied. Also, there is no internal variability of these models without any additional parameterization. That means that the temporal evolution of the model is predictable and does not represent, for example, the variability of the cloud coverage, or the non-linear interactions between the atmosphere and the ocean.

EBMs are numerically inexpensive, thus they are useful to explore a large parameter space of processes influencing the climate, such as the contribution of the vegetation to the equilibrium of the climate. The main advantages and disadvantages of this category of models are presented in Table 1.2. I developed and used this type of model as discussed in Chapter 6.

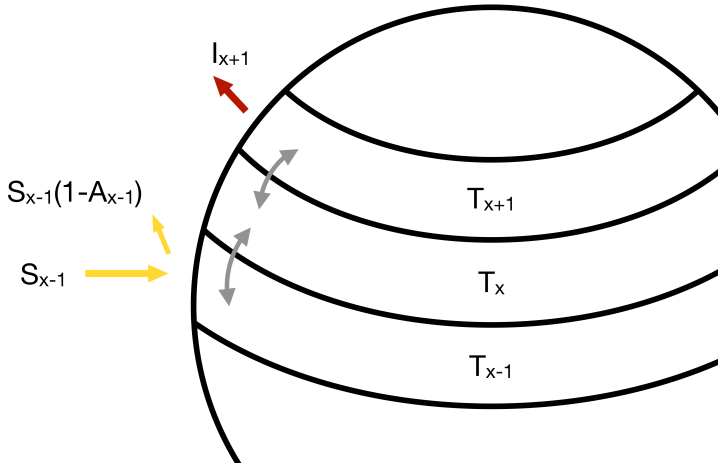


Figure 1.6: Schematic view of an EBM. The different quantities correspond to the physical variables presented in Eq. (1.1). The gray arrows represent the heat transport along the latitude.

Table 1.2: Advantages and disadvantages of 1-D EBMs

Pros	**Cons**
Easy to use	No vertical and longitudinal dimensions
Computationally inexpensive	Parameterization of the OTR and ASR
Parameterization of the dynamics	Parameterization of the dynamics
Temporal evolution	No consistent calculation of the clouds
	No internal variability

1.4.3 The Generic-PCM

The most advanced type of models are the GCMs. The Generic-PCM I used during my PhD (see Chapter 5) was originally developed at the *Laboratoire de Météorologie Dynamique* (LMD) under the name of LMD-Generic GCM (Forget et al. in prep.). The model was historically developed to study the Earth and the anthropological global warming. Then, it was adapted to study Mars in 1993 (Hourdin et al. 1993) and later a more generic version was developed to study early Mars and finally exoplanets. The aim of GCMs is to model as accurately as possible the climate of a planet by accounting for complex 3-D processes, such as the global dynamics, the cloud formation and the radiative effect of different gases.

An overview of the main processes of the Generic-PCM is presented in Fig. 1.7. More precisely, our model includes the following components (Forget et al. in prep.).

- **A 3-D hydrodynamical "core"** to solve the primitive fluid dynamical equations (Navier-Stokes equations) for a rotating sphere. These equations are solved in a latitude $\times$ longitude $\times$ altitude grid. The horizontal typical resolution is 48x64 (latitude $\times$ longitude) grid points, corresponding to 3.75° latitude (417 km) by 5.625° longitude (626 km at the equator). A limit of this type of grid is that the area of the cells near the poles decreases, causing numerical constrains[12]. Therefore,

[12]The numerical time-step Δt is determined as a function of the horizontal resolution Δx following $\frac{u\Delta t}{\Delta x} < 1$, where u is the typical wind speed amplitude (in m.s^{-1}). If the resolution increases, the time-step increases as well. This is the Courant-Friedrichs-Levy (CFL) condition.

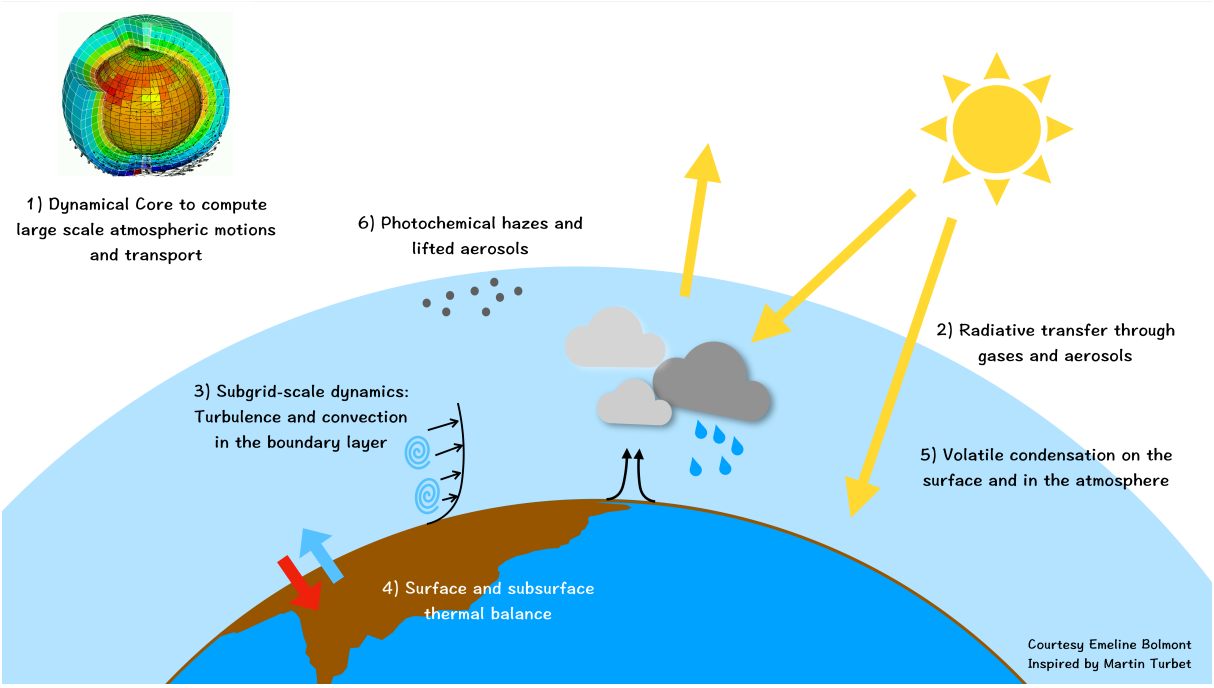


Figure 1.7: Scheme of the main physical processes of the Generic-PCM.

a latitude filter is applied to solve this issue and keep a roughly constant area per grid around the whole globe. For my work, I used the classical latitude/longitude grid. To improve the weaknesses of the classical grid, a new grid named DYNAMICO (Dubos et al. 2015) has been developed. This new grid also improves the parallel computing efficiency, a critical aspect of GCMs. It is a hexagonal mesh organized around an original icosahedral mapping that is much more uniform than the original latitude/longitude grid.

- **A radiative transfer calculation** through gases and aerosols, assuming the plane-parallel and two-streams approximations (Meador & Weaver 1980). First, the plane parallel approximation assumes that the horizontal resolution of the model is precise enough to neglect the local curvature of the planet in a grid cell. Second, the two-streams approximation (Meador & Weaver 1980 ; Toon et al. 1989) means that photons can propagate upward or downward in one single atmospheric column. The thermal flux from the planet and the absorbed stellar radiation coming from the star are computed separately for efficiency. A detailed description of the calculation of the radiative transfer for aerosols and clouds is given in Madeleine (2011). The radiative transfer is the most numerical expensive step, thus the Generic-PCM uses the correlated-k approach (see Sect. 2.3.2) to compute the opacity of the atmosphere in each grid column.

- **Parametrizations of the vertical mixing and transport** induced by the turbulence and the convection, not resolved by the dynamical core (Forget et al. 1999). The global dynamics is resolved by the dynamical core, but smaller scales motions, such as small eddies, are not consistently computed because they happen inside a grid cell (and not across grid cells). Therefore, there is a need to parameterize them based on other models resolving the small scale processes, such as cloud

resolving models (Lefèvre et al. 2021).

- **A thermal model of the surface** and near subsurface for the storage and the conduction of the heat for terrestrial planets, and/or the properties of the ocean if there is. The Generic-PCM includes an optional simple two-layers ocean (Codron 2012 ; Charnay et al. 2013) accounting for heat and sea ice transport.

- Schemes to account for the **phase change of volatiles** both on the surface and in the atmosphere. This includes formation of clouds, precipitation, and aerosols lifted by the winds. A complete description of the water cycle can be found in Leconte et al. (2013). A particularity of the Generic-PCM is that it has been designed to be able to deal with water as a major component (Leconte et al. 2013). This made possible the work presented in Chapter 5. Due to required subtle micro-physics parameterizations, cloud formation is the main source of differences between the models (Wolf & Toon 2015 ; Yang et al. 2019 ; Sergeev et al. 2021).

From a more general point of view, as done in most of the GCMs, the Generic-PCM considers the hydrostatic equilibrium, meaning that vertically-propagating acoustic oscillations are neglected. A second global approximation is to consider that the depth of the atmosphere is small compared to the radius of the planet. This is named the shallow-atmosphere assumption. This approximation is valid for the Earth (or similar planets with a thin atmosphere) but could be a strong inaccuracy for planet with an extended atmosphere compared to their radius, such as Titan (Tort 2015)[13]. This could also be an issue for post-runaway planets with an extended water dominated atmosphere (see Sect. 1.3 and Goldblatt 2015). The main advantages and disadvantages of this category of models are presented in Table 1.3.

Table 1.3: Advantages and disadvantages of GCMs

Pros	**Cons**
Most accurate and complete climate models	Subgrid parameterization
Temporal evolution	Very complex numerical tool
Effects of the clouds and of the dynamics	Computationally expensive
Consistent calculation of all the physical processes	Needs to be run on computer clusters

1.5 Toward a complete understanding of terrestrial planets

My work focuses on the study of the climate through climate modelling that is concerning roughly the atmosphere from the surface of the planet to approximately an altitude corresponding to a pressure of 10 Pa (about 64 km on Earth). Boundary conditions of climate models are thus the surface exchanges between the atmosphere and the rocky interior (Sect. 1.5.1) and the physical processes happening at the very top of the atmosphere, that is in the exosphere (Sect. 1.5.2).

[13] DYNAMICO has been also developed to overcome this issue.

1.5.1 Atmosphere-interior interactions

The evolution of the rocky interior is extremely important during the formation of the planet. The heat available in the interior of the planet and the efficiency of its transfer toward the surface determines the state of this surface, and will in particular have a crucial role on sustaining a magma ocean over geological time scales. This magma ocean stage is a key process to constrain the potential atmospheric composition of exoplanets. Indeed, the volatiles degassing of the early magma ocean determines the composition of the secondary atmosphere (Lebrun et al. 2013 ; Hamano et al. 2013 ; Dorn et al. 2018 ; Lichtenberg et al. 2022 ; Salvador & Samuel 2023). For this reason, since a few years a real effort is done in developing climate models coupling consistently the atmosphere and the interior, in order to study precisely the cooling processes of the magma ocean of young planets (Bower et al. 2019 ; Spaargaren et al. 2020 ; Lichtenberg et al. 2021 ; Wang et al. 2022 ; Krissansen-Totton & Fortney 2022). Moreover, as discussed in Sect. 5.4, there is a debate in the literature to know if post-runaway states could potentially be hot enough to melt the surface. If this happens, gas exchanges between the magma ocean and the atmosphere will be reactivated, modifying strongly the atmospheric composition. A significant loss of water through dilution into the magma ocean could strongly affect the long term evolution of post-runaway planets. Therefore, there is a real interest to consider interactions between the atmosphere and the rocky interior in order to have an accurate overview of the potential pathway of terrestrial planets living a runaway greenhouse process.

After the formation of the planet, when the rocky interior is solidified, volcanic outgassing can strongly modify the atmospheric composition. The evolution of the content of greenhouse gases (like CO_2) due to interior outgassing takes place over geological timescales, but this can strongly influence the long term evolution of the planet. Tidal forces, particularly strong in close-in systems, can intensify this volcanism. The archetype of tidally induced volcanic active world in our Solar System is Io, owing to its strong interactions with Jupiter. These tidal forces can be responsible for an intense internal heat flux, estimated to be of the order of 2.5 $W.m^{-2}$ (e.g., Veeder et al. 1994 ; Lainey et al. 2009) in the case of Io. This can also delay the cooling of the early magma ocean existing at the formation of the planet.

A large number of detected exoplanets orbit close to their host star, thus they are more prone to experience strong tidal forces (e.g., Peterson et al. 2023). Even if the tidal heat flux is much lower than 1 $W.m^{-2}$ on Earth (Turcotte & Schubert 2002), it can reach more than a few $W.m^{-2}$ for the inner planets of the famous TRAPPIST-1 system, where tidal dissipation is expected to be the primary internal heat source (e.g., Turbet et al. 2018 ; Makarov et al. 2018 ; Barr et al. 2018 ; Bolmont et al. 2020). Such values are not negligible in the radiative balance of the planet and could affect the position of the inner edge of the HZ.

1.5.2 Atmospheric escape

Several processes happening at the top of the atmosphere could affect its composition and characteristics. More precisely, molecules constituting the high atmosphere can escape toward space, reducing the atmospheric content and modifying the mixing ratio between heavy and light elements. (e.g., Owen

2019 ; Gronoff et al. 2020 ; Modirrousta-Galian & Korenaga 2023)

From a very simplistic point of view, molecules in the atmosphere have a velocity following a Maxwell-Boltzmann distribution, as a function of the temperature. At the top of the atmosphere, if the velocity of a particle exceeds the escape velocity (determined by the gravitational attraction of the planet), it will continue its trajectory toward space and will be lost for the planet. This is called thermal escape, and it is the most efficient escape process (Gronoff et al. 2020). There are two main regimes of this thermal escape: 1) the energy-limited regime for which the maximum escape rate is given by the incoming flux from the star, 2) the diffusion-limited regime for which the reservoir of light elements (e.g., H_2) dragged upward by the atmospheric dynamics is the limitation factor (see Gronoff et al. 2020 for more details). There are also several non-thermal processes which can lead to atmospheric escape (Owen 2019 ; Gronoff et al. 2020). First, under the effect of high UV fluxes (extreme and X-UV), exothermic chemical reactions could happen in the ionosphere of the planet, providing enough kinetic energy for the escape of non-ionised constituents. This process is more efficient for highly irradiated planets, that is usually planets orbiting closely to their host star. Ionized atoms can also be dragged toward space under the effect of the magnetic field of the star. This is also more efficient for close-in systems (e.g., Cohen et al. 2015).

Atmospheric escape is particularly studied to understand the gap in radius (named the radius valley, see Fulton et al. 2017) between observed populations of volatile-rich Neptune size planets and smaller terrestrial bodies with a thin atmosphere (e.g., Attia et al. 2021 ; Modirrousta-Galian & Korenaga 2023). This process is also of major importance for close-in systems with planets receiving high UV fluxes. Several works estimated the atmospheric escape of planets of the TRAPPIST-1 system (e.g., Bolmont et al. 2017 ; Bourrier et al. 2017), in order to infer their potential atmospheric composition. Another boiling question is to know if planets in the HZ but orbiting close to their star (or very active star) can retain water in their atmosphere, or if they lose their water reservoir through photodissociation then atmospheric escape (Tian et al. 2018 ; Johnstone 2020 ; Nakayama et al. 2022). This question is particularly relevant for planets in a moist greenhouse state, with a water rich stratosphere. This is also a key point to study the long-term stability of post-runaway states, as discussed in Sect. 5.4.

Atmospheric escape of exoplanets was originally studied for Neptune-size planets (e.g., Lecavelier Des Etangs 2007) assuming atmospheres dominated by H_2, H and H_e. Under such conditions, following the energy limited assumption, the Extreme and X Ultra-Violet efficiency (EUV and XUV), that is the absorption efficiency of the considered atoms and molecules, is about 10% (e.g., Lopez et al. 2012 ; Shematovich et al. 2014). However, for small rocky exoplanets with atmospheres made of heavier molecules (e.g., H_2O), this XUV should be reduced to about 1% according to Ercolano & Clarke (2010) and Lopez (2017). This factor accounts for direct escape of water, but does not change the potential escape rate of H_2 created by photo-dissociation of H_2O. Without accounting for this difference in composition, the escape rates of terrestrial planets could be largely overestimated when studying post-runaway states, for example.

1.6 Organization of the manuscript

In this chapter, I presented the main concepts and knowledge required to go through the science presented in this manuscript. The questions around the definition of habitability and the understanding of the small terrestrial exoplanets we start to detect motivated this work, and the deep investigation of the runaway greenhouse I did. The various climate models existing in the literature or under development are useful tools to try to explain observations. They can also pave the way for future observations.

This manuscript is organized in three parts covering the three main topics I studied during my PhD. First of all, I discuss spectroscopy, from theory to the numerical calculation of opacity data required by climate models. In the second part, I present a study of the runaway greenhouse done using first a 1-D model and then revisited with a 3-D climate model. Finally, in the last part I discuss the notion of climate multistability.

Part I

Absorption spectroscopy

Chapter 2

Absorption spectroscopy for climate modeling

Contents

2.1 Fundamental notions of spectroscopy 26

2.2 State-of-the-art 26

2.2.1 Line intensity 26

2.2.2 Line broadening 27

2.2.3 Shape of the absorption lines 28

2.2.4 Collision induced absorption and dimers 31

2.2.5 The challenge of gas mixtures 32

2.3 From high resolution spectra to opacity data 33

2.3.1 Mean-Rosseland and gray calculation 33

2.3.2 The correlated-*k* approach 34

2.1 Fundamental notions of spectroscopy

In the early 1900s, a fundamental revolution happened, initiated by Max Planck. While energy was considered as a continuous quantity, Planck, then followed by Niels Bohr, Albert Einstein, Louis de Broglie and many others, proposed a theory in which energy is made of small discrete quantities: the old quantum theory. This has led later to modern quantum mechanics. The consequence of a discrete distribution of energy is quite spectacular for molecules, introducing the notion of excitation levels at precise values. Molecules absorbing/emitting energy (i.e., photons) at very specific values absorb/emit light at very specific wavelengths. If we know the quantum response of a molecule absorbing energy under the form of a photon, we can thus determine its spectral signature. This is absolutely key in the quest of exoplanet characterization as discussed in Sect. 1.1.2, because one of the main information we get is the light passing through the atmosphere. Therefore, this light can keep the signature of the different molecules there is in the atmosphere of the planet. However, the aim of this chapter is to understand how it is possible to produce opacity data for different gas mixtures, that is different kind of atmospheres, usable by climate models.

2.2 State-of-the-art

2.2.1 Line intensity

The absorption of a photon induces a transition to a higher rotational or vibrational level, or a combination of both (ro-vibrational level). Absorption of energy can also raise an electron of the molecule to a higher electron energy, which is the electronic transition. While ro-vibrational level can be populated with low energy photons (IR photons), electronic transition requires much more energy to be exited (UV photons). The aim of this chapter is to discuss IR spectroscopy, which is focused on ro-vibrational transitions.

By absorbing multiple photons, a molecule can populate multiple energy levels. By emitting a photon, an excited molecule will release an energy ΔE[1] equal to $hc\nu$ where h is the Planck constant, c the speed of light and ν the wavenumber of the photon. This creates a transition line (in absorption or emission) at the wavenumber ν. The sum of all the individual lines at different wavenumbers form a forest of lines, constituting the absorption or emission spectrum. The intensity of each absorption - or emission - line (S_{ij} in $\mathrm{cm}^{-1}/(\mathrm{molec\ cm}^{-2})$ corresponding to a transition between energy levels i and j (at the reference temperature T_{ref}) is given by the following equation (Rothman et al. 2005) and used in the HITRAN[2] database:

$$S_{\mathrm{ij}}(T_{\mathrm{ref}}) = I_{\mathrm{a}} \frac{A_{\mathrm{ij}}}{8\pi c \nu_{\mathrm{ij}}^2} \frac{g_j e^{-hcE_i/k_{\mathrm{B}}T_{\mathrm{ref}}} \left(1 - e^{-hc\nu_{\mathrm{ij}}/k_{\mathrm{B}}T_{\mathrm{ref}}}\right)}{Q(T_{\mathrm{ref}})} \tag{2.1}$$

[1] The difference of energy between the two excitation levels of energy E_{i} and E_{j}: $\Delta E = E_{\mathrm{i}} - E_{\mathrm{j}}$ with $E_{\mathrm{i}} < E_{\mathrm{j}}$.

[2] `https://hitran.org/docs/definitions-and-units/`

where I_a is the natural isotopic abundance of the molecule, A_{ij} is the Einstein A-coefficient (coefficient of spontaneous emission, in s^{-1}), E_i the lower-state energy of the transition (cm^{-1}), g_j the upper statistical weight[3] and ν_{ij} the wavenumber of the spectral transition (cm^{-1}) in vacuum. $Q(T)$ is the total internal partition sum, that is the sum over all the allowed transitions[4]:

$$Q(T) = \sum_k g_k e^{-hcE_k/k_B T} \tag{2.2}$$

where $g_k \equiv g_{ij}$ is the statistical weight for the energy level E_k. Equation 2.1 is computed at a reference temperature $T_{ref} = 296\,K$. However, it is possible to compute the intensity of an absorption line (S_{ij} in $cm^{-1}/(molec\ cm^{-2})$) at a temperature T by deriving the following equation from Eq. (2.1):

$$S_{ij}(T) = S_{ij}(T_{ref}) \frac{Q(T_{ref})}{Q(T)} \frac{1 - e^{\frac{-hc\nu_{ij}}{k_B T}}}{1 - e^{\frac{-hc\nu_{ij}}{k_B T_{ref}}}} e^{\frac{-hcE_i}{k_B}\left(\frac{1}{T} - \frac{1}{T_{ref}}\right)} \tag{2.3}$$

All the parameters of these equations are provided by the HITRAN database (Rothman et al. 2005, 2013 ; Gordon et al. 2017, 2021) allowing to compute the absorption spectra of a wide variety of molecules, and for various pressure/temperature conditions.

2.2.2 Line broadening

The absorption lines are not Dirac functions, but they have a natural broadening given by quantum physics laws. More precisely, the Heisenberg uncertainty principle ($\Delta t \Delta E' \geq \frac{\hbar}{2}$) determines the maximum lifetime of an isolated excited molecule, where $\Delta E'$ is associated with the uncertainty on the difference of energy between two excited levels[5] and Δt the duration lifetime of the highest excited level. As every energy transition corresponds to a very specific wavelength, $\Delta E' \neq 0$ induces a natural width of the absorption line. Moreover, the width of the absorption line is inversely proportional to the lifetime of the excited level as $\Delta E' \geq \frac{\hbar}{2\Delta t}$. This natural broadening is valid for an isolated molecule without any velocity. In a gas, at a given pressure and temperature, two other mechanisms broaden the absorption lines:

- When a molecule is not isolated, collisions happen in the gas and the lifetime of excited states is given by the mean free path between two collisions. It is shorter than the timescale of spontaneous emissions, and it depends on the pressure. This induces a **pressure broadening** of the absorption lines which is usually larger than the natural broadening.
- When the temperature of a gas is not zero, the velocity of the molecules follows a Maxwell-Boltzmann distribution (function of the temperature). This induces a broadening of the absorption lines through the Doppler effect: the **Doppler broadening**.

These two broadening sources, and especially the pressure broadening, overshoot largely the natural broadening in planetary atmosphere conditions. However, in the exosphere the pressure is so low that

[3] The number of degeneracy of the transition, that is the number of transitions with the exact same energy level.
[4] This is a statistical weight used to calculate the intensity of an absorption line induced by a given transition.
[5] $\Delta E'$ is different from ΔE the energy released by the transition between two excited levels.

collisions almost never happen. In such conditions, spectroscopic processes are not considered at the Local Thermal Equilibrium[6] (LTE) thus modifying the position and the intensity of absorption or emission lines. As this work is focused on the bottom part of the atmosphere, we do not discuss more of these processes in this manuscript (see for example Wright et al. 2022 for discussions on non-LTE processes). At the first order, the effect of the temperature is to increase the line intensity (Eq. 2.3 is only function of the temperature) while an increase of pressure broadens the lines and flattens the absorption spectrum. This is driven by the fact that the pressure broadening is more efficient than the Doppler broadening in pressure/temperature conditions of atmospheres of terrestrial planets.

2.2.3 Shape of the absorption lines

2.2.3.1 Line-center

As described above, the shape of an absorption line is a function of its intensity, but also of the pressure and temperature conditions. We define this shape as a function of the distance to the line-center, and following a function $f(\Delta\nu, T, P)$, where $\Delta\nu = \nu - \nu_{ij}$ is the distance to the line-center located at ν_{ij} (in cm^{-1}). The absorption cross-section $\sigma_{\mathrm{abs}}(\Delta\nu, T, P)$ (in $\mathrm{cm}^2.\mathrm{molec}^{-1}$) is given by Eq. (2.4).

$$\sigma_{\mathrm{abs}}(\Delta\nu, T, P) = S_{ij}(T) f(\Delta\nu, T, P) \tag{2.4}$$

A convenient quantity derived from Eq. (2.4) is the absorption coefficient $k_{\mathrm{abs}}(\Delta\nu, T, P)$ (in cm^{-1}) defined as the following (Turbet 2018):

$$k_{\mathrm{abs}}(\Delta\nu, T, P) = N\sigma_{\mathrm{abs}}(\Delta\nu, T, P) = \frac{P}{10^6 k_{\mathrm{B}} T}\sigma_{\mathrm{abs}}(\Delta\nu, T, P) \tag{2.5}$$

where N is the number of gas molecules per volume unit (in $\mathrm{molec}^{-1}.\mathrm{cm}^{-3}$). This is expressed in Eq. (2.5) as a function of the pressure and the temperature by using the perfect gas law, with P (in Pa) the partial pressure and T (in K) the temperature.

The analytical function describing the line shape determined by pressure broadening is the Lorentz profile:

$$f_L(\Delta\nu, T, P) = \frac{1}{\pi}\frac{\gamma(T,P)}{\gamma^2(T,P) + (\Delta\nu - \delta(P_{\mathrm{ref}})P)^2} \tag{2.6}$$

The pressure has an effect on the position of each individual lines and is taken into account through the $\delta(P_{\mathrm{ref}})$ coefficient provided by HITRAN. The half-width at half-maximum (HWHM) of pressure broadening $\gamma(p,T)$ is computed for a mixture with $n_{\mathrm{foreign}} + 1$ gases using the following equation (Turbet 2018):

$$\gamma(p,T) = \left(\frac{T_{\mathrm{ref}}}{T}\right)^{n_{\mathrm{self}}} \gamma_{\mathrm{self}}(P_{\mathrm{ref}}, T_{\mathrm{ref}}) P_{\mathrm{self}} + \sum_{\mathrm{f}=1}^{n_{\mathrm{foreign}}} \left(\frac{T_{\mathrm{ref}}}{T}\right)^{n_{\mathrm{f}}} \gamma_f(P_{\mathrm{ref}}, T_{\mathrm{ref}}) P_{\mathrm{f}} \tag{2.7}$$

[6] The system cannot be considered at thermodynamic equilibrium, even locally.

where $\gamma_f(P_{\text{ref}}, T_{\text{ref}})$ and $\gamma_{\text{self}}(P_{\text{ref}}, T_{\text{ref}})$ are the HWHM of the foreign and the self pressure broadening at reference pressure and temperature from HITRAN, n_{f} and n_{self} are the temperature dependency exponents and P_{f} and P_{self} are the partial pressures.

To account for the Doppler broadening, a Gaussian profile is indicated:

$$f_G(\Delta\nu, T) = \sqrt{\frac{\ln 2}{\pi\alpha_D^2}} e^{-\frac{\ln 2 \Delta\nu^2}{\alpha_D^2}} \tag{2.8}$$

where $\alpha_D(T)$ is the HWHM defined as:

$$\alpha_D(T) = \frac{\nu_{ij}}{c}\sqrt{\frac{2\text{N}_\text{a} k_\text{B} T \ln 2}{M}} \tag{2.9}$$

with M the molar mass of the absorber and N_a the Avogadro constant. In a physical gas, both pressure and Doppler broadening are impacting the absorption line. The most accurate way to account for this combined effect is to use a Voigt profile, which is a convolution of a Lorentz and a Gauss function. As there is no analytical solution for this, numerical tools are required to compute such realistic profiles. Moreover, the Voigt profile is accurate close to the line-center where the profile is proportional to P. Further in the wings, the absorption is proportional to P^2 and it does not follow an analytical function anymore, thus it needs to be corrected.

2.2.3.2 Farwings and χ factors

As written in the previous section, the dependency to the pressure near the center of the line is not the same as the farwings. The line-center is proportional to P while the farwings are proportional to P^2. Therefore, the contribution of the continuum (i.e., the sum of each of the farwings of each individual line) is much more significant at high pressures. Unfortunately, the actual shape of the farwings does not correspond to a Voigt profile or to a Lorentz profile, thus corrections factors need to be used to account for differences between theoretical profiles and lab measurements. Such correction factors, named χ factors, are a function of the distance to the line-center. Close to the core of the line, where experimental measurements are usually in accordance with a Voigt profile, χ=1. In the wings, where the Voigt profile is no more accurate, $\chi > 1$ values defined a "super-Lorentzian" profile, while $\chi < 1$ values are named "sub-Lorentzian" profiles.

A classical definition of the continuum is given by Tran et al. (2018), as the sum of the absorption coefficient of the farwings $k_\chi(\Delta\nu, T, P)$ (in cm^{-1}), including χ factor corrections, over the entire spectrum:

$$\begin{aligned} k_\chi(\Delta\nu, T, P) = \frac{\rho_{\text{tot}} x_X}{\pi} \sum_n S_n(T) \exp\left(\frac{hc\Delta\sigma}{2k_\text{B}T}\right) \times \frac{1-\exp\left(-\frac{hc\sigma}{k_\text{B}T}\right)}{1-\exp\left(-\frac{hc\sigma_n}{k_\text{B}T}\right)} \times \frac{\sigma}{\sigma_n} \\ \times \sum_{\text{Pert=X,Y}} \frac{\gamma_n^{X-\text{Pert}}(T)\chi^{X-\text{Pert}}(T, |\Delta\sigma|)}{[\Delta\sigma - \delta_n^{X-\text{Pert}}(T)]^2 + [\gamma_n^{X-\text{Pert}}(T)]^2} \end{aligned} \tag{2.10}$$

with $S_n(T) \equiv S_{ij}(T)$ is the integrated line intensity (in $\mathrm{cm}^{-2}.\mathrm{amagat}^{-1}$, where an amagat is a unit of volumetric number density) from Eq. (2.3). It is possible to express $S_n(T)$ in cm^{-1} by using the Loschmidt number knowing that 1 amagat $= 2.6867774 \times 10^{19}\,\mathrm{cm}^{-3}$. The parameters σ_n, δ_n, and $\Delta\sigma$ are the line position (in cm^{-1}), the line shift (in cm^{-1}) and the distance to the line-center, respectively. $\gamma_n^{X-\mathrm{Pert}}(T)$ is the HWHM of the line (see Eq. (2.7)) induced by the collision between a molecule X and a perturbator molecule Pert. x_X is the molar fraction of the molecule X. The $\exp\left(\frac{hc\Delta\sigma}{2k_\mathrm{B}T}\right)$ term is the quantum asymmetry factor (Hartmann et al. 2021) which does not exist in Eq. (2.3) defining the line-center. This factor accounts for an asymmetry existing between the left and right farwings (i.e., toward low or high wavenumbers) which is negligible close to the line center when $\Delta\sigma$ tends to zero. This equation replaces the usual Eq. (2.5) used to compute the line-centers. Without these χ factor corrections, the absorption is largely overestimated between the absorption bands, as shown by the differences between the red and black curves in Fig. 2.1.

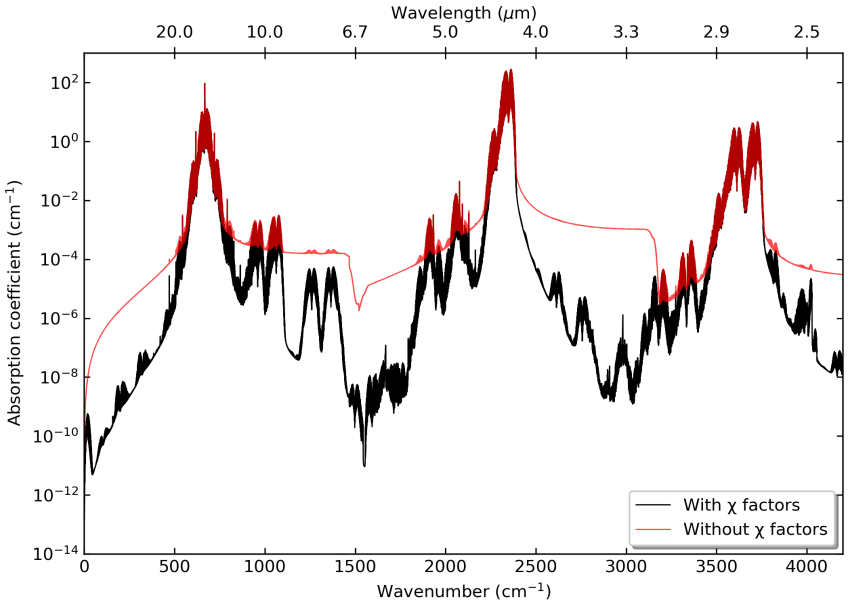


Figure 2.1: Absorption spectrum of a pure CO_2 gas at 300 K and 1 bar, with and without χ factor corrections. The black curve corresponds to the true absorption spectrum of CO_2 including χ factor corrections. The red curve has been computed using Eq. (2.10) assuming $\chi = 1$ (no χ factor correction).

Many papers provide χ factors for different molecules and mixtures (see Chapter 3 for more details). They are computed for different distance ranges to the line-center and in various spectral bands. When the χ factors are measured in one single band of a given molecule, it is usual to use them to correct the entire spectrum, which is inaccurate. Indeed, overestimating - or underestimating - the continuum could induce a bias in the opacity data, leading to potentially incorrect results when performing climate simulations. There is therefore a real need to carefully validate the process of spectra computation, to produce accurate opacity data to avoid any misinterpretation of exoplanetary climates.

From a mathematical point of view, an absorption line is defined from the line-center to $\pm\infty$. Of course this is not realistic from a computational point of view, thus a limit is defined at few hundreds cm^{-1} from the line-center. This limit depends on the pressure, the temperature, and the composition

of the gas and should be adjusted to the studied conditions. Only the part of the farwings contributing to the global continuum is calculated to minimize the computation time. Moreover, as written earlier, pressure dependency of the absorption line is not the same in the center of the line and in the farwings, thus, these two components are historically computed separately. The usual boundary was defined by the MT_CKD consortium[7] (Mlawer et al. 2012, 2019) at $\pm 25 \text{cm}^{-1}$ from the line-center. This convention, commonly used in the community, was defined for water in the Earth's atmospheric conditions and could be irrelevant for higher temperature, especially in the context of exoplanets. This point is discussed in detail in Chapter 3.

2.2.4 Collision induced absorption and dimers

The absorption sources described in Sects 2.2.1 and 2.2.2 are driven by absorption and emission of photons, but when two molecules collide, they can exchange electronic charges, inducing a transient dipole (e.g., Frommhold 1994 ; Karman et al. 2018). This creates Collision Induced Absorptions (CIA). The lifetime of these dipoles is very short, in the order of the duration of the collision. Therefore, following the Heisenberg uncertainty principle mentioned previously, the absorption band is very large. We need to account for this extra absorption sources to accurately compute the absorption spectrum of a gas. Several studies aim to measure such CIA and data are available through the HITRAN CIA[8] database (Karman et al. 2019). CIA are usually inversely proportional to the temperature, while classic absorption sources increase in intensity with an increase of temperature.

Molecular collisions are assumed to be short-term collisions, but under given conditions they can briefly form a pair, thus interacting for a longer time. This forms a dimer, creating a third absorption source we have to account for. As the lifetime of such collisions is much longer, the absorption features produced by dimers are narrower in terms of wavelength extension. They are usually treated in the same way as CIA as absorption sources not permitted by quantum mechanics[9]. In the same way, their intensity is inversely proportional to the temperature because it is more difficult to form "pairs" at high velocities and short-term collisions are dominants.

These two processes, CIA and dimers, are the only significant absorption sources of symmetrical molecules such as N_2 or H_2. The H_2-H_2 CIA (Lafferty et al. 1996) band absorbs between 1-500 μm, covering the entire near-IR domain and making it key to study the radiative transfer of hydrogen dominated planets such as gas giant planets. For radiatively active molecules such as H_2O and CO_2, CIA and dimers can close spectral windows, modifying drastically the radiative effect of the gases. For example, a CO_2-CO_2 dimer (Baranov et al. 2004) is located between 5-14 μm (700-2000 cm^{-1}), exactly in between the two main bands absorbing in the IR, as shown by Fig. 2.2. By neglecting it, we underestimate the greenhouse effect of this gas, thus we inaccurately estimate the global temperature of the planet (e.g., Wordsworth et al. 2010).

[7] `http://rtweb.aer.com/`
[8] `https://hitran.org/cia/`
[9] That mean absorption sources which are not only induced by the collision, but by a more complex interaction (exchange of electronic charges or transient dipole).

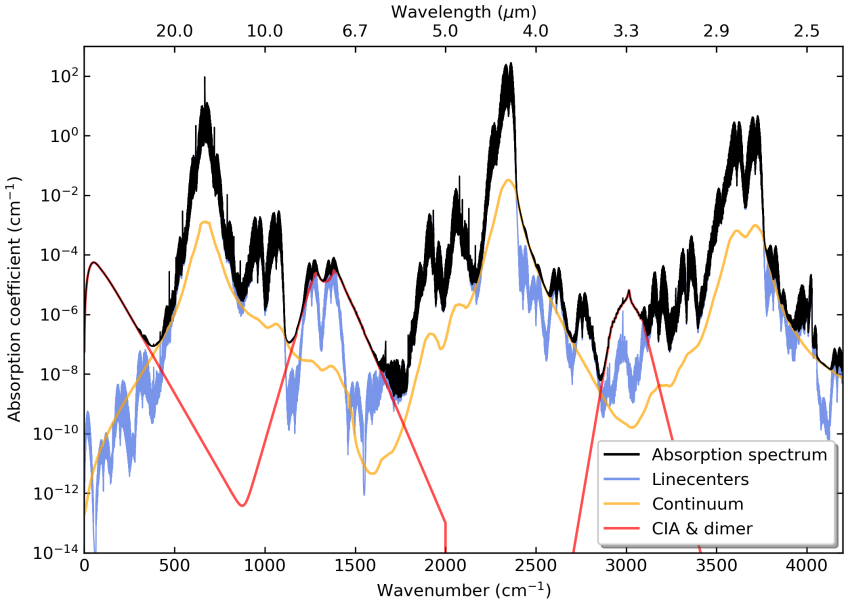


Figure 2.2: Absorption spectrum of a pure CO_2 gas at 300 K and 1 bar. The total absorption spectrum is in black, while blue, orange and red curves are the contribution from the line-centers, the farwings and the CIA, respectively. The separation between the line-centers and the continuum is assumed to be at $\pm 25\,\mathrm{cm}^{-1}$ from the center of the line.

2.2.5 The challenge of gas mixtures

Planetary atmospheres are never composed of one single gas and opacity data need to account for this complexity. By adding active species, that is species with their own absorption, the absorption spectrum of the overall atmosphere is obtained simply by summing all the individual spectra. Unfortunately, in such gas mixture, multi-species collisions happen, modifying the pressure broadening of the absorption lines of every active molecule. This effect is taken into account in Eq. (2.7) defining the pressure broadening as the sum of the broadening induced by self collisions (intraspecies collisions) and by foreign collisions (interspecies collisions). The more different molecules in a mixture, the more specie-to-specie collisions can happen, multiplying the complexity of mutual broadening.

This has also an impact on the farwing corrections because each species-to-species interaction needs to be measured, in different band and for various temperature and pressure conditions. This is obviously challenging and even if several teams are making these experiments since many years, a lot of data are still missing. A way to circumvent this issue is to assume that collisions between the main gas and trace species never happen from a statistical point of view and can be neglected. For example, we could consider that the Earth is composed of nitrogen and oxygen[10], accounting for other active species only through their self-absorption. When the atmosphere is not dominated by a single gas, these interspecies interactions cannot be neglected to accurately estimate the radiative balance of the atmosphere (Chaverot et al. 2022). This is a case-by-case study which is hardly generalizable because of the lack of data or because of the limitations of these data. Indeed, lab experiments are often limited in terms of pressure

[10]That is corresponding to 99% of the gases in the Earth's atmosphere.

and temperature, which is an issue to model the wide variety of environments we observe on exoplanets.

In order to produce accurate opacity data usable over a wide range of gas mixing ratio, I developed a tool named SpeCT to compute high resolution absorption spectra for mixtures including H_2O, N_2 or CO_2 (see Chapter 3). This was necessary to study the onset of the runaway greenhouse for which the dominant gas in the atmosphere changes, as a consequence of the evaporation of the surface ocean.

2.3 From high resolution spectra to opacity data

In Sect. 2.2 we describe the state-of-the-art definition of the absorption lines forming a spectrum. Regarding the complexity of the absorption sources, of the required experimental corrections and the number of interactions between the molecules, such computation is time expensive. Other methods were developed to reduce the interpolation time of opacity data, in order to use them in climate models. We discuss in this section two main techniques: the Mean-Rosseland (Sect. 2.3.1) and the correlated-k method (Sect. 2.3.2).

2.3.1 Mean-Rosseland and gray calculation

Historically, the easiest way to produce opacity data efficiently usable by climate models was to average the entire spectrum at one single value in a given band. Usually, for climate modeling, two values are computed, one for IR and one for visible wavelengths. This allows to remove the spectral dimension from the numerical computation, reducing drastically the computation time. The temperature and pressure dependencies can be included by pre-computing several gray absorption points in the two spectral bands for various temperatures. The issue is that regarding the shape of a spectrum, a simple average will be biased, and the gray calculation tends to overestimate the actual spectroscopic absorption of the gas, as shown in Fig. 2.3. This overestimation depends on the numerical resolution of the spectrum. Even a gray calculation per band does not represent well the actual absorption spectrum (gray dashed lines in Fig. 2.3). To avoid this, Rosseland (1924) proposed a weighted averaged of the spectrum, called Mean-Rosseland approximation (red dashed curve in Fig. 2.3). The method gives good results at the first order and is largely used in simple 1D climate models (e.g., Ingersoll 1969 ; Nakajima et al. 1992 ; Ishiwatari et al. 2002 ; Koll & Cronin 2019). However, inaccuracy due to the loss of the wavelength dimension can induce large errors. More specifically, the Mean-Rosseland approximation does not represent well the difference between "noisy" spectra at low pressures and "flat" spectra at high pressures. The thin spectral windows existing at low pressure are not modeled, and the radiative transfer is strongly impacted. Indeed, these small spectral features can have a strong impact by allowing some flux to pass through the atmosphere. By summing this over an entire spectral range can affect the radiative balance by a few $W.m^{-2}$.

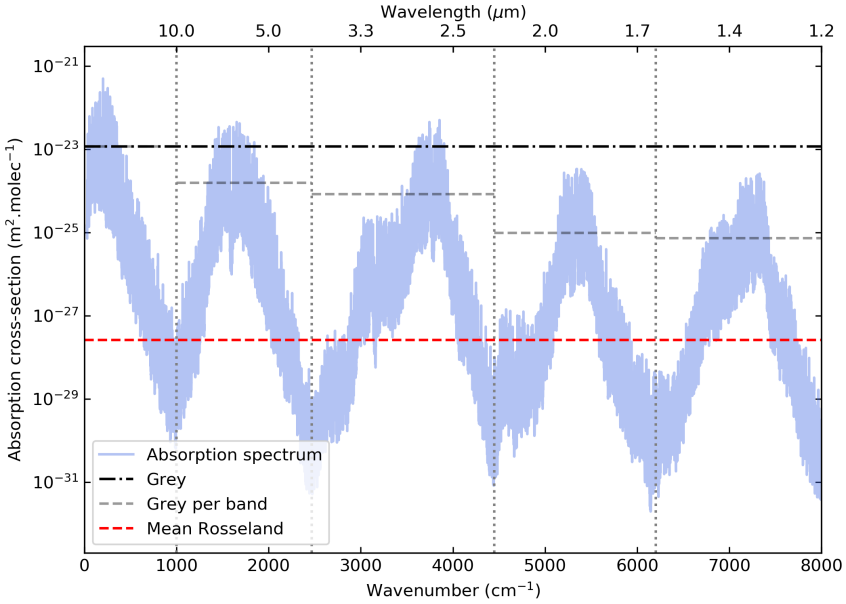


Figure 2.3: Grey and mean-Rosseland opacities of a pure H_2O gas at 300 K and 1 bar. The absorption spectra of water vapor is shown in blue. The black dash-dotted and gray dashed curves correspond to the gray and gray-per-band methods, respectively. The mean-Rosseland value obtained over the entire spectral range corresponds to the red dashed curve. The calculations are done by using the `Exo_k` library and absorption cross-sections from Exo-REM.

2.3.2 The correlated-*k* approach

To try to keep the information on the "noisiness" of a spectrum, some studies used binned cross-section tables. That is a line-by-line spectrum which is binned down in order to reduce the computation time. Garland & Irwin (2019) showed that this method provides inaccurate opacity data when the final resolution used is not high enough, and unusable computation times when the resolution is good enough.

An alternative solution, the correlated-*k* method (Liou 1980 ; Lacis & Oinas 1991) was developed to combine high accuracy and fast computation time. The idea is to divide the spectrum in several bands and to derive the opacity distribution in each band. In other words, the *k*-coefficient and their associated weights quantify the distribution of "high absorption lines", "mid absorption lines" and "low absorption lines". Therefore, a very narrow opacity distribution means a very flat spectrum, induced for example by high pressures. A very wide distribution is generally a sign of a very noisy spectrum, potentially including thin spectral windows. The *k*-coefficient distribution follows a Gauss quadrature in order to accurately represent a wide variety of spectrum shapes, but this can vary from a case to another. For this reason, the *k*-coefficients are often called "Gauss-points". Figure 2.4 shows an example of the cumulative probability (right panel) corresponding to the absorption coefficient of the 9.6 μm band of O_3 (left panel) from Fu & Liou (1992). The shape of the cumulative probability is given by the "noisiness" of the considered absorption band. In the given example in Fig. 2.4, the cumulative probability increases roughly linearly meaning that there is the same number of weak, intermediate and intense absorption lines, which is the sign of a noisy spectrum. For an atmosphere with a single species, the correlated-*k* tables have 4 dimensions, for the temperature, the pressure, the Gauss-points and the spectral bands. For

an atmosphere with 2 species, an additional dimension is required: the mixing ratio. The method allows reducing the computation time by several orders of magnitude while keeping the same accuracy as a line-by-line calculation (e.g., Amundsen et al. 2017 ; Garland & Irwin 2019 ; Leconte 2021 ; Chaverot et al. 2022). Correlated-k tables are largely used in the exoplanet community for both climate modeling and retrievals which aim to retrieve the atmospheric structure from observations. SpeCT is developed to compute high resolution spectra of gas mixtures (see Chapter 3) but such spectra are not directly usable in GCMs. Therefore, they are used to producing accurate correlated-k tables by using post-processing tools, for example `Exo_k`[11] (Leconte 2021).

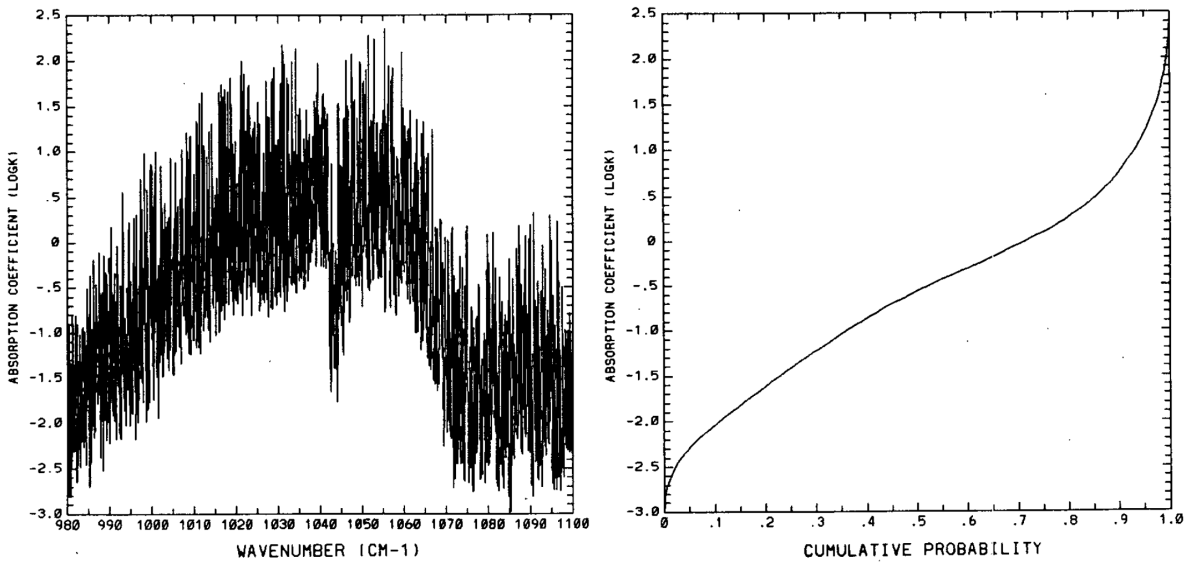


Figure 2.4: Absorption coefficient (in $cm^{-1}.atm^{-1}$) as a function of wavenumber (*left panel*) and cumulative probability (*right panel*) for the O_3 9.6 μm band for a pressure of 25 mbar and a temperature of 220 K. Figure from Fu & Liou (1992).

The radiative transfer calculation is often the most time-consuming step of climate models, and especially of GCMs. As an example, the classical resolution of the Generic-PCM is 64x48 (corresponding to longitude x latitude) that is 3072 vertical columns[12]. The physics is generally computed 90 times per simulated day (one step every 16 min) and the radiative transfer is called every 4 physical time-step. With this resolution, the radiative transfer is thus computed 69120 times per day making numerical simulations extremely slow if this step is not optimized enough. Knowing this, it is key to optimize the efficiency of the correlated-k tables we use in such models. More Gauss-points will provide a better accuracy, but this will slow down the model at the same time. In the same way, by adding more spectral bands, we increase the number of interpolations done when using the table. The art of optimizing correlated-k tables is a Pandora box, but this should not be neglected when creating a new table. There are multiple ways to find a good equilibrium between accuracy and efficiency, and it is a case-by-case problem. One of the main control parameter is the number of spectral bands. The classical resolution used in the correlated-k

[11] `http://perso.astrophy.u-bordeaux.fr/~jleconte/exo_k-doc/index.html`

[12] This number is slightly over-estimated. Indeed, for a latitude/longitude grid, the number of cells around the poles is reduced to keep a roughly constant area per cell over the globe. See Sect. 1.4.3.

tables produced for the Generic-PCM is ≈38 bands in the IR and ≈35 bands in the visible. By making different correlated-k tables at different resolutions, I noticed that the positioning of the spectral bands influences the accuracy of the table. More specifically, it seems that centering the spectral bands of the table on the main absorption bands of the spectrum could help to increase the accuracy. This point needs to be investigated in more detail to confirm this tendency. A second adjustment parameter is the number of Gauss-points. This is mainly determined by the accuracy required by the user, and typically a table includes around 15 Gauss-points. A more subtle option is to change the Gauss quadrature of the k-coefficients. In `Exo_k` the default parameterization uses a Gauss-Legendre quadrature (Leconte 2021), but other works use for example a Gauss-Lobatto quadrature as Garland & Irwin (2019).

The aim of the next chapter is to present the numerical tool SpeCT, which is design to compute high resolution spectra based on the state-of-the-art spectroscopy equations presented in this chapter. These spectra are the basis required to produce opacity data usable in climate modeling, by using one of the method presented in Sect. 2.3.

Chapter 3

SpeCT: SPEctra for Correlated-k Tables

Contents

3.1 Motivation: From lab experiments to climate modeling 38

3.1.1 Focus on CO_2 38

3.2 Technical description of SpeCT 39

3.2.1 Computation of line-centers & continua 40

3.2.2 Data limitations 41

3.3 Databases & line-lists 43

3.4 Discussion and prospects 43

3.1 Motivation: From lab experiments to climate modeling

The onset of the runaway greenhouse is a specific study case in the sense that, taking the example of the Earth, the atmosphere switches from nitrogen dominated to water dominated. Of course this modifies the climate through the evolution of, among others, the vapor distribution and cloud coverage affecting directly the radiative equilibrium of the planet. To accurately account for changes happening during this critical step, an insight of the potential spectroscopic effects is required. As described in the previous chapter, molecules collide in a gas mixture and this affects the shape of the absorption lines. As the aim of Chaverot et al. (2022) was to deeply investigate the radiative processes happening during the onset of the runaway greenhouse using a 1D radiative-convective model, the preliminary step was to derive an accurate correlated-*k* table accounting for interspecies collisions. To do so, I developed a numerical tool named SpeCT (SPEctra for Correlated-k Tables) in order to compute high resolution absorption spectra for different gas mixtures (H_2O+N_2, H_2O+CO_2, CO_2+N_2). In a second time, I used these spectra to produce a correlated-*k* table using the post-processing library of `Exo_k` (Leconte 2021).

3.1.1 Focus on CO_2

Because of the anthropological global warming on Earth, CO_2 is a well studied molecule. It is a key greenhouse gas which is common in the rocky planets of the solar system (Mars and Venus) and which could be common on terrestrial exoplanets (e.g., Rustamkulov et al. 2023 ; Ahrer et al. 2023). Therefore, there is a strong interest to produce accurate opacity data for it. In this section, I present a brief overview of the spectroscopic properties of CO_2 because experiment correction factors used in SpeCT depend on them.

In the IR, there are 3 main excitation levels for CO_2:

- ν_1 corresponding to an energy[1] equal to $1388\,\mathrm{cm}^{-1}$ (that is corresponding to $7.2\,\mu$m)
- ν_2 corresponding to an energy equal to $667\,\mathrm{cm}^{-1}$ (that is corresponding to $14.9\,\mu$m)
- ν_3 corresponding to an energy equal to $2349\,\mathrm{cm}^{-1}$ (that is corresponding to $4.3\,\mu$m)

These 3 excitation modes are composed of multiple absorption lines and correspond to different "movements" of the molecule. The ν_1 is a symmetric stretch, ν_2 a doubly degenerate bend and ν_3 an asymmetric stretch as illustrated on Fig. 3.1. From the spectroscopic point of view, these 3 bands are absorbing efficiently, but ν_1 is weak compared to the other two. However, the ν_1+ν_3 band which is a combination of ν_1 and ν_3, absorbing at $3737\,\mathrm{cm}^{-1}$ ($2.7\,\mu$m) is as intense as ν_2 or ν_3. The transitions corresponding to these energy levels are shown on Fig. 3.2. Even is ν_1 is visible around $1388\,\mathrm{cm}^{-1}$, the three main absorption bands considered in IR spectroscopy are ν_2, ν_3 and ν_1+ν_3 (see Fig. 3.3).

[1] Knowing that $1\,\mathrm{cm}^{-1} \equiv 1.986\times10^{-23}$ J.

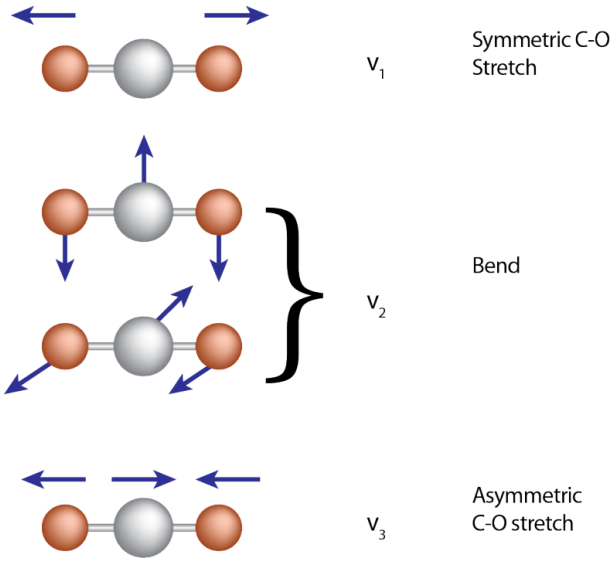


Figure 3.1: Scheme of ro-vibrationnal modes of CO_2. Credit: Kristin Spear, NASA Glenn Research Center

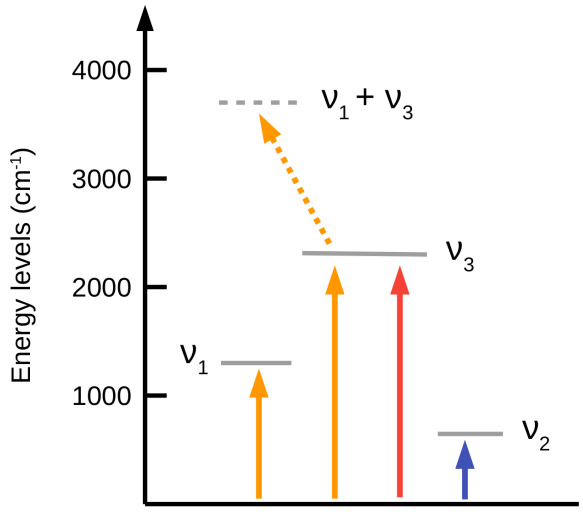


Figure 3.2: Scheme of the three IR absorption bands of CO_2. The ν_2 and ν_3 bands are in blue and red respectively. The ν_1+ν_3 band which corresponds to the combination of the ν_1 and ν_3 bands is in orange.

3.2 Technical description of SpeCT

The code is written in Fotran90 and is highly parallel using MPI and openMP in order to efficiently compute the hundreds of spectra required to produce a correlated-*k* table. The structure is the following: 1) The code reads the spectroscopic linelists from HITRAN or HITEMP files, 2) the code does a loop over pressure, temperature and mixing ratio conditions (defined by the user) which is parallelized using MPI, 3) the code does a second loop over the linelist itself to compute each individual line, 4) it finally sums all the lines to compute the entire spectra, giving one file per initial condition.

3.2.1 Computation of line-centers & continua

Following the historical convention proposed by the MT_CKD consortium (Mlawer et al. 2012, 2019), we separate the line-centers from the farwings at $\pm 25\,\mathrm{cm}^{-1}$ from the center of the line. By doing this, it is possible to compute the continuum at a lower resolution in order to reduce the computation time. The typical resolution required to resolve any individual lines is $1\times10^{-3}\,\mathrm{cm}^{-1}$ while the continuum is computed at a resolution equal to $1\,\mathrm{cm}^{-1}$. Moreover, this allows climate models to adapt the interpolation scheme to the different pressure dependency of the line-centers and the farwings, proportional to P and P^2 respectively, where P is the partial pressure.

The line-centers are computed assuming a Voigt profile following equations provided by HITRAN (Rothman et al. 2005) (see Chapter 2 for a complete description of the calculation of the line-centers). For absorption sources driven by collisions between different molecules (line broadening, farwings, CIAs and dimers), interactions are written X-Y where X is the considered active molecule and Y the collider (which is different from Y-X). The continua for H_2O-H_2O and H_2O-N_2 are taken from MT_CKD v3.3 (Mlawer et al. 2012, 2019) and the H_2O-CO_2 continuum is from Tran et al. (2019). As there is no continuum available for CO_2 mixtures, I self consistently compute it by including all the required χ factors. I use the generic equation proposed by Tran et al. (2018) (see Eq. (2.10) in Chapter 2), which allow us to have a generic routine, easily adaptable to different χ factors, or for different molecules. The references for the χ factors, the continua, and the CIA are resumed in Table 3.1. An overview of the CIA provided by HITRAN is given in Karman et al. (2019). For CO_2-H_2O and CO_2-N_2 collisions, the χ factors were measured in one single absorption band of CO_2 (see Tran et al. 2018 and Perrin & Hartmann 1989 respectively). As this is the only correction available, we apply it over the entire spectrum. The CO_2-CO_2 χ factors were measured for the 3 main absorption bands of CO_2 (ν_2, ν_3 and ν_1+ν_3). It is possible to numerically delimit these bands by assuming a wavelength threshold or by using the ro-vibrational transitions. There is no consensus so far on the best way to do this (Ha Tran, private communication) but for consistency, I chose to define them using the ro-vibrational transitions shown in Fig. 3.2. The corresponding spectral bands are shown on Fig. 3.3. All the absorption lines induced by other ro-vibrational transitions (green curve on Fig. 3.3) are corrected using the χ factors derived for ν_3.

The χ factors are a function of the distance to the line-center, and they usually do not match with the arbitrary cutoff delimiting the line-center and the farwings at $\pm 25\,\mathrm{cm}^{-1}$. That means that there are χ factors corrections in what we call the "line-centers". On the other side, the absorption contribution of the farwings tend to zero when too far from the line-center. For computation time reasons, we define a maximum cutoff, delimiting the definition domain of the farwings. This value is supposed to prevent the calculation of a part of the farwings which does not contribute to the total absorption spectrum. Sensitivity tests showed that a maximum cutoff fixed at $\pm 500\,\mathrm{cm}^{-1}$ from the line-center provides accurate results, while $\pm 800\,\mathrm{cm}^{-1}$ gives the exact spectrum. As the aim is to produce correlated-k tables, I advise computing the continuum up to $\pm 800\,\mathrm{cm}^{-1}$ as done in SpeCT.

Following Mlawer et al. (2012) I include in the continuum the plinth of the absorption lines, that is the pedestal of the line-center assuming a constant value equal to the absorption at $\pm 25\,\mathrm{cm}^{-1}$ from the line-center. Therefore, I do not include it in the computation of the line-centers.

Mixture	Data	Ref.
H_2O-H_2O	MT_CKD v3.3	Mlawer et al. (2012)
H_2O-N_2	MT_CKD v3.3	Mlawer et al. (2012)
H_2O-CO_2	Continuum	Tran et al. (2019)
CO_2-CO_2	χ factors	Tran et al. (2011)
CO_2-H_2O	χ factors	Tran et al. (2018)
CO_2-N_2	χ factors	Perrin & Hartmann (1989)
N_2-N_2	HITRAN CIA	Lafferty et al. (1996)
		Baranov et al. (2005)
		Hartmann et al. (2017)
		Chistikov et al. (2019)
N_2-H_2O	HITRAN CIA	Hartmann et al. (2018)
CO_2-CO_2	HITRAN CIA	Gruszka & Borysow (1997)
		Baranov & Vigasin (1999)
		Baranov et al. (2003)
		Baranov (2018)
CO_2-CO_2	CIA	Stefani et al. (2018)
CO_2-CO_2	dimer	Baranov et al. (2004)
H_2O-CO_2	CIA	Fleurbaey et al. (2022)

Table 3.1: References for the continua and CIAs used in SpeCT. The top part of the table provide references for the continua (database or χ factors) while the bottom part concerns the CIAs and dimers.

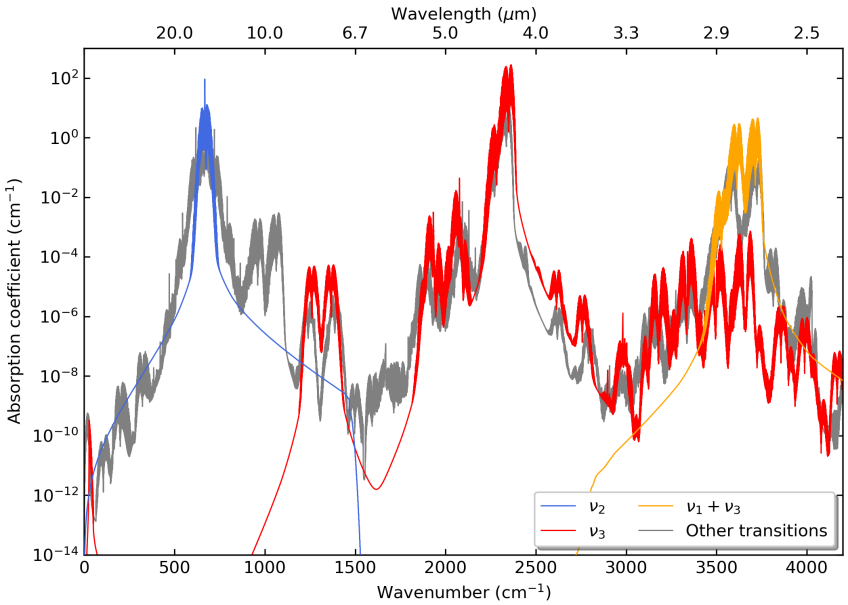


Figure 3.3: Absorption spectrum of CO_2 at 1 bar and 300 K. Different colors correspond to the lines induced by the main ro-vibrational transitions of CO_2 as provided by HITRAN. The blue curve corresponds to ν_2, the red one to ν_3, the orange one to ν_1+ν_3 and the gray one to all the other transitions.

3.2.2 Data limitations

The 3 main parameters provided by HITRAN and depending on the molecules involved in the collisions are the HWHM at reference temperature (γ), the temperature dependency exponent (n) and

pressure-induced drift of the line position (δ) (see Sect. 2.2.3.1). Unfortunately, HITRAN does not provide these parameters for every interspecies collisions. An overview of the available data for the molecules of interest is given in Table 3.2. I also consider that "Air", defined in HITRAN as the Earth's atmospheric composition, is equivalent to pure N_2. The H_2O-CO_2 HWHM coefficient ($\gamma_{H_2O-CO_2}$) is derived from the one for H_2O-Air by using a correction factor proposed by Brown et al. (2007)

X \ Y	H_2O	CO_2	Air
H_2O	γ	γ^*	γ, n, δ
CO_2	γ, n	γ, n, δ	γ, n, δ

Table 3.2: Spectroscopic data available in HITRAN. The coefficients correspond to the collisions between molecules X and Y, where X is the active molecule and Y the foreign species. The H_2O-CO_2 HWHM coefficient (γ^*) is derived from γ_{H_2O-Air} by using a correction factor proposed by Brown et al. (2007)

Another critical limitation of lab spectroscopic data concerns the pressure and temperature dependency. Even if experiments are usually done for different pressures and temperatures, lab conditions are limited. This can become a problem to model the wide variety of environment we observe on other (exo)planets. Extrapolations are inevitable to fill the gap between our data and the conditions we want to simulate, especially to study extreme objects such as Hot-Jupiters with a temperature of few thousand degrees. From a numerical point of view, this is not a problem for the computation of the line-centers, as well as for the farwings even if the validity domain of data provided by HITRAN and HITEMP is not well-defined. For the CIAs, this becomes more challenging as the interpolation is supposed to be done by the user. To try to extend as much as possible the definition domain of the CIA while keeping coherent values, I set manually the extrema of the extrapolation of the CIA (see Table 3.3). As the H_2O-CO_2 CIA from Fleurbaey et al. (2022) is available only at the room temperature (296 K), we do not interpolate it, and we assume it is constant over every temperature changes. We defined only upper limits for the temperature extrapolation because low temperature extrapolations provide consistent results.

CIA	Spectral domain	Temperature threshold
H_2O-CO_2	5,780 - 6,215 cm^{-1}	-
CO_2-CO_2	1 - 1000 cm^{-1}	1500 K
CO_2-CO_2	2,500 - 3,500 cm^{-1}	700 K
CO_2-CO_2 (dimer)	700 - 2,000 cm^{-1}	700 K
N_2-N_2	1 - 650 cm^{-1}	600 K
N_2-N_2	1,800 - 2,700 cm^{-1}	370 K
N_2-N_2	4,300 - 5,000 cm^{-1}	700 K
N_2-H_2O	1,900 - 2,800 cm^{-1}	600 K

Table 3.3: Definition domain of the CIA with their extrapolation temperature threshold. The H_2O-CO_2 CIA from Fleurbaey et al. (2022) is defined only at the room temperature (296 K) thus there is no interpolation and the absorption is assumed to be constant with temperature.

A final issue is related to the χ factors themselves. As mentioned previously, they are not available for every interspecies collisions, for every absorption bands, and for every pressure/temperature conditions. Due to this lack of data, we have sometimes to apply a coefficient which is derived for a specific

band to the entire spectrum. This induces an error, but it is a way better than to not apply any χ factors. In the same way, to produce opacity data to model extreme object such as Hot-Jupiters we need to compute absorption spectra at extremely high temperatures (few thousands Kelvin) for which there are no experimental data to compare with. This is a limitation we should keep in mind when discussing the accuracy of exoplanet climate modeling or interpreting the observations.

3.3 Databases & line-lists

The code is designed to compute spectra using the HITRAN[2] (Gordon et al. 2021) or HITEMP[3] (Rothman et al. 2010) databases. This was motivated by differences in the line-lists inducing differences in the radiative transfer beyond a given temperature (Goldblatt et al. 2013 ; Kopparapu et al. 2013). The HITEMP database contains way more absorption lines than HITRAN, especially at high wavenumber (see Goldblatt et al. 2013). There are 4.8×10^5 and 5.4×10^5 absorption lines for H_2O and CO_2, respectively, in HITRAN, while there are 1.1×10^8 and 1.1×10^7 in HITEMP. From a computational point of view, and knowing that the radiative transfer is the most computationally expensive step in climate models, this difference cannot be neglected. Kopparapu et al. (2013) argue using a 1D radiative-convective model that HITRAN and HITEMP are indistinguishable below 350 K, thus HITRAN should be preferred for these conditions to reduce the computation time. As done in SpeCT, I advise switching from HITRAN to HITEMP around 400 K (see comparisons in Ramirez 2014).

The issue is that water vapor continua from MT_CKD were computed using HITRAN. Regarding the number of extra line in the HITEMP database, it could be an issue to combine line-centers from HITEMP with continua computed using HITRAN. This point needs to be investigated to quantify the differences between the continua computed with HITRAN and with HITEMP.

3.4 Discussion and prospects

The conventional cutoff separating the line-center from the farwings is assumed to be $\pm25\,\mathrm{cm}^{-1}$. This is valid for spectra close to room temperature, but not for higher temperatures and pressures. This separation is supposed to be representative of the pressure dependency which is different in the line-center and in the wings, but it is by definition a function of the pressure. Using this convention for spectra at high pressures (few tens of bar) induces a continuum which is not continuous in wavelength, potentially propagating numerical errors during the interpolation step of the climate modeling. A better solution could be to define this cutoff as a function of the pressure, but this requires deep model development to adapt the models to this new convention.

All the χ factors, as well as the water vapor continua from MT_CKD were computed using the HITRAN database. Using the HITEMP database as discussed in Sect. 3.3 could induce an error we are not able to quantify for now.

[2] `https://hitran.org/lbl/`
[3] `https://hitran.org/hitemp/`

The following step is to add the χ factors for other molecules (especially CH_4) and to develop the model to increase the number of gas mixtures we can compute using SpeCT, for example H_2O+CO_2+N_2 or H_2O+CO_2+CH_4+N_2.

Part II

The runaway greenhouse

Chapter 4

The onset of the runaway greenhouse

Contents

4.1 Motivation: The importance of subtle spectroscopic effects 48

4.1.1 A detailed description of 1-D inverse radiative convective models 48

4.2 How does the background atmosphere affect the onset of the runaway greenhouse ? 51

4.3 The onset of the runaway greenhouse for atmospheres with CO_2 72

4.4 Evolution of planetary albedo 74

4.5 Limits for dense atmospheres 77

4.1 Motivation: The importance of subtle spectroscopic effects

The runaway greenhouse is studied since many years by different groups using various models. Historical works (Simpson 1929 ; Nakajima et al. 1992) paved the way for more complex studies using 1-D climate models (Ingersoll 1969 ; Kasting 1988 ; Kasting et al. 1993 ; Nakajima et al. 1992). They all highlight the importance of the infrared absorption of water vapor limiting the (OTR) in the definition itself of the runaway greenhouse. However, even in the recent literature, large gaps exist in the estimation of this OTR for terrestrial planets (e.g., Goldblatt et al. 2013 ; Kopparapu et al. 2014 ; Koll & Cronin 2019 ; Zhang & Yang 2020) especially in presence of background gases such as nitrogen. To explain the differences in the literature, I performed a thorough investigation of all the radiative transfer processes, and of the analytical equations defining the adiabatic profiles. This allowed me to identify all the major radiative transfer processes which play a role in the onset of the runaway greenhouse and to show that multispecies interactions affect the whole radiative balance by modifying strongly the absorption lines of the gases. Thanks to this deep investigation we were able to explain the differences in the literature, and we provide - when possible - advices on the processes of major importance to estimate accurately the OTR.

To obtain that result, I developed an original 1-D radiative-convective model based on PyRADS[1] (Koll & Cronin 2018) for the radiative transfer, and on RADCONV1D (Marcq et al. 2017) for the convective scheme. By combining the best part of these two models, I was able to perform multiples sensitivity tests in order to fine-tune the model, named PyRADS-Conv1D in Chaverot et al. (2022). This led to the publication of an article presented in Sect. 4.2. A detailed presentation of my 1-D radiative-convective model is done in Sect. 4.1.1.

Following Chaverot et al. (2022), I supervised two Master internships in order to extend the study to atmospheres containing large quantities of CO_2 (Sect. 4.3), then to compute the flux absorbed by the atmosphere for various gas compositions (Sect. 4.4). Thanks to recent developments, I included a modified version of SpeCT in my 1-D radiative-convective model in order to consider different gas mixtures, including especially CO_2. I aim to make this model open-source as soon as possible.

4.1.1 A detailed description of 1-D inverse radiative convective models

4.1.1.1 Computation of the pressure-temperature profile

The first step of a 1-D inverse radiative-convective models is the computation of the temperature profile. Usually, 1D vertical models use the pressure as vertical coordinates instead of an altitude in kilometers. This gives more generic equations usable to model various planets with different gravity. An equation defining the temperature as a function of the pressure for a mixed atmosphere containing a condensable gas (indices c, e.g., water), and a non-condensable gas (indices n, e.g., nitrogen) is proposed by Kasting (1988), based on Ingersoll (1969). This equation, called adiabatic lapse rate, is the following:

[1] `https://github.com/ddbkoll/PyRADS`

$$\frac{d\ln P}{d\ln T} = \frac{P_c}{P}\frac{d\ln P_c}{d\ln T} + \frac{P_n}{P}\left(1 + \frac{d\ln \rho_c}{d\ln T} - \frac{d\ln \alpha_c}{d\ln T}\right), \tag{4.1}$$

where

$$\frac{d\ln \alpha_c}{d\ln T} = \frac{\frac{R^*}{M_n}\left(\frac{d(ln\rho_c)}{d\ln T}\right) - c_{vn} - \alpha_c \frac{ds_c}{d\ln T} - \alpha_l \frac{ds_l}{d\ln T}}{\alpha_c(s_c - s_l) + \frac{R^*}{M_n}}. \tag{4.2}$$

Indices of variables in Eqs. (4.1) and (4.2) indicate what gas is considered: c for the condensable gas, n for the non-condensable gas, and l for liquid. Here, P is the pressure, T the temperature, M the molecular weight, ρ the density, R^* the perfect gas constant, R the specific gas constant, $\alpha_i = m_i/m_n$ the mass-mixing ratio per unit of non-condensable gas (m_n) for the species i, c_p and c_v the heat capacity at constant pressure or constant volume, and s the entropy. An alternative equation for the adiabatic lapse rate is proposed by Pierrehumbert (2010). These two formulations differ only on the definition of the entropy (Chaverot et al. 2022). Pierrehumbert (2010) defines it using the perfect gas laws, while Kasting (1988) keeps it as a variable in the equation. A more detailed explanation of this difference is given in Sect. 4.2. The adiabatic lapse rate defines the temperature as a function of the pressure assuming an atmosphere at the convective equilibrium, which is a good approximation for the troposphere. Usually, the stratosphere is assumed isothermal, as prescribed by Kasting (1988). This approximation does not impact the global radiative balance.

When the pressure/temperature conditions allow water to condense, the temperature profile is called moist adiabat. As 1-D models do not account for the global dynamics of the atmosphere, clouds cannot be computed consistently, thus the condensa (i.e., clouds) are removed instantaneously by precipitation. This is called the pseudo-adiabatic hypothesis. The consequence is that at a given pressure, the temperature cannot be lower than the saturation temperature. When the pressure/temperature conditions are not favorable to water condensation, the temperature profile is called dry adiabat.

4.1.1.2 Radiative transfer

When the pressure-temperature conditions are known at every point of the model, the opacity of the atmosphere can be computed. To do so, it is possible to use tabulated opacity data, as a function of the pressure and of the temperature, such as mean-Rosseland. As explained in Sect. 2.3.1, this approximation is not adapted to a precise calculation, thus we chose to use a state-of-the-art line-by-line calculation in Chaverot et al. (2022). The pressure and the mixing ratio of the gas vary with altitude, therefore absorption spectra need to be independently computed at every vertical grid point of the model in order to represent the variation of opacity. As discussed in Chapter 2, the line-by-line computation of a spectrum is time-consuming, thus alternative accurate techniques such as correlated-k tables can be used in 1-D radiative-convective models for large parameter space explorations. When the opacity as a function of wavelength is known in the entire atmosphere, it is possible to compute the radiative transfer in each layer to eventually compute the OTR and the ASR. These two fluxes are computed separately.

The IR thermal flux of a planet comes from its surface, but also from the atmosphere above. Consequently, each atmospheric layer absorbs a part of the flux coming from below it, and emits in the IR toward the upper layers. The OTR corresponds to the total IR flux at the top of the atmosphere, escaping toward space. More precisely, at a given wavelength, the opacity of an atmospheric layer is a function of its pressure and temperature. As the pressure and the temperature decrease with altitude, opacity decreases as well. Therefore, we define the opacity between the surface of pressure P_0 and an atmospheric layer of pressure P as $\tau_\nu(P)$. The value of $\tau_\nu(P)$ depends on the atmospheric composition and on the wavelength. Then we define the optical thickness (Γ_ν) between two layers of pressure P_1 and P_2 assuming $P_1 < P_2$ as:

$$\Gamma_\nu(P_1,P_2) = e^{\tau_\nu(P_2)-\tau_\nu(P_1)} \tag{4.3}$$

The OTR is finally computed using the following equation (see also Pierrehumbert 2010):

$$OTR(\nu) = B(\nu,T(P_0)) \times \Gamma_\nu(P_0,P) + \int_{P_0}^{P} B(\nu,T(P')) \times \Gamma_\nu(P',P)\, dP' \tag{4.4}$$

where $B(\nu,T(P))$ is the Planck function at wavenumber ν and at the temperature of the atmosphere layer of pressure P. The pressures P_0 and P are at the surface of the planet and at the top of the atmosphere, respectively. The relation between the temperature and the pressure is given by Eq. (4.1). This calculation is illustrated in Fig. 4.1, showing the incoming and outgoing fluxes of an atmospheric layer delimited by pressure levels P_1 and P_2 (with $P_1 < P_2$).

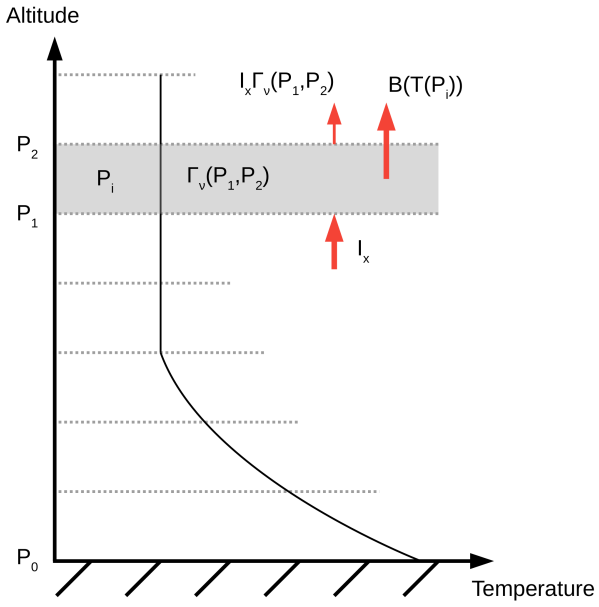


Figure 4.1: Schematic view of a 1-D radiative convective model. The black curve represents the adiabatic profile computed on a vertical pressure grid (gray dotted lines). Red arrows are the incoming (I_x), outgoing ($B(\nu,T(P_i))$) and transmitted ($I_x\Gamma_\nu(P_1,P_2)$) fluxes of an atmospheric layer of pressure P_i (gray area).

The ASR, computed separately, depends on the incoming flux from the star, which is usually in vis-

ible and UV wavelengths. The Rayleigh scattering happening preferentially at the top of the atmosphere in an important process which needs to be considered here (Pierrehumbert 2010). It is an anisotropic scattering of the light which is not absorbed by molecules or particles. This effect can strongly modify the Bond albedo of a planet, thus affecting the whole radiative balance as well as the climate. This complex physical process requires advanced numerical tools to be accurately calculated. This is usually a numerically expensive step which is discussed more in detail in Sect. 4.4.

4.2 How does the background atmosphere affect the onset of the runaway greenhouse ?

The following article is referenced in the manuscript as Chaverot et al. (2022). *Warning: the captions of figs 6 and 7 were switched during the edition process of the journal.*

A&A 658, A40 (2022)
https://doi.org/10.1051/0004-6361/202142286
© ESO 2022

Astronomy & Astrophysics

How does the background atmosphere affect the onset of the runaway greenhouse?

Guillaume Chaverot[1], Martin Turbet[1], Emeline Bolmont[1], and Jérémy Leconte[2]

[1] Observatoire de Genève, Université de Genève, Chemin Pegasi 51b, 1290 Sauverny, Switzerland
e-mail: guillaume.chaverot@unige.ch
[2] Laboratoire d'astrophysique de Bordeaux, Univ. Bordeaux, CNRS, B18N, allée Groffroy Saint-Hilaire, Pessac, 33615, France

Received 23 September 2021 / Accepted 27 October 2021

ABSTRACT

As the insolation of an Earth-like (exo)planet with a large amount of water increases, its surface and atmospheric temperatures also increase, eventually leading to a catastrophic runaway greenhouse transition. While some studies have shown that the onset of the runaway greenhouse may be delayed due to an overshoot of the outgoing longwave radiation (OLR) – compared to the Simpson-Nakajima threshold – by radiatively inactive gases, there is still no consensus on whether this is occurring and why. Here, we used a suite of 1D radiative-convective models to study the runaway greenhouse transition, with particular emphasis on taking into account the radical change in the amount of water vapour (from trace gas to dominant gas). The aim of this work is twofold: first, to determine the most important physical processes and parametrisations affecting the OLR; and second, to propose reference OLR curves for N_2+H_2O atmospheres. Through multiple sensitivity tests, we list and select the main important physical processes and parametrisations that need to be accounted for in 1D radiative-convective models to compute an accurate estimate of the OLR for N_2+H_2O atmospheres. The reference OLR curve is computed with a 1D model built according to the sensitivity tests. These tests also allow us to interpret the diversity of results already published in the literature. Moreover, we provide a correlated-k table able to reproduce line-by-line calculations with high accuracy. We find that the transition between an N_2-dominated atmosphere and an H_2O-dominated atmosphere induces an overshoot of the OLR compared to the (pure H_2O) Simpson–Nakajima asymptotic limit. This overshoot is first due to a transition between foreign and self-broadening of the water absorption lines, and second to a transition between dry and moist adiabatic lapse rates.

Key words. planets and satellites: terrestrial planets – planets and satellites: atmospheres

1. Introduction

Terrestrial planets can retain liquid water at their surface when the absorbed stellar radiation is balanced by the thermal emitted flux. If this balance is broken and if the absorbed flux is the highest, the planet warms to reach a new stable state at a higher temperature. Due to the strong opacity of water in the infrared, the thermal emission can be fully absorbed by the atmosphere when the temperature is high enough. Consequently, the thermal emission reaches a maximum, named the Simpson-Nakajima limit (Simpson 1929; Nakajima et al. 1992). Therefore, the planet stays in an unstable state and a catastrophic positive feedback arises and dramatically increases its temperature.

There is a strong interest to study this runaway greenhouse effect (Komabayasi 1967; Ingersoll 1969; Kasting 1988; Nakajima et al. 1992; Goldblatt & Watson 2012; Boukrouche et al. 2021), in particular to accurately determine the Simpson-Nakajima limit. This would allow us to know how close the Earth is to the runaway greenhouse threshold, but also to determine the inner edge of the habitable zone (HZ) more precisely (e.g. Kasting et al. 1993; Kopparapu et al. 2013; Zhang & Yang 2020). Some studies (e.g. Goldblatt et al. 2013; Kopparapu et al. 2014; Ramirez 2020) have shown that the outgoing longwave radiation (OLR) may be strongly modified by radiatively inactive gases (e.g. N_2 or O_2, as in the Earth's atmosphere). Other studies (Pierrehumbert 2010; Koll & Cronin 2019) have shown that such gases may lead to an overshoot of the Simpson-Nakajima limit, thus delaying the runaway greenhouse positive feedback. These OLR values, overshot compared to the pure water runaway greenhouse, are interpreted in Pierrehumbert (2010) as a coupled effect of the pressure broadening – which increases the absorption – and a lapse rate – which shifts towards a dry adiabatic lapse rate, thus reducing the absorption. Kopparapu et al. (2013) also suggested that the differences could come from the parametrisation of the adiabatic lapse rate. Kopparapu et al. (2013) used the Kasting (1988) formulation, while other papers used the Ding & Pierrehumbert (2016) formulation. Moreover, Koll & Cronin (2019) interpreted the OLR overshoot as a modification of the scale height of the atmosphere due to a change of the mean molecular weight. Possible interpretations are multiple, but there is still no consensus in the literature as of whether an OLR overshoot is really expected or not (see Fig. 1). The Simpson–Nakajima limit is quite well constrained for a pure vapour atmosphere (see Fig. 1, first panel), but differences between the various studies appear even with 0.1 bar of N_2, and reach up to 35 W m^{-2} for 10 bar of N_2. These discrepancies increase with the nitrogen pressure. Thus, at least one important process may be unknown - or not well constrained - to accurately compute the OLR of such atmospheres.

The first aim of this work is to determine, through sensitivity tests, the main physical processes and parametrisations involved in the computation of the OLR with a 1D radiative-convective model. This can be useful to better constrain 3D GCM simulations through a better understanding of some of the main

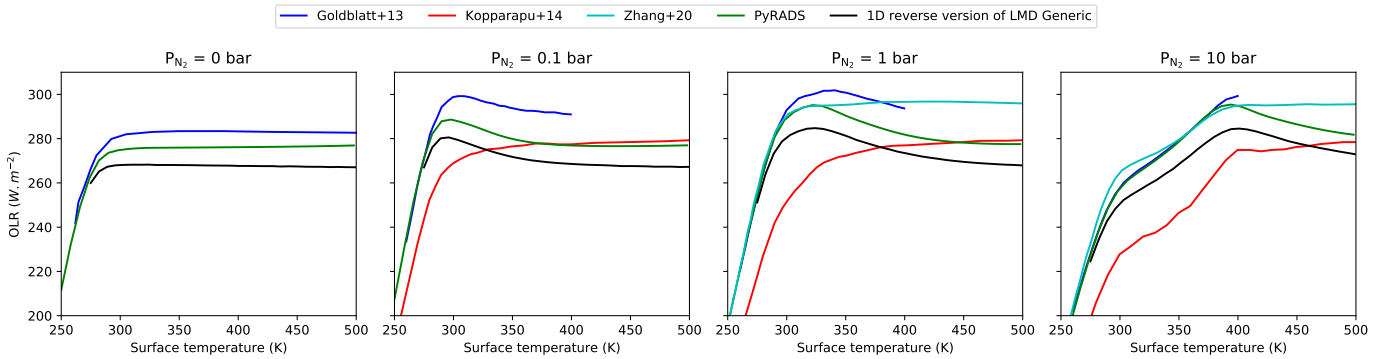


Fig. 1. OLR as a function of surface temperature for different N_2 partial pressures (P_{N_2} = {0, 0.1, 1, 10} bar) found in the literature (Kopparapu et al. 2014; Goldblatt et al. 2013; Zhang & Yang 2020) or computed in this work using the following existing models: the 1D reverse version of LMD-Generic (also known as kcm1d; Turbet et al. 2019) and PyRADS (Koll & Cronin 2018). Kopparapu et al. (2014) also added 350 ppm of CO_2 to the radiative transfer calculation (Ravi K. Kopparapu, priv. comm.).

Table 1. Main characteristics of 1D radiative-convective models used in this work.

Models overview

Models	Convection method	Radiative transfer method	Ref.
kcm1d	Conv_K88	kcm1d-RT	Turbet et al. (2019)
Exo_k	Conv_K88	Exo_k-RT	Leconte (2021)
PyRADS	Conv_D16	PyRADS-RT	Koll & Cronin (2018)
PyRADS-Conv1D	Conv_K88	PyRADS-updated	This work

Convection schemes

Conv. methods	Adiabatic lapse rate	Levels	Pres. boundary conditions	Entropy def.
Conv_D16	Ding & Pierrehumbert (2016)	100	Fixed diff. top and bottom	Perfect gas
Conv_K88	Kasting (1988)	200	Fixed top pressure	Experiments

Radiative transfer methods

R.T. methods	Absorb. coeff.	Line shape	HITRAN	H_2O cont.	N_2–N_2 cont.	H_2O iso.
kcm1d-RT	Correlated-k	Voigt (high res.)	2016	MT_CKD2.5 - [0.1, 10k]cm^{-1}	HITRAN CIA	Yes
Exo_k-RT	Correlated-k/cross section	Voigt (high res.)	2016	MT_CKD3.2 - [0.1, 20k]cm^{-1}	HITRAN CIA	Yes
PyRADS-RT	Line-by-line (0.01 cm^{-1})	Lorentz	2016	MT_CKD3.2 - [0.1, 10k]cm^{-1}	Without	No
PyRADS-updated	Line-by-line (0.01 cm^{-1})	Lorentz	2016	MT_CKD3.2 - [0.1, 20k]cm^{-1}	HITRAN CIA	no

Notes. The models kcm1d, PyRADS, and Exo_k are available in the literature while PyRADS-Conv1D is an original model. In bold, we give the models used to produce reference curves using the line-by-line or the correlated-k radiative transfer methods. The convection scheme and the radiative transfer method of each model are detailed in the corresponding tables. The convection scheme sub-table includes the adiabatic lapse rate used (Adiabatic lapse rate), the number of levels in the atmosphere (Levels), the pressure boundary conditions at the top and at the bottom of the atmosphere (Pres. boundary conditions), and the assumption used to define the entropy of the condensable gas (entropy def.). The radiative transfer method table includes the method to compute absorption coefficients (Absorb. Coeff.), the shape of the absorption lines (Line shape), the database used to compute the absorption lines (HITRAN) (Gordon et al. 2017), the database of the H_2O–H_2O and H_2O–N_2 continua (H_2O Cont.) (Amundsen et al. 2017), the database of the N_2–N_2 continuum (N_2–N_2 Cont.) (Karman et al. 2019), and if the method considers the water isotopes lines from HITRAN database at terrestrial abundances (De Biévre et al. 1984) (H_2O iso.).

physical processes that may be at play. Secondly, we propose a reference OLR curve (Fig. 3, top panel), done with a model built according to the sensitivity tests, for a $H_2O + N_2$ atmosphere, and to solve the question of the potential overshoot. We also propose a $H_2O + N_2$ correlated-k table, which provides similar results as a line-by-line computation.

In this work, we used a suite of 1D radiative-convective models already described in the literature. These models, presented in Table 1 (see also Sect. 2.3), are composed of a convection scheme and a radiative transfer model. For this reason, in the method section (Sect. 2) we firstly introduce different convection schemes (Sect. 2.1) and radiative transfer methods (Sect. 2.2), and finally we present the set of models we used (Sect. 2.3). We present our results in Sect. 3 and we discuss them in Sect. 4. We provide our conclusions in Sect. 5.

2. Method

With the aim of reconciling the large range of results proposed in the literature (Fig. 1), we explored physical mechanisms induced by the addition of nitrogen in a pure steam atmosphere. We built a line-by-line 1D radiative-convective model usable as reference model, named PyRADS-Conv1D, to compute the OLR of the atmosphere. The radiative transfer calculation is derived from

the PyRADS[1] model (Koll & Cronin 2018), and the convective scheme is derived from the RADCONV1D model (Marcq et al. 2017).

To be confident with the physical processes to be included in PyRADS-Conv1D, we performed multiple sensitivity tests using different convective schemes (Sect. 2.1) and radiative transfer methods (Sect. 2.2) from 1D models already described in the literature and presented in Table 1. An exhaustive list of these tested processes and parametrisations is presented below (see also Table A.1). The complete overview of the impact of each parametrisation on the OLR value is available in Appendix A. A similar comparison was done by Yang et al. (2016) with other 1D models, and they found the same wide range of results. More precisely, they show that differences appear using similar models and they explain that these differences are mainly induced by the choice of the water continuum. Our more detailed sensitivity tests were motivated by the interesting conclusions of this study. We tested the following parametrisations: (1) the convection scheme, (2) the resolution of the vertical grid, (3) the shape of the absorption lines, (4) the spectral resolution of the absorption spectrum, (5) a self- of foreign broadening of the absorption lines, (6) the quantity of water isotopes, (7) the truncation of the water continuum, (8) with or without the H_2O-N_2 continuum, (9) the version of the H_2O-H_2O and H_2O-N_2 continua, (10) with or without the N_2–N_2 Collision Induced Absorption (CIA) continuum, (11) the effect an additional fixed amount of CO_2, (12) the solution of the two-stream equations, (13) the interpolation scheme of the correlated-k method.

2.1. Convection schemes

The atmospheres we studied are made of a variable amount of condensable gas (water) and a fixed amount of background gas (nitrogen). The quantity of each gas in the atmospheric layer is dictated by the surface temperature and the surface partial pressures and following a moist adiabatic lapse rate (hereafter 'moist adiabat'). Generally, we assume that condensates are immediately removed by precipitation. This pseudo-adiabatic hypothesis is motivated by the fact that 1D models lack a self-consistently calculated description of (inherently 3D) cloud formation and thus precipitation. Consequently, these models are considered cloud free without other assumptions. The atmospheric profiles are assumed to be fully saturated, and thus the pressure of the condensable gas (here water) is equal to the saturation pressure. In other words, the relative humidity (RH) is equal to unity except in the stratosphere.

The main moist adiabats provided by (and used in) the literature are proposed by Kasting (1988) and Ding & Pierrehumbert (2016). An analytic comparison is made in Appendix B, and it highlights that the main difference between them is the assumption used to define the entropy of the condensable gas. With the aim of comparing and discussing the assumptions and parametrisations done to compute the atmospheric profiles of 1D radiative-convective models, we used two different convective schemes in our study, which are based on the two different adiabats of the literature. The first one, Conv_K88, is based on the adiabat proposed in Kasting (1988), and the second one, Conv_D16, uses the adiabat proposed in Ding & Pierrehumbert (2016). These schemes also assume two different definitions of the vertical grid (see Appendix A.2.1). A complete description of these schemes is given here.

The temperature profiles made by the Conv_K88 scheme follow a lapse rate computed using the equation from Kasting (1988) with 200 atmospheric levels and a minimum total pressure at the top fixed at 0.1 Pa. The saturation pressure and the water entropy are computed using experimental look-up tables (Haar et al. 1984). When the temperature reaches 200 K, the atmosphere is considered isothermal with a constant water-mixing ratio (Kasting et al. 1993). The change of gravity in the atmosphere due to the altitude is taken into account. This method was developed for RADCONV1D (Marcq et al. 2017).

The Conv_D16 scheme uses the Ding & Pierrehumbert (2016) adiabatic lapse rate, with 100 levels and a fixed pressure difference between the top and the bottom of the atmosphere (10^6 Pa). The pressure of the highest level is not fixed, but the two previous parameters are interdependent and chosen to correctly represent the whole atmosphere (see Appendix A.2.1 for more details). The saturation pressure is computed using the Clausius-Clapeyron equation. By definition of the Ding & Pierrehumbert (2016) formulation of the adiabatic lapse rate, the water entropy is computed using the perfect gas approximation (see Appendix B). When the temperature reaches 150 K, the atmosphere is considered isothermal and the water-mixing ratio is fixed. This method was developed for PyRADS and the original parameters are available in Koll & Cronin (2018).

We fixed the number of atmospheric levels of each method thanks to a test of convergence of the OLR value relative to the vertical resolution (see Appendix A.2.1). Figure 2 highlights differences of the thermal profiles and of the water-mass-mixing ratio profiles computed using one convection scheme or the other. The Conv_K88 scheme is more accurate because it is based on look-up tables, while the Conv_D16 scheme is based on perfect gas equations (e.g. Clausius–Clapeyron equation). This induces a non-negligible difference on the estimation of the OLR value (Fig. A.7). For this reason, we used the Conv_K88 scheme as a reference convective scheme (see Sect. 2.3). Figure 2 also shows that for a high surface temperature, that is a high surface pressure, the Conv_D16 scheme is not able to represent the stratosphere because of the fixed difference of pressure between the top and the bottom of the atmosphere. For both methods, we considered an Earth-like planet with a gravity acceleration at the surface equal to 9.81 m s^{-1}.

It is important to keep in mind that for both convection schemes presented in this work the pseudo-adiabatic hypothesis induces a water pressure equal to the saturation pressure (i.e. given by the temperature). Therefore, as the surface boundary conditions are fixed (temperature and nitrogen pressure), the surface water pressure stays unchanged whatever the background gas pressure is.

2.2. Radiative transfer methods

In this work, we used different radiative transfer methods from four different models presented in Table 1. These methods are sub-divided between the two families of radiative transfer calculations detailed below: line-by-line and correlated-k.

PyRADS-RT and PyRADS-updated are line-by-line methods, while kcm1d-RT and `Exo_k`-RT are correlated-k methods. Our aim here is to use a line-by-line method, through the PyRADS-Conv1D model, to produce a result as accurate as possible to benchmark the calculations performed using a correlated-k method, which is computationally much more efficient. We used `Exo_k` as reference model for the correlated-k method. This approach is motivated by the large dispersion of results in the literature and to reconcile line-by-line and correlated-k studies, which seemingly lead to different results (Fig. 1).

[1] https://github.com/ddbkoll/PyRADS

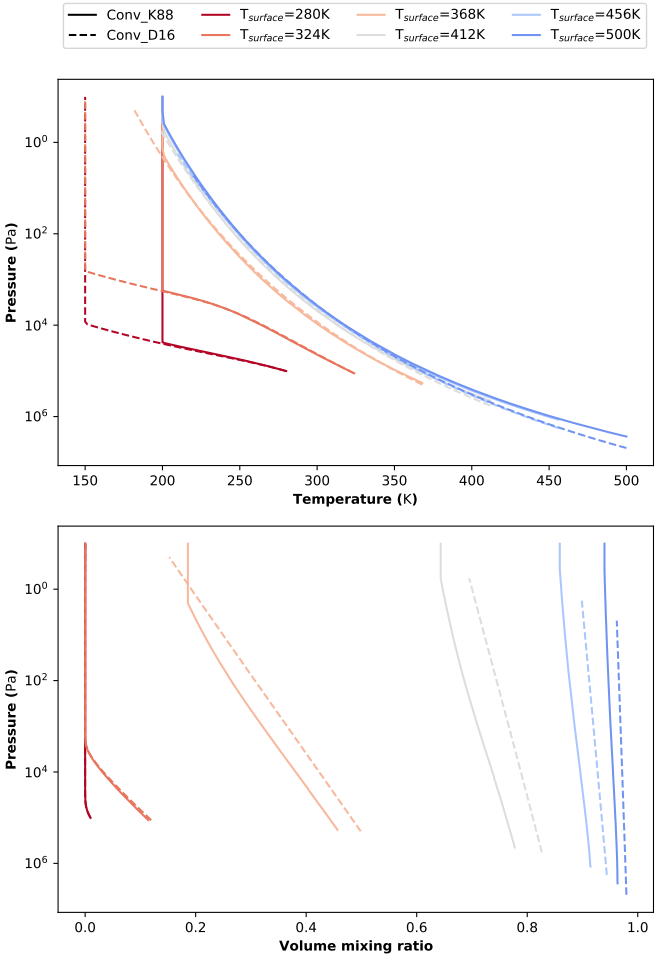


Fig. 2. Comparison between Conv_K88 (full lines) and Conv_D16 (dotted lines) convection schemes for different surface temperatures. The *top panel* represents the temperature profiles, and the *bottom panel* represents the volume-mixing ratio of the water for different surface temperatures. Here, P_{N_2} = 1 bar.

The specificities of the line-by-line and correlated-k methods are detailed below. Several sensitivity tests were performed to quantify the influence of each of the assumptions usually done in the literature on the final estimation of the OLR (Appendix A).

As shown in Table 1, for all methods the H_2O-H_2O and H_2O-N_2 continua are taken into account using the MT_CKD database (Mlawer et al. 2012). The N_2–N_2 collision-induced absorption (CIA) is taken from the HITRAN CIA database (Karman et al. 2019). According to the MT_CKD formalism (Mlawer et al. 2012) the water vapour absorption lines are truncated at 25 cm^{-1} and the plinth[2] is removed from the line centre calculation. In PyRADS-updated, we use the MT_CKD3.2 continuum as explained in Appendix A.1.2. We choose to include only the main isotope water absorption lines in the radiative transfer calculation of PyRADS-updated to increase the computation speed. This is also motivated by our of knowledge of the typical isotopic fraction of the water on terrestrial exoplanets. This assumption does not significantly change the final result (see Appendix A.1.3). Finally, to compute the pressure broadening of the lines we need to have the exponents that describe the temperature dependence for N_2 and H_2O (see Eq. (1)). The exponent for N_2 was taken equal to that of the (Earth) 'air' composition (Gordon et al. 2017). We do not include Rayleigh scattering by water vapour for either methods because it becomes important beyond 10000 cm^{-1} (Kopparapu et al. 2013) where the thermal emission (i.e. the Planck law) is null for the studied range of temperature.

The radiative methods presented here assume different approximations to solve the two-stream equations used to describe the radiative transport of an atmosphere through a upward and downward flux (Meador & Weaver 1980). The kcm1d-RT method uses the classical hemispheric mean approximation while PyRADS-RT and PyRADS-updated and `Exo_k`-RT assume $F^+ = \pi I(\bar{\mu})$ with $\bar{\mu} = 0.6$. This approximation is only valid in the context of a non-scattering atmosphere.

PyRADS-RT and PyRADS-updated assume $\bar{\mu} = 0.6$ which yields less than 1 W m^{-2} of difference compared to the modified hemispheric mean method (see Appendix A.1.5 for more details).

2.2.1. Line-by-line method

The most direct radiative transfer method is to compute the exact absorption spectrum at each level of the atmosphere, that is for each pressure to temperature couple. In other words, the line-by-line method computes the absorption at each wavelength while the correlated-k method considers a statistical distribution of the absorption spectrum. This method avoids interpolations of spectra intrinsic to the correlated-k computation and allows greater flexibility relative to the composition of the atmosphere. However, it makes the computation more time-expensive. As line-by-line computations provide an exact result, we chose PyRADS-updated as a reference radiative transfer method.

The PyRADS-RT and PyRADS-updated methods (Table 1) use low-resolution spectra computed using the HITRAN 2016 line list (Gordon et al. 2017) and assume the shape of the lines follows a Lorentz profile. We show in the Appendix that a spectral resolution of 0.01 cm^{-1} is sufficient to keep a high accuracy, in agreement with Koll & Cronin (2018). We adapted the PyRADS-RT method to create the PyRADS-updated method by adding the N_2–N_2 CIA computation from PyRADS-shortwave[3] (Koll & Cronin 2019) and using a version of MT_CKD continuum extended up to 20 000 cm^{-1} (see Table 1).

2.2.2. Correlated-k method

Models based on the correlated-k method (Fu & Liou 1992) are convenient to use because of their much shorter computation time. Here, absorption spectra are pre-computed for pressure, temperature, and mixing ratio reference values in a so-called correlated-k table. During the radiative transfer calculation, a statistical wavelength distribution of these spectra is interpolated (e.g. Fu & Liou 1992; Leconte 2021) on the pressure to temperature values of each atmospheric level. The correlated-k method can in principle provide the same results as a line-by-line calculation, but at a much lower computational cost. To achieve this purpose the number of bands of the correlated-k table needs to be high enough, as well as the resolution of the pressure, temperature, and mixing ratio grids. In this paper, we provide an $H_2O + N_2$ table that gives similar results to an exact calculation (Fig. 3, top panel).

To build the correlated-k table used in this work, we computed a dataset of high-resolution spectra using the HITRAN

[2] For each spectral line ν, the MT_CKD continuum formalism assumes a constant absorption value between $\nu - 25$ cm^{-1} and $\nu + 25$ cm^{-1} equal to the absorption at $\nu \pm 25$ cm^{-1}. Consequently this 'plinth' needs to be removed in the line centre calculation.

[3] https://github.com/ddbkoll/PyRADS-shortwave

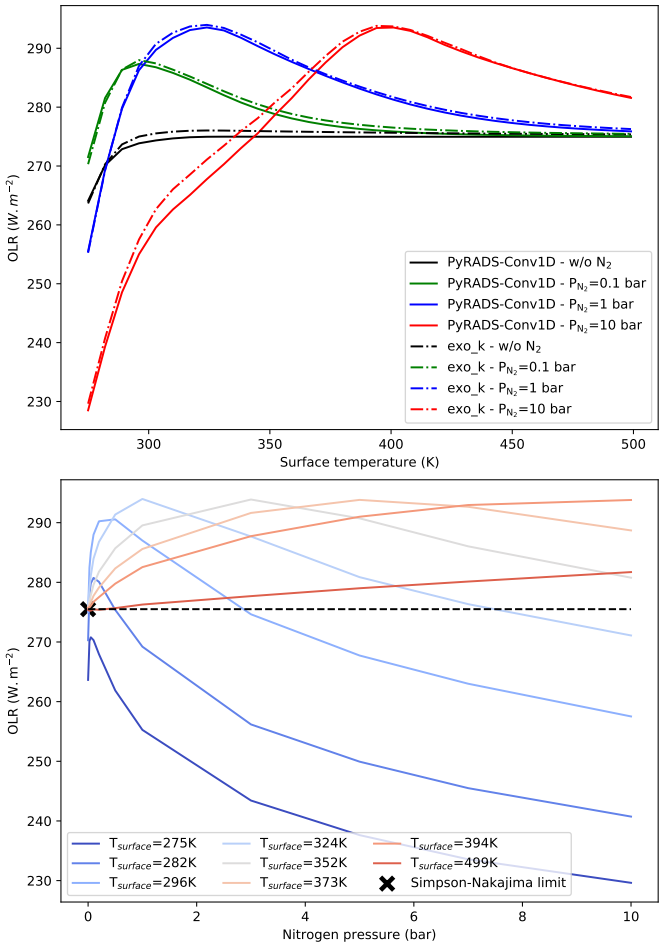


Fig. 3. OLR as a function of the surface temperature (*top panel*) or as a function of the nitrogen pressure (*bottom panel*). The *top panel* represents the OLR curve for different N_2 pressures (black: P_{N_2} = 0 bar, green: P_{N_2} = 0.1 bar, blue: P_{N_2} = 1 bar, red: P_{N_2} = 10 bar) computed with PyRADS-Conv1D (full lines) and `Exo_k` (dotted lines). The *bottom panel* represents the OLR as a function of the surface nitrogen pressure for different fixed surface temperatures computed using `Exo_k`. The black cross represents the Simpson-Nakajima limit for a pure vapour atmosphere.

2016 database (Gordon et al. 2017). These spectra are calculated for multiple values of temperature ($T = \{50, 110, 170 \dots 710, 5000\}$ K), pressure ($P = \{0.1, 1, 10 \dots 10^7\}$ Pa), and water-mass-mixing ratio ($Q = \{10^{-6}, 10^{-5}, 10^{-4} \dots 1\}$). The 21 Gauss points of the table follow a Legendre distribution. The infrared (IR) band is defined in the [10; 4000] cm^{-1} range with a resolution R = 8 (48 bands), which is sufficient to accurately compute water absorption spectra. We also include absorption lines of the water isotopes at terrestrial abundances (De Biévre et al. 1984) in the absorption spectra, but as shown in Appendix A.1.3 this does not significantly change the OLR value. We share the correlated-k table used in this work[4] for a larger spectral range ([0.1; 30000] cm^{-1}) and a higher resolution (R = 300). A usable table at lower resolution can easily be made by using the `Exo_k` package[5].

[4] https://zenodo.org/record/5359158
[5] http://perso.astrophy.u-bordeaux.fr/~jleconte/exo_k-doc/index.html

2.3. Description of the models

Every 1D radiative convective model presented in Table 1 is composed of a convection scheme and a previously described radiative transfer method. The models used are presented here.

The 1D reverse version of LMD-Generic, also named kcm1d (Turbet et al. 2019), uses the Conv_K88 scheme (developed for RADCONV1D; Marcq et al. 2017) and the kcm1d-RT radiative transfer method. This method, described above, is derived from the LMD-Generic model and includes some GCM-specific parametrisations (see Appendices A.1.5 and A.2.4).

The `Exo_k` model (Leconte 2021) also uses the Conv_K88 scheme. Its radiative transfer method, `Exo_k`-RT is a correlated-k method that provides results in accordance with our reference model PyRADS-Conv1D (see top panel in Fig. 3). For this reason, we use it as reference model for sensitivity tests related to the correlated-k method.

The PyRADS model (Koll & Cronin 2018) uses the Conv_D16 scheme with the PyRADS-RT method. We adapted several parameters to fit our needs (e.g. the vertical grid, see Appendix A.2.1). The original parameters are available in Koll & Cronin (2018).

We built the PyRADS-Conv1D model using the most accurate convection scheme (Conv_K88) and radiative transfer method (PyRADS-updated) to produce reference OLR curves according to our sensitivity tests.

3. Results

We present our results in this section. First, we describe the processes that induce a runaway greenhouse effect for a pure steam atmosphere (Sect. 3.1). Secondly, we highlight the differences that arise by adding nitrogen and the processes that allow the OLR overshoot relative to the Simpson-Nakajima limit (Sect. 3.2). Finally, we discuss the two physical processes that induce the overshoot of the OLR in detail (Sects. 3.3.1 and 3.3.2).

3.1. Runaway greenhouse of a pure water atmosphere

The global physical processes that induce a runaway greenhouse effect for a pure water atmosphere are now very well constrained (Ingersoll 1969; Nakajima et al. 1992; Goldblatt & Watson 2012), but numerical estimations of the value of the greenhouse asymptotic limit vary between the different studies, as shown in Fig. 1. These small differences may come from the assumptions made in models or from second-order neglected processes. To understand origins of these differences, we first describe the physical processes involved in a warming atmosphere.

Consider an Earth-like rocky (exo)planet with a global ocean without background gases. At very low temperatures, typically lower than 290K, almost all water is condensed or solidified at the surface of the planet; thus, the (H_2O-dominated) atmosphere is very thin and the planet radiates similarly to a black body. If the surface temperature increases, the thermal emission increases because of the Planck radiation law, and the surface water is expected to progressively evaporate. The thin water vapour atmosphere induces a greenhouse effect via IR absorption by water vapour, consequently the OLR is not strictly equal to the black body emission law. If the temperature increases again, the surface pressure reaches a limit, $P_{\rm thick}$, for which the atmosphere becomes optically thick at long wavelengths (i.e. in the IR absorption bands of water). The OLR is then decoupled from the surface temperature (Nakajima et al. 1992; Pierrehumbert 2010; Goldblatt et al. 2013;

Boukrouche et al. 2021). As the temperature profile follows a purely wet adiabat, the structure of the atmosphere in the thin layers (i.e. 'radiatively active layers' from the optically thick limit $P_{\rm thick}$) up to the top stay unchanged by increasing the surface temperature (see blue curves, i.e. high temperatures, in Fig. 2). Therefore, the absorption in these layers also remains unchanged. For this reason, the OLR reaches an asymptotic limit known as the moist troposphere limit or the Simpson–Nakajima limit (Goldblatt & Watson 2012). As a result, if the absorbed stellar radiation (ASR) is higher than this asymptotic limit, the radiative balance is broken and the surface temperature increases, inducing even more evaporation and progressively building up a thick water-steam-dominated atmosphere. This is the runaway greenhouse effect. When the entire ocean is evaporated and when the planet reaches extremely high temperatures of thousands of kelvins (e.g. Kasting et al. 1993; Kopparapu et al. 2013; Turbet et al. 2019), the OLR increases again. For these temperatures, the planet radiates in the visible, where the water is optically thin.

3.2. Runaway greenhouse of an $H_2O + N_2$ atmosphere: the overshoot effect

In this section, we describe physical processes that may lead to or prevent an OLR overshoot, presented in the top panel of Fig. 3, for an $H_2O + N_2$ atmosphere and computed with PyRADS-Conv1D and `Exo_k`. Regarding Figs. 4 and 5, the evolution of the OLR value is mainly determined by the water-volume-mixing ratio value, whatever the nitrogen pressure, according to three ranges of mixing ratio values: below 5×10^{-5}, between 5×10^{-5} and 0.2, and above 0.2. Therefore, in the following we describe the evolution of the OLR through three cases: low, high, or intermediate mixing ratios.

At very low mixing ratios, the surface temperature is rather low (Fig. 4). Consequently, the vapour pressure is also low and N_2 is dominant; thus, the lapse rate is very close to a dry adiabatic lapse rate. For the following, we assumed a dry adiabat. Moreover, the broadening of the water absorption lines is dominated by foreign broadening (Fig. 6).

The atmospheric absorption is mainly in the first layers that contain water (with a partial water pressure roughly greater than 5 Pa). The temperature of a dry atmosphere is lower than for a wet one, that is the temperature decreases faster relatively to altitude (Fig. 2). Therefore, for a given low surface temperature, the total amount of steam in the whole atmosphere is low if the nitrogen pressure is high (because the lapse rate is close to a dry adiabatic lapse rate; see Fig. 4); thus, the intensity of absorption lines decreases by increasing the nitrogen pressure (e.g. bottom panel of Fig. 3 for $T_{\rm surface}$ = 275 K). However, as the vapour pressure is limited by the pseudo-adiabatic hypothesis, it cannot exceed the saturation pressure ($P_{\rm H_2O} \leq P_{\rm saturation}$); therefore, the self-broadening is limited as well. As nitrogen is a non-condensable gas here, its pressure is not limited and the foreign broadening may be stronger than the self-broadening. Therefore, when the atmosphere is nitrogen dominated, the total broadening of the absorption lines is stronger than for a pure vapour atmosphere, the atmosphere absorbs in more wavelengths, and the OLR is weaker than for a pure vapour atmosphere, as shown in the bottom panel of Fig. 3 and for the $P_{\rm N_2}$=10 bar in the top panel of Fig. 3.

At high mixing ratios, the temperature is high and water becomes dominant; hence, the temperature profile follows a moist adiabatic lapse rate. By evaporating more and more water, the absorption line broadening becomes dominated by the self-coefficient, and the mean molecular weight tends towards the water molecular weight. Properties of the atmosphere (temperature profile, mixing ratio, molecular weight, etc.) tend towards the properties of a pure water atmosphere; thus, the OLR tends towards the Simpson–Nakajima limit (Fig. 3, bottom panel).

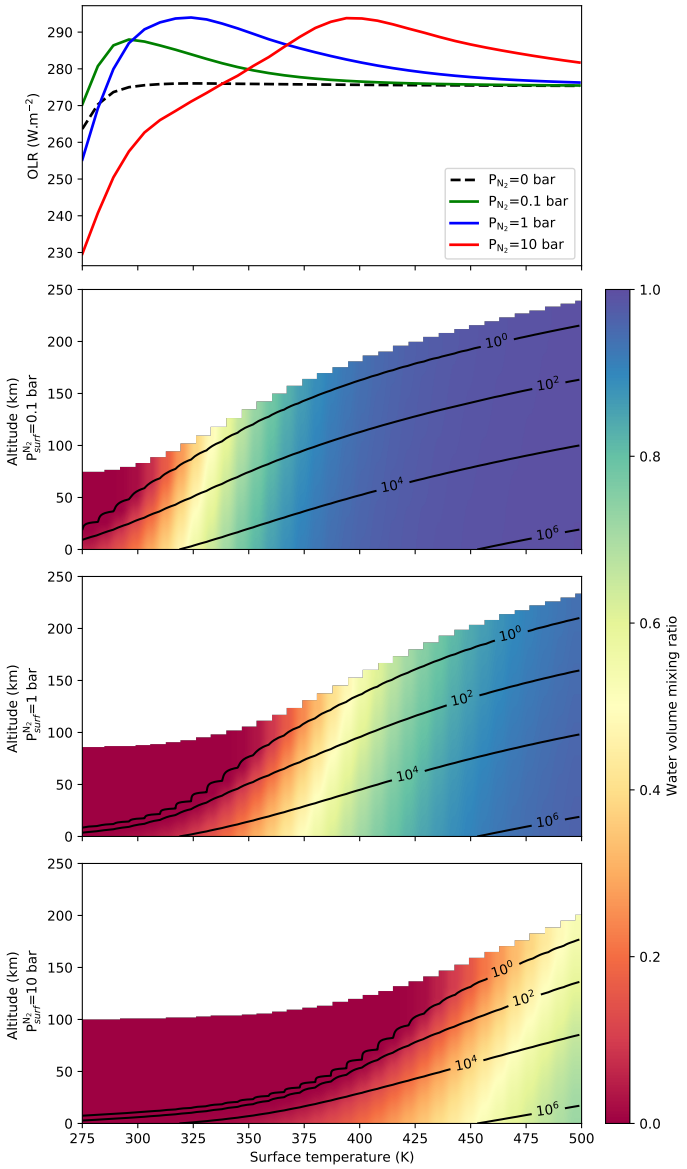


Fig. 4. OLR and corresponding atmospheric water content as a function of the surface temperature. The *top panel* is the OLR as a function of the surface temperature for different nitrogen pressure, computed with PyRADS-Conv1D. The *three bottom panels* represent the size of the atmosphere (up to 0.1 Pa) for different nitrogen pressures where the colour bar indicates the water-volume-mixing ratio ($\frac{P_{\rm H_2O}}{P_{\rm H_2O}+P_{\rm N_2}}$) of each atmospheric level. The contour lines indicate the partial pressure of the water in Pa units.

At intermediate mixing ratios (the OLR overshoot), the corresponding intermediate temperatures corresponds to the transition between an N_2-dominated and an H_2O-dominated atmosphere (Fig. 4). First, this induces a transition between a foreign broadening and a self-broadening of the water absorption lines. As the self-broadening is stronger than the foreign broadening, the absorption increases strongly during this transition. As shown in Fig. 6, the overshoot itself exists through this broadening transition and may be missed by neglecting the change of broadening species (for more details, see Sect. 3.3.1).

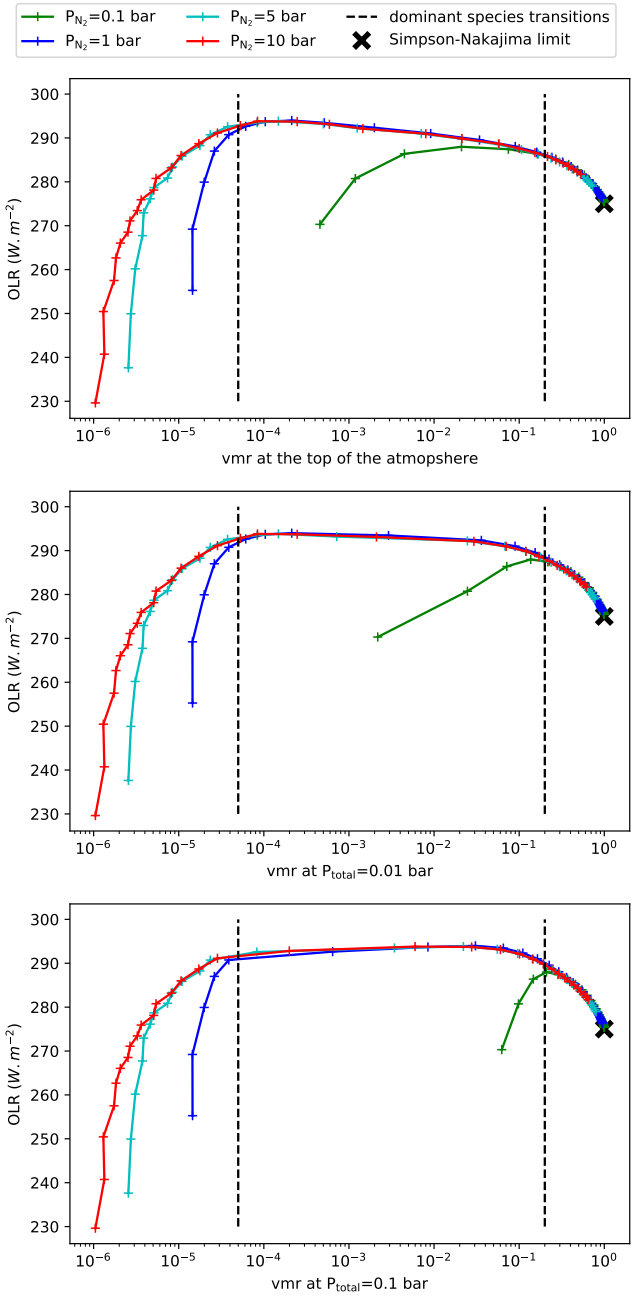


Fig. 5. OLR as a function of the volume-mixing ratio for different nitrogen surface pressures using `Exo_k`. The volume-mixing ratio (vmr) values are given at the top of the atmosphere (*top panel*), at 0.01 bar (*middle panel*), and at 0.1 bar (*bottom panel*) of total pressure. The black cross represent the Simpson-Nakajima limit for a pure vapour atmosphere, and the vertical dashed lines approximately delimit the range of vmr values for which there is a transition of dominant species.

Second, the transition between an N_2 -dominated and an H_2O-dominated atmosphere induces a transition between a dry and a wet adiabatic lapse rate (Figs. 2 and 7). Even if N_2 is still dominant (volume-mixing ratio below 0.2), the water pressure becomes non-negligible (Figs. 4 and 5). Because of that, a small increase in the surface temperature tends to turn the dry adiabatic lapse rate into a wet adiabatic lapse rate. As the adiabat becomes wetter, the structure of the atmosphere changes and the temperature decreases more slowly with the altitude (Fig. 7), which tends to allow more water in the upper layers. This has the effect of increasing the size of the atmosphere strongly and

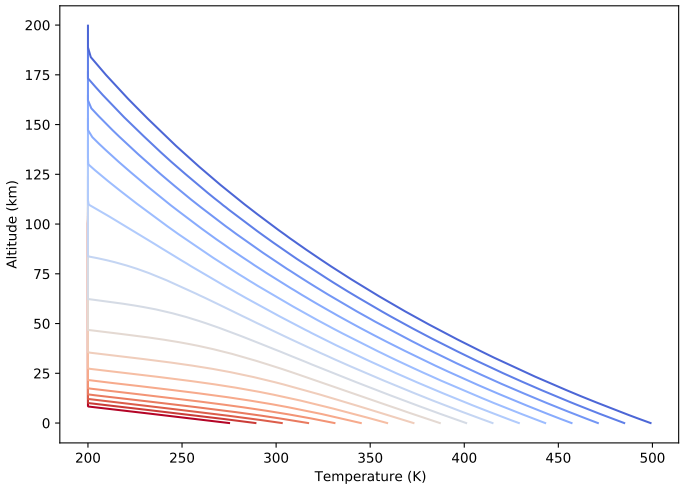


Fig. 6. OLR as a function of the temperature for P_{N_2}=10 bar. The full lines were computed with PyRADS-Conv1D. The full red line corresponds to the OLR curve for a self-broadening only, and the full blue line corresponds to a foreign broadening. The full black line corresponds to a mixed broadening, such as that presented in the top panel of Fig. 3. The dotted red line is obtained using `Exo_k` with a correlated-k table made with pure water absorption lines (i.e. self-broadening only). Here, both self- and foreign continua are included in the computations.

quickly (Fig. 4). Due to this positive feedback effect, the transition of dominant species can be done over a small temperature range (Fig. 7).

Nevertheless, we can see that the transition between wet and dry atmospheres spans a wider temperature range for higher nitrogen pressures. If N_2 pressure is higher, H_2O pressure required to be vapour dominated is higher, and thus the required surface temperature is higher. Therefore, the temperature difference between the first visible effects of non-negligible vapour quantity and a vapour-dominated atmosphere is bigger. That is the reason why the overshoot spans a wider temperature range for 10 bar of nitrogen (Fig. 3).

Finally, the transition of dominant species also induces a transition of the mean molecular weight, from nitrogen molecular weight to water molecular weight. As explained in detail in Sect. 3.3.2, changing the mean molecular weight affects both the atmospheric profile and the radiative transfer calculation. Increasing molecular weight of the background gas tends to reduce the R/c_p value, and thus the OLR decreases. On the other hand, increasing the molecular weight of the background gas also tends to reduce the opacity of the atmosphere, and thus the OLR increases. As shown in Fig. 8, this second effect is stronger; therefore, as shown on the bottom panel of the Fig. 8, it increasing the molecular weight of the background gas means increasing the OLR. When water becomes dominant, the mean molecular weight – and all the physical properties of the atmosphere – tend towards water values, and the OLR converges on the Simpson–Nakajima limit. Consequently, the height of the overshoot is mainly determined by the molecular weight of the background gas (nitrogen here), while the overshoot itself is due to the broadening transition.

3.3. Physical effects of the nitrogen

In this section, we discuss the two main effects of the nitrogen in detail. These are introduced in Sect. 3.2. The first one is the broadening effect (Sect. 3.3.1), and the second one is the mean molecular weight effect (Sect. 3.3.2).

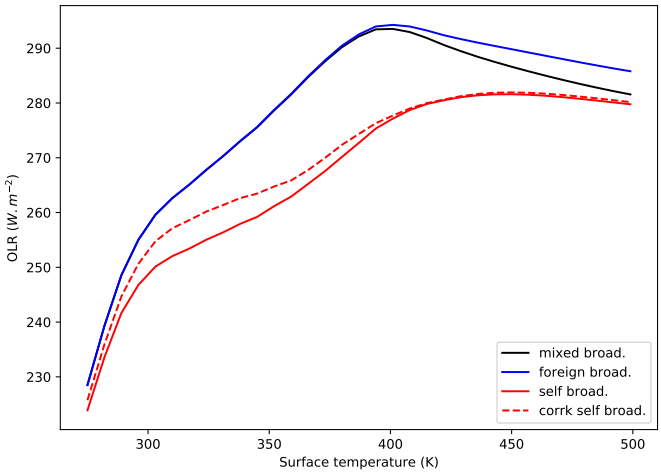


Fig. 7. Temperature profiles computed with the Conv_K88 scheme for different surface temperatures with P_{N_2} = 10 bar. This figure highlights the transition from dry to wet steeper profiles.

3.3.1. Broadening effect

In radiative transfer calculations, whatever the method used, the half width at half maximum (HWHM) of the absorption lines due to the pressure broadening can be described by Eq. (1) from Gordon et al. (2017):

$$\gamma(P_{\rm tot}, P_{\rm H_2O}, T) = \left(\frac{T_{\rm ref}}{T}\right)^{n_{\rm N_2}} \gamma_{\rm N_2}(P_{\rm ref}, T_{\rm ref})\,(P_{\rm tot} - P_{\rm H_2O}) + \left(\frac{T_{\rm ref}}{T}\right)^{n_{\rm H_2O}} \gamma_{\rm H_2O}(P_{\rm ref}, T_{\rm ref})\,P_{\rm H_2O}, \quad (1)$$

where $P_{\rm tot}$ is the total pressure, $P_{\rm H_2O}$ the partial water pressure, and T the temperature. $\gamma_{\rm N_2}(P_{\rm ref}, T_{\rm ref})$ and $\gamma_{\rm H_2O}(P_{\rm ref}, T_{\rm ref})$ are the HWHM of the foreign- and the self-pressure broadening at the reference temperature. As explained previously, we assume that the nitrogen temperature dependency exponent is equal to the air exponent: $n_{\rm N_2} = n_{\rm AIR}$. This assumption is motivated by the lack of an experimental value for N_2 alone, but the difference should be small. For the same reasons, we also assume that the self-component of the pressure-induced shift of the line centre (δ in Gordon et al. 2017) is equal to that of the air component: $\delta_{\rm self} = \delta_{\rm AIR}$.

If the background gas is a trace gas, it is possible to neglect the HWHM of the foreign broadening and assume that the line broadening only depends on the self-broadening (Eq. (2)). However, as explained before, for low surface temperatures the water pressure is limited by the pseudo-adiabatic hypothesis, while the nitrogen pressure is not. Therefore, by only considering the self-broadening to compute the pressure broadening (Eq. (2)), the HWHM and thus the absorption is largely over-estimated, which leads to incorrect OLR values where the overshoot is hardly visible (red lines in Fig. 6):

$$\gamma_{\rm self}(P_{\rm tot}, T) = \left(\frac{T_{\rm ref}}{T}\right)^{n_{\rm H_2O}} \gamma_{\rm H_2O}(P_{\rm ref}, T_{\rm ref})\,P_{\rm tot}, \quad (2)$$

where $P_{\rm tot}$ is the total pressure. This effect is strong in our case study because of the transition between an N_2-dominated and an H_2O-dominated atmosphere. The black curve in Fig. 6 highlights the transition between the N_2-dominant (i.e. foreign) and the H_2O-dominant (i.e. self) broadening, corresponding to the curves proposed in Fig. 3.

It is possible to build a correlated-k table from high-resolution spectra of pure water even by neglecting the foreign broadening. This possibility is commonly used to skip the tedious step of calculating a large number of spectra in the case of a unusual mix of gases. By doing that, we assume a self-broadening only, and thus we over-estimate the absorption (dotted red line in Fig. 6) as explained just above. Regarding our conclusions, the error induced by this method is only negligible if the background gas is a trace gas. However, Amundsen et al. (2017) discussed different possibilities to easily produce correlated-k for mixed gases. They show that in particular cases, correlated-k table built by mixing the tables of pure species, that is by neglecting the mutual broadening, may produce accurate results with a greater flexibility than by creating pre-mixed correlated-k tables.

It can be counter-intuitive to state that an OLR curve produces an overshoot by only assuming the foreign broadening but

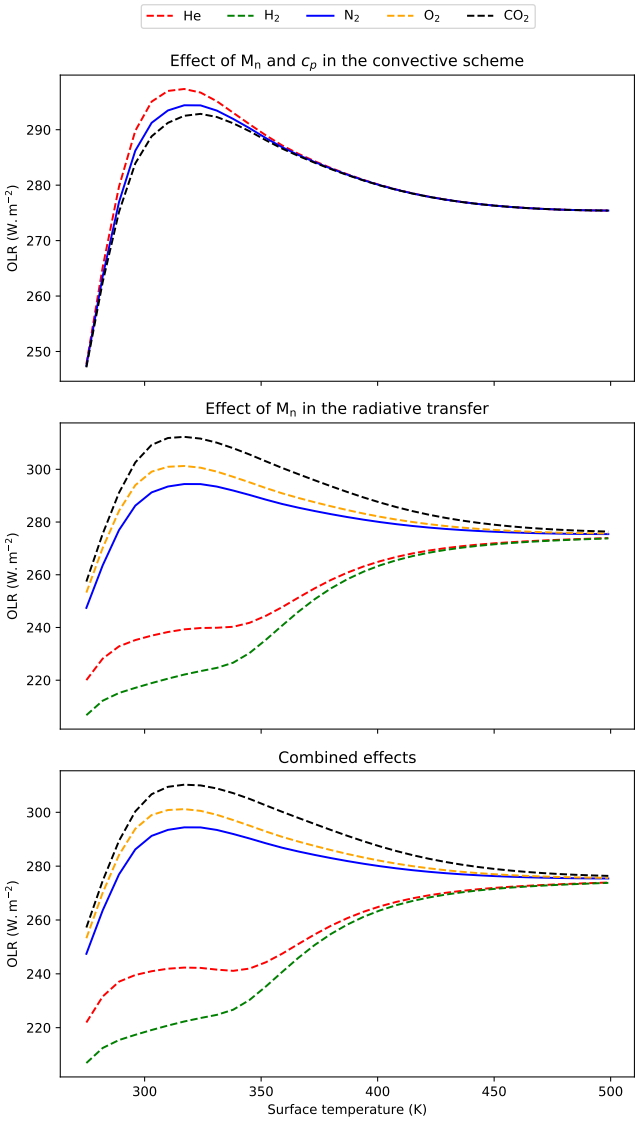


Fig. 8. OLR as a function of the surface temperature by only using the physical properties of other gases in the convective scheme calculation (*top panel*), in the radiative transfer calculation only (*middle panel*) and in both of them (*bottom panel*). The full blue line corresponds to the curve presented in the top panel of Fig. 3 with the true value of the nitrogen molecular weight. The dotted lines correspond to M_n and c_p values of other gases (see Table 2). Here, we used the Conv_D16 scheme and the `Exo_k`-RT radiative transfer method assuming 1 bar of background gas.

not by only assuming the self-broadening (Fig. 6). This may be explained by a subtle effect of the broadening power of water and nitrogen. As the self-broadening is stronger than the foreign one, the absorption lines of the 'self-only case' are probably already more broadened than for the 'foreign-only case'. Therefore, the overshoot effect described previously is probably weaker if we only consider the self-broadening. Nevertheless, a deeper study of this point is needed before any conclusion can be drawn.

3.3.2. Molecular weight effect

As discussed in Pierrehumbert (2010), the addition of a background gas modifies the atmospheric structure, which plays an important role on the shape of the OLR curve. We can study this effect by analysing the effect of the molecular weight of the background gas on the atmospheric profile and on the radiative transfer calculation separately. For convenience and as we only analysed tendencies, we chose to use the Conv_D16 scheme and the `Exo_k`-RT radiative transfer method. In the same way, radiative properties of the background gas (mainly the broadening) are those of nitrogen in order to only study the effect of the molecular weight on the OLR value.

With regard to the effect on the atmospheric profile, by rewriting the equation proposed by Ding & Pierrehumbert (2016) (see Eq. (B.3)) and assuming a constant number of background molecules (n_n), it is possible to show that the adiabatic lapse rate depends on the molecular weight of the background gas (M_n) only through the R_n/c_{pn} value (in red in Eq. (3)), where R_n is the specific gas constant of the background gas (Eq. (3)):

$$\frac{\mathrm{d}\ln P}{\mathrm{d}\ln T} = \frac{P_\mathrm{c}}{P}\frac{L}{R_\mathrm{c}T} + \frac{P_n}{P} \times \frac{\frac{c_{pn}}{R_n} + \left(c_\mathrm{pc} + \left(\frac{L}{R_\mathrm{c}T} - 1\right)\frac{L}{T}\frac{m_\mathrm{c}}{R^* n_n}\right)\alpha_\mathrm{c}}{1 + \frac{L}{T}\frac{m_\mathrm{c}}{R^* n_n}\alpha_\mathrm{c}}. \quad (3)$$

Indices of variables in Eq. (3) indicate what gas is considered: c for the condensable gas (water here) and n for the background gas. Here, P is the pressure, T the temperature, M the molecular weight, R^* the perfect gas constant, R the specific gas constant, L the latent heat, and c_p the heat capacity. By changing the background gas, both M_n and c_{pn} change as shown in Table 2. However, for diatomic gases (N_2, O_2, H_2 ...), the molecular heat capacity ($c_{\mathrm{p,molec}} = c_\mathrm{p} \times M$) is remarkably similar. By definition, the R_n/c_{pn} value is also remarkably similar whatever the considered diatomic gas. This means that for such gases, most of the atmospheric profiles will be the same, as will the OLR curve as shown on the top panel of Fig. 8. For triatomic molecules such as CO_2, the R_n/c_{pn} value decreases, which means that the temperature decreases more slowly with altitude. Therefore, the atmosphere warms up and because of the pseudo-adiabatic hypothesis, the total amount of water increases, and the OLR decreases.

Concerning the effect on the radiative transfer, the molecular weight of the background gas has a much stronger impact on the radiative transfer calculation. By assuming a radiatively inactive background gas, the opacity of the atmosphere (τ) can be simply written by Eq. (4):

$$\tau = \int \frac{x_\mathrm{c}\sigma_c}{x_\mathrm{c}M_\mathrm{c} + x_n M_n}\frac{\mathrm{d}p}{N_A g}, \quad (4)$$

where x_i, σ_i are the volume-mixing ratio and the cross-section per molecule (in m^2/molecule) of the species i. N_A is the Avogadro number.

Interestingly, if the molecular weight of the background gas (M_n) changes without altering the atmospheric temperature profile (i.e. if R_n/c_{pn} remains constant), then the vapour-volume-mixing ratio profile does not change either because it only depends on $T(p)$. In other words, at any pressure level, the water-molecule-to-background-gas ratio stays the same. However, rather counter intuitively, changing M_n at a constant surface pressure changes the total number of molecules of background gas, and hence the total number of water molecules, although the ratio and total mass stay the same.

Table 2. Molecular weight (M), heat capacity (c_p), and molecular heat capacity ($c_{\mathrm{p,molec}}$) for different background gases (Gas), where $c_{\mathrm{p,molec}} = c_\mathrm{p} \times M$.

Gas	M (g mol^{-1})	c_p (J g^{-1} K^{-1})	$c_{\mathrm{p,molec}}$ (J mol^{-1} K^{-1})
He	4.003	5.196	20.80
H_2	2.016	14.23	28.69
N_2	28.02	1.037	28.02
O_2	31.99	0.916	29.30
CO_2	44.01	0.820	36.09

Notes. The heat capacity values are taken at 0°C and 1 bar from Pierrehumbert (2010).

Therefore, for a given atmospheric profile, if the molecular weight of the background gas (M_n) decreases, the mass of water vapour in the atmosphere increases and the latter becomes more opaque, as demonstrated by Eq. (4). This leads to a decrease in the OLR, as shown on the middle panel of Fig. 8.

Concerning the global effect of the molecular weight, as is visible in Fig. 8, the effect of the molecular weight on the radiative transfer calculation (middle panel) is largely dominant compared to the modification of the atmospheric profile (top panel). For this reason, the OLR curve obtained by taking into account both effects (bottom panel) is similar to the one for which we take into account only the effect on the radiative transfer.

For gas mixtures with other inactive gases (e.g. O_2, H_2), the proposed analysis may help to understand how the OLR evolves regarding changes of the mean molecular weight of the atmosphere. For example, gases lighter than N_2 – such as H_2 – tend to reduce the OLR, as shown by previous studies (e.g. Koll & Cronin 2019). For radiatively active gases such as CO_2, the molecular weight effect still plays a role but may become a second-order process compared to the absorption of the gas itself (see e.g. Appendix A.1.4). However, when changing the mixture, the radiative properties of the atmosphere will change and the OLR will be slightly impacted.

It is interesting to notice that when the global effect of the molecular weight is taken into account (bottom panel on Fig. 8), there is a qualitative change in the shape of the OLR curve, and even a hump when using the He gas properties. This hump, which arises below the Simpson–Nakajima limit, is discussed in Koll & Cronin (2019) as a 'soufflé' effect with the example of H_2. This effect is more pronounced in Koll & Cronin (2019) because they assume a grey gas for the radiative transfer calculation. On the He curve (Fig. 8), the two physical effects described in Sect. 3.2 are clearly visible. First, the overshoot itself, due to the transition between a foreign-broadening and a self-broadening (Sect. 3.3.1) and, second, the convergence of the physical properties of the atmosphere toward pure steam atmosphere properties (e.g. the mean molecular weight).

In this section, we show that the height of the overshoot is given by the background gas molecular weight, but Fig. 3

shows that the OLR overshoot assuming 0.1 bar of nitrogen is weaker than it is for higher nitrogen pressures. As presented previously, the transition between nitrogen-dominated and vapour-dominated atmospheres is key to understanding the overshoot, but this induces a minimal N_2 pressure to achieve this transition. With 0.1 bar of nitrogen, low vapour pressures induced by low temperatures are sufficient to be non-negligible, with a volume-mixing ratio higher than 5×10^{-5} (see Figs. 4 and 5). Consequently, the atmosphere is never fully nitrogen dominated, and the height of the OLR overshoot is weaker. Koll & Cronin (2019) defined a similar 'dilute limit'.

4. Discussion

In this section, we discuss our results (Sect. 4.1), and we propose explanations to understand the differences in the results of the literature (Sect. 4.2).

4.1. Discussion of the results

The OLR curves presented in Fig. 3 are proposed as reference curves because they include all the major physical processes of an $H_2O + N_2$ atmosphere. However, these processes were tested for Earth-like planets with surface temperatures between 275 K and 500 K. We are confident in the applicability of our conclusions with other similar inactive background gases (e.g. H_2), particularly concerning the hierarchy of importance induced by the sensitivity tests presented in Table A.1. In the same way, Sects 3.3.1 and 3.3.2 describe the effect of the broadening and of the molecular weight with the example of nitrogen, but our conclusions are applicable for other background gases.

This work can be a first step towards a complete overview of effects of different background gases on an Earth-like atmosphere. The accuracy obtained on OLR values in this paper is higher than the precision required for a GCM simulation regarding to other uncertainty sources, but presented sensitivity tests could be useful for GCM intercomparisons (e.g. Yang et al. 2016, 2019; Fauchez et al. 2021). Also, we do not discuss the variations of the absorbed solar radiation (ASR) in this work (which is necessary to compute up to the top-of-atmosphere radiative budget), but it is a major quantity to study the runaway greenhouse and compute the inner edge of the HZ.

In our model, we assume a relative humidity (RH) equal to unity, but this is a strong assumption that can lead to incorrect estimations of the OLR, particularly regarding values from most complex and accurate simulations using GCMs (e.g. Leconte et al. 2013). A good improvement should be to adapt the RH of our model as prescribed by Leconte et al. (2013), or to use a variable value such as that of Goldblatt et al. (2013). Ramirez et al. (2014) used 1D self-consistent RH parametrisation, which can also be a solution to improve our calculation. In the same way, we followed the description of the stratosphere from Kasting (1988), assuming a constant temperature and mixing ratio. This is valid when the stratospheric part of the atmosphere is small compared to the troposphere, that is at a high temperature. At a low temperature, when the adiabat is close to a dry adiabat, this assumption should induce strong inaccuracies. It could be interesting to quantify the differences between our radiative-convective model with a time-marching model that takes into account the radiative heating of the star. This may be helpful to understand the error induced by the stratospheric hypothesis. We parametrise PyRADS-Conv1D to reach an error at most equal to 1 W m^{-2}, but we neglect the dynamics and assume a cloud free atmosphere. This assumption is motivated by the fact that the dynamical effects (e.g. advection) are at best parametrised in 1D models. However, the strong greenhouse power of the clouds and the redistribution of the heat and humidity due to advection have a strong impact on the OLR, as shown by many studies (e.g. Yang et al. 2013, 2019; Leconte et al. 2013).

Appendix A.2.1 discusses the definition of the vertical grid and the minimal required number of atmospheric levels. This can be a critical point for GCMs where the number of levels is limited. The height of the atmosphere strongly increases with increasing surface temperature, that is the amount of vapour. This can become problematic if the number of levels is not sufficient – or if the atmosphere is not extended enough – leading to a truncation of the 'radiatively active part' of the atmosphere. A solution would be to modify the vertical grid to keep a low vapour pressure in the upper layers and to adapt the altitude of the atmospheric levels to accurately represent the lower part of the atmosphere.

4.2. Literature comparison

A large model intercomparison was done in Yang et al. (2016) for an $H_2O + N_2$ atmosphere with 376ppmv of CO_2. They highlighted the fact that differences between the models increase with the temperature and reach 25 W m^{-2} at 360 K. This is similar to the range of values we observed in Fig. 1 at low nitrogen pressure with our set of models. Thanks to our multiple sensitivity tests, we are able to explain this wide range of results by discussing parametrisations and assumptions used in different 1D models from the literature.

Kopparapu et al. (2014) added 350 ppm of CO_2 to the radiative transfer calculation (Ravi K. Kopparapu, priv. comm.) compared to other results presented in Fig. 1. This can strongly modify the OLR, as explained in Appendix A.1.4. However, the computations done by that group show that even with a pure N2 atmosphere they do not reproduce the overshoot of the OLR (anonymous referee, priv. comm.). They used the adiabat proposed by Kasting (1988) to compute the atmospheric profiles, assuming 101 levels and a constant stratospheric temperature equal to 200 K (Kopparapu et al. 2013). The radiative transfer calculation is based on a correlated-k method that uses a combination of the HITRAN and HITEMP databases (Kopparapu et al. 2013). To compute the water continuum, Kopparapu et al. (2014) used BPS (Paynter & Ramaswamy 2011), while we used MT_CKD in PyRADS-Conv1D. As presented in Appendix A.1.2, the choice of the continuum may shift the asymptotic limit of the runaway greenhouse. Finally, Kopparapu et al. (2014) did not obtain an OLR overshoot, unlike other studies presented in Fig. 1. They used separated H_2O and N_2 correlated-k coefficients instead of mixed coefficients (anonymous referee, priv. comm.), and as highlighted by our sensitivity tests, the easiest way to miss the overshoot is to neglect the foreign broadening of the water absorption line. Therefore, this assumption could explain a part of the difference observed in Fig. 1.

To compute the radiative transfer of the atmosphere, Goldblatt et al. (2013) used a line-by-line code called SMART (Meadows & Crisp 1996) between 0 and 30000 cm^{-1} (for the water) using HITEMP2010. The HITRAN and HITEMP databases are not strictly equal and may produce different OLR values (e.g. Goldblatt et al. 2013), but this is negligible below 350K (Kopparapu et al. 2013). They also compute their own water continuum which slightly underestimates the absorption (Goldblatt et al. 2013). Moreover, as shown in Fig. A.2, different

continua may induce a different estimation of the Simpson-Nakajima limit. This may partially explain the high OLR values obtained by Goldblatt et al. (2013). They also assume a variable RH, which is more accurate than assuming an RH equal to unity, as is frequently done in 1D radiative-convective models (including PyRADS-Conv1D). As shown by Leconte et al. (2013), this may have a strong impact on the shape of the OLR curve and also on the Simpson-Nakajima asymptotic value. This is probably the main difference between the results of Goldblatt et al. (2013) and others in Fig. A.2.

The asymptotic value of the runaway greenhouse obtained by Zhang & Yang (2020) is much higher than that from Goldblatt et al. (2013), Kopparapu et al. (2014), or ours. They used ExoRT[6], which is derived from the GCM named ExoCAM. GCMs sometimes contain strong assumptions that are necessary regarding the computation time; thus, additional analyses are required to understand the difference between the results of Zhang & Yang (2020) and those of others.

In the same way, the 1D reverse version of the LMD-Generic model (kcm1d; see Turbet et al. 2019) provides results that are shifted lower compared to PyRADS-Conv1D, `Exo_k`, and PyRADS. This is due to both the two-stream solution used (constrained by the LMD-Generic requirements) and the correlated-k interpolation scheme. In kcm1d, the average angle of the outgoing flux used (μ_0) is fixed by the Hemispheric mean method.

5. Conclusion

In this work, we built a new 1D radiative-convective model named PyRADS-Conv1D – based on Koll & Cronin (2019) and Marcq et al. (2017) – to propose OLR reference curves (Fig. 3) for an $H_2O + N_2$ atmosphere. Through multiple sensitivity tests (see Appendix A), we were able to identify the most important physical processes required to accurately model such atmospheres. These reference curves confirm the occurrence of an overshoot of the OLR relatively to the Simpson-Nakajima limit by adding nitrogen in a pure vapour atmosphere. We provide an accurate $H_2O + N_2$ correlated-k table that reproduces the results obtained by the line-by-line calculation.

We show that the overshoot is due to a non-usual transition between an N_2-dominated atmosphere and an H_2O-dominated atmosphere (see Sect. 3). This transition challenges the modelling by making important, usually second-order, processes. More precisely, we explain that the OLR overshoot is due, firstly, to a transition between a foreign or self-broadening of the water absorption lines (see Sect. 3.3.1), and, secondly, to a transition between a dry adiabatic lapse rate and a moist adiabatic lapse rate. In other words, the overshoot itself is due to a broadening transition, and its height is determined by the molecular weight of the background gas (nitrogen here) through a modification of the dry part of the adiabat (see Sect. 3.3.2). A heavier gas induces a stronger overshoot, and a lighter one induces a weaker overshoot.

Our sensitivity tests also allow us to highlight that differences between previous studies are mainly due to missing physics or inaccurate or over-simplified parametrisations. For this reason, we list the most important physical processes and parametrisations needed to obtain an accurate value of the OLR for the considered atmosphere, and we quantify the error or the uncertainty induced by each of them (see Table A.1). Several of these physical processes induce negligible errors if they are omitted, but some of them may induce a large error, large enough to lead to their missing the OLR overshoot. First of all, the foreign broadening cannot be neglected (Fig. 6), otherwise the overshoot vanishes because the pressure broadening of the water absorption lines is over-estimated. Secondly, the water continua (H_2O–H_2O, H_2O–N_2) should be carefully chosen because they have a non-negligible impact on the computed OLR value, about a few watt per square meter, and on the value of the asymptotic limit of the runaway greenhouse (Appendix A.1.2). The convection scheme may also induce a difference in the estimation of the content of water vapour by using the perfect gas approximation. Finally, the two-stream solution used (i.e. the μ_0 angle chosen, see Appendix A.1.5) and the correlated-k interpolation scheme may modify the asymptotic limit of the runaway greenhouse by inducing a OLR difference of several W m^{-2}.

Following a similar approach to Kasting (1988) or Kopparapu et al. (2013) to compute the inner edge of the HZ leads us to consider the maximum OLR value as a threshold value for the onset of the runaway greenhouse. The OLR overshoot we obtained tends to validate that the inner limit of the HZ depends on the nitrogen pressure (e.g. Ramirez 2020). Moreover, this inner limit is probably closer to the host star compared to previous studies that missed the overshoot (e.g. Kopparapu et al. 2014).

Modelling an $H_2O + N_2$ atmosphere using a GCM may probably provides very different OLR values because of the dynamics and the radiative effects of the clouds (e.g. Yang et al. 2013, 2019; Leconte et al. 2013; Wolf 2017). The radiative effect of the clouds is usually a dominant process in the computation of the OLR (e.g. Leconte et al. 2013; Turbet et al. 2021), and the water-dominated atmosphere induced by high temperatures is probably highly cloudy. Leconte et al. (2013) also showed that the stabilising effect of the Hadley circulation shifts the greenhouse limit higher. For these reasons, we plan to revisit this work using a GCM that includes large-scale dynamics and clouds. Nevertheless, the processes we describe in this work and the pressure-broadening transition should still play a role in such simulations.

Acknowledgements. This work has been carried out within the framework of the National Centre of Competence in Research PlanetS supported by the Swiss National Science Foundation. The authors acknowledge the financial support of the SNSF. This project has received funding from the European Union's Horizon 2020 research and innovation program under the Marie Sklodowska-Curie Grant Agreement No. 832738/ESCAPE and under the European Research Council (ERC) grant agreement n°679030/WHIPLASH. M.T. thanks the Gruber Foundation for its support to this research.

References

Amundsen, D. S., Tremblin, P., Manners, J., Baraffe, I., & Mayne, N. J. 2017, A&A, 598, A97
Boukrouche, R., Lichtenberg, T., & Pierrehumbert, R. T. 2021, ApJ, 919, 130
De Biévre, P., Gallet, M., Holden, N. E., & Barnes, I. L. 1984, J. Phys. Chem. Ref. Data, 13, 809
Ding, F., & Pierrehumbert, R. T. 2016, ApJ, 822, 24
Fauchez, T. J., Turbet, M., Sergeev, D. E., et al. 2021, PSJ, 2, 106
Fu, Q., & Liou, K. N. 1992, J. Atmos. Sci., 49, 2139
Goldblatt, C., & Watson, A. J. 2012, Philos. Trans. R. Soc. A: Math. Phys. Eng. Sci., 370, 4197
Goldblatt, C., Robinson, T. D., Zahnle, K. J., & Crisp, D. 2013, Nat. Geosci., 6, 661
Gordon, I. E., Rothman, L. S., Hill, C., et al. 2017, J. Quant. Spectr. Rad. Transfer, 203, 3
Haar, L., Gallagher, J. S., & Kell, G. S. 1984, NBS/NRC Steam Tables: Thermodynamic and Transport Properties and Computer Programs for Vapor and Liquid States of Water in SI Units (Washington (D.C.) : Hemisphere)

[6] https://github.com/storyofthewolf/ExoRT

Ingersoll, A. P. 1969 J. Atm. Sci., 26, 1191
Karman, T., Gordon, I. E., van der Avoird, A., et al. 2019, Icarus, 328, 160
Kasting, J. F. 1988, Icarus, 74, 472
Kasting, J. F., Whitmire, D. P., & Reynolds, R. T. 1993, Icarus, 101, 108
Koll, D. D. B., & Cronin, T. W. 2018, Proc. Natl. Acad. Sci. U.S.A., 115, 10293
Koll, D. D. B., & Cronin, T. W. 2019, ApJ, 881, 120
Komabayasi, M. 1967, J. Meteorol. Soc. Jpn. Ser. II, 45, 137
Kopparapu, R. k., Ramirez, R., Kasting, J. F., et al. 2013, ApJ, 765, 131
Kopparapu, R. k., Ramirez, R. M., SchottelKotte, J., et al. 2014, ApJ, 787, L29
Leconte, J. 2021, A&A, 645, A20
Leconte, J., Forget, F., Charnay, B., Wordsworth, R., & Pottier, A. 2013, Nature, 504, 268
Leconte, J., Selsis, F., Hersant, F., & Guillot, T. 2017, A&A, 598, A98
Marcq, E., Salvador, A., Massol, H., & Davaille, A. 2017, J. Geophys. Res. (Planets), 122, 1539
Meador, W. E., & Weaver, W. R. 1980, J. Atmos. Sci., 37, 630
Meadows, V. S., & Crisp, D. 1996, J. Geophys. Res., 101, 4595
Mlawer, E. J., Payne, V. H., Moncet, J.-L., et al. 2012, Philos. Trans. R. Soc. Lond. A, 370, 2520
Nakajima, S., Hayashi, Y.-Y., & Abe, Y. 1992, J. Atmos. Sci., 49, 2256
Paynter, D. J., & Ramaswamy, V. 2011, J. Geophys. Res. (Atmospheres), 116, D20302
Pierrehumbert, R. T. 2010, Principles of Planetary Climate (Cambridge; New York: Cambridge University Press), oCLC: ocn601113992
Popp, M., Schmidt, H., & Marotzke, J. 2016, Nat. Commun., 7, 10627
Ramirez, R. M. 2020, MNRAS, 494, 259
Ramirez, R. M., Kopparapu, R. K., Lindner, V., & Kasting, J. F. 2014, Astrobiology, 14, 714
Simpson, G. C. 1929, Q. J. R. Meteorol. Soc., 55, 73
Toon, O. B., McKay, C. P., Ackerman, T. P., & Santhanam, K. 1989, J. Geophys. Res., 94, 16287
Turbet, M., Ehrenreich, D., Lovis, C., Bolmont, E., & Fauchez, T. 2019, A&A, 628, A12
Turbet, M., Bolmont, E., Chaverot, G., et al. 2021, Nature, 598, 276
Wolf, E. T. 2017, ApJ, 839, L1
Yang, J., Cowan, N. B., & Abbot, D. S. 2013, ApJ, 771, L45
Yang, J., Leconte, J., Wolf, E. T., et al. 2016, ApJ, 826, 222
Yang, J., Leconte, J., Wolf, E. T., et al. 2019, ApJ, 875, 46
Zhang, Y., & Yang, J. 2020, ApJ, 901, L36

Appendix A: Sensitivity tests

A number of sensitivity tests were performed to constrain the relevant different physical processes we have to take into account to compute the OLR of the atmosphere we consider (Appendix A.1). We tested also the errors induced by the convergence of several numerical parameters - or by numerical assumptions (Appendix A.2). An overview of these tests is proposed in Table A.1.

Appendix A.1: Sensitivity studies on physical processes

The first set of sensitivity tests is focused on physical processes or hypotheses.

Appendix A.1.1: Shape of the absorption lines

The most accurate approximation to represent the absorption lines is to assume a Voigt profile, which is a convolution of a Gauss and a Lorentz profile. Unfortunately, there is no analytic solution to compute this profile, and the numerical computation is time expensive. As explained by Koll & Cronin (2018), assuming a Lorentz shape is sufficient (in our case study) to obtain an accurate value of the OLR (Error lower than 1 W.m^{-2}). To create the correlated-k table used in this work, we computed high-resolution spectra assuming a Voigt profile. Being a statistical description of the absorption over a large range of temperature (pressure and mixing ratio values), this method requires extremely accurate initial spectra. As shown in Fig. A.1, the Lorentz profile tends to reduce the absorption at the centre of the line and increase it in the wings, but this difference is negligible for the OLR calculation. At higher pressure, that is higher broadening, the width of the lines is larger and the difference between the Lorentz and the Voigt profile decreases.

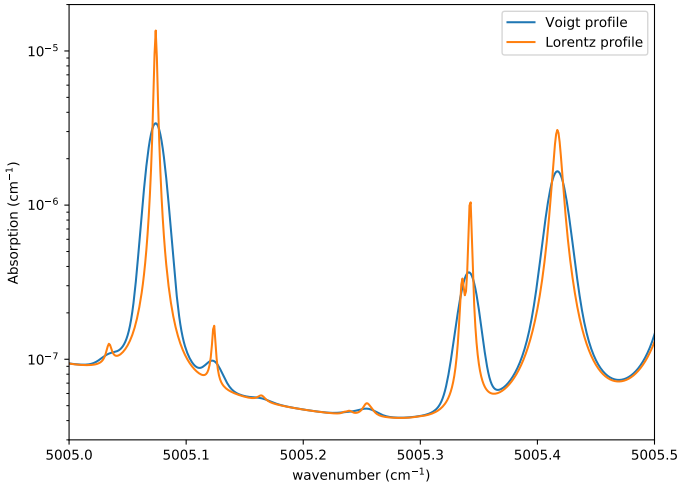


Fig. A.1: Absorption spectrum assuming a Voigt or a Lorentz profile at the same resolution (0.001 cm^{-1}) with P=1000 Pa and T=300 K. As the wings of the absorption lines do not follow a Voigt profile, we only considered the centre of the lines up to 25 cm^{-1}here.

Appendix A.1.2: Continua

In this work, for both radiative transfer methods, we used the MT_CKD formalism with a cut-off of the centre of the water absorption lines at 25 cm^{-1} and a removed plinth. A continuum is added to take into account the far-wing absorption. Yang et al. (2016) showed through a model inter-comparison that a source of difference of the OLR values comes from the radiative transfer, and more particularly from the continua used. It is interesting to note that a part of the difference between our results and those of Kopparapu et al. (2013) is due to the choice of the H_2O continuum database. They used BPS (Paynter & Ramaswamy 2011), while we used MT_CKD.

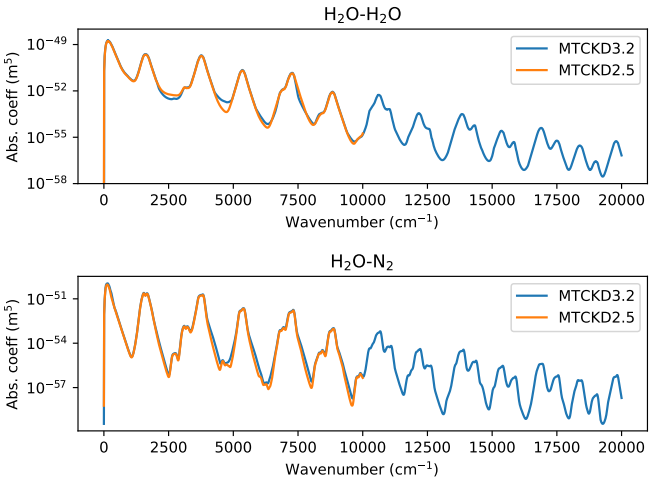


Fig. A.2: Comparison of H_2O-H_2O and H_2O-N_2 continua from MT_CKD2.5 and 3.2 databases. Here, the y-axis is in logscale.

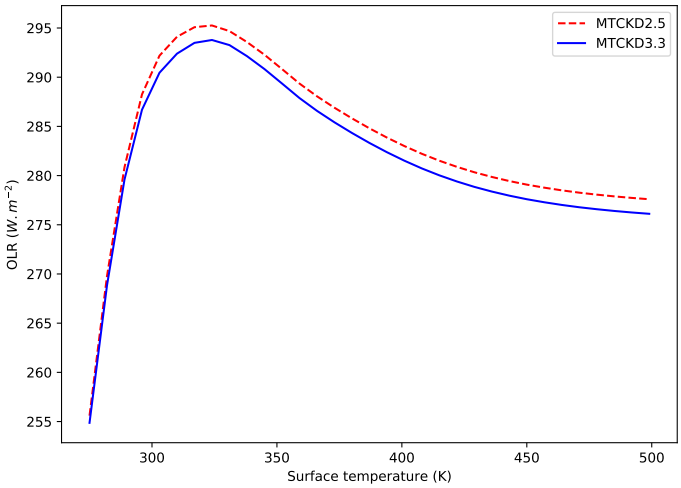


Fig. A.3: OLR values as a function of the surface temperature for P_{N_2}=1 bar for different versions of the MT_CKD database.

A spectral comparison of the water continua used in this work is provided in Fig. A.2. The main difference between MT_CKD2.5 and MT_CKD3.2 comes from the wavelength definition domain. The MT_CKD2.5 continuum is defined between 0 cm^{-1} and 10000 cm^{-1} , while the MT_CKD3.2 continuum is defined up to 20000 cm^{-1} , as shown in Fig. A.2. Nevertheless, as the vast majority of the absorption of the water is between 0 cm^{-1} and 5000 cm^{-1} , the difference in the OLR value is at most 1.5 W.m^2 (Fig. A.3). We used the MT_CKD3.2 continua in PyRADS-Conv1D to increase our accuracy but also for computational reasons. If the continnum is not defined for a spectral range, it becomes necessary to compute the absorption lines up

Table A.1: Overview of sensitivity tests performed with the impact on the computed OLR value. The *Original param.* column indicates the parametrisation used in the considered model, and the *Tested param.* column shows the tested parametrisation. The OLR difference between original and modified parametrisations is indicated in the *OLR difference* column.

Model tested	Original param.	Tested param.	OLR difference
PyRADS-Conv1D	Lorentz shape	Voigt shape	< 1 W.m^2
PyRADS-Conv1D & `Exo_k`	with foreign broad.	without foreign broad.	up to 20 W.m^2
PyRADS-Conv1D	MT_CKD3.2 [0.1 - 10k]cm^{-1}	MT_CKD3.2 [0.1 - 20k]cm^{-1}	< 2 W.m^2
`Exo_k`	MT_CKD3.2	MT_CKD2.5	< 2W.m^2
`Exo_k`	with H_2O-N_2 cont.	without H_2O-N_2 cont.	up to 12 W.m^2 (at low T)
`Exo_k`	with N_2-N_2 cont.	without N_2-N_2 cont.	up to 4 W.m^2 (at low T)
PyRADS-Conv1D	without water iso.	with water iso.	< 2 W.m^2
kcm1d & `Exo_k`	without CO_2	376ppm of CO_2	up to 40 W.m^2
`Exo_k`	two-stream: $\bar{\mu}$=0.6	two-stream: Hemis. mean	~ 6 W.m^2
PyRADS-Conv1D	Conv_K88	Conv_D16	< 5 W.m^2
PyRADS-Conv1D	high res. vertical grid	low res. vertical grid	up to 10 W.m^2
PyRADS-Conv1D	spec. res. 10^{-2} cm^{-1}	spec. res. 10^{-3} cm^{-1}	< 1 W.m^2
`Exo_k`	`Exo_k` interp. scheme	kcm1d interp. scheme	~ 3 W.m^2

to a few hundreds of cm^{-1} to accurately represent the spectrum. This increases the computation time drastically. The N_2-N_2 continuum from the HITRAN CIA database even has a negligible impact on the OLR (less than 1 W/m^2) at a low temperature for P_{N_2}=10 bar when the nitrogen pressure is largely dominating the vapour pressure.

Appendix A.1.3: Water isotopes

There is no real consensus to include (or not include) the absorption lines of the secondary water isotopes in the radiative transfer computation. Similarly, there is no consensus as to what their abundances may be in other worlds. To have an idea of the potential impact of water isotopes on the OLR computation for an Earth-like planet, we considered different case studies with different isotopes abundances: Iso1 (terrestrial abundances, De Biévre et al. 1984; Gordon et al. 2017), Iso2 (all the secondary isotopes are two times more abundant), Iso10 (all the secondary isotopes are ten times more abundant), Iso100 (all the secondary isotopes are 100 times more abundant), Iso2HD (the $HD^{16}O$, $HD^{17}O$ and $HD^{18}O$ isotopes are two times more abundant), Iso10HD (the $HD^{16}O$, $HD^{17}O$ and $HD^{18}O$ isotopes are ten times more abundant), Iso100HD (the $HD^{16}O$, $HD^{17}O$ and $HD^{18}O$ isotopes are 100 times more abundant).

For each case study, we adjusted the abundance of the main isotope to keep a total abundance equal to unity (see Table A.2). Figure A.4 shows that secondary isotopes slightly reduce the height of the overshoot even at a terrestrial abundance (Iso1), but this difference is lower than 2 W.m^2. At higher abundances (Iso2, Iso10, Iso100), the strong absorption of the secondary isotopes reduces the OLR value over the entire studied temperature range. The tendency is the same when only increasing abundances of the HD^XO isotopes (Iso2HD, Iso10HD, Iso100HD) Nevertheless, Fig. A.4 shows that increasing the abundance of all the secondary isotopes more efficiently reduces OLR than only increasing HD^XO abundances (Iso100 and Iso100HD).

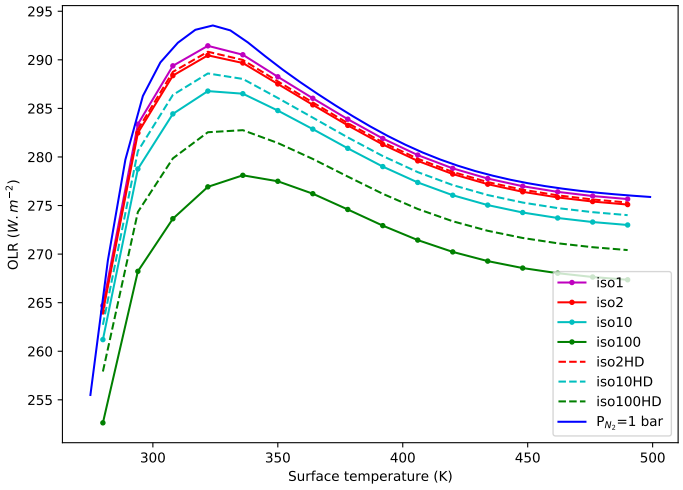


Fig. A.4: OLR values as a function of the surface temperature for P_{N_2}=1 bar for different water isotopes quantities and using PyRADS-Conv1D at high spectral resolution (0.001 cm^{-1}).

Appendix A.1.4: CO_2

The typical atmospheric compositions of moderately irradiated rocky exoplanets is currently unknown. A common solution to fill this gap is to consider an Earth-like atmosphere. Therefore, several studies added a few parts-per-million of CO_2 in the atmospheric composition, such as Kopparapu et al. (2014), who added 350 ppm (Ravi K. Kopparapu, priv. comm.). Such an amount of CO_2 can strongly change the OLR values but also the shape of the OLR curve (Fig. A.5). The difference induced by CO_2 is higher at low temperatures, where water is not the dominant gas. In other words, for such low temperatures the absorption due to CO_2 is non-negligible. At high temperatures, the absorption due to water is high enough to overlap the CO_2 absorption. For this reason, if there is CO_2 in the simulated atmosphere, it is important to consider it in the analysis to avoid incorrect conclusions.

In this work, as we explored the effects of nitrogen, we considered an H_2O + N_2 atmosphere without CO_2. A few papers (e.g. Ramirez et al. 2014; Popp et al. 2016) discuss the effect of CO_2 on the onset of the runaway greenhouse in more detail. In Fig. A.5, as the CO_2 quantity is a percentage of the N_2 pressure (we used 376 ppm of CO_2, as Leconte et al. 2013), the amount of CO_2 increases when increasing the N_2 pressure. This is the reason why the difference between simulations with and without CO_2 is stronger at high N_2 pressure. The strong greenhouse power of the CO_2 also strongly reduces the height of the overshoot. Finally, CO_2 absorption explains a large part of the gap between the results of Kopparapu et al. (2014) and those of other.

Table A.2: Overview of the isotope abundances per isotope (Isotopes) for the different case studies. The Iso1 case study corresponds to terrestrial abundances (Terr. abun.) while, for the Iso2, Iso10, and Iso100 cases, secondary isotope abundances are multiplied by 2, 10, and 100. For the Iso2HD, Iso10HD, and Iso100HD cases we increase only the abundance of HD^XO isotopes by multiplying them by a factor of 2, 10, or 100.

Isotopes	Terr. abun.	Iso2	Iso10	Iso100	Iso2HD	Iso10HD	Iso100HD
$H_2{}^{16}O$	0.997	0.994	0.973	0.731	0.997	0.995	0.967
$H_2{}^{18}O$	0.002	0.004	0.020	0.200	1.99e-3	1.99e-3	1.94e-3
$H_2{}^{17}O$	3.72e-4	7.44e-4	3.72e-3	3.72e-2	3.72e-4	3.72e-4	3.61e-4
$HD^{16}O$	3.11e-4	6.21e-4	3.11e-3	3.11e-2	6.21e-4	3.11e-3	3.11e-2
$HD^{18}O$	6.23e-7	1.25e-6	6.23e-6	6.23e-5	1.25e-6	6.23e-6	6.23e-5
$HD^{17}O$	1.16e-7	2.32e-7	1.16e-6	1.16e-5	2.32e-7	1.16e-6	1.16e-5
$D_2{}^{16}O$	2.42e-8	4.84e-8	2.42e-7	2.42e-6	2.42e-8	2.41e-8	2.35e-8

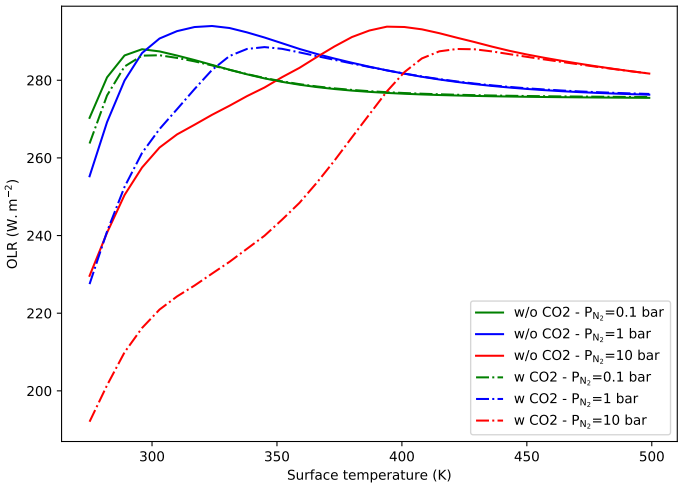


Fig. A.5: OLR values as a function of the surface temperature with and without CO_2 computed with `Exo_k`. The full lines are the reference OLR curves proposed in Fig. 3 using `Exo_k`, and the dotted lines include 376 ppm of CO_2 in the radiative transfer computation.

Appendix A.1.5: Two-stream approximation

All the radiative transfer models used here employ a two-stream approximation in the infrared where the radiative transport in the atmosphere is described by an upward and a downward flux (Meador & Weaver 1980; in fact, as we are focused on the thermal emission in a non-scattering atmosphere, we are only really dealing with one stream).

Since the seminal work of Toon et al. (1989), it is known that, while this approach is numerically efficient, the assumptions made (e.g. the two-stream coefficients used) need to be adapted to the problem at hand to ensure accuracy. For example, as can be seen in Fig. A.6, the classical hemispheric mean approximation (where the intensity is considered constant over each hemisphere) systematically underestimates the outgoing emitted flux compared to a proper integration over the cosine of the zenith angle (μ). This is due to the fact that for a given specific intensity (considered independent of the azimuth angle), $I(\mu)$, the integral for the upward flux,

$$F^+ = 2\pi \int_0^1 \mu I(\mu) d\mu, \tag{A.1}$$

gives more weight to the rays close to the vertical. Because these rays probe deeper, they have a higher than average intensity (see Fig. A.6, where we show $\pi I(\mu)$ to use the same scale as the flux).

From this figure, we see that the total flux would be better approximated by $\pi I(\mu \sim 0.6)$; thus, one might be tempted to use the classical quadrature method and choose $\bar{\mu} \sim 0.6$ as the quadrature point. As pointed out by Toon et al. (1989), however, this approach leads to a well-known unphysical emissivity that is highly undesirable if one wants to conserve energy.

To avoid having to use an expensive angular integration while preserving an accurate and physical solution, the `Exo_k`-RT method (Table 1) uses the following approximation in the infrared, which is a variation on the hemispheric approximation. Following notations from Toon et al. (1989), the equation for the upward flux (and similarly for the downward flux, F^-) writes

$$\epsilon \frac{\partial F^+}{\partial \tau} = \gamma_1 F^+ - \gamma_2 F^- - 2\pi(1-\omega_0)B, \tag{A.2}$$

where $\gamma_1 = 2 - \omega_0(1+g)$ and $\gamma_2 = \omega_0(1-g)$, ω_0 and g are the single scattering albedo and asymmetry factor of the medium, and B is the Planck function. The difference with the classical hemispheric approximation is the factor ϵ that accounts for the fact that, when assuming the hemi-isotropy of the intensity, choosing an effective optical depth ($d\tau/\epsilon$) that is different from the vertical one does not introduce a greater level of approximation.

Interestingly, choosing an effective zenith angle whose cosine is $\bar{\mu}$ and defining $\epsilon \equiv 2\bar{\mu}$ [7], Eq. (A.2) rewrites

$$\frac{\partial F^+}{\partial \tau} = \left(\frac{2-\omega_0(1+g)}{2\bar{\mu}}\right) F^+ - \left(\frac{\omega_0(1-g)}{2\bar{\mu}}\right) F^- - \frac{\pi}{\bar{\mu}}(1-\omega_0)B. \tag{A.3}$$

By comparison with Table 1 of Toon et al. (1989), one can directly see that this assumption is completely equivalent to the quadrature approximation where an arbitrary quadrature point $\bar{\mu}$ is chosen instead of the Gauss-Legendre choice ($1/\sqrt{3}$), except for the change to the source term. This change is what makes our approximation retain the physical consistency of the hemispheric mean approach as $F^+ \to \pi B$ in an opaque, non-scattering medium, whatever $\bar{\mu}$ we choose.

Our modified hemispheric-mean approximation, which is the default method in `Exo_k`, thus combines the energy-conserving feature of the classical hemispheric-mean with the flexibility of choosing the best effective zenith angle for a given problem. In practice it is easy to adapt any numerical implementation of the classical two-stream approach to solve this system: i) use the γ coefficients from Eq. (A.3) and ii) change the $2\pi\mu_1$ coefficient in

[7] The factor of 2 comes from the fact that the hemispheric-mean approximation can be seen as looking at a ray with $\bar{\mu} = 1/2$, so that ϵ can be seen as a correction factor accounting for the departure from the hemispheric-mean effective zenith angle.

Eq. (27) of Toon et al. (1989) into π to enforce energy conservation.

In the context of a non-scattering atmosphere, it is easy to show that our modified hemispheric-mean approximation is equivalent to computing the intensity for a given $\bar{\mu}$ and assuming $F^+ = \pi I(\bar{\mu})$. As can be seen in Fig. A.6 and is discussed above, $\bar{\mu} = 0.6$ yields a less than 1 W.m^{-2} difference over the whole range of atmospheres modelled here. However, we highlight that care should be given to the radiative transfer method used when comparing model results as different methods can lead to differences of ~ 6 W/m^2. These differences are visible between kcm1d (which uses the classical hemispheric mean approximation) and PyRADS (which assumes $F^+ = \pi I(\bar{\mu})$ with $\bar{\mu} = 0.6$) in Fig. 1.

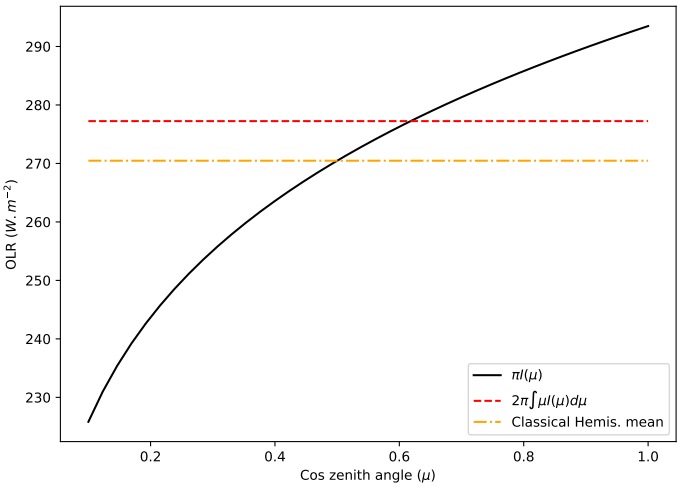


Fig. A.6: Variation of OLR with respect to the effective zenith angle used to compute the upward intensity (solid curve). The dashed curve shows the OLR computed by properly integrating the intensity over all zenith angles. The horizontal dash-dot curve shows the result of the classical hemispheric mean approximation (Toon et al. 1989), which systematically underestimates the flux by ~6 W.m^{-2}. The atmosphere model used has T_{surf}=500 K and P_{N_2}=1 bar.

Appendix A.1.6: Convection scheme

The two convection schemes used in this work and presented in Sect. 2.1 are based on the two main adiabatic lapse rates available in the literature. In Appendix B, we show that the difference between them comes from the definition of the entropy of the condensable gas. As explained in Sect. 2.1, we used the Conv_K88 scheme as reference because it is based on look-up tables, which is more accurate than the perfect gas laws used in the Conv_D16 scheme. It is interesting to quantify the uncertainty bewteen OLR curves computed using one scheme or the other. We modified PyRADS-Conv1D to use the Conv_K88 of the Conv_D16 scheme and we obtained the curves presented in Fig. A.7. We show that the difference is smaller than 5 W.m^2. We also notice that the Conv_D16 scheme systematically underestimates the OLR, probably mainly by overestimating the water content.

Appendix A.2: Sensitivity studies on numerical setup

The second set of sensitivity tests is focused on numerical parametrisations.

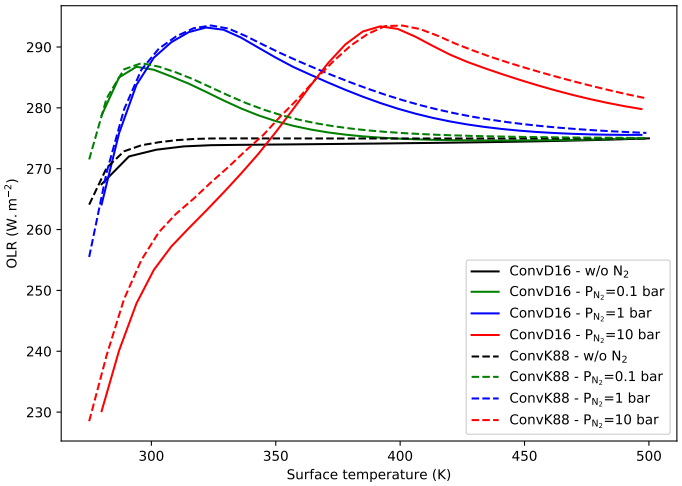


Fig. A.7: OLR values as a function of the surface temperature for different nitrogen pressures assuming the Conv_K88 or the Conv_D16 scheme using PyRADS-Conv1D.

Appendix A.2.1: Vertical grid resolution

Aside from using two different adiabats, the convective schemes used in this work assume two different definitions of the vertical grid. The Conv_D16 scheme provides a logarithmic distribution of the levels with a fixed difference between the surface pressure and pressure at the top of the atmosphere, while the Conv_K88 scheme adapts the height of the levels relatively to the amount of water from the surface up to 0.1 Pa (Fig. A.8). In other words, in the Conv_K88 scheme the wet atmospheric levels near the surface are thinner than the drier ones at the top of the atmosphere. The aim is to increase the vertical resolution of the 'radiatively active' part of the atmosphere. The number of vertical levels required to compute an accurate value of the OLR does not depend on the nitrogen pressure or on the surface pressure, but this number is higher than for the Conv_D16 scheme. Consequently, using the Conv_K88 scheme is more accurate even if the computation time is more expensive. For this reason, we used it in PyRADS-Conv1D. A convergence curve of the OLR relative to the number of vertical levels highlights that 200 levels are needed for the Conv_K88 scheme to keep an error smaller than 1W/m^2 compared to the converged OLR value. We assumed a stratospheric temperature equal to 200 K according to Kasting (1988). That work showed that a value lower than 250 K does not influence the OLR because for such low stratospheric temperatures the vapour pressure is radiatively negligible in the upper layers of the atmosphere (by assuming a pseudo-adiabatic approximation).

In the Conv_D16 scheme, the vertical grid does not depend only on the number of levels but also on the difference in pressure between the top and the bottom of the atmosphere. This induces a dependency on the number of levels on the surface temperature as shown in Table A.3. Indeed, because of the pseudo-adiabatic approximation the total surface pressure increases strongly between 280 K and 500 K (≈1 bar to ≈26 bar if P_{N_2}=1 bar), and the difference between pressures at the top and at the bottom of the atmosphere may be high to accurately represent the whole atmosphere. Moreover, increasing the nitrogen pressure reduces the height of the radiatively active part of the atmosphere by drying it up; thus, the required number of levels increases. We also observed that using a stratospheric temperature equal to 150 K (and not 200 K as in the Conv_K88 scheme)

allows us to slightly reduce the required number of levels. Finally, according to Table A.3, in the Conv_D16 scheme we assume 100 vertical levels and a difference between the pressure at the bottom and at the top of the atmosphere equal to 10^6 Pa. This setup provides a good compromise between accuracy and computation time with an error at most equal to 1 W/m^2 compared to the converged value.

Table A.3: Overview of the number of atmospheric levels needed in the Conv_D16 scheme relatively to the nitrogen pressure, the surface temperature (Tsurf), the stratospheric temperature (Tstrat), and the difference between the pressure at the bottom and at the top of the atmosphere (Pres. diff.).

Nitrogen pressure	Tsurf	Tstrat	Pres. diff.	Nb. of levels
0.1 bar	300 K	150 K	10^4 Pa	30
1 bar	300 K	150 K	10^5 Pa	100
10 bar	300 K	150 K	10^6 Pa	200
0.1 bar	500 K	150 K	10^7 Pa	60
1 bar	500 K	150 K	10^7 Pa	60
10 bar	500 K	150 K	10^7 Pa	60

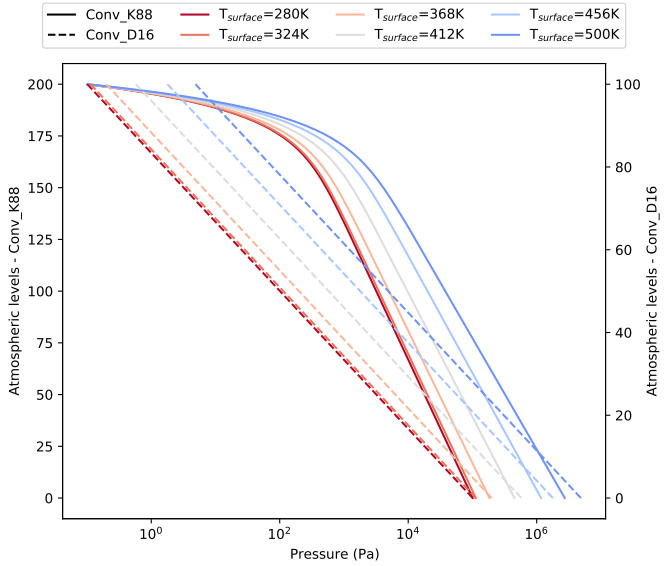


Fig. A.8: Comparison of pressure distribution over the vertical grid of the model for the Conv_K88 and the Conv_D16 methods. Here, P_{N_2}=1 bar.

Appendix A.2.2: Spectral resolution

For the line-by-line method, as we assume a Lorentz profile for the absorption lines, the spectral resolution needs to be high enough to accurately reproduce the real spectrum. The line-by-line method needs a minimal spectral resolution of 0.01 cm^{-1} to give an accurate value of the OLR (Fig. A.9) as shown by Koll & Cronin (2018). The absorption lines are not exactly resolved, as is visible in Fig. A.10, but the cumulative error on the entire spectrum is negligible. Producing a correlated-k table requires high-resolution spectra; therefore, we used a spectral resolution of 0.001 cm^{-1} , which is able to resolve each absorption line.
Fig. A.10 shows that by increasing the pressure and the temperature, the width of the line becomes larger; thus, a lower resolution is sufficient. Nevertheless, in the highest atmospheric levels the pressure is low, and a high spectral resolution is always required.

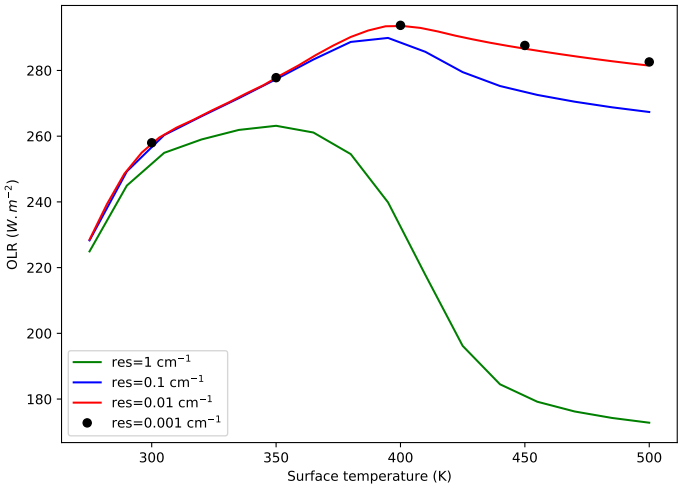


Fig. A.9: OLR values as a function of the surface temperature for different spectral resolution with P_{N_2}=10 bar and using PyRADS-Conv1D.

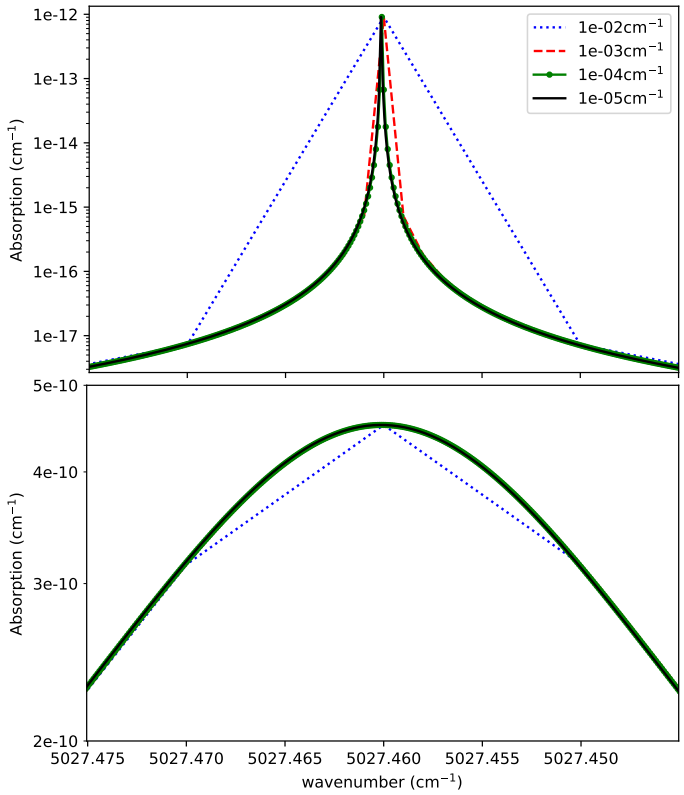


Fig. A.10: Absorption line at 5027.460050 cm^{-1} for different spectral resolutions and using a Lorentz profile. The top panel is the absorption for P=6 Pa and T=220 K, and the bottom panel is the absorption for P=3500 Pa and T=300 K.

Appendix A.2.3: Correlated-k-mixing ratio grid

Because of the non-usual transition between an N_2 - dominated and an H_2O atmosphere, we tested the resolu-

tion of the volume-mixing ratio (vmr) grid of the correlated-k table. The original resolution of the vmr grid ($Q = \{1e^{-6}, 1e^{-5}, 1e^{-4}, 1e^{-3}, 1e^{-2}, 1e^{-1}, 1\}$) was increased to $Q = \{1e^{-6}, 1e^{-5}, 1e^{-4}, 1e^{-3}, 1e^{-2}, 5e^{-2}, 1e^{-1}, 5e^{-1}, 1\}$, but it does not significantly change the OLR values.

Appendix A.2.4: Correlated-k-interpolation scheme

Correlated-k tables contain absorption spectra for given pressure, temperature, and vmr grids. To be able to compute the absorption of each atmospheric level, the models need to interpolate these tables on different pressure, temperature, and vmr values. Because of the wide diversity of interpolation schemes, we do not describe them in detail. However, by using two different schemes (from two different models), we caveat that a part of the differences highlighted in Fig. 1 can come from the choice of the correlated-k-interpolation scheme.

The two correlated-k radiative transfer models we used in this work (`Exo_k` and kcm1d in Table 1) have different interpolation schemes and produce different OLR curves for the same correlated-k table. Nevertheless, this difference is smaller than 3 W.m^2. We were able to reproduce OLR curves from kcm1d with a modified version of `Exo_k` that uses the same interpolation scheme as kcm1d, with an error lower than 1 W.m^2. This proves that the only difference in Fig. A.11 comes from the interpolation scheme. As kcm1d is derived from the LMD-Generic model, it inherits an interpolation scheme optimised for such 3D models; thus, this difference of 3 W.m^2 is a second-order error regarding other uncertainties of GCMs.

Although the detail of the interpolation of `Exo_k` and kcm1d are different, the global scheme is the same. The absorption spectrum (K) is interpolated on the pressure (P), temperature (T), and vmr (x) as follows:

$$\ln \mathrm{K} = \mathrm{fct}(\ln \mathrm{P}, \mathrm{T}, \ln \mathrm{x}).$$

This global scheme provides the most accurate interpolated spectra, which makes sense regarding the logarithmic distribution of the pressure and vmr grids of the correlated-k tables.

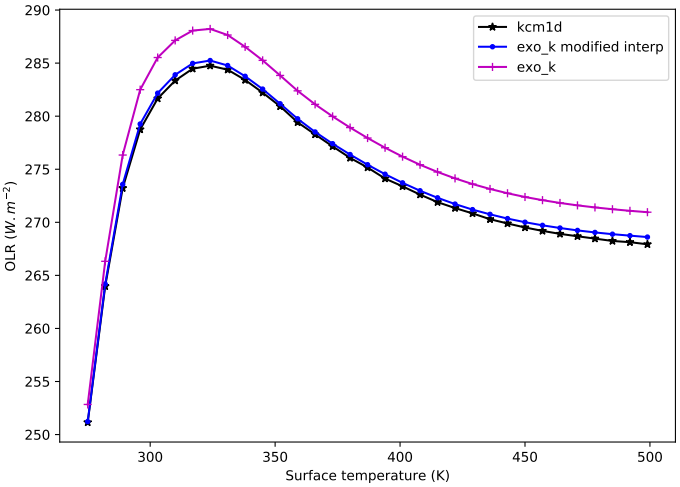


Fig. A.11: OLR as a function of the surface temperature for different interpolation schemes: kcm1d (black line) and `Exo_k` (magenta line). The blue line corresponds to `Exo_k` using the kcm1d interpolation scheme. Here, P_{N_2}=1 bar.

Appendix B: Adiabatic lapse rate formulations

One-dimensional radiative-convective climate models usually use a pseudo-adiabatic lapse rate (also referred to as adiabat) to compute the temperature profile of the atmosphere. There are two widely used formulations of this adiabat in the literature for a moist atmosphere. The first one is proposed by Kasting (1988) based on Ingersoll (1969):

$$\frac{d\ln P}{d\ln T} = \frac{P_c}{P}\frac{d\ln P_c}{d\ln T} + \frac{P_n}{P}\left(1 + \frac{d\ln \rho_c}{d\ln T} - \frac{d\ln \alpha_c}{d\ln T}\right), \tag{B.1}$$

with

$$\frac{d\ln \alpha_c}{d\ln T} = \frac{\frac{R^*}{M_n}\left(\frac{d(ln\rho_c)}{d\ln T}\right) - c_{vn} - \alpha_c \frac{ds_c}{d\ln T} - \alpha_l \frac{ds_l}{d\ln T}}{\alpha_c(s_c - s_l) + \frac{R^*}{M_n}}. \tag{B.2}$$

The second one is proposed by Ding & Pierrehumbert (2016) based on the dry adiabat of Pierrehumbert (2010):

$$\frac{d\ln P}{d\ln T} = \frac{P_c}{P}\frac{L}{R_c T} + \frac{P_n}{P}\frac{c_{pn}}{R_n} \times \frac{1 + \left(\frac{c_{pc}}{c_{pn}} + \left(\frac{L}{R_c T} - 1\right)\frac{L}{c_{pn}T}\right)\alpha_c}{1 + \frac{L}{R_n T}\alpha_c}. \tag{B.3}$$

Both moist lapse rates presented above are valid for a non-dilute atmosphere (i.e. for an atmosphere where water is a trace gas). Leconte et al. (2013, 2017) proposed a third formulation equivalent - but not strictly equal - to Ding & Pierrehumbert (2016) (see Eq. (B.4)). Nevertheless, Leconte et al. (2017) highlighted an interesting molecular mass gradient effect.

Through a few mathematical reformulations of the adiabat proposed by Leconte et al. (2013), we obtain the following equation, which is strictly equal to Eq. (B.3) under the pseudo-adiabatic approximation (i.e. $\alpha_l = 0$):

$$\frac{d\ln P}{d\ln T} = \frac{P_c}{P}\frac{L(T)}{R_c T} + \frac{P_n}{P}\frac{c_{pn}}{R_n} \times \frac{1 + \left(\frac{c_{pc}}{c_{pn}} + \left(\frac{L}{R_c T} - 1\right)\frac{L}{c_{pn}T}\right)\alpha_c + \frac{c_{pl}}{c_{pn}}\alpha_l}{1 + \frac{L}{R_n T}\alpha_c}. \tag{B.4}$$

Indices of variables in the Eqs. (B.3), (B.1), (B.2), and (B.4) indicate what gas is considered: c for the condensable gas, n for the non-condensable gas, and l for the condensed gas. Here, P is the pressure, T the temperature, M the molecular weight, ρ the density, R^* the perfect gas constant, R the specific gas constant, $\alpha_i = m_i/m_n$ the mass-mixing ratio per unit of non-condensable gas (m_n) for the species i, L the latent heat, and c_p the heat capacity.

These equations are different but can be equalised through three simple equations. The main difference between Eqs. (B.3) and (B.1) comes from the initial definition of the entropy. Indeed, Eq. (B.3) defines the entropy of the condensable gas as a perfect gas entropy. Equation (B.1) does not state the entropy of the condensable gas. Therefore, it is possible to use values from experiments for the condensable entropy to reduce inaccurate results at high temperatures (i.e. near the critical point). In both cases, the total gas pressure is defined using the perfect gas law.

Appendix B.1: Development of the adiabatic lapse rate of Ding & Pierrehumbert (2016)

We start with the definition of the total heat budget per unit of mass δQ_m. Here, we consider a volume per unit of mass (dV/m):

$$\delta Q_m = c_v dT + P d\rho^{-1} = c_p dT - \rho^{-1} dP, \tag{B.5}$$

where $Pd\rho^{-1} \leftrightarrow P\frac{dV}{m}$ and $c_p = c_v + \frac{R^*}{M}$.
Using Eq. (B.5), we define the total heat budget δQ of a gas mixture (Pierrehumbert 2010):

$$\delta Q = (m_n + m_c)\delta Q_m = m_n c_{pn} dT - \frac{m_n}{\rho_n} dP_n + m_c c_{pc} dT - \frac{m_c}{\rho_c} dP_c + L dm_c,$$

where δQ is the total heat budget and δQ_m is the total heat budget per unit of mass. We consider a pseudo-adiabatic system, and thus all the condensation is immediately removed by precipitation. In other words, the pressure of the condensable gas is equal to the saturation pressure.

By dividing the previous equation by the mass of the non-condensable gas (m_n) we obtain the total heat budget per unit of non-condensable gas:

$$\delta Q_{m_n} = (1 + \alpha_c)\delta Q_m = \left(c_{pn} dT + R_n T \frac{dP_n}{P_n}\right) + \left(c_{pc}\alpha_c dT - \alpha_c R_c T \frac{dP_c}{P_c}\right) + L d\alpha_c, \quad \text{(B.6)}$$

where $\alpha_c = m_c/m_n$. By dividing the previous equation by the temperature then by rewriting it, we obtain

$$\frac{\delta Q_{m_n}}{T} = \left(c_{pn}\left(c_{pc} + \left(\frac{L}{R_c T} - 1\right)\frac{L}{T}\right)\alpha_c\right) d\ln T - \left(1 + \frac{L}{R_n T}\alpha_c\right) R_n \, d\ln P_n. \quad \text{(B.7)}$$

By definition of an adiabatic (or pseudo-adiabatic) transformation, $\delta Q = 0$. Therefore, it is possible to define the dry adiabatic lapse rate (Pierrehumbert 2010):

$$\frac{d\ln P_n}{d\ln T} = \frac{c_{pn}}{R_n} \times \frac{1 + \left(\frac{c_{pc}}{c_{pn}} + \left(\frac{L}{R_c T} - 1\right)\frac{L}{c_{pn} T}\right)\alpha_c}{1 + \frac{L}{R_n T}\alpha_c}. \quad \text{(B.8)}$$

By assuming that the total pressure is the sum of both condensable and non-condensable pressures, we obtain

$$\frac{d\ln P}{d\ln T} = \frac{P_c}{P}\frac{d\ln P_c}{d\ln T} + \frac{P_n}{P}\frac{d\ln P_n}{d\ln T}. \quad \text{(B.9)}$$

Then, by using Eqs. (B.8) and (B.9) and the equation of Clausius-Clapeyron (Eq. (B.10)),

$$\frac{d\ln P_c}{d\ln T} = \frac{L}{R_c T}. \quad \text{(B.10)}$$

We obtain the moist adiabatic lapse rate proposed by Ding & Pierrehumbert (2016) (Eq. (B.3)). We assume that c_p does not depend on temperature, but this assumption becomes false near the critical point.

Appendix B.2: Development of the adiabatic lapse rate of Kasting (1988)

The moist adiabatic lapse rate proposed by Kasting (1988) uses equations from Ingersoll (1969). First, Ingersoll (1969) assumed the entropy of an adiabatic system S, per unit of mass of non-condensable gas:

$$S = s_n + \alpha_c s_c + \alpha_l s_l, \quad \text{(B.11)}$$

where s_n, s_c, and s_l are the entropies of the non-condensable, the condensable, and the liquid part, and $\alpha_X = \frac{\rho_X}{\rho_n}$. Near the critical point, it may not be valid to treat each constituent separately. By rewriting Eq. (B.11), we obtain

$$\frac{dS}{dT} = \frac{\partial s_n}{\partial T} + \frac{\partial s_n}{\partial \rho_n}\frac{d\rho_n}{dT} + \alpha_c \frac{ds_c}{dT} + s_c \frac{d\alpha_c}{dT} + \alpha_l \frac{ds_l}{dT} + s_l \frac{d\alpha_l}{dT}. \quad \text{(B.12)}$$

The law of mass conservation during an adiabatic expansion provides the following equality:

$$\frac{d\alpha_l}{dT} = -\frac{d\alpha_c}{dT},$$

and, using $\rho_n = \frac{\rho_c}{\alpha_c}$,

$$\frac{d\rho_n}{dT} = \frac{1}{\alpha_c}\frac{d\rho_c}{dT} - \frac{\rho_c}{\alpha_c^2}\frac{d\alpha_c}{dT}.$$

Thanks to these equalities, we can rewrite Eq. (B.12):

$$\frac{dS}{dT} = \frac{\partial s_n}{\partial T} + \frac{1}{\alpha_c}\frac{\partial s_n}{\partial \rho_n}\left(\frac{d\rho_c}{dT} - \frac{\rho_c}{\alpha_c}\frac{d\alpha_c}{dT}\right) + \alpha_c \frac{ds_c}{dT} + \alpha_l \frac{ds_l}{dT} + (s_c - s_l)\frac{d\alpha_c}{dT}.$$

If the non condensable gas behaves as an ideal gas, we can assume $T\frac{\partial s_n}{\partial T} = \frac{c_{vn}}{M_n}$ and $\rho_n \frac{\partial s_n}{\partial \rho_n} = -\frac{R^*}{M_n}$; thus,

$$\frac{dS}{dT} = \frac{c_{vn}}{T M_n} - \frac{R^* d\rho_c}{M_n \rho_c dT} + \frac{R^*}{\alpha_c M_n}\frac{d\alpha_c}{dT} + \alpha_c \frac{ds_c}{dT} + \alpha_l \frac{ds_l}{dT} + (s_c - s_l)\frac{d\alpha_c}{dT}. \quad \text{(B.13)}$$

From Eq. (B.13) by assuming the adiabatic hypothesis ($dS = 0$), we obtain Eq. (B.14) (Ingersoll 1969) and Eq. (B.15) (Kasting 1988):

$$\frac{d\alpha_c}{dT} = \frac{\frac{R^*}{M_n}\frac{d\ln\rho_c}{dT} - \frac{c_{vn}}{T M_n} - \alpha_c \frac{ds_c}{dT} - \alpha_l \frac{ds_l}{dT}}{s_c - s_l + \frac{R^*}{\alpha_c M_n}}, \quad \text{(B.14)}$$

$$\frac{d\ln\alpha_c}{d\ln T} = \frac{\frac{R^*}{M_n}\left(\frac{d(\ln\rho_c)}{d\ln T}\right) - c_{vn} - \alpha_c \frac{ds_c}{d\ln T} - \alpha_l \frac{ds_l}{d\ln T}}{\alpha_c(s_c - s_l) + \frac{R^*}{M_n}}. \quad \text{(B.15)}$$

As in Kasting (1988), from now we assume a pseudo-adiabatic expansion; hence, $\alpha_l = 0$. By assuming that the total pressure is the sum of both condensable and non-condensable pressures, and using the perfect gas law, we obtain

$$P = \frac{R^*}{M_n}\rho_n T + \frac{R^*}{\beta M_c}\rho_c T, \quad \text{(B.16)}$$

where $\beta = \beta(\rho_c, T)$ is a parameter that expresses the degree to which the condensable gas departs from ideality. By rewriting Eq. (B.16) and using Eq. (B.15), we obtain the adiabatic lapse rate proposed by Kasting (1988):

$$\frac{d\ln P}{d\ln T} = \frac{P_c}{P}\frac{d\ln P_c}{d\ln T} + \frac{P_n}{P}\left(1 + \frac{d\ln\rho_c}{d\ln T} - \frac{d\ln\alpha_c}{d\ln T}\right). \quad \text{(B.17)}$$

Here, the entropy of the condensable part (s_c) is explicitly defined in the equation. In the Conv_K88 scheme, which uses Kasting (1988) equations, we compute the water entropy thanks to experimental look-up tables (Haar et al. 1984).

Appendix B.3: Equalisation of the adiabatic lapse rates

The two formulations of the adiabatic lapse rate (Eqs. (B.3) and (B.1)) can be equalised assuming the following assumptions:

A. $(s_c - s_l) = \frac{L}{T}$

B. $\frac{ds_c}{d\ln T} = c_{pc} - \frac{L}{T}$

C. $\frac{d\ln \rho_c}{d\ln T} = \frac{L}{R_c T} - 1$

By definition, equality A is always verified and corresponds to the entropy of phase change. Equalities B and C are only verified if we use the equation of Clausius-Clapeyron (Eq. B.10) to link vapour pressure, temperature, and latent heat.

We show here that the main difference between adiabatic lapse rates from Kasting (1988) and Ding & Pierrehumbert (2016) comes from the definition of the entropy of the condensable gas. Indeed, Eq. (B.3) (Ding & Pierrehumbert 2016) implicitly uses the definition of the entropy of a perfect gas (Pierrehumbert 2010), which becomes incorrect at high temperatures (i.e. near the critical point). The second difference is the use of the Clausius-Clapeyron equation (Eq. (B.10)), which is an approximation of the more general Clausius equation. This Clausius-Clapeyron equation is only valid for a perfect gas far from the critical point. For these reasons, we choose to use the Conv_K88 method based on the moist adiabatic lapse rate from Kasting (1988) for PyRADS-Conv1D, used as a reference in this paper.

4.3 The onset of the runaway greenhouse for atmospheres with CO_2

The large consequences of spectroscopic processes described in Chaverot et al. (2022) motivated a similar study, considering a gas mixture with a greenhouse gas such as CO_2 instead of an inactive species. In this context, I proposed and supervised the 3-month Master internship of Hélène Bienenfeld for which the objective was to extend the work done in Chaverot et al. (2022) to H_2O+CO_2 atmospheres. The final aim was to compute OTR curves as a function of the surface temperature of the planet for different CO_2 pressures. To do so, an improvement of the climate model developed for Chaverot et al. (2022) by adding the line-by-line opacity calculation of H_2O+CO_2 gas mixtures (see Chapter 3) was required. First, this was the scientific motivation to develop SpeCT, the tool described in Chapter 3 which generates high resolution absorption spectra for climate modeling. The key point was to identify the χ factors required to accurately account for molecular interspecies collisions in CO_2 mixtures, and to implement them in SpeCT. In a second time, I included SpeCT in the 1-D radiative-convective model developed in Chaverot et al. (2022) to be able to study atmospheres made of large quantities of CO_2.

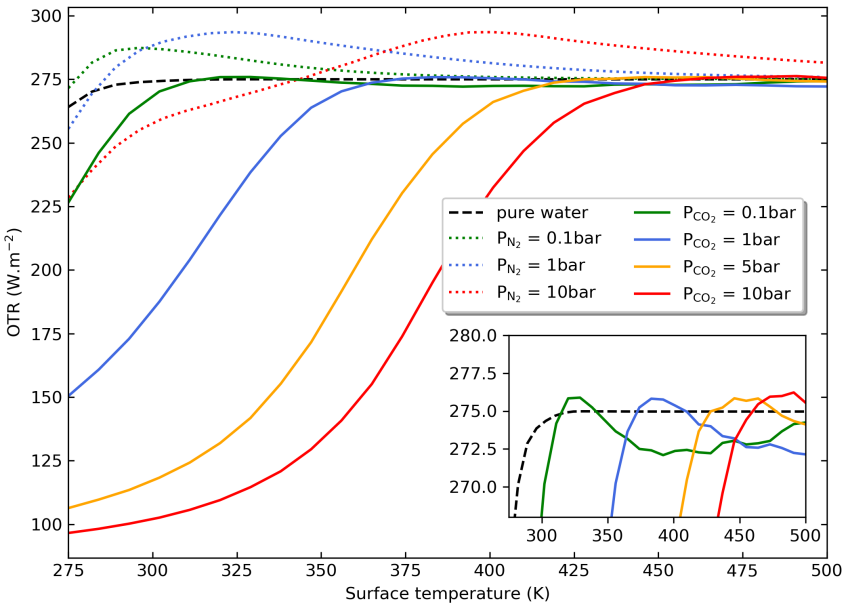


Figure 4.2: OTR as a function of the global surface temperature for H_2O+CO_2 mixtures. Colored solid curves are the OTR as a function of the surface temperature for different CO_2 pressures. Dotted lines are for a H_2O+N_2 mixture and the black dashed line is for a pure water vapor atmosphere, both from Chaverot et al. (2022).

The obtained results are presented in Fig. 4.2. The curves for a H_2O+N_2 mixtures (dotted lines) are from Chaverot et al. (2022) while curves for a H_2O+CO_2 mixtures (plain lines) are original results obtained in the context of the internship of Hélène. First of all, as CO_2 is a strong greenhouse gas, the OTR is drastically lower than by considering nitrogen. Second, there is no strong overshoot of the Simpson-Nakajima limit as obtained with nitrogen. This is due to the fact that CO_2 is an active species, absorbing by itself. To be more precise, there is a tiny overshoot of about 1 W.m^{-1} visible in the small panel of Fig. 4.2, but nothing comparable to the shape of the OTR curve assuming more than 0.1 bar of N_2 (OTR values $\approx$ 20 W.m^{-2} above the Simpson-Nakajima limit). However, the self-absorption of CO_2,

and especially the ν_3 band (see Sect. 3.1.1) is intense enough to contribute to the radiative balance even when the atmosphere is water dominated. This creates a small decrease of the OTR right after the onset of the runaway greenhouse (green curve in the small panel of Fig. 4.2).

The pseudo-adiabatic hypothesis[2] used in the model (see Sect. 4.1.1) links directly the temperature and the partial vapor pressure through the Clausius-Clapeyron equation. Therefore, by only knowing the surface temperature, it is possible to compute the water partial pressure. The absorption spectra of the atmosphere close to the surface for different temperatures (i.e., different water vapor partial pressures) are shown on Fig. 4.3. At 400 K, the vapor pressure is equal to 2.5 bar, and the absorption of the ν_3 band of CO_2 (at 2349 cm^{-1}) is of the same order of magnitude than the absorption induced by the water. At 500 K (26 bar of water) the contribution of CO_2 is diminished (orange curve) and at 600 K (120 bar of vapor) it becomes negligible compared to water absorption bands (red curve). For this reason, the "extra" absorption from CO_2 affects the OTR curve in a limited range of temperature. Beyond, the OTR is equal to the Simpson-Nakajima limit.

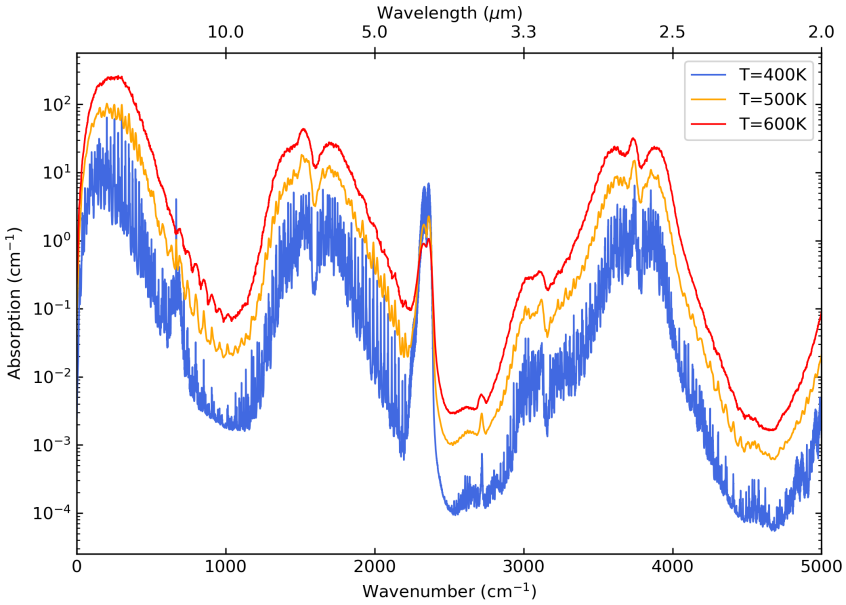


Figure 4.3: Absorption spectra for a H_2O+CO_2 mixture including 0.1 bar of CO_2 and various temperatures and vapor pressures. The three different spectra are computed at 400 K and with 2.5 bar of vapor (blue curve), 500 K and with 26 bar of vapor (orange curve) and 600 K and with 120 bar of vapor (red curve). The vapor pressure is equal to the saturation pressure of water (given by the Clausius-Clapeyron equation), thus directly function of the temperature.

This small feature on the OTR curve seems negligible, but it could be of great importance when discussing the notion of equilibrium states. By definition, a planet is at the equilibrium if the outgoing thermal flux is equal to the absorbed stellar radiation (ASR), that is OTR=ASR. If the ASR increases, the temperature of the planet increases as well to increase the OTR and keep the equilibrium[3]. Regarding the shape of the OTR curve presented in Fig. 4.2, for a given range of ASR values, there are multiple equilibrium surface temperature possible. For example, assuming 0.1 bar of CO_2 and ASR=274 $W.m^{-2}$,

[2] All the water in the condensed phase is removed instantaneously from the atmosphere by precipitating.
[3] The OTR depends on the temperature of the planet.

there are 3 equilibrium temperatures available: 310 K, 351 K and 490 K. For an atmosphere made of H_2O and N_2, there is only two equilibrium states because there is no increase of the OTR after the maximum reached at the onset of the runaway greenhouse. The stability of these different equilibrium states is discussed more in detail in the next section. However, in the context of habitability, the inner edge of the HZ is found by increasing step-by-step the insolation (thus the ASR) to reach the tipping point of the runaway greenhouse. By doing such experiment, the maximum ASR accepted by the planet is given by the maximum of OTR. Therefore, all the equilibrium states beyond the temperature of this maximum are not reachable. The ASR is function of the insolation which is function of the distance to the star. The higher the OTR, the closer the inner edge of the HZ is to the star. However, as the composition of the atmosphere is also of great importance, a proper computation of the ASR as a function of the surface temperature of the planet is required to calculate the inner edge of the HZ. This is the purpose of the next section.

4.4 Evolution of planetary albedo

In the continuity of the work presented in Sect. 4.3, I proposed and supervised a 7-month Master Internship done by Maëva Bréard. The idea was to extend the work done on the estimation of the OTR for different gas mixtures to calculate the absorbed flux as well. The aim was to compute the inner edge of the HZ for various atmospheric composition in order to revisit the key work of Kopparapu et al. (2013) with updated opacity data. In this context, I modified the 1-D radiative-convective model presented in Chaverot et al. (2022) to add a radiative transfer calculation in the visible. To do so, I adapted PyRADS-shortwave[4] which is based on pyDISORT[5] (Stamnes et al. 1988). This development step was necessary to have an accurate and efficient climate model able to compute both the OTR and the ASR. For the computation of the OTR in the IR, the intrinsic thermal emission of each atmospheric layer needs to be taken into account (see equations in Sect. 1.4.1). On the other side, there is no emission from the planet in the visible but the Rayleigh scattering (happening especially in the upper atmosphere) is a key process to compute accurately the ASR. It is numerical more expensive to compute the Rayleigh scattering than to integrate the fluxes in the IR using Eq. (4.4) from Pierrehumbert (2010). For this reason, optimized numerical routines are required, such as Disort (Stamnes et al. 1988, 2017).

Estimating the inner edge of the HZ considering various atmospheric compositions and various stellar types is easily doable knowing the OTR and the ASR of the planet. As by definition of the runaway greenhouse, the OTR value is limited (see Sect. 1.3 for more details), there is a distance below which the ASR is always larger than the OTR whatever the surface temperature of the planet. This delimits the inner edge of the HZ. Therefore, it is necessary to estimate accurately the OTR and the ASR for various atmospheric compositions and distances to the host star to be able to compute the inner limit of the HZ.

As shown in Chaverot et al. (2022), Kopparapu et al. (2013) used some approximations which

[4] https://github.com/danielkoll/PyRADS-shortwave
[5] https://github.com/chanGimeno/pyDISORT

induce an error in the estimation of the OTR. As the useful parameterization they provide to compute the HZ boundaries is largely used in planetary detection works (e.g., Hill et al. 2022), there is a real need to provide updated estimates based on the most recent models including up-to-date spectroscopic data. Moreover, regarding the wide variety of molecules we detect in exoplanetary atmosphere of hot-Jupiters (Guillot et al. 2022), we can expect a wide variety of atmospheres for low mass planets as well (Forget & Leconte 2014 ; Grenfell et al. 2020). Therefore, an exploration of the evolution of the position of the HZ for different gas mixtures seems important to prepare the future characterization of small rocky planets.

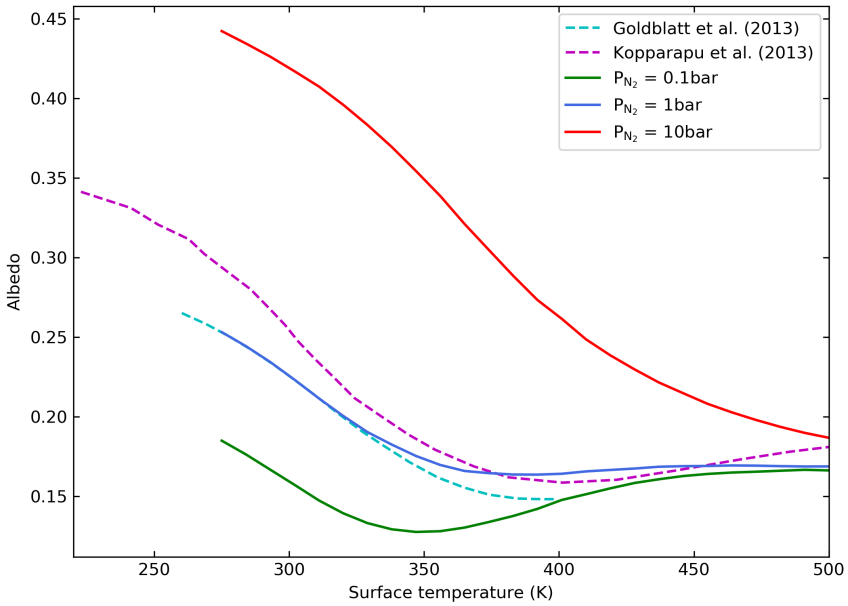


Figure 4.4: Evolution of the Bond albedo, for a H_2O+N_2 atmosphere, as a function of the surface temperature for 0.1 bar, 1 bar and 10 bar of N_2 (green, blue and red curves respectively). Cyan and magenta dashed curves are albedos from Goldblatt et al. (2013) and Kopparapu et al. (2013). They assume a surface albedo of 0.25 and 0.32 respectively, while we use 0.2. Goldblatt et al. (2013) consider an atmosphere including 1 bar of N_2 while Kopparapu et al. (2013) consider 1 bar of N_2 and 350 ppm of CO_2.

To estimate the ASR, I first performed simulations to compute the Bond albedo for different nitrogen pressures, assuming a H_2O+N_2 atmosphere, for a range of surface temperatures corresponding to the onset of the runaway greenhouse. The obtained results are presented in Fig. 4.4. Here, I assumed an Earth-twin orbiting the Sun at 1 AU, which corresponds to an insolation of 1376 $W.m^{-2}$. Also, I arbitrarily fix the surface albedo at 0.2 while Goldblatt et al. (2013) and Kopparapu et al. (2013) uses 0.25 and 0.32, respectively, to account for clouds. More precisely Goldblatt et al. (2013) increased arbitrary the surface albedo from 0.12 to 0.25 to parameterize the albedo effect of the clouds, and Kopparapu et al. (2013) assumed a value of 0.32 to model water dominated atmospheres. They both use HITEMP instead of HITRAN because the HITEMP database is known to include more absorption lines in the visible, thus it is more relevant for ASR and albedo computations. Indeed, as shown by Ramirez et al. (2014), there is a large difference on the estimate of the Bond albedo depending on the choice of the database beyond 400 K. Further, beyond 600 K, the albedo computed using HITRAN converges on ≈ 0.23, while the one computed using HITEMP converges on ≈ 0.17. Here I use HITRAN 2020 (Gordon et al. 2021) which accounts for more lines in the visible than HITRAN 2012 (Rothman et al. 2013) used in Ramirez et al.

(2014). This is probably why albedo curves in Fig. 4.4 seem closer to calculations done using HITEMP (dashed curves) than previous calculations done in Ramirez et al. (2014).

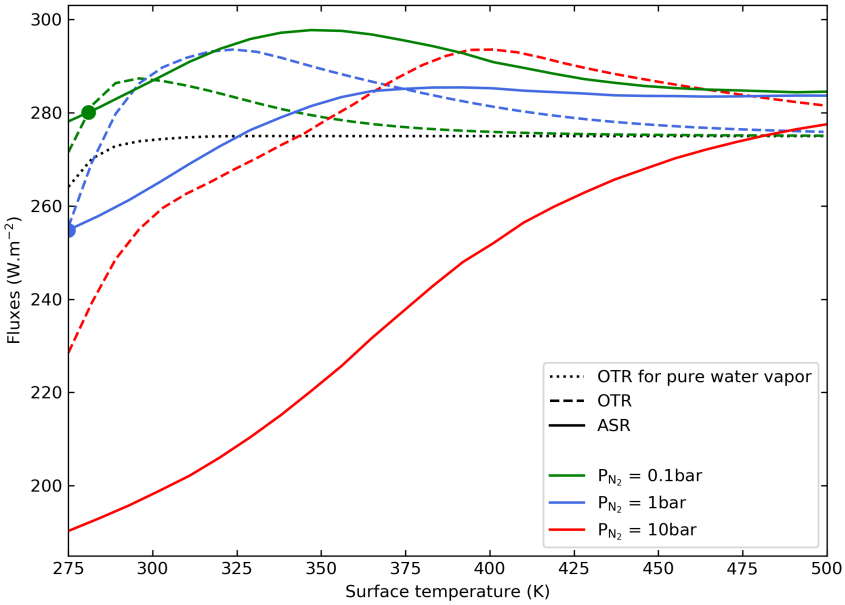


Figure 4.5: Evolution of the OTR (dashed curves) and the ASR (solid curves), for a H_2O+N_2 atmosphere, as a function of the surface temperature for 0.1 bar, 1 bar and 10 bar of N_2 (green, blue and red curves respectively). The dotted black line is the OTR for a pure water vapor atmosphere. Colored dots are temperate stable states, that is the temperature for which OTR = ASR before the onset of the runaway greenhouse.

Secondly, I computed the ASR for the same atmospheres by using the albedo curves. The results are presented in Fig. 4.5 together with OTR curves from Chaverot et al. (2022) in order to estimate the corresponding temperate equilibrium temperature (colored dots). As said in the previous section, there is an equilibrium state when OTR=ASR, which occurs twice on the presented curves (Fig. 4.5). For example, there is an equilibrium state at 275 K and at 375 K for the case with 1 bar of nitrogen. When considering the 375 K equilibrium state, if we decrease slightly the temperature, the radiative imbalance will be in favor of a cooling of the planet (OTR > ASR). Consequently, the global temperature of the planet will decrease to finally converge on the 275 K equilibrium state. Similarly, if we increase slightly the temperature of the 375 K equilibrium state, the radiative imbalance will be in favor of a warming (OTR < ASR), leading the planet in a runaway state. Therefore, we define the 375 K equilibrium state as an unstable state, while the 275 K equilibrium state is stable. We consider only the stable equilibrium states in the following discussion.

It has been shown that the Earth requires the greenhouse effect of CO_2 to maintain liquid water. Without this greenhouse contribution, it will fall in a waterbelt state, for which almost all the planet is covered by ice. In Fig. 4.5, we show that, assuming 1 bar of nitrogen and no CO_2, the stable equilibrium temperature is equal to 275 K. This is above the freezing point because in the 1-D model I use, we do not account for the modification of the surface albedo due to the large ice caps existing at low temperature. By parameterizing it, the surface albedo will increase, decreasing the temperature at the same time and leading to a runaway glaciation of the planet. Another value of the surface albedo, assuming a stronger

albedo of the clouds for example, could also decrease the equilibrium temperature. An interesting point is that for N_2 pressures lower than 1 bar (compare the cases with 0.1 bar and 1 bar, green and blue curves in Figs. 4.4 and 4.5) the albedo is lower due to a lower contribution of the Rayleigh scattering of nitrogen (Fig. 4.4), thus the ASR is larger (Fig. 4.5). Consequently, the equilibrium temperature is slightly higher (281 K for 0.1 bar instead of 275 K for 1 bar). At nitrogen pressure higher than 1 bar (compare the cases with 1 bar and 10 bar, blue and red curves in Figs. 4.5 and 4.5), the intense Rayleigh scattering increases the albedo (Fig. 4.4) thus the planet cools, inducing an equilibrium temperature below the freezing point of water (not visible in Fig. 4.5).

This work needs to be extended to other atmospheric compositions, including for example large quantities of CO_2, to have an overview of the evolution of the HZ for various planets. To do so, it is first necessary to compute the ASR for different distances between the planet and the star in order to estimate the inner edge of the HZ. This could be a great continuity of the key work of Kopparapu et al. (2013) and Kopparapu et al. (2014), studying respectively the influence of the stellar spectrum and of the planetary mass.

4.5 Limits for dense atmospheres

The work described in this chapter is done by using a 1-D radiative-convective model. As said in Sect. 1.4.1 the main assumption of this family of model is to assume that the temperature profile follows a purely adiabatic profile. This assumption is valid for light atmospheres but becomes inaccurate for very opaque atmospheres, for example water vapor dominated atmospheres. This could be a problem for studying the transition toward post-runaway states, and more advanced models should be used. This question of dense water dominated atmospheres was studied by Selsis et al. (2023) with a 1-D time-marching model. The purpose of such model is still to assume that the entire behavior of an atmosphere is well represented by a single vertical atmospheric column, but taking into account its evolution over time. The temperature profile is no more an initial condition, but evolves as a function of the radiative heating, and following a convective scheme. Consequently, the converged profile depends on the stellar-type as well as on the insolation. In the continuity of papers studying post-runaway states with 1-D models (e.g., Kopparapu et al. 2013, 2014 ; Boukrouche et al. 2021), Selsis et al. (2023) models the temperature profiles of water rich atmospheres up to 270 bar, that is the pressure of the evaporated water surface reservoir of the Earth. They show that the convective profile approximation is valid for water partial pressures up to $\approx$ 20 bar for a Sun like star assuming an OTR equal to 274 $W.m^{-2}$ (Simpson-Nakajima limit value in their framework). Therefore, the conclusions of Chaverot et al. (2022) are valid as we never consider more than 15 bar of water vapor. At higher pressures, the temperature profile tends to be isothermal and driven by the radiative heating only. The high opacity of the intermediate atmospheric levels prevents any heating from the incoming flux from the star. Consequently, by assuming a convective profile for dense water-rich atmospheres, we largely overestimate the temperature of the inner part of the atmosphere with direct consequences for the outer edge of the HZ (see Selsis et al. 2023 for more details). In case of compact planetary systems with strong gravitational interactions, the tidal forces can create

internal heating (see e.g., Turbet et al. 2018 ; Makarov et al. 2018 ; Barr et al. 2018 ; Bolmont et al. 2020 for the inner planets of the TRAPPIST-1 system) breaking the isothermal profile of the lower atmosphere. This breaks the isothermal equilibrium and induces a small convective layer close to the surface.

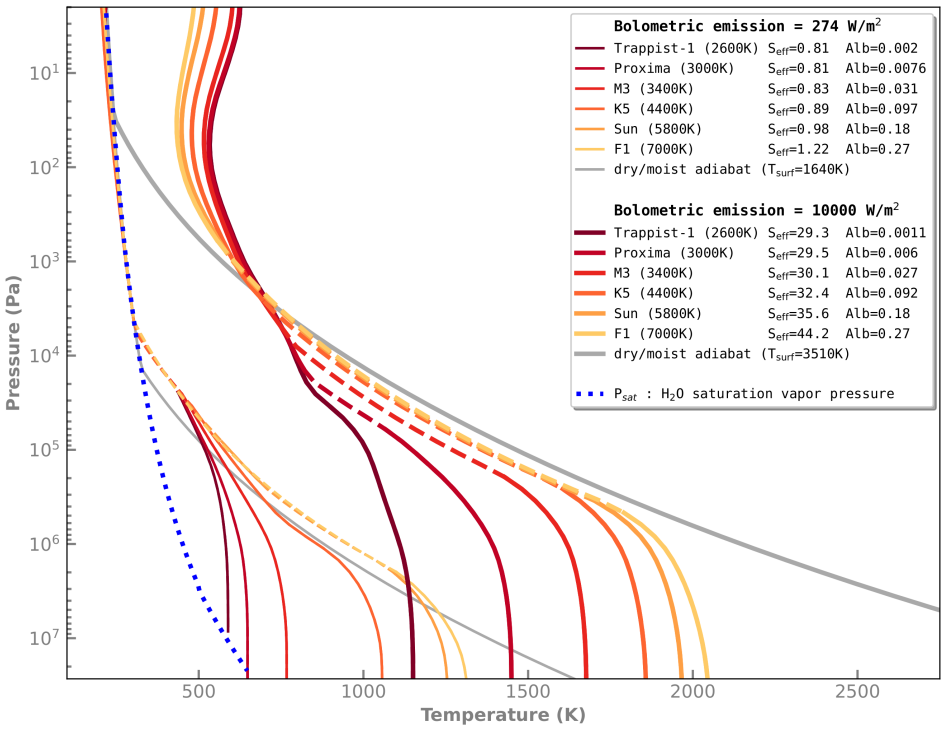


Figure 4.6: Thermal profiles of pure water atmospheres of planets orbiting different star (colored lines) and assuming two different OTR values (274 and 10,000 W.m^{-2}, thin and thick lines, respectively). Dashed lines indicate part of the atmosphere where convection can happen. This figure is from Selsis et al. (2023).

This work highlights the limits of 1-D radiative-convective models and challenges recent articles studying water-rich Neptune size planets assuming purely adiabatic profiles (e.g., Innes et al. 2023 ; Kempton et al. 2023 ; Pierrehumbert 2023). More precisely, Selsis et al. (2023) show that such models are not adapted to accurately estimate the inner temperature of Neptune size planets, if water-rich. The large overestimate of the temperature of the inner part of these planets done by 1-D radiative-convective models could induce an underestimation of their density. Knowing this could give a precious insight for planetary interior modeling (e.g., Dorn & Lichtenberg 2021) as well as to infer the actual density of the envelop of the planet (e.g., Otegi et al. 2020 ; Luque & Pallé 2022). This limit of 1-D radiative-convective models could also be an issue to study both post-runaway states and the transition between habitable and uninhabitable states. To overcome this issue, and to take into account all the 3D processes which are involved in the physics of the climate, more complex models such as 3D GCMs are required. This is the purpose of the next chapter.

Chapter 5

The entire transition of the runaway greenhouse

Contents

5.1 Motivation: from habitable to uninhabitable 80

5.2 First exploration of the entire runaway greenhouse transition with a GCM 81

5.3 Observability of temperate and post-runaway states 97

5.4 Long-term evolution of post-runaway states 100

5.5 Reversibility of the runaway greenhouse 101

5.1 Motivation: from habitable to uninhabitable

In the continuity of Chaverot et al. (2022), I studied the onset of the runaway greenhouse with the Generic-PCM (see Sect. 1.4.3) in order to quantify the contribution of intrinsically 3D processes such as clouds and the global dynamics. In the literature, several articles do this exercise and highlight different specific patterns and processes.

A first key point is that the global OTR computed with a GCM is larger than the one estimated by a 1D model. As explained in Leconte et al. (2013), the global dynamics and more precisely the Hadley cells of fast rotators (similar to the Earth's rotation) tend to reduce the relative humidity around the tropics. This creates a radiative cooling by reducing locally the water vapor pressure thus the infrared absorption, increasing the global OTR. As the cooling of the planet is more efficient, it can stay habitable for higher insolation and consequently the inner edge of the HZ is closer to the star than when estimated using a simple 1D model. Clouds are also of major importance. They strongly affect the radiative balance of the atmosphere, both by absorbing the thermal emission from the surface and by changing the Bond albedo of the planet. For slow rotating planets with a surface ocean, clouds preferentially form on the day-side, delaying the onset of the runaway greenhouse by acting as a shield against the incoming flux (Yang et al. 2013 ; Way et al. 2016). This shifts even more the inner limit of the HZ toward the star (Yang et al. 2014 ; Kopparapu et al. 2016). For faster rotators (i.e., Earth's rotation), the efficient heat redistribution affects the global radiative balance of the atmosphere, thus the onset of the runaway greenhouse and the position of the inner limit of the HZ (Kopparapu et al. 2017). Last but not least, some papers showed an intermediate stable moist runaway state (e.g., Wolf & Toon 2015 ; Popp et al. 2016 ; Kopparapu et al. 2017) while others do not (Leconte et al. 2013). Even different possible processes can be involved to explain the existence of these moist states are raised in the literature (see Chaverot et al. (2023), and references therein), there is no clear consensus so far on whether or not they are prevailing on the runaway greenhouse. More specifically, Kopparapu et al. (2017) and Yang et al. (2019) pointed out that the specific humidity of the stratosphere could be a key factor to understand this difference between the different models. The convection scheme is also mentioned as a possible source of difference (Popp et al. 2016).

Studying the runaway greenhouse with a GCM is numerically challenging. As discussed by Kopparapu et al. (2017) and Kane et al. (2018) the continuous evaporation induced by the positive feedback of the runaway greenhouse increases the radiative imbalance of the atmosphere. This may cause numerical instabilities in the models. Because of this, many studies defined the onset of the runaway greenhouse when simulations fail because of high water vapor pressures. Thanks to past developments (Leconte et al. 2013), the Generic-PCM is able to deal with high vapor content and water dominated atmospheres. This unique characteristic allowed us to go beyond the single onset of the runaway greenhouse to model the transition from temperate states to hot post-runaway states. The aim of the work presented in Sect. 5.2 was to link two major papers studying temperate states (Leconte et al. 2013) and post-runaway states (Turbet et al. 2021) with the Generic-PCM, in order to have the first complete overview of the 3D processes allowing the transition between these two distinct populations of planets.

In this chapter, I present and discuss simulation done with the Generic-PCM to study the entire transition of the runaway greenhouse (Sect. 5.2). In Sect. 5.3, I discuss the potential observability of these two different populations of planets separated by the runaway greenhouse. Eventually, I put this work in a larger context by discussing the long-term stability - or instability - of the post-runaway state (Sect. 5.4) as well as the reversibility of the runaway greenhouse (Sect. 5.5).

5.2 First exploration of the entire runaway greenhouse transition with a GCM

The following article is referenced in the manuscript as Chaverot et al. (2023).

Astronomy & Astrophysics manuscript no. output
October 20, 2023
©ESO 2023

First exploration of the runaway greenhouse transition with a 3D General Circulation Model

Guillaume Chaverot[1,2], Emeline Bolmont[1,2], Martin Turbet[3,4,1]

[1] Observatoire astronomique de l'Université de Genève, chemin Pegasi 51, CH-1290 Versoix, Switzerland
[2] Life in the Universe Center, Geneva, Switzerland
[3] Laboratoire de Météorologie Dynamique/IPSL, CNRS, Sorbonne Université, École Normale Supérieure, PSL Research University, École Polytechnique, 75005 Paris, France
[4] Laboratoire d'astrophysique de Bordeaux, Univ. Bordeaux, CNRS, B18N, allée Geoffroy Saint-Hilaire, 33615 Pessac, France

Accepted in A&A

ABSTRACT

While their detections remain challenging at present, observations of small terrestrial planets will become easier in a near future thanks to continuous improvements of detection and characterisation instruments. In this quest, climate modeling is a key step to understanding their characteristics, atmospheric composition, and possible histories.
If a surface water reservoir is present on such a terrestrial planet, an increase in insolation may lead to a dramatic positive feedback induced by water evaporation: the runaway greenhouse. The resulting rise in the global surface temperature leads to the evaporation of the entire water reservoir, separating two very different population of planets: 1) temperate planets with a surface water ocean and 2) hot planets with a puffed atmosphere dominated by water vapor. Therefore, the understanding of the runaway greenhouse is pivotal to assess the different evolution of Venus and the Earth, as well as every similar terrestrial exoplanet.
In this work we use a 3D General Circulation Model (GCM), the Generic-PCM, to study the runaway greenhouse transition, linking temperate and post-runaway states. Our simulations were comprised of two phases. First, assuming initially a liquid surface ocean, there is an evaporation phase, which enriches the atmosphere with water vapor. Second, when the ocean is considered to be entirely evaporated, there is a dry transition phase for which the surface temperature increases dramatically. Finally, the evolution ends with a hot and stable post-runaway state. By describing in detail the evolution of the climate over these two steps, we show a rapid transition of the cloud coverage and of the wind circulation from the troposphere to the stratosphere. By comparing our result to previous studies using 1D models, we discuss the effect of intrinsically 3D processes such as the global dynamics and the clouds, which are key to understanding the runaway greenhouse. We also explore the potential reversibility of the runaway greenhouse that is limited by its radiative unbalance.

Key words. planets and satellites: terrestrial planets – planets and satellites: atmospheres

1. Introduction

The continuous improvement of telescopes, instruments, and techniques allow us to detect and characterize a growing number of exoplanets. The new generation of instruments will enable the characterization of the atmospheres of small, rocky, and temperate planets, which are now within reach thanks to the James Webb Space Telescope (JWST, e.g. Morley et al. 2017; Lustig-Yaeger et al. 2019; Fauchez et al. 2019; Wunderlich et al. 2019). The first results of the JWST are likely to open up a new era in the characterization of such targets. Future astronomical ground-based instruments in development such as RISTRETTO@VLT (Lovis et al. 2022) and ANDES@E-ELT (Marconi et al. 2022) will allow the community to go even further and study Earth-like planets. The possibility of detecting objects similar to our planet brings up the ancestral question of life (and "habitability") in the Universe. Astrobiology is the field of science that aims to answer this question, while exoplanetology is now a big piece of that gigantic puzzle. In particular, an essential condition for the emergence and the maintenance of life as we know it is the presence of liquid water. Therefore, modeling the potential climate of planets we aim to characterize is essential to determining the conditions under which water can exist in liquid phase at their surface or in the atmosphere as clouds. This modeling effort, coupled with advanced spectroscopy techniques, will allow us to make progress in the search for life in the Universe.

For an Earth-like planet with a given amount of water, there is a range of distances to the host star for which this water can be liquid at the surface. Too close and the water evaporates and too far, then it freezes. This ideal zone is the Habitable Zone (HZ) (Kasting et al. 1993; Kopparapu et al. 2013). This concept is extremely useful in the exoplanet community to statistically study large samples of targets under the spectrum of habitability and search for life. The HZ is function of the brightness of the star, the size of the planet, and the composition of its atmosphere Kopparapu et al. (2013, 2014, 2017). If the planet is close enough to the star, the temperature rises and oceans start to evaporate which may add enough vapor in the bottom part of the atmosphere to completely absorb the thermal emission because of the strong greenhouse effect of water vapor. Once thermal emission reaches the Simpson-Nakajima limit (Simpson 1929; Nakajima et al. 1992), the planet is not able to cool down anymore and the positive feedback of the runaway greenhouse arises (Komabayasi 1967; Ingersoll 1969; Kasting 1988; Gold-

Send offprint requests to: G. Chaverot,
email: guillaume.chaverot@unige.ch

blatt & Watson 2012). This leads to the evaporation of the entire surface ocean and a dramatic increase in global surface temperature of several hundreds of Kelvin. This climatically unstable transition separates two population of planets: temperate planets and hot post-runaway planets (e.g., Hamano et al. 2013; Turbet et al. 2021). This is one of several scenarios that are meant to explain the difference between the Earth and early-Venus (Way et al. 2016). Temperate planets are similar to the Earth with surface condensed water and a thin atmosphere, while hot planets have an extended water-dominated atmosphere with high surface temperature, up to a few thousand Kelvins (Turbet et al. 2019). The inner edge of the HZ is determined in part by the runaway greenhouse process. The key question of the existence of surface liquid water on terrestrial planets is thus inherently connected to the runaway greenhouse with strong implications for our understanding of the possible evolution of exoplanets. As shown in Turbet et al. (2020), this process may also strongly influence the mass-radius relationships of terrestrial planets by clearly separating temperate planets hosting a water ocean and hot steam planets.

Regarding the importance of this process, many papers studied it using simple 1D climate models. However, as shown by some 3D General Circulation Models (GCMs) studies (e.g., Leconte et al. 2013; Kopparapu et al. 2017), approximations assumed in 1D models lead to a wrong estimation of the climate. For example, Hadley cells on Earth-like planets tend to reduce the relative humidity around the tropics, allowing for a greater Outgoing Longwave Radiation (OLR) than the one estimated by 1D models (Leconte et al. 2013). Moreover, specific clouds pattern may appear for slow rotating planets planets (Yang et al. 2013) or for post-runaway states (Turbet et al. 2021), which (by definition) cannot be accounted for in a 1D model.

Even if 1D models are useful in many cases because of their adaptability and fast computation time, more complex 3D models should be preferred to capture intrinsically 3D physical processes, such as clouds and global dynamics. Several studies explored the runaway greenhouse effect on Earth-like planets with different GCMs (e.g., Leconte et al. 2013; Yang et al. 2013; Wolf & Toon 2014, 2015; Popp et al. 2016; Kopparapu et al. 2017) in order to determine under which insolation this positive feedback arises. Unfortunately, highly unstable climates and high water vapor content may cause numerical instabilities or reveal model limitations. As explained by Kopparapu et al. (2016) and Kane et al. (2018), usually, existing studies assume a runaway greenhouse when the simulation fails due to high water content and large differences between the OLR and the Incident Stellar Radiation (ISR). Some other studies found moist stables states (e.g., Popp et al. 2016), for which the planet can be in a stable regime with a wet troposphere and a global temperature lower than 350 K. This prevents any dramatic huge increase in the global temperature that would lead to a post-runaway state, thereby challenging the definition of the inner edge of the HZ, as well as the implications for habitability.

The original aspects of our work are rooted in our efforts to push the study beyond the tipping point and to describe the evolution of the climate across the runaway greenhouse transition in order to link the temperate and post-runaway states. We also explore the reversibility of the runaway greenhouse and we discuss the possible existence of an intermediate moist greenhouse state. We describe inherently 3D processes in detail to have a complete and accurate overview of the evolution of the atmosphere, mainly through its enrichment in water vapor and the consequences of the modification of the cloud coverage. In Sect. 2, we describe the method followed to explore the runaway greenhouse transition, as well as the GCM we use and the considered numerical setups. We present our results in Sect. 3 and we discuss the limits and the prospects of this work in Sect. 4.

2. Modeling the climate

2.1. Modeling the runaway greenhouse

Our method is similar the one used by previous works that studied the onset of the runaway greenhouse with GCMs (Yang et al. 2013; Leconte et al. 2013; Wolf & Toon 2014, 2015; Popp et al. 2016; Kopparapu et al. 2017). First, we modeled a temperate planet similar to present-day Earth, then we increased (step by step) the insolation (ISR) to find the tipping point at which the well-known positive feedback arises. We kept the shape of the stellar spectrum unchanged when we modified the insolation. The novelty of this work is in our modeling of the climate beyond the onset of the runaway greenhouse, that is, for a higher temperature and water vapor mixing ratio. When the insolation is high enough to initiate a runaway greenhouse, we fixed it to let the ocean evaporate in order to study the evolution of the climate during this critical transition phase. The insolation and the global surface temperature for which this threshold arises depend on the configuration of the simulation (e.g., presence of continents, CO_2 content). Our aim is not here to find the exact value of the insolation corresponding to the tipping point, but to study the differences among the climate patterns. It could be interesting to find the exact tipping point, as done by Leconte et al. (2013) or Kopparapu et al. (2017), for example, for various atmospheric compositions; however, this is not the aim of this study. We performed simulations following this method for different atmospheric configurations: with and without Earth's continents, as well as with and without CO_2 and for different N_2 pressures (see Table 1). In this work, our reference simulation is a waterworld, including 1 bar of N_2, without CO_2 (W1), as a representative example of the evolution of the climate during the runaway transition. Other simulations (presented in Table 1) are discussed in the context of a sensitivity study.

The key process allowing a runaway greenhouse is the evaporation of the surface ocean. To model the ocean, we used a two-layer slab ocean without heat transport, coupled to the atmosphere (see Sect. 2.2). Evaporating the totality of the Earth's oceans will induce a vapor surface pressure of 273 bar. Regarding the large heat capacity of the water vapor, any temperature modification will be extremely slow in this situation, making such a simulation unachievable from a numerical point of view. Moreover, the timescale required to evaporate enough water to reach this pressure are also hugely long. To circumvent that difficulty, we choose to stop the evaporation process when a given quantity of water is evaporated (see the evaporation phase described in Sect. 3.1). For numerical reasons, we only tested two different evaporated water vapor pressures: 1 and 1.5 bar, which correspond to 10 and 15 m of a global layer equivalent (GEL), respectively; namely, the depth of the equivalent liquid ocean covering the entire planet. Then we removed the ocean from the simulation (i.e., we turned off the surface evaporation and consistently adjusted the surface albedo and the thermal inertia) and we set a new simulation by using the final state of the evaporation phase as the initial state (this is the dry transition phase described in Sect. 3.2). This method allowed us to study the impact of the size of the water reservoir on the obtained post-runaway state. In addition, based on the conclusions of Chaverot et al. (2022) on the radiative transfer for non-diluted water atmospheres, we used

Table 1: Parameters of the simulations

Planetary parameters	
Stellar spectrum	Sun
Orbital period	365 days
Rotation period	24 hours
Obliquity	23°
Planetary radius	6400 km
Gravity	9.81

Simulation	W01	W1	W10	WCO2	E1	ECO2
Topography	waterworld	waterworld	waterworld	waterworld	Earth's continents	Earth's continents
Surface albedo	0.07	0.07	0.07	0.07	Earth's albedo	Earth's albedo
H_2O	variable	variable	variable	variable	variable	variable
N_2	0.1 bar	1 bar	10 bar	1 bar	1 bar	1 bar
CO_2	-	-	-	376 ppm	-	376 ppm

opacity data and took into account the transition of broadening species from nitrogen-dominated to water-dominated.

2.2. Numerical setup

The Generic-PCM (G-PCM) (e.g., Wordsworth et al. 2011; Leconte et al. 2013; Turbet et al. 2016, 2018; Fauchez et al. 2019; Turbet et al. 2021), previously known as the LMD Generic GCM, has been adapted to model water-rich atmospheres (Leconte et al. 2013). This makes it particularly appropriate for studying the runaway greenhouse. The horizontal resolution is 64×48 (longitude × latitude) with 30 vertical levels from 0.1, 1, or 10 bar (depending on the simulation setup; see Table 1) to 10 Pa. We consider the Earth's obliquity and all the simulations are initialized assuming summer in the northern hemisphere. The dynamical time step is equal to 90 seconds. The physics (evaporation, convection, etc.) is computed every 15 minutes while the radiative transfer is computed every hour. The radiative transfer, assuming a Sun-like star, is done using a correlated-k table from Chaverot et al. (2022) for the mixture H_2O+N_2 and from Leconte et al. (2013) for the mixture including 376ppm of CO_2. The absorption line-list are taken from HITRAN 2012 (Rothman et al. 2013) and HITRAN 2016 (Gordon et al. 2017), respectively. We include also the N_2–N_2 collision-induced absorption (CIA) from the HITRAN CIA database (Karman et al. 2019). The H_2O-H_2O and H_2O-air continua are from version 3.3 of the MT_CKD database (Mlawer et al. 2012). In our simulation, water is a variable gas which may condense or evaporate from the surface ocean, but this is also the case in the atmosphere, and the relative humidity is computed consistently. The subgrid-scale dynamical processes (turbulent mixing and convection) as well as the moist convection scheme are described in Leconte et al. (2013). The number of cloud condensation nuclei (CCNs) per unit mass of moist air used is fixed: 4×10^6 kg^{-1} for liquid water clouds and 2×10^4 kg^{-1} for ice clouds, while their radius is variable (see Leconte et al. 2013 for more details).

The model includes also a two-layer slab ocean without heat transport (Codron 2012; Charnay et al. 2013). The thermal inertia is equal to 18,000 J.s$^{-1/2}$.m^{-2}.K^{-1} for oceans and 2,000 J.s$^{-1/2}$.m^{-2}.K^{-1} for continents. The albedo of the ocean is 0.07 and varies for continents up to 0.35, following Leconte et al. (2013) The heat capacity (c_p) and the mean molecular weight are consistently initialized for every setup, but they stay constant during the simulation, which means that we do not account for the modification induced by the addition of water vapor.

3. The runaway greenhouse transition

In this section, we present evolutions of the climate from temperate stable states to stable post-runaway states, following the method described in Sect. 2. First, we describe the onset of the runaway greenhouse (Sect. 3.1), called the "evaporation phase" here, in reference to the enrichment of the atmosphere in water vapor. Second, we describe the "dry transition phase" (Sect. 3.2) for which the ocean is considered entirely evaporated.

3.1. Onset of the runaway greenhouse

3.1.1. Evolution of the OLR during the onset

We performed simulations for the different configurations presented in Table 1 to quantify the influence of continents and strong infrared (IR) absorbers such as CO_2 on the onset of the runaway greenhouse.

Figure 1 provides an overview of the different simulations carried out in this work. The bottom panel is the OLR as a function of the mean surface temperature while the top panel indicates the different values of the insolation considered for every setup. in Fig. 1, we indicate the stable states with black dots; in other words, these are simulations for which an equilibrium is possible. The surface temperature of stable states is function of the insolation; therefore, we found different stables states by increasing (step by step) the insolation (colored dots on top panel of Fig. 1) as described in Sect. 2.1. When the insolation is high enough, a tipping point is reached and the atmosphere enters an unstable state (colored arrows on top panel of Fig. 1). Due to a large amount of water vapor, the bottom part of the atmosphere becomes optically thick to the thermal emission and the OLR is limited. Therefore, there is no longer any equivalence between the OLR and the Absorbed Stellar Radiation (ASR), as shown in Fig. 2, and the global temperature increases continuously due to this radiative imbalance (solid colored lines on the bottom panel of Fig. 1).

For every configuration presented in Fig. 1, the relation between the OLR and the mean surface temperature for stable states is roughly linear, which is consistent with previous studies (e.g., Leconte et al. 2013; Wolf & Toon 2015). For a given insolation, the presence of continents contributes to the reduction of the global surface temperature of few Kelvins because of their high albedo (higher than the deep ocean), as shown on the top panel of Fig. 1 (W1 versus E1 and WCO2 versus ECO2). For atmospheres with 1 bar of nitrogen (W1, E1, ECO2, and WCO2), the evolution of the OLR during the runaway transition (i.e.,

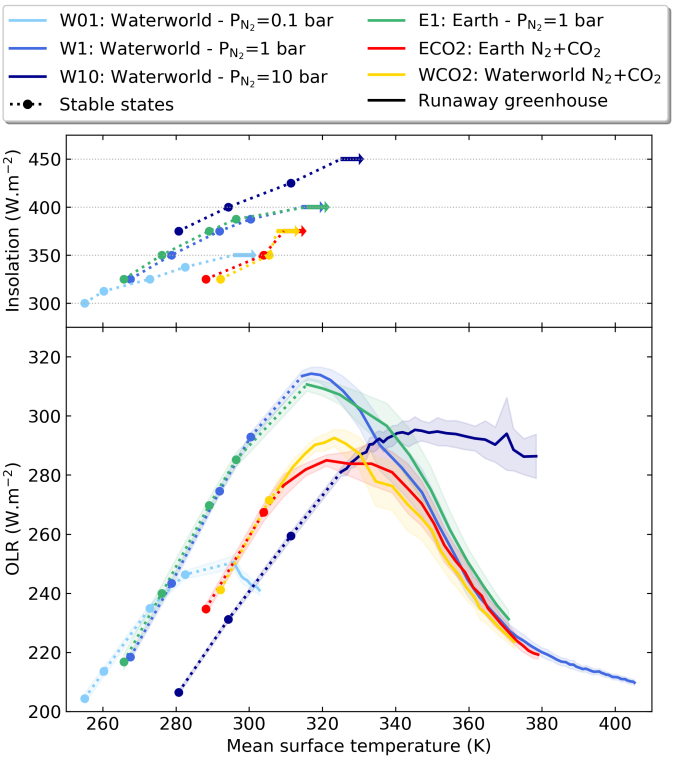


Fig. 1: Evolution of the thermal emission during the onset of the runaway greenhouse. Bottom panel: Values of the OLR function of the global surface temperature for each simulation setup described in Table 1. Colored dots are the stables states corresponding to various insolations, while the full curves are the instable state of the runaway greenhouse. Top panel: Insolation values of each stable state. The colored arrows represent the insolation for which the runaway greenhouse arises for each setup. The OLR and temperature values are averaged over two years (for both the stable states and the runaway greenhouse) and the colored fills are the 1-sigma uncertainties due to variability on the OLR calculation.

when the surface temperature reaches ~340 K) is not sensitive to the presence of continents and/or the presence of low concentration of CO_2 for a given total surface pressure; that is, every simulation converges roughly on the same OLR curve. This is because when the surface temperatures are high enough, background gases become negligible compared to the radiative effect of high vapor pressures (Chaverot et al. 2022). Moreover, the radiatively active part of the atmosphere is decoupled from the surface conditions; therefore, the surface albedo (i.e., continents) does not influence the radiative balance any longer. For higher background gas pressures (W10 in Fig. 1), the onset of the runaway greenhouse arises at higher temperature and for a higher insolation (450 W.m^{-2}). For this extreme case with 10 bar of nitrogen, the temperature profile is closer to a purely dry adiabatic profile, which is "less steep" than a wet adiabatic profile. Consequently, for a given global surface temperature, the atmosphere is colder and, thus, it is dryer. Therefore, even if there is less water in the atmosphere (vapor and clouds), the averaged OLR is lower, as shown in Fig. 1. This effect of high nitrogen pressures on the steepness of the temperature profile is also discussed in Chaverot et al. (2022), but they did not find smaller OLR values for high nitrogen pressure. This is probably linked to the pseudo-adiabatic assumption fixing the water vapor partial pressure as a function of the temperature. This assumption usually done in 1D models fixes the relative humidity to unity and underestimates the OLR (Ishiwatari et al. 2002; Leconte et al. 2013). On the other side, lower background gas pressures (0.1 bar of nitrogen; see W01 in Fig. 1) lead to a runaway greenhouse transition at a lower temperature, OLR value, and insolation (350 W.m^{-2}). A lower OLR bump for a low nitrogen pressure is consistent with results obtained by Chaverot et al. (2022) with a 1D model. The strong pressure broadening of H_2O-H_2O collisions makes the absorption more efficient than in the diluted case assuming 1 bar of nitrogen. The temperature profile is also closer to a wet adiabat which warms the stratosphere (compare to the dry adiabat case) and trigger the onset of the runaway greenhouse.

Finally, adding 376 ppm of CO_2 shifts the onset of the runaway greenhouse to lower the insolation (375 W.m^{-2} for ECO2 and WCO2 instead of 400 W.m^2 for E1 and W1) because of the strong greenhouse power of CO_2. This drop is discussed using simpler 1D models as well (e.g., Nakajima et al. 1992; Goldblatt & Watson 2012; Goldblatt et al. 2013; Koll & Cronin 2019; Chaverot et al. 2022). For a given insolation value, the global surface temperature is also about 20 K higher in presence of CO_2 (top panel in Fig. 1), which is consistent with respect to the greenhouse power of this gas.

During the runaway greenhouse, the insolation is kept unchanged to let the system evolve. The OLR reaches a maximum then decreases strongly. This is due to a combination of radiative effects and a quick modification of the cloud pattern. Spectroscopic processes are described by using a 1D radiative-convective model in Chaverot et al. (2022) and the modification of the cloud coverage is described in Sect. 3.1.3. In Fig. 1, the colored envelope delimiting the one-sigma variability of the OLR increases largely during the first steps of the runaway greenhouse. The continuous evaporation characteristic of this process densifies the cloud coverage. For medium temperatures (between 320 K and 360 K), the global dynamics induces variable patterns in this cloud coverage, thus strong variations of the spatial distribution of the OLR. When the global surface temperature is high enough to maintain a large amount of water vapor in the atmosphere (beyond 360 K), the cloud coverage becomes more homogeneous, thereby reducing the thermal emission windows as well as the OLR and its variability.

3.1.2. Radiative imbalance

To study the evolution of the cloud coverage and its radiative effects, we compare in Fig. 2 the OLR and the ASR to their clear sky equivalent (csOLR and csASR). To compute the csOLR and csASR, we ran a simulation, including clouds but we neglect their radiative effect to estimate the emitted and absorbed fluxes. On the same figure, the red curve correspond to OLR values obtained using the 1D cloud-free version of the Generic-PCM[1] described in Chaverot et al. (2022), with an atmosphere including H_2O and 1 bar of N_2 and a relative humidity value fixed to unity. The aim is to compare 1D and 3D models sharing the same radiative transfer calculation.

At low and high temperatures, respectively, when the atmosphere is nitrogen- or water-dominated, csOLR values from 1D and 3D simulations tend to converge. As there are no clouds in the 1D simulation, the only remaining difference is the absence of dynamics in the 1D model. Therefore, at low temperatures, the atmosphere is very thin and the csOLR is not much affected by the global dynamics. In other words, it is close to the Planck

[1] named 1D reverse version of LMD-Generic in Chaverot et al. (2022)

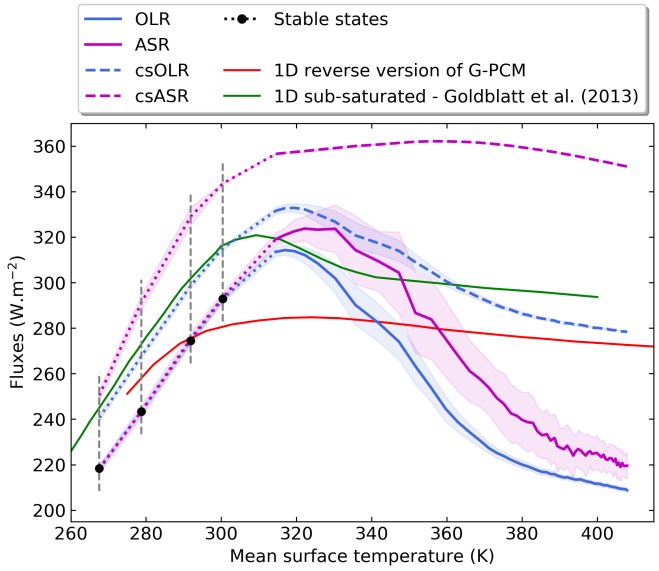


Fig. 2: Thermal emission and absorbed flux as a function of the mean surface temperature. Blue and purple solid lines are OLR and ASR, respectively, while the blue and purple dashed lines are their clear-sky equivalent (csOLR and csASR). Black dots are the stable states and the blue solid line is the runaway greenhouse for an insolation equal to 400 W/m^2. The simulation setup is a waterworld with 1 bar of nitrogen without CO_2 (W1). For comparison, the red line is the OLR computed with the 1D reverse version of the Generic-PCM which uses the same radiative transfer module and assume a fully saturated atmosphere (named the 1D reverse version of LMD-Generic in Chaverot et al. 2022). The green line is the OLR computed using a 1D reverse model assuming a subsaturated atmosphere (saturation mixing ratio less than 5%) from Goldblatt et al. (2013). The flux and temperature values are averaged over a two-year period and the colored areas are the 1 sigma uncertainties due to variability on the fluxes calculation.

function. On the other hand, at high temperatures, the water vapor is well distributed around the planet and the csOLR is not affected by the dynamics. For intermediate temperatures and especially for the onset of the runaway greenhouse when the evaporation begins, the distribution of the vapor is not homogeneous and the 1D version of the Generic PCM largely underestimates the global OLR. As explained in Ishiwatari et al. (2002) and Leconte et al. (2013), this underestimation of the OLR of 1D models assuming a saturated atmosphere is due to the downward branches of the Hadley cells which reduce the relative humidity around the tropics, creating radiative windows by reducing the quantity of water vapor. To circumvent this issue, 1D models with variable humidity ought to be preferred (e.g., Ramirez et al. 2014). In Fig. 2, the green curve which is from Goldblatt et al. (2013) is obtained by using a cloud free 1D model assuming a saturation mixing ratio of less than 5%. This allows us to fit accurately csOLR from GCM simulations for temperate states. Even if some differences remain for the runaway greenhouse, the shape of the csOLR (and particularly the bump) is quite well represented. Thus, the major difference between results from 1D and 3D simulations is induced by the evolution of the cloud coverage. The differences remaining between Goldblatt et al. (2013) (green curve) and the csOLR could come from dynamics, the different opacity database used or a mix of the two. Indeed, Goldblatt et al. (2013) used HITEMP, whereas we use HITRAN in this work.

The difference between the OLR and csOLR curves in Fig. 2 is only due to the radiative effect of the clouds. While this difference is rather constant for stable states, it expands during the runaway greenhouse. This is due to the strong evaporation, which allows for a densification and a drift of the cloud coverage toward the upper layers of the atmosphere (see Sect. 3.1.3), thereby increasing their radiative effect (see also Fig. 11, which shows the usual cloud forcing metrics). This is visible through the sharp increase in the Bond albedo and the drop in the ASR (pink solid line in Fig. 2). Nevertheless, as the OLR decreases as well, the effective flux (Seff=ASR/OLR) is greater than unity and the atmosphere warms-up. The energy imbalance is constant beyond 390 K (≈12 W.m^{-2}) and never exceed ≈25 W.m^{-2}, while it reaches ≈150 W.m^{-2} in Kopparapu et al. (2017) for a global surface temperature equal to 350 K around a 3700 K star. We found that this energy imbalance may reach higher values for higher insolations (e.g., ≈80 W.m^{-2} for ISR=475 W.m^{-2} instead of ISR=400 W.m^{-2} for the reference simulation W1).

During the runaway greenhouse, the difference between the csOLR and the csASR increases, highlighting the increase of the water vapor content in the atmosphere and, thus, of its absorption. This means that the OLR drops due to a combined absorption induced by the clouds and by a efficient horizontal homogenization of the increasing content of water vapor in the atmosphere. As the csASR is roughly constant during the runaway greenhouse, the drop in the ASR is mainly due to the increase of the Bond albedo due to the evolution of the cloud coverage.

3.1.3. Evolution the cloud coverage

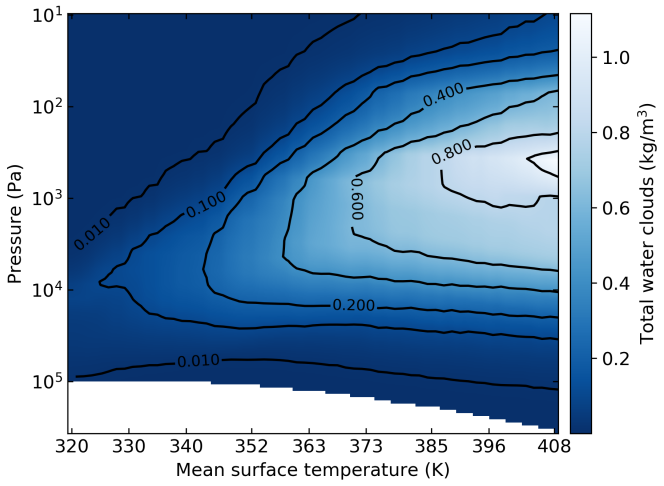


Fig. 3: Map of the evolution of the mean vertical profile of the total water cloud (liquid + ice) content as a function of the global surface temperature during the evaporation phase. The simulation setup is the waterworld with 1 bar of nitrogen without CO_2 (W1). The profiles are averaged over one year.

As explained in Sect. 3.1.2, during the runaway greenhouse, the thickness of the cloud coverage grows (due to a strong evaporation) and the altitude of the cloud deck drifts toward the upper layers of the atmosphere. This effect is visible through the evolution of the mean vertical profile of the cloud coverage as a function of the temperature (given in Fig. 3.) The increase in the surface pressure through the evaporation of the ocean is also

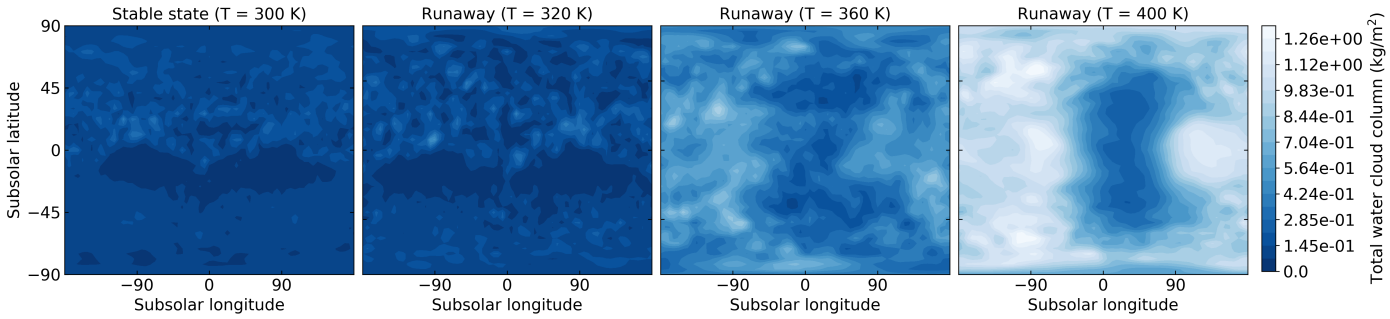


Fig. 4: Latitude-longitude map of the clouds (liquid + ice) distribution during the evaporation phase. The maps were calculated in the heliocentric frame, that is keeping the subsolar point at 0° longitude and 0° latitude, and using an annual average. The simulation setup is the waterworld with 1 bar of nitrogen without CO_2 (W1).

visible on the same figure. The same evolution of the clouds has been observed by Wolf & Toon (2015) using CAM4. The water cloud content is constant in the bottom part of the atmosphere while the top-of-atmosphere layers are enriched from $\approx 10^{-7}$ to $\approx 10^{-1}$ kg.m^{-3}. In the same way, the stratosphere becomes wetter with the augmentation of temperature. At 400 K the vapor profile is quasi-constant and tends toward 1 kg.kg^{-1} (see Appendix A for more details). This tendency is consistent with the results obtained by Turbet et al. (2021) studying the runaway greenhouse with hot and water-dominated initial conditions. As the quantity of clouds at the top of the atmosphere increases, the Bond albedo increases (from 0.2 to 0.45, see Fig. 12), inducing a drop in the ASR, as discussed in Sect. 3.1.2.

The day-to-night distribution of the clouds is not homogeneous during the runaway greenhouse, as shown on the latitude-longitude maps averaged over a year and centered at the substellar point presented in Fig. 4. The pattern observed at 400 K (right panel on the figure) is similar to that observed and discussed in Turbet et al. (2021) for hot and steam post-runaway atmospheres – except that in this case, a liquid surface ocean is still present and, thus, the albedo on the day side is not strictly zero. The ocean allows cloud formation on the day-side, even if they are mainly located on the night-side. The cloudy night-side provides an efficient greenhouse effect, contributing to the warming of the atmosphere. While it is non-existent for temperate stable states, the contrast of this specific pattern is amplified during the evaporation of the ocean. In this work, we assume a rapidly rotating Earth-like planet which induces an uniform cloud coverage of temperate stables states. Previous studies (Yang et al. 2013; Kopparapu et al. 2017) have shown that slow-rotating planets preferentially form cloud at the sub-stellar point for temperate stables states, preventing an intense warming and delaying the runaway greenhouse thanks to a high albedo on the day-side. These two different scenarios are discussed in Turbet et al. (2021). The evaporation of the clouds at the sub-stellar point during the onset of the runaway greenhouse described in detail in this section was also observed by Kopparapu et al. (2017) for planets orbiting various stellar types.

3.1.4. Atmospheric circulation

The global circulation of the atmosphere changes during the runaway greenhouse. The usual Hadley cells are shown in Fig. 5 for temperate states (bottom left panel), with an upward branch at the equator and downward branches at the tropics. This terrestrial circulation disappears during the runaway greenhouse while a new circulation arises at the top of the atmosphere (bottom right). As the water vapor pressure increases in the bottom part of the atmosphere, the opacity increases and there is less and less stellar flux reaching the surface. Because of this, the temperature is more homogeneously distributed around the planet, which has a decreasing effect on the surface wind jets. On the other side, as the absorption in the upper layers rises, the radiative heating strongly increases, inducing strong meridional jets at the top of the atmosphere. This stratospheric circulation characteristic of the runaway greenhouse and decorrelated from the surface conditions is visible in every simulation we performed. The same circulation was found by Turbet et al. (2021) for similar conditions and by Fujii et al. (2017), using ROCKE-3D, for water-dominated tidally locked planets.

As described in Sect. 2, we used a slab ocean without heat transport. For simulations without continents, we observe a hemispheric difference of the average annual temperature; more precisely, the northern hemisphere is warmer. This hemispheric difference can also be seen in Fig. 4, where the cloud coverage is slightly more important for the two left panels. This induces an atmospheric circulation around the equator along the north-south direction that is visible on the two first panels of Fig. 5. In our simulations, the atmosphere is initially water vapor-free and the surface temperature is homogeneous. Due to the non-zero obliquity of the planet (see Table 1), heating and intense evaporation happen alternatively in both hemispheres. For the waterworld setup, the evaporation of the ocean is continuous over time, unlike the Earth's continent setup for which the evaporation rate over time is perturbed by the presence of continents during the rotation of the planet. Consequently, for a given insolation, the atmosphere of the waterworld hosts more water vapor. In addition to this, the non-symmetric evaporation due to the obliquity of the planet induces a difference of the opacity between the two hemispheres. Therefore, this creates a north-south forcing of the heat transport and one Hadley cell overrides the other. The downward branch of the Hadley cell reduces the relative humidity, as described in Leconte et al. (2013), which allows locally a larger thermal emission, thus preventing the evaporation. This induces a feedback which maintain this specific circulation. This modification of the Hadley cells is not function of the seasons and seems stable along the entire year. When the runaway greenhouse occurs, as the physics is de-coupled from the surface this circulation weakens to converge on a unique stratospheric circulation pattern (last two panels in Fig. 5, see also Fujii et al. 2017)

This non-symmetric temperate circulation seems stable in the simulation W1 as the zonal averaged temperature is constant over time as well as the water vapor pressure. However, as the numerical integration time is limited by our resources, a

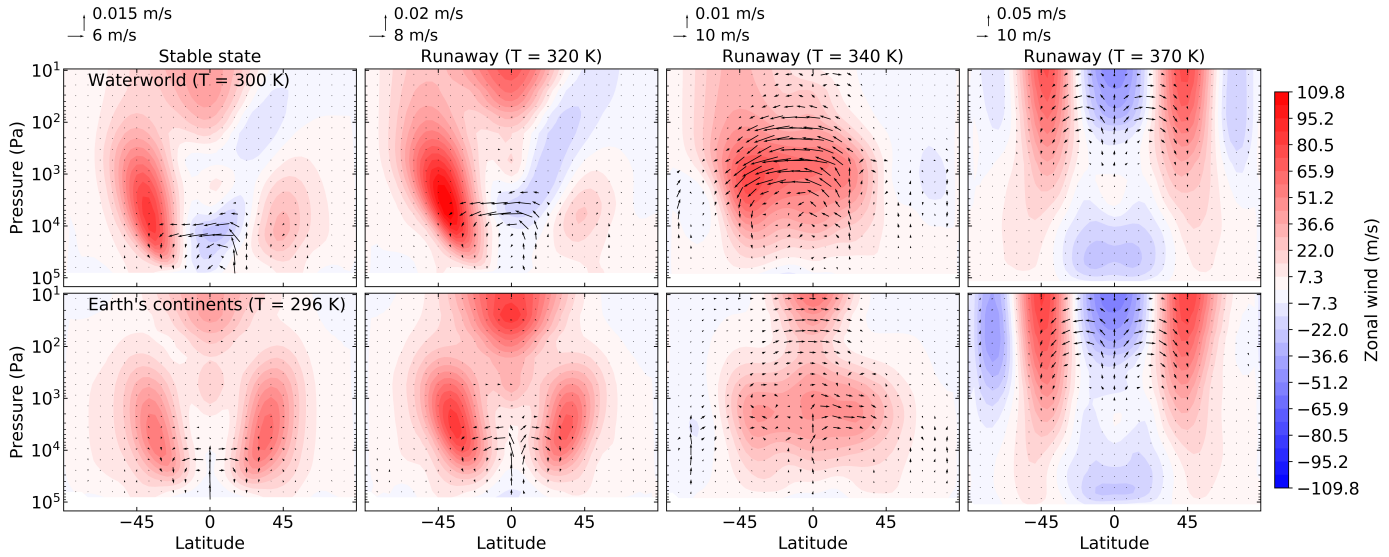


Fig. 5: Evolution of the wind circulation during the runaway greenhouse. The color map represent the zonal wind (positive values represent eastward winds) and the arrows the vertical and meridional winds averaged over 1 year. The first row is the evolution of the winds for the waterworld setup (W1) and the bottom row is considering the Earth's continents (E1), both without CO_2. The first panel of each row is the warmer stable state obtained for the two considered setups at I=375 W.m^2. Others show the evolution during the runaway greenhouse for different temperatures. Wind speeds corresponding to the length of the arrows vary with temperature.

very long equilibrium time (longer than a hundred years) should not be excluded. Even if this state seems stable, it is function of the initial conditions of the simulation. The north to south hemispheric circulation shown in Fig. 5 (top left panel) corresponds to a simulation initialized assuming summer in the northern hemisphere. By initializing the simulation assuming summer in the southern hemisphere, the obtained circulation is reversed, meaning that the dominant wind is from south to north. For simulations with continents (E1 and ECO2), the evaporation rate and the cloud distribution are less homogeneous along the longitude than for their waterworld equivalents (W1, WCO2). This disturbs the feedback described above, thus allowing more symmetrical circulation around the equator that is similar to Hadley cells we see on Earth. Moreover, a symmetrical circulation is observed for a planet without obliquity as well as for low insolations (i.e., global surface temperatures below 280 K). This confirms that the modified circulation can happen preferentially on a waterworld, and it is induced by combining obliquity and high evaporation rates due to an insolation higher than the one of the Earth. Nevertheless, the sensitivity of this particular circulation needs to be deeply investigated to understand the contribution of each processes on it, as well as its stability criteria. Moreover, the oceanic circulation could largely affect it.

3.1.5. Reversibility of the runaway greenhouse

In each simulation presented above, we studied the evolution of the atmosphere during the warming phase of the runaway greenhouse transition. We performed a set of simulations, presented in Fig. 6, where we started from a planet in runaway and reduce the insolation it receives in order to condense back the vapor into the surface ocean. First, a simulation following the method described in Sect. 2 was performed in order to partially evaporate the ocean (blue curve in Fig. 6; also see W1 in Table 1). This induced an increase of the global surface temperature, symbolized by the blue arrow in Fig. 6. Then we selected a runaway greenhouse state with a global temperature equal to 369 K as initial state for a second set of simulation (shown as a black star in Fig. 6). For this second step, we decrease the insolation compared to the one required to trigger a runaway greenhouse transition (ISR=400 W.m^{-2}) in order to find the insolation required to condense back the vapor into the surface ocean (i.e., to cool down the planet). The bottom panel of Fig. 6 presents the obtained OLR curves for different insolations (yellow: ISR=300 W.m^{-2}, orange: ISR=325 W.m^{-2}, brown: ISR=350 W.m^{-2}, red: ISR=375 W.m^{-2}). Colored arrows on the two panel represent the tendency evolution of the global surface temperature for each corresponding insolation (cooling or warming).

The non-zero difference between the OLR and the ASR during the runaway (see Fig. 2) suggests that a small decrease of insolation is not enough to condense back the water vapor and cool the planet. While ISR=400 W.m^{-2} is required to initiate the runaway greenhouse for the W1 setup, ISR=375 W.m^{-2} is not low enough to condense back the water vapor onto the surface starting at a global surface temperature of 369 K. An insolation equal to 350 W.m^{-2} is able to cool down the planet, converging on a temperate stable state. For every cooling simulation, we recovered the same stable stables as those found by increasing step-by-step the insolation (see Sect. 2.1). We show in Fig. 6 that during this cooling phase, the OLR increases following the same pathway than the warming W1 simulation. This is also true for the evolution of the albedo and the cloud coverage. This resilience of the runaway greenhouse is visible on the top panel of Fig. 6 through the hysteresis loop on the insolation.

3.2. Runaway greenhouse dry transition

As explained in Sect. 2.1, to study the transition of the runaway, we arbitrarily remove the surface ocean when the surface water vapor pressure reaches some threshold values (1 and 1.5 bar). In the evaporation phase, we evaporate up to 2.6 bar of water but

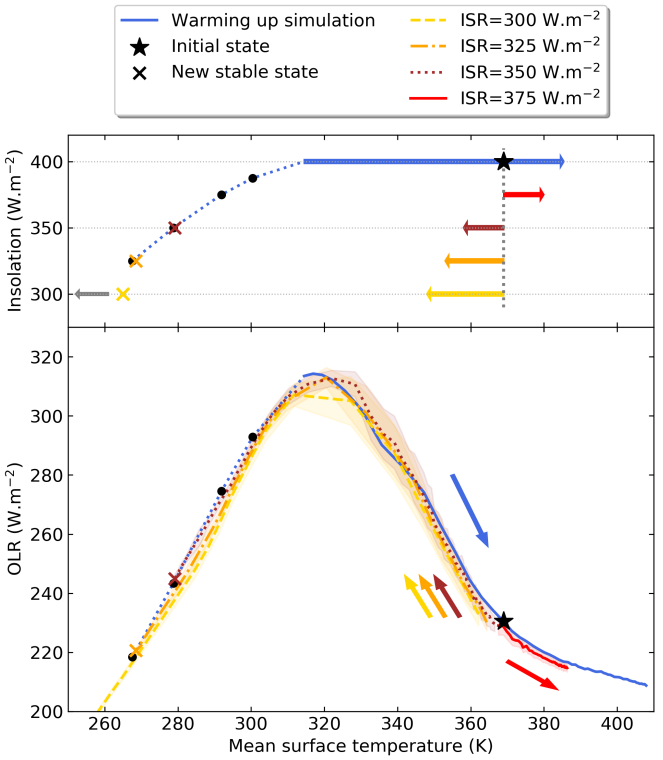


Fig. 6: Evolution of the thermal emission when water vapor condense back into the surface ocean. The bottom panel is the OLR function of the mean surface temperature. The top panel is the insolation of each simulation. The blue curve is the warming simulation presented in Fig. 1 with an insolation equal to 400 W.m^{-2}. Black dots are stable states assuming a two-year average. Other colored curves (yellow, orange, brown, and red) are the evolution of the OLR for lower insolations and assuming a initial temperature equal to 369 K (the black star). Arrows represent the tendency of the evolution of the global surface temperature (warming or cooling) for different insolations. Colored crosses represent the stable stable found for cooling simulations (ISR=300 W.m^{-2}, 325 W.m^{-2}, and 350 W.m^{-2}, respectively). The top panel highlight the hysteresis loop induced by the clouds feedback during the runaway greenhouse. However, the bottom panel shows that there is no dependence of the OLR on the insolation for a given surface temperature. The simulation setup is a waterworld with 1 bar of nitrogen without CO_2 (WCO2).

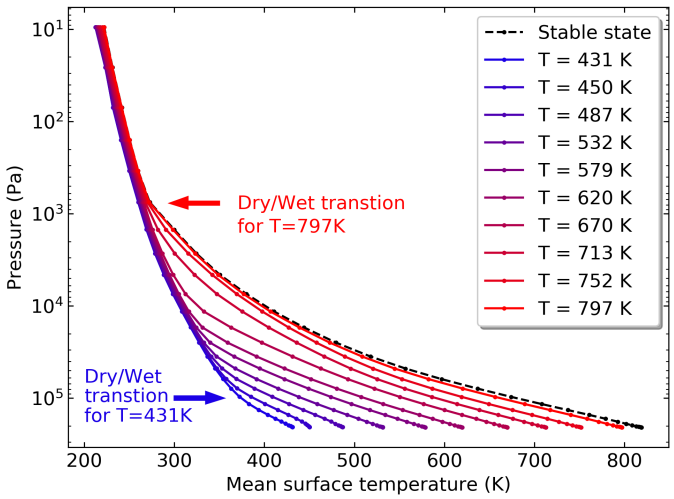


Fig. 7: Temperature profile for different surface temperature during the dry transition with 1 bar of water vapor. Arrows indicate the transition between a dry adiabat in the lower part of the atmosphere (high pressures) and a wet one in the bottom part (low pressures) for the coldest (blue) and hottest (red) cases. Dry region is below the transition while moist one is above (Abe & Matsui 1988; Kasting 1988). The simulation setup is the waterworld with 1 bar of nitrogen without CO_2 (W1).

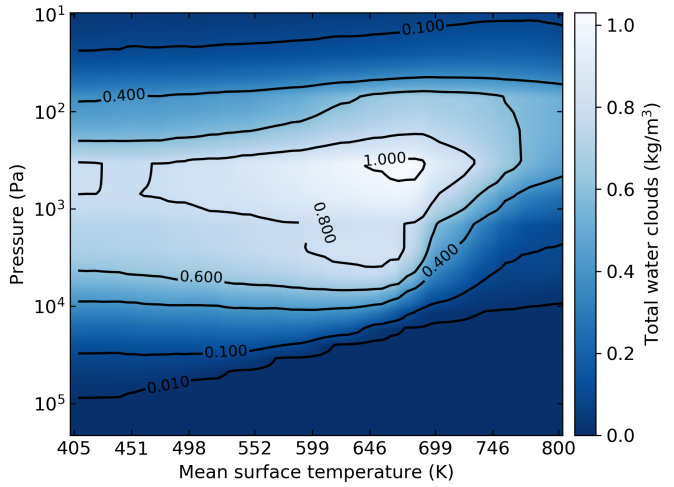


Fig. 8: Map of the evolution of the mean vertical profile of the total water cloud (liquid + ice) content as a function of the global surface temperature during the dry transition phase. The simulation setup is the waterworld with 1 bar of nitrogen without CO_2 (W1) assuming 1 bar of water vapor. The profiles are averaged over one year.

we were not able to model the dry transition phase for vapor pressure higher than 1.5 bar because of numerical instabilities. High vapor pressures induce a huge radiative imbalance leading to numerical failures similar to those discussed by Kopparapu et al. (2017).

We did two simulations for two different vapor surface pressures (1 bar and 1.5 bar corresponding to 10 and 15 m of GEL) in order to explore the impact of the water reservoir on the obtained post-runaway states. We used the corresponding runaway greenhouse states as initial conditions then we remove the surface ocean from the simulation and we let the system evolve by keeping the atmospheric composition unchanged, as well as the insolation. As there is no longer any humidity source, the temperature profile of the atmosphere changes. More precisely, there is a transition from a previously wet to a dry adiabatic profile in the bottom part of the atmosphere (as seen in Boukrouche et al. 2021 with a 1D model) as visible in Fig. 7, thus we choose to name this second simulation phase the "dry transition." As the pressure-temperature profile of a dry adiabat is steeper than a wet one, the global surface temperature rises quickly. During the evaporation phase, the large thermal inertia of the ocean produces a cooling in the bottom part of the atmosphere preventing a quick increase of the surface temperature. In the dry transition, such forcing does not exist allowing a strong and fast increase of the global surface temperature. For the evaporation phase (W1 simulation, ISR=400 W.m^{-2}), more than a hundred years are needed to increase the temperature by about 80 K (i.e., evapo-

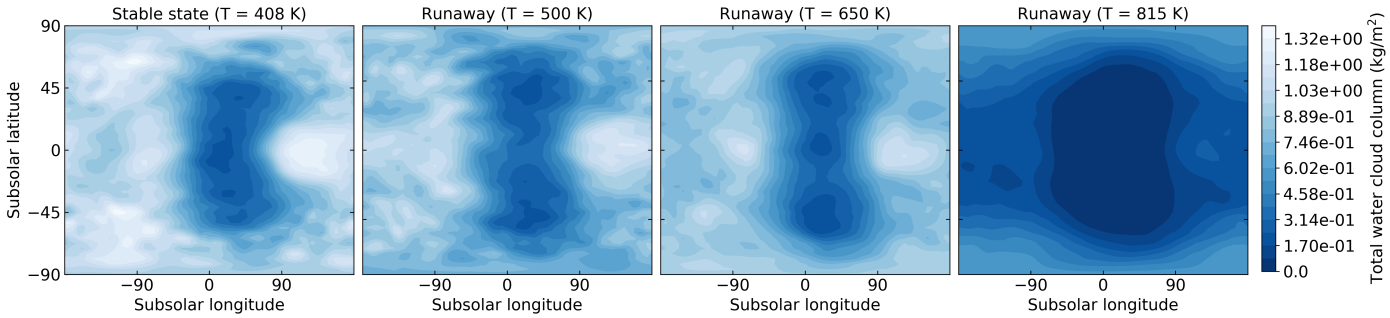


Fig. 9: Latitude-longitude map of the cloud (liquid + ice) distribution during the dry transition phase with 1 bar of vapor. The maps were calculated in the heliocentric frame that is keeping the subsolar point at 0° longitude and 0° latitude, and using an annual average. The simulation setup is the waterworld assuming 1 bar of nitrogen without CO_2 (W1).

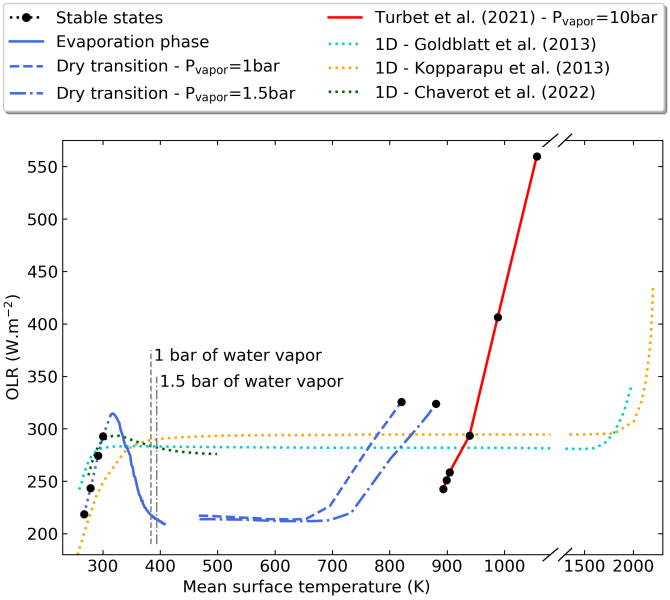


Fig. 10: Evolution of the OLR as a function of the mean surface temperature from temperate stable states to post-runaway stable states. For blue curves, the simulation setup is the waterworld, 1 bar of nitrogen without CO_2 (W1). The red curve is taken from Turbet et al. (2021) assuming 10 bar of water vapor, 1 bar of nitrogen and no CO_2. The insolation of the evaporation phase and the dry transition is equal to 400 $W.m^{-2}$. The vertical grey lines are the temperatures for which 1 bar and 1.5 bar of water vapor are evaporated. Stable post-runaway states from Turbet et al. (2021) assume different insolations. The OLR values are averaged over 2 years which explain the gap between the evaporation and the dry transition phases. Cyan, orange and green dotted lines are OLR curves from reference works using 1D models and assuming 273 bar of water (pure water from Goldblatt et al. 2013, Earth's case from Kopparapu et al. 2013 and with 1 bar of N_2 from Chaverot et al. 2022, respectively).

rating 1.5 bar of water); whereas for the "dry" phase, only few tens of years are needed to increase the temperature to ≈400 K.

Figure 8 shows the evolution of the total water cloud content (liquid + ice) during the dry transition. We see re-evaporation taking place in the bottom part of the cloud layer. This contributes to the enrichment of the upper part of the atmosphere in water vapor. Moreover, due to the high temperatures at the surface, the water vapor migrates towards the upper layers and the vapor mass mixing ratio profile tends toward a constant value equal to 0.5 $kg.kg^{-1}$ (see Appendix A for more details). We notice also a slightly increase of the cloud coverage at the very top of the atmosphere.

Figure 10 gives the evolution of the OLR as a function of the global mean surface temperature. The evaporation phase (below 420 K) corresponds to the simulation W1 presented in Fig. 1. The blue dashed and dashed-dotted lines are respectively the dry transitions when 1 bar and 1.5 bar of water vapor is evaporated. The red curve is taken from Turbet et al. (2021) assuming 10 bar of vapor, 1 bar of nitrogen and no CO_2. Black dots are the different stables states obtained in each cases, and for different insolations. Blue and red curves are computed using different methods. Blue curves are obtained by increasing the insolation from temperate stable states (warming simulation) while for the red curve, the insolation is reduced step-by-step to find the tipping point for which condensation occurs (cooling simulation). We show that the size of the water reservoir determines the equilibrium temperature of the post-runaway state (black dots beyond 800 K in Fig. 10), as suggested by 1D models (Turbet et al. 2019; Boukrouche et al. 2021; Turbet et al. 2021). Dotted lines are reference OLR curves computed using different 1D models and for different atmospheric compositions. Cyan, orange, and green dotted lines correspond to a pure water atmosphere (Goldblatt et al. 2013), a pre-industrial Earth (Kopparapu et al. 2013), and an atmosphere containing 1 bar of nitrogen without CO_2 (Chaverot et al. 2022), respectively. All these models consider a fully saturated atmosphere (see Sect. 3.1.2 for more details about differences between 3D and 1D saturated and subsaturated models).

The reason for which we consider small amounts of water (1 and 1.5 bar) come from the fact that the addition of vapor in the atmosphere increases its thermal inertia, thereby decreasing the evaporation rate. Due to numerical constraints, we were not able to evaporate more than 2.6 bar of water vapor in our simulations. Moreover, we were not able to model the dry transition phase itself for vapor pressures beyond 1.5 bar because of numerical instabilities. Indeed, for such pressures, the radiative unbalance skyrockets inducing numerical failures similar to those described by Kopparapu et al. (2017) for the onset of the runaway greenhouse. There is no strong evolution of the wind pattern during the dry transition. The day-to-night cloud dichotomy discussed in Sect. 3.1.3 remains during this phase (as shown in Fig. 9) and becomes even more contrasted. It is accentuated by the re-evaporation of the clouds to converge on the exact same pattern, as described in Turbet et al. (2021), with a purely cloud-free day-side. OLR values obtained in this work are also consistent with those obtained for different insolations in Turbet et al.

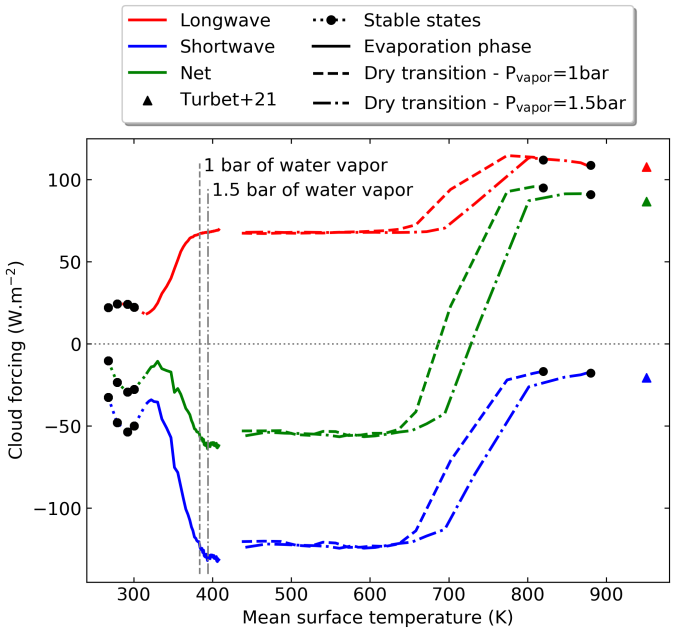


Fig. 11: Evolution of the cloud forcing during the runaway greenhouse. Solid lines are the evaporation and dry transition phases while black dots are stable states assuming a two-year average. Negatives values indicate a cooling effect of the clouds and positive ones a warming effect. In the longwave (blue curves), clouds have a cooling effect due to their high albedo reflecting the incoming stellar flux back to space. The red curve correspond to the warming contribution due to the greenhouse effect of the clouds (i.e., thermal mission absorbed by the clouds). The green curve is the net effect of the clouds, including shortwave and longwave contributions. The vertical grey lines are the temperatures for which 1 bar and 1.5 bar of water vapor are evaporated. These are used as initial conditions for the dry transition phase (colored dotted lines). Colored triangles are the values obtained in Turbet et al. (2021) for the same insolation (400 W.m^{-2}), but including 10 bar of water vapor. The fluxes values are averaged over two years, which explain the gap between the evaporation and the dry transition phases. The simulation setup is the waterworld with 1 bar of nitrogen without CO_2 (W1).

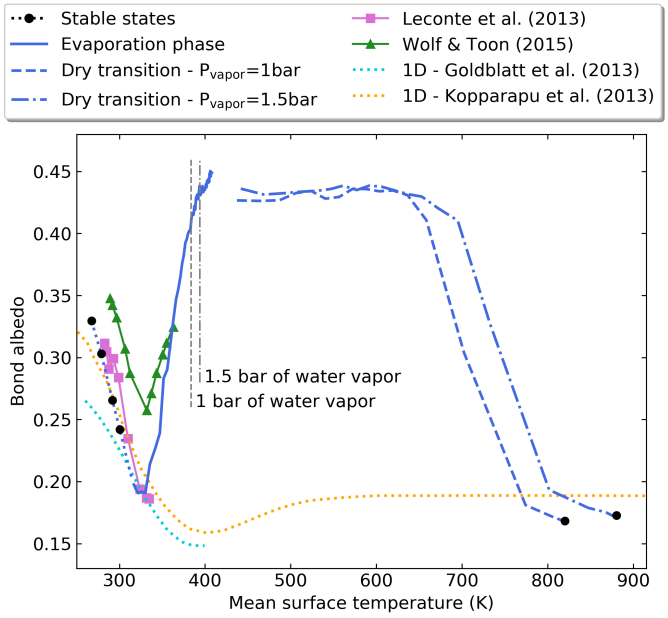


Fig. 12: Evolution of the bond albedo as a function of the mean surface temperature from temperate stable states to post-runaway stable states. The simulation setup is the waterworld with 1 bar of nitrogen without CO_2 (W1). The insolation of the evaporation phase and the dry transition is equal to 400 W.m^{-2}. The vertical grey lines are the temperatures for which 1 bar and 1.5 bar of water vapor are evaporated. The albedo values are averaged over 2 years which explain the gap between the evaporation and the dry transition phases. Pink squares and green triangles are steady states of the Earth's case from Leconte et al. (2013) and Wolf & Toon (2015) respectively. Dotted lines are albedo curves from reference works using 1D models (1 bar of N_2 from Goldblatt et al. 2013 and Earth's case from Kopparapu et al. 2013).

(2021). Moreover, even with a quantity as high as 10 bar of water vapor in the atmosphere, they obtain global circulation, temperature, and cloud distributions strongly similar to those presented here. Therefore, we can reasonably expect the same climate pattern and evolution for post-runaway states with higher water pressures (few tens of bar).

Figure 11 shows the evolution of the cloud forcing during both phases of the runaway greenhouse. For temperate habitable states, the cooling effect of the clouds in the shortwave (blue curve) is more efficient than the warming due to their greenhouse effect in the longwave (red curve). During the evaporation phase, as the cloud deck densifies, the Bond albedo increases (Fig. 12) and the colling effect of the clouds is even more efficient (blue curve in Fig. 11). However, when the surface ocean is considered entirely evaporated (vertical grey dotted lines at 383 K and 393 K corresponding, respectively, to 1 bar and 1.5 bar), after a strong increase of the global temperature, the net radiative effect of the clouds switches from cooling to warming (green curve) around 700 K. We show that during the dry transition phase, as the Bond albedo decreases (see Fig. 12 and blue curve in Fig. 11), the greenhouse effect of clouds becomes the dominant process and the net effect of the clouds tends to warm the planet (Fig. 11). In other words, the thick layer of clouds at the top of the atmosphere acts as a shield that retains the thermal emission of the planet. The cloud forcing of the obtained post-runaway states is very similar to the one from Turbet et al. (2021), even though those authors considered ten times more water vapor. This suggest that 1 bar of vapor is enough to stabilize the climate in a post-runaway configuration, with a thick cloud deck at the top of the atmosphere, preferentially on the night side of the planet. The temperature for which the net effect of the clouds switch from cooling to warming is concomitant with the increase of OLR and function of the water vapor content. More vapor and clouds will require a higher temperature to evaporate and modify the cloud albedo. The 50 K gap between the evaporation phase and the dry transition in Figs. 10, 11, and 12 is due to the very fast evolution of the system during the first stages of the simulation.

4. Discussion

4.1. Literature comparison

We show in Sect. 3.1.2 that the radiative imbalance is constant during all the evaporation phase. Similarly to Leconte et al. (2013), we did not find any moist stable states; whereas Wolf

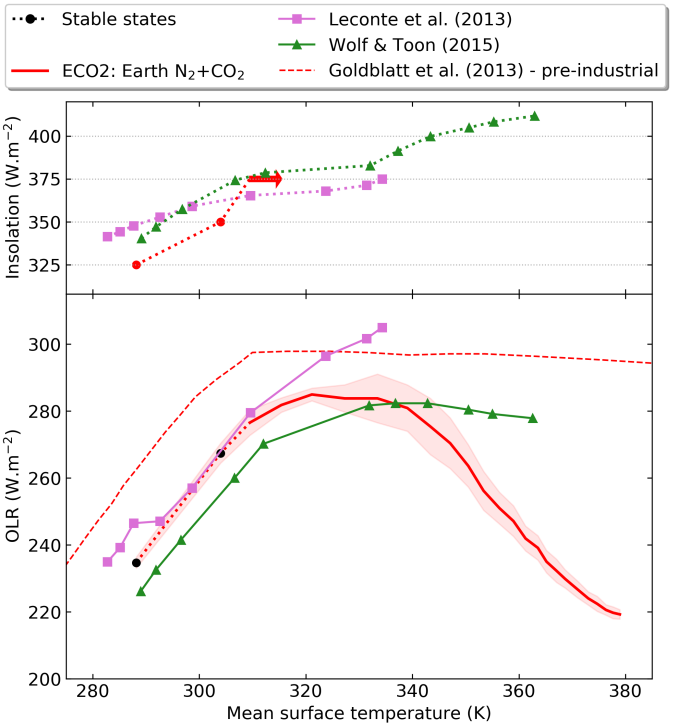


Fig. 13: Literature comparison of the OLR and the insolation as a function of the temperature. The black dots are the stables states corresponding to various insolations, while the full curves are the unstable state of the runaway greenhouse. The top panel indicates the insolation values of each stable state. The colored arrows represent the insolation for which the runaway greenhouse arises for each setup. The OLR and temperature values are averaged over two years and the colored fills are the 1 sigma uncertainties due to variability on the OLR calculation. Pink squares and green triangles are steady states of the Earth's case from Leconte et al. (2013) and Wolf & Toon (2015), respectively. The red dashed curve is a reference result from Goldblatt et al. (2013) for a pre-industrial atmosphere and using a 1D model, assuming saturation mixing ratio below 5%.

& Toon (2015) did, using CAM4, or Popp et al. (2016), using ECHAM6. There are multiple discussions in the literature around this open question (e.g., Kopparapu et al. 2017; Yang et al. 2019), some pointing out that the specific humidity of the stratosphere is a key factor in explaining this difference. Indeed, the GCM inter-comparison done by Yang et al. (2019) highlights that the Generic-PCM[2] tends to be wetter than CAM4 for planets around G-type stars. In the same time, the cloud fraction and the cloud thickness is higher in CAM4 inducing a cooling of the planet. This was discussed in Kopparapu et al. (2017), showing that Wolf & Toon (2015) found higher stratospheric temperatures than Leconte et al. (2013) for a same surface temperature. High relative humidity in the stratosphere reduces the thermal emission from the upper layers, allowing a larger difference between the OLR and the ASR. This is the commonly accepted answer to explain the existence (or not) of a moist stable state. More inter-comparisons based on the method used in Yang et al. (2019), as well as high-resolution cloud resolving simulations (e.g., Lefèvre et al. 2021), should be done to solve this question. By using a 1D climate model, Popp et al. (2015) suggests that the convection scheme could be the answer to explain potential moist runaway greenhouse. The number of Cloud Condensation Nucleii (CCN) present may also impact the cloud formation thus the possibility of a moist state.

We compare our results for the Earth case with pre-industrial CO_2 quantities (ECO2), with major results from the literature (Leconte et al. 2013; Wolf & Toon 2015) in Fig. 13. We do not show a direct comparison of the ASR, but we compare the Bond albedo from simulation W1 with Leconte et al. (2013) and Wolf & Toon (2015) in Fig. 12. As shown by Fig. 13, we found slightly different global surface temperature and OLR values compared to Leconte et al. (2013) and Wolf & Toon (2015), even for a same insolation. This is not surprising regarding numerous differences between the models highlighted by Yang et al. (2019). In Leconte et al. (2013), they used the Generic-PCM as this work, but they mimic the ocean thank to a large thermal inertia of the ground; whereas, we used a more complex slab ocean (without heat transport). These aspects, combined with the development of the model, may explain the differences between our results – especially on the relation between insolation and the global surface temperature. Even if Wolf & Toon (2015) found a moist stable state, the evolution of the OLR as a function of the global surface temperature is qualitatively consistent with our simulations.

The red dashed line is taken from Goldblatt et al. (2013), corresponding to a pre-industrial composition with a subsatured atmosphere. This curve is comparable with our ECO2 case to estimate the impact of 3D processes. The constant offset of OLR values for temperate states between 1D and 3D simulations is due to the greenhouse effect of the clouds. In the same way, the large difference of OLR during the runaway greenhouse is due to the contribution of the thick cloud coverage. As discussed in several works (e.g., Ishiwatari et al. 2002; Abe et al. 2011; Leconte et al. 2013), reducing the relative humidity of 1D models can produce results in a good agreement with 3D modelling for temperate stable states. However, substantial differences remain for the runaway greenhouse as the key process is the evolution of the cloud coverage that is not estimable using 1D models. From a qualitative point of view, the shape of the OLR curve we show is similar to historical estimations of the thermal emission of an atmosphere composed of H_2O and N_2 (e.g., Nakajima et al. 1992), but the quantitative values are different because of the addition of more complex physical processes (non-grey atmosphere, clouds, global dynamics).

4.2. Limitations and prospects

The H_2O+N_2 correlated-k table used in this work was made by Chaverot et al. (2022) using the HITRAN database (Gordon et al. 2017). Goldblatt et al. (2013) showed that the HITEMP database is more accurate and complete than HITRAN for high temperatures and this impacts the estimation of OLRs and ASRs (see also Kopparapu et al. 2013 and Ramirez 2014). More precisely, they highlight using a 1D climate model, which HITRAN overestimates the albedo and thus underestimates the ASR for temperatures beyond ≈360 K. As in 3D GCM simulations, the relative humidity (thus the vapor partial pressure) is lower than in 1D models (Leconte et al. 2013), we can assume no significant difference in our simulations up to ≈400 K. Therefore, this does not affect much the evaporation phase but may change the dry transition phase and the final equilibrium temperature by slightly modifying the Bond albedo of the planet an the heating rates. This could be investigated but we are confident on the global evolution described in this paper and on the reliability of gen-

[2] named LMDG in Yang et al. (2019)

eral mechanisms which determine the climate pattern transition between pre- and post-runaway. We describe general processes and tendencies and our results are in accordance with previous works using different GCMs.

In every simulation, the heat capacity (c_p) and the mean molecular weight are assumed to be constant. This is inaccurate when the temperature increases strongly (because of the dependence of c_p on the temperature) and when the dominant gas changes (from nitrogen-dominated to water -dominated during the evaporation phase, see Fig. A.1 and Chaverot et al. 2022). Our version of the Generic-PCM does not include variable heat capacity or molecular weight, but ongoing developments will allow for studies of the impact of variations of these quantities in the near future. For reasons of consistency, we did not update the value of c_p when we initialized the simulation of the dry transition phase.

In this work, we describe in detail the simulation with 1 bar of nitrogen without CO_2 (W1) to explore the effect of the water without additional absorption sources (nitrogen is assumed to be optically thin, except for the CIA). Therefore, the minimal absorption given by the correlated-k table is for a water volume mixing ratio equal to 10^{-6}. When the mixing ratio is lower (e.g., in the stratosphere at low temperature), the water vapor absorption is given by this threshold value. This approximation may induce an error for very low water content, but it becomes negligible when water is the dominant gas (i.e., during the runaway greenhouse, which we focus on in this work).

In Sect. 3.2, we describe a transition between a wet to a dry adiabat. This is true for low partial water pressures, but as shown by Selsis et al. (2023), it becomes wrong for pressures higher than roughly 20 bar (function of the considered host star). In this case, the temperature profile follows a radiative profile.

Finally, as we did not search for the exact tipping point triggering the runaway greenhouse, we probably overestimated the radiative imbalance by a few $W.m^{-2}$. This does not change the physics described in this work, however, a study focused on this could be interesting in the context of estimating the evaporation timescale of different water reservoirs.

5. Conclusions

We studied the runaway greenhouse with the 3D Generic-PCM in order to link temperate stables states to post-runaway stable states. The positive feedback of the runaway greenhouse is triggered by the strong absorption of the water vapor and driven by a large water inventory (i.e., surface ocean) available through evaporation. From terrestrial climate conditions, we increase the insolation step-by-step in order to find the onset of the runaway greenhouse, following the method used by previous works (Leconte et al. 2013; Wolf & Toon 2014; Popp et al. 2016). The originality of this work is to go beyond the onset and to study the transition toward post-runaway states[3]. We show that there are two phases:

1. An "evaporation phase" in which the water vapor content and the cloud thickness increase rapidly.
2. When the ocean is considered to be entirely evaporated, a "dry transition phase" begins, characterized by a switch from a wet adiabatic profile to a dry adiabatic profile. During this second step, the temperature increases quickly, then the climate converges onto a new stable state at high temperature, namely, a post-runaway state.

We describe the evolution of the composition of the atmosphere as well as the changes of the cloud pattern in Sect. 3.1. We show that even if the tipping point of the runaway greenhouse depends on the simulation setup (e.g., continents, with CO_2 as a minor constituent), the evolution path during the transition does not, for a given background gas pressure. As the bottom part of the atmosphere is water-dominated, it becomes optically thick and the physics is decoupled from the surface conditions. In the same way, a low content of CO_2 (376 ppm) does not influence the climate beyond the onset (Fig. 1).

The main characteristic of the first phase of the runaway greenhouse (evaporation phase) is the evolution of the cloud coverage. It grows because of the intense evaporation and it migrates toward the upper layers (Fig. A.1). This migration increases the Bond albedo creating a drop in the ASR (Fig. 2). The day to night distribution of the clouds is also affected. As shown by Fig. 4, the night-side is more cloudy than the day-side, which tends to increase the greenhouse effect of the clouds. This competition between the warming and cooling effect of the clouds is shown in Fig. 12. We highlight that during the entire evaporation phase, the net effect of the clouds tends to cool down the planet. However, the addition of water vapor due to evaporation creates an extra absorption able to overshoot this cooling, leading to a roughly constant radiative imbalance (Fig. 2) that continuously warms the planet. The general atmospheric circulation is strongly affected by the evaporation and the evolution of the cloud coverage. As the top part of the atmosphere becomes wetter, it absorbs more stellar flux and the heating rate rises creating an intense global circulation (Fujii et al. 2017). As visible in Fig. 5, strong stratospheric jets appear substituting the usual Hadley cells of the temperate Earth. We explore also the potential reversibility of the runaway greenhouse. The idea is to use a runaway state as a initial state, then to reduce the insolation in order to condense back the water in the surface ocean. We show in Fig. 6 that the radiative unbalance characteristic of the runaway greenhouse creates a hysteresis loop on the insolation making it resilient to any small variations of incoming flux. We also show that if a re-condensation happens, the OLR increases when the surface temperature decreases, following the exact same evolution pathway than during the evaporation phase.

In a second step, when a given quantity of water is evaporated (1 bar or 1.5 bar), we consider the ocean to have entirely evaporated and we remove it from the simulation (see Sect. 3.2). The absence of humidity sources at the bottom of the atmosphere induced a transition from a wet to a dry adiabatic profile (Fig. 7). Water vapor migrates towards the upper layers of the atmosphere and lower clouds evaporate (Fig. A.2). We also observed a more contrasted dichotomy between a cloudy night-side and a cloud free day-side (see Fig. 9,) which is consistent with the results from Turbet et al. (2021) on post-runaway states for similar atmospheres. Because of the re-evaporation of the clouds, the albedo decreases (Fig. 12) and the their net effect amounts to a tendency to warm the planet (Fig. 11, see also Turbet et al. 2021). This reduces also the radiative unbalance, allowing the simulation to converge on a post-runaway state as shown in Fig. 10. This final state strongly depends on the quantity of water available in the atmosphere, in other words: on the size of the initial water reservoir.

Finally, by comparing our results to historical studies using 1D models, we show that 3D processes (clouds and dynam-

[3] The GCM outputs of the stable states (temperate and post-runaway) of each setup, as well as several snapshots along the runaway transition for setup W1 are available here: https://zenodo.org/record/8325631. Other data underlying this article will be shared on request to the corresponding author.

ics) strongly impact the evolution of the climate during the first stages of the runaway greenhouse, as well as during the dry transition phase. This is of major importance for discussions of the potential observability of this kind of planet with reflected or emitted light.

Acknowledgements

This work has been carried out within the framework of the NCCR PlanetS supported by the Swiss National Science Foundation under grants 51NF40_182901 and 51NF40_205606. GC and EB acknowledge the financial support of the SNSF (grant number: 200021_197176 and 200020_215760) MT thanks the Gruber Foundation for its generous support to this research. MT acknowledges support from the Tremplin 2022 program of the Faculty of Science and Engineering of Sorbonne University. The authors thank the Generic-PCM team for the teamwork development and improvement of the model. The Generic-PCM (and documentation on how to use the model) can be downloaded from the SVN repository https://svn.lmd.jussieu.fr/Planeto/trunk/LMDZ.GENERIC/ (version 2521). More information and documentation are available on http://www-planets.lmd.jussieu.fr. The computations were performed at University of Geneva on the Baobab and Yggdrasil clusters. This research has made use of NASA's Astrophysics Data System. We thank the two referees Ravi K. Kopparapu and Colin Goldblatt for their helpful comments.

References

Abe, Y., Abe-Ouchi, A., Sleep, N. H., & Zahnle, K. J. 2011, Astrobiology, 11, 443, publisher: Mary Ann Liebert, Inc., publishers
Abe, Y. & Matsui, T. 1988, Journal of Atmospheric Sciences, 45, 3081, aDS Bibcode: 1988JAtS...45.3081A
Boukrouche, R., Lichtenberg, T., & Pierrehumbert, R. T. 2021, The Astrophysical Journal, 919, 130, aDS Bibcode: 2021ApJ...919..130B
Charnay, B., Forget, F., Wordsworth, R., et al. 2013, Journal of Geophysical Research: Atmospheres, 118, 10,414, _eprint: https://onlinelibrary.wiley.com/doi/pdf/10.1002/jgrd.50808
Chaverot, G., Turbet, M., Bolmont, E., & Leconte, J. 2022, Astronomy & Astrophysics, 658, A40, publisher: EDP Sciences
Codron, F. 2012, Climate Dynamics, 38, 379, aDS Bibcode: 2012ClDy...38..379C
Fauchez, T. J., Turbet, M., Villanueva, G. L., et al. 2019, The Astrophysical Journal, 887, 194
Fujii, Y., Del Genio, A. D., & Amundsen, D. S. 2017, The Astrophysical Journal, 848, 100, aDS Bibcode: 2017ApJ...848..100F
Goldblatt, C., Robinson, T. D., Zahnle, K. J., & Crisp, D. 2013, Nature Geoscience, 6, 661
Goldblatt, C. & Watson, A. J. 2012, Philosophical Transactions of the Royal Society A: Mathematical, Physical and Engineering Sciences, 370, 4197
Gordon, I. E., Rothman, L. S., Hill, C., et al. 2017, Journal of Quantitative Spectroscopy and Radiative Transfer, 203, 3
Hamano, K., Abe, Y., & Genda, H. 2013, Nature, 497, 607, aDS Bibcode: 2013Natur.497..607H
Ingersoll, A. P. 1969, Journal of the Atmospheric Sciences, 26, 1191
Ishiwatari, M., Takehiro, S.-i., Nakajima, K., & Hayashi, Y.-Y. 2002, Journal of the Atmospheric Sciences, 59, 3223, publisher: American Meteorological Society Section: Journal of the Atmospheric Sciences
Kane, S. R., Ceja, A. Y., Way, M. J., & Quintana, E. V. 2018, The Astrophysical Journal, 869, 46, aDS Bibcode: 2018ApJ...869...46K
Karman, T., Gordon, I. E., van der Avoird, A., et al. 2019, Icarus, 328, 160
Kasting, J. F. 1988, Icarus, 74, 472
Kasting, J. F., Whitmire, D. P., & Reynolds, R. T. 1993, Icarus, 101, 108
Koll, D. D. B. & Cronin, T. W. 2019, The Astrophysical Journal, 881, 120, aDS Bibcode: 2019ApJ...881..120K
Komabayasi, M. 1967, Journal of the Meteorological Society of Japan. Ser. II, 45, 137
Kopparapu, R. K., Ramirez, R., Kasting, J. F., et al. 2013, The Astrophysical Journal, 765, 131, aDS Bibcode: 2013ApJ...765..131K
Kopparapu, R. K., Ramirez, R. M., SchottelKotte, J., et al. 2014, The Astrophysical Journal, 787, L29, aDS Bibcode: 2014ApJ...787L..29K
Kopparapu, R. k., Wolf, E. T., Arney, G., et al. 2017, The Astrophysical Journal, 845, 5
Kopparapu, R. k., Wolf, E. T., Haqq-Misra, J., et al. 2016, The Astrophysical Journal, 819, 84, publisher: The American Astronomical Society
Leconte, J., Forget, F., Charnay, B., Wordsworth, R., & Pottier, A. 2013, Nature, 504, 268, aDS Bibcode: 2013Natur.504..268L
Lefèvre, M., Turbet, M., & Pierrehumbert, R. 2021, The Astrophysical Journal, 913, 101, aDS Bibcode: 2021ApJ...913..101L
Lovis, C., Blind, N., Chazelas, B., et al. 2022, 12184, 121841Q, conference Name: Ground-based and Airborne Instrumentation for Astronomy IX Place: eprint: arXiv:2208.14838 ADS Bibcode: 2022SPIE12184E..1QL
Lustig-Yaeger, J., Meadows, V. S., & Lincowski, A. P. 2019, The Astronomical Journal, 158, 27
Marconi, A., Abreu, M., Adibekyan, V., et al. 2022, 12184, 1218424, conference Name: Ground-based and Airborne Instrumentation for Astronomy IX ADS Bibcode: 2022SPIE12184E..24M
Mlawer, E. J., Payne, V. H., Moncet, J.-L., et al. 2012, Philosophical Transactions of the Royal Society of London Series A, 370, 2520
Morley, C. V., Kreidberg, L., Rustamkulov, Z., Robinson, T., & Fortney, J. J. 2017, The Astrophysical Journal, 850, 121
Nakajima, S., Hayashi, Y.-Y., & Abe, Y. 1992, Journal of the Atmospheric Sciences, 49, 2256
Popp, M., Schmidt, H., & Marotzke, J. 2015, Journal of Atmospheric Sciences, 72, 452, aDS Bibcode: 2015JAtS...72..452P
Popp, M., Schmidt, H., & Marotzke, J. 2016, Nature Communications, 7, 10627, number: 1 Publisher: Nature Publishing Group
Ramirez, R. 2014, PhD thesis
Ramirez, R. M., Kopparapu, R. K., Lindner, V., & Kasting, J. F. 2014, Astrobiology, 14, 714
Rothman, L. S., Gordon, I. E., Babikov, Y., et al. 2013, Journal of Quantitative Spectroscopy and Radiative Transfer, 130, 4
Selsis, F., Leconte, J., Turbet, M., Chaverot, G., & Bolmont, É. 2023, Nature, 620, 287, number: 7973 Publisher: Nature Publishing Group
Simpson, G. C. 1929, Quarterly Journal of the Royal Meteorological Society, 55, 73
Turbet, M., Bolmont, E., Chaverot, G., et al. 2021, Nature, 598, 276, aDS Bibcode: 2021Natur.598..276T
Turbet, M., Bolmont, E., Ehrenreich, D., et al. 2020, Astronomy and Astrophysics, 638, A41
Turbet, M., Bolmont, E., Leconte, J., et al. 2018, Astronomy and Astrophysics, 612, A86
Turbet, M., Ehrenreich, D., Lovis, C., Bolmont, E., & Fauchez, T. 2019, Astronomy and Astrophysics, 628, A12
Turbet, M., Leconte, J., Selsis, F., et al. 2016, Astronomy and Astrophysics, 596, A112
Way, M. J., Del Genio, A. D., Kiang, N. Y., et al. 2016, Geophysical Research Letters, 43, 8376, aDS Bibcode: 2016GeoRL..43.8376W
Wolf, E. T. & Toon, O. B. 2014, Geophysical Research Letters, 41, 167
Wolf, E. T. & Toon, O. B. 2015, Journal of Geophysical Research (Atmospheres), 120, 5775
Wordsworth, R. D., Forget, F., Selsis, F., et al. 2011, The Astrophysical Journal, 733, L48, aDS Bibcode: 2011ApJ...733L..48W
Wunderlich, F., Godolt, M., Grenfell, J. L., et al. 2019, Astronomy & Astrophysics, 624, A49
Yang, J., Cowan, N. B., & Abbot, D. S. 2013, The Astrophysical Journal, 771, L45
Yang, J., Leconte, J., Wolf, E. T., et al. 2019, The Astrophysical Journal, 875, 46

Appendix A: Evolution of water vapor and clouds during the runaway greenhouse

As discussed in Sect. 3, the two phases of the runaway greenhouse strongly modify the distribution of water vapor as well as the cloud coverage. In this section, we provide additional information concerning these quantities. During the evaporation phase, the evolution of the average water vapor profile (left panel of Fig. A.1) shows a strong enrichment of the upper layers of the atmosphere in water vapor from 1×10^{-13} kg.kg^{-1} to 0.1 kg.kg^{-1}. This is coherent with the densification and the drift of the cloud coverage towards the stratosphere shown on the right panel of Fig. A.1 (this panel corresponds to the results presented in Fig. 3). This drift of the clouds is also discussed in Kopparapu et al. (2017).

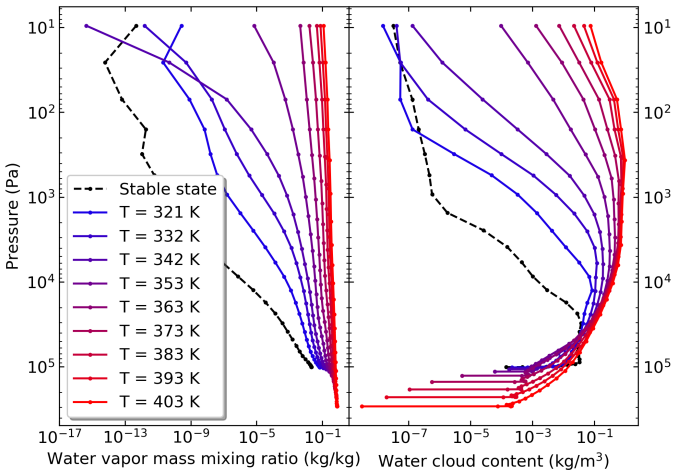


Fig. A.1: Evolution of the water vapor mass mixing ratio and of the mean vertical profile of the water cloud (liquid + ice) content during the evaporation phase. The simulation setup is the waterworld with 1 bar of nitrogen without CO_2 (W1). The profiles are averaged over one year. The dashed black line corresponds to the temperate stable state with the highest insolation (ISR=375 W.m^{-2}).

During the dry transition, as there is no longer any moisture source from the surface and the surface temperature rises, leading to a migration of the water vapor and of the water clouds toward the upper layers of the atmosphere. The left panel of Fig. A.2 shows the evolution of the water vapor mass mixing ratio profile. We see that the bottom part of the atmosphere become dryer (i.e., the water vapor content decreases) and the mass mixing ratio profile tends toward a constant value up to 1×10^3 Pa. This is the pressure above which the pressure temperature conditions are favorable to the formation of clouds (see left panel of Fig. A.2 and Fig. 8). At the same time, the bottom part of the cloud layer evaporate due to the increase of surface temperature. This is clearly visible on the right panel in Fig. A.2 (this panel corresponds to the results presented in Fig. 8).

The latitudinal distribution of the clouds coverage during the runaway greenhouse is presented in Fig. A.3 for global surface temperatures of 320 K, 340 K and 370 K (panels A, B, and C, respectively). The setup is the Earth without CO_2 (E1). While the usual cloud pattern we see on the Earth remains during the onset of the runaway greenhouse (panel A), it is modified when the water vapor content becomes sufficient to drift the cloud toward the upper atmosphere (panel B). When the stratospheric circulation described in Sect. 3.1.4 appears (panel C, which corresponds

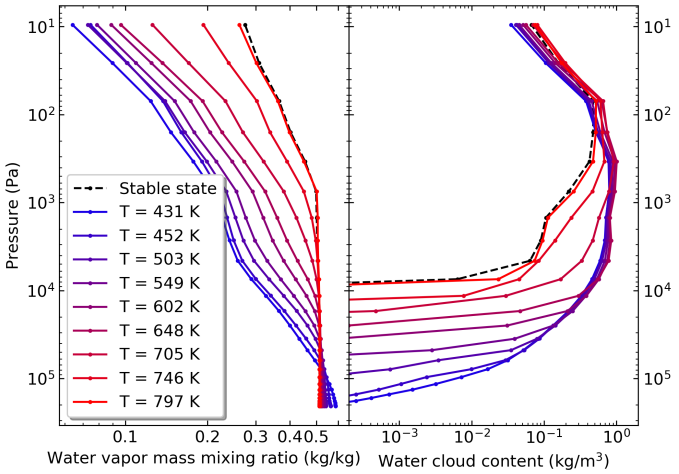


Fig. A.2: Evolution of the water vapor mass mixing ratio and of the mean vertical profile of the water cloud (liquid + ice) content during the dry transition phase. The simulation setup is the waterworld with 1 bar of nitrogen without CO_2 (W1) assuming 1 bar of water vapor. The dashed black line corresponds to the post-runaway stable state obtained after the runway greenhouse transition.

to a global surface temperature equal to 370 K), the cloud deck is located at the top of the atmosphere with a maximum density around the equator where the upward winds are the strongest. Cloud minima are around the tropics because of the downward winds (see Fig. 5 for the wind circulation).

Appendix B: Effect of the out-of-equilibrium evolution

By definition, the runaway greenhouse is an out-of-balance process making its analysis quite complex. In order to study the impact of the insolation on the evolution of the climate, we performed four different simulations with the W1 setup and various insolations, with all of them sharing the same initial conditions. Results are shown in Fig. B.1, where the left panel is the vertical water cloud profile, and the right panel is the temperature profile (both annually averaged). For every curve, the global surface temperature is equal to 370 K. For high insolations, the cloud coverage is less dense at equivalent global surface temperature (left panel) and where the temperature is lower in the upper layers (right panel). Due to highly imbalanced radiative conditions at high insolations, the evolution is so fast that there is a delay of the growth of the cloud coverage compared to the increase of global surface temperature. This affects the global evolution of the atmosphere by reducing the cooling effect of the clouds at a given surface condition. The enrichment in water vapor of the top part of the atmosphere is also delayed. However, as the cloud coverage is less dense at high insolations, the difference between cloud maxima at the equator and cloud minima around the tropics is less contrasted, smoothing the latitudinal distribution of both the water vapor and the temperature.

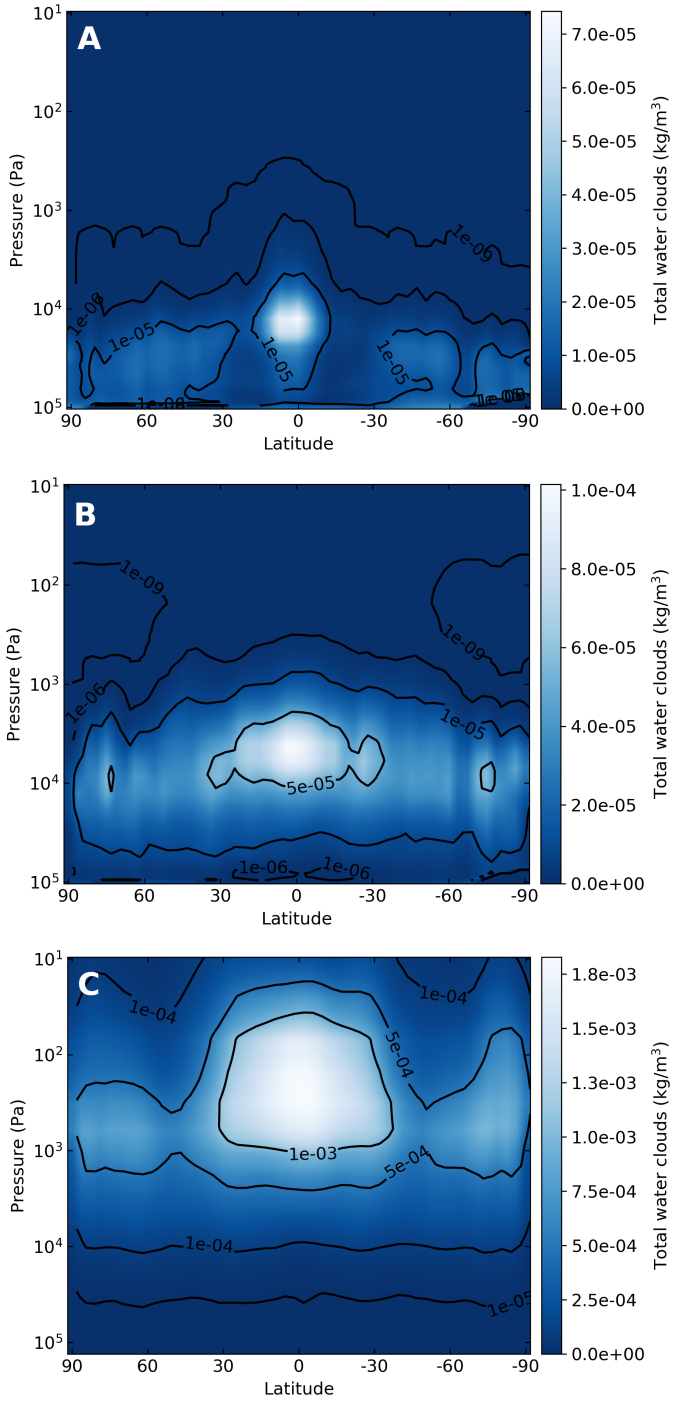


Fig. A.3: Evolution of the latitude-altitude map of the water cloud (liquid + ice) distribution during the evaporation phase. The simulation setup is the Earth with 1 bar of nitrogen without CO_2 (E1). The maps are averaged over two years. The A, B and C panels correspond to global surface temperatures of 320 K, 340 K, and 370 K, respectively.

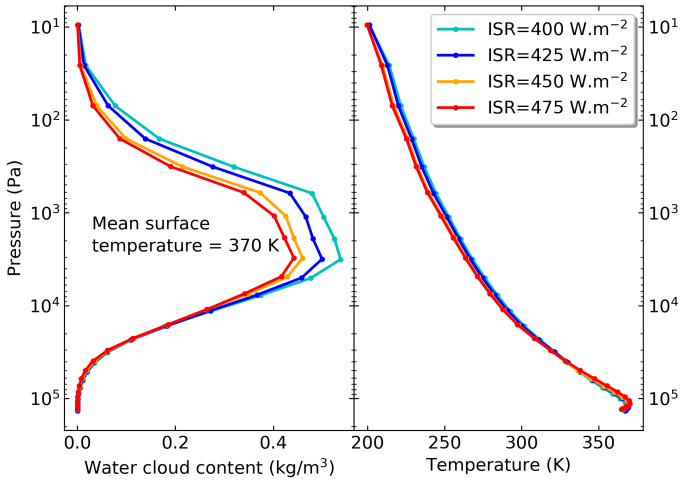


Fig. B.1: Cloud (liquid + ice) profiles and temperature profiles during the runaway greenhouse when the global surface temperature is equal to 370 K, from simulations assuming different insolations and a common initial condition. The simulation setup is the waterworld with 1 bar of nitrogen without CO_2 (W1). The profiles are averaged over one year.

5.3 Observability of temperate and post-runaway states

As discussed in Sect. 5.2, there is a strong difference of climate, cloud pattern and water content between temperate and post-runaway state. The question is to know if this dichotomy is observable using the transmitted light technique. The simulations presented in Chaverot et al. (2023) provide a unique opportunity to analyze the entire runaway transition from an observational point of view.

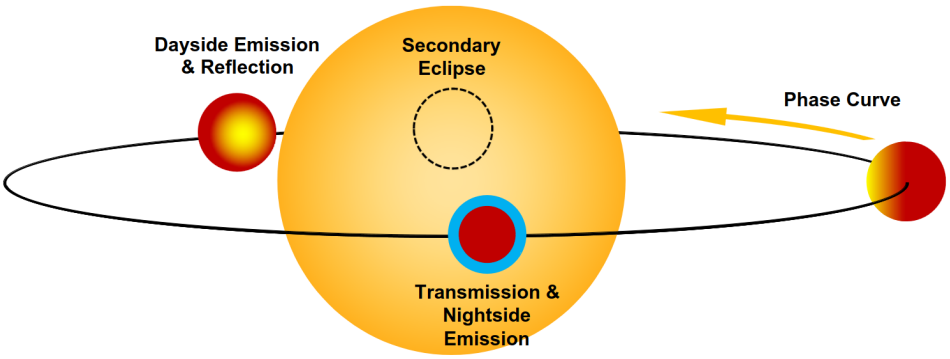


Figure 5.1: Schematic overview of the different star-planet configurations along the phase curve for which we can detect light from the planet. This light can be reflected by the atmosphere or emitted directly from the planet. Figure from Gao et al. (2021).

To do so, I used Pytmosph3R[1] (Caldas et al. 2019 ; Falco et al. 2022) to produce transmittance maps and transmission spectra at key steps along the runaway greenhouse transition. This open-source library uses GCM outputs to produce observables based on transmitted and emitted light. The corresponding planetary system configuration is presented in Fig. 5.1. I selected few key steps in the runaway greenhouse transition to make an overview of its impact on the observations (see Fig. 5.2):

A) a temperate stable state with a global surface temperature equal to 279 K,

B) the onset of the runaway greenhouse, that is the very first time steps for which the ocean starts to evaporate for a global surface temperature equal to 315 K,

C) a planet in runaway greenhouse with 2.6 bar of water vapor in the atmosphere that is corresponding to a global surface temperature equal to 405 K,

D) the middle of the dry transition assuming a dry surface and 1 bar of water vapor in the atmosphere with approximately 600 K of global surface temperature,

E) the post-runaway state obtained after the dry transition considering 1 bar of water vapor in the atmosphere and a global surface temperature of 820 K,

F) the post-runaway state obtained after the dry transition considering 1.5 bar of water vapor in the atmosphere and a global surface temperature of 880 K,

[1] `http://perso.astrophy.u-bordeaux.fr/~jleconte/pytmosph3r-doc/index.html`

G) a similar post-runaway state from Turbet et al. (2021), at higher insolation and considering 10 bar of water vapor with a global surface temperature of 988 K.

Here I assume an Earth size planet orbiting a Sun, with an atmosphere containing 1 bar of nitrogen and variable water vapor and clouds, both consistently computed as function of the temperature and of the global circulation (W1 setup in Chaverot et al. 2023). Transmittance maps are the visible size of a planet passing in front of a star at a given wavelength. The thicker is the atmosphere, the larger is the planet and the deeper is the planetary transit. By combining this information about the radius of the planet with a mass measurement done thanks to the radial velocity technique for example, it is possible to infer the density of the planet.

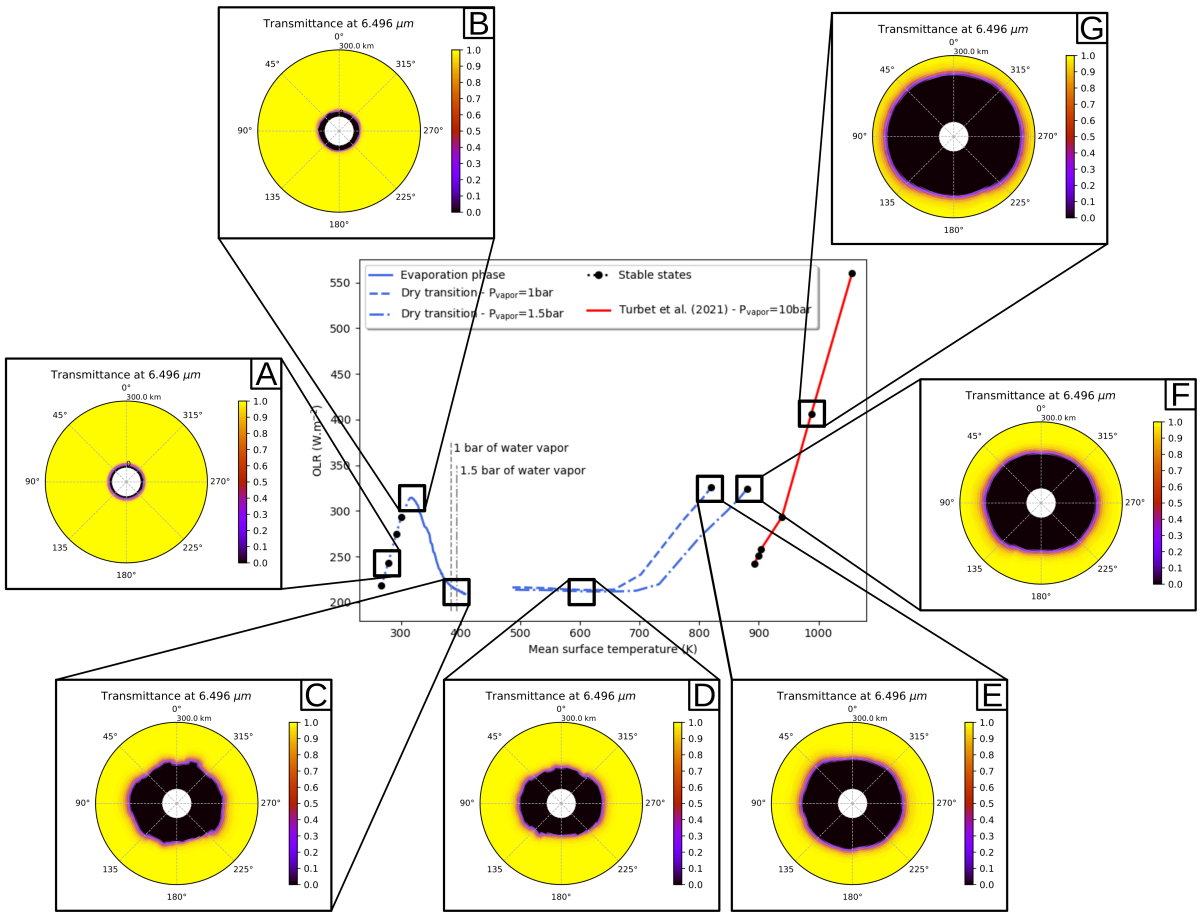


Figure 5.2: Transmittance maps corresponding to different key steps along the runaway greenhouse transition: A) Temperate state, B) onset of the runaway greenhouse, C) Runaway greenhouse ($P_{\text{vapor}} = 2.6$ bar), D) Dry transition ($P_{\text{vapor}} = 1$ bar), E) Post-runaway ($P_{\text{vapor}} = 1$ bar), F) Post-runaway ($P_{\text{vapor}} = 1.5$ bar), G) Post-runaway from Turbet et al. (2021) with 10 bar of vapor and 500 W.m^{-2} (1.46 times the Earth's insolation). In the transmittance maps, yellow parts mean no absorption from the atmosphere of the planet and black parts correspond to no transmitted flux. The OTR curve is from Chaverot et al. (2023). To make the figures clearer, the visible size of the core of the planet (white central circle) has been reduced by a factor 100.

The obtained maps are presented in Fig. 5.2 for the 6.496 μm absorption band of water. The yellow part of the map corresponds to zero opacity (no absorption from the atmosphere of the planet) while the black part is for an opacity equal to unity (no transmitted light). For temperate states (panel A), almost

all the water is condensed in the surface ocean thus the atmosphere is very thin like the one of the Earth. There is not much difference for the onset of the runaway greenhouse (panel B) because even when the runaway of the evaporation is triggered, the water vapor pressure is still low.

During the runaway greenhouse, when 2.6 bar of water are evaporated, the cloud coverage is denser than for temperate planets and located at the top of the atmosphere. Due to high water vapor content and because of the high albedo of the clouds, the planet looks more inflated (Turbet et al. 2019), as visible on panel C of Fig. 5.2 compared to panel A. We can see also inhomogeneities in the opacity maps on panel C created by the growing cloud coverage (e.g., May et al. 2021 ; Fauchez et al. 2022).

The runaway greenhouse radius inflation effect is even more visible for the post-runaway states (panels E, F and G). By evaporating more water vapor, the atmosphere is more extended and the observed radius is larger as visible on panels F (1.5 bar of vapor) and G (10 bar of vapor). The insolation is also higher for panel G (500 $W.m^{-2}$ compared to 400 $W.m^{-2}$ for panel F) increasing the global temperature and increasing even more the atmosphere. The rugby balloon shape of panel D is probably created by strong winds in the high part of the atmosphere (Fujii et al. 2017 ; Chaverot et al. 2023), induced by the largely unstable climate of the dry transition.

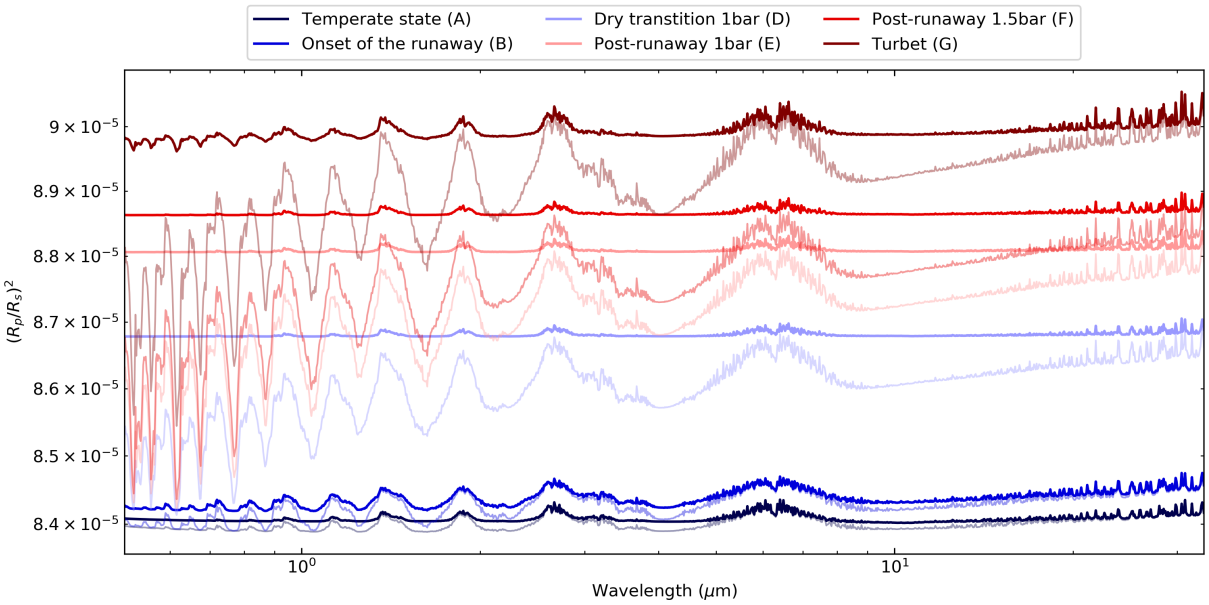


Figure 5.3: Transmission spectra corresponding to different key steps along the runaway greenhouse transition: A) Temperate state, B) onset of the runaway greenhouse, D) Dry transition ($P_{vapor} = 1$ bar), E) Post-runaway ($P_{vapor} = 1$ bar), F) Post-runaway ($P_{vapor} = 1.5$ bar), G) Post-runaway from Turbet et al. (2021) with 10 bar of vapor and 500 $W.m^{-2}$ (1.46 times the Earth's insolation). Case C representing the runaway greenhouse with 2.6 bar of vapor does not appear on this figure. Full lines are spectra accounting for the clouds, semi-transparent curves are for cloud free atmospheres.

To probe the composition of the atmosphere, transmission spectroscopy is currently the most useful technique. The idea is to analyze the light from the star passing through the atmosphere of the planet. By measuring it at multiple wavelengths, it is possible to detect absorption features from different molecules. Theoretical transmission spectra made using simulations from Chaverot et al. (2023) are presented in Fig. 5.3 for the key steps listed previously (see also Fig. 5.2). Full curves correspond

to cloudy simulations, while semi-transparent curves correspond to cloud-free simulations. As clearly visible on the figure, the main issue is due to the thick cloud deck at the top of the atmosphere, which flattens the transmission spectra. This is a well known problem (e.g., Fauchez et al. 2019) which is even more dramatic for runaway planets. Nevertheless, some very thin patterns remain thanks to the strong absorption of the water vapor largely present in the stratosphere. As the presented spectra are done assuming an Earth-like planet orbiting a Sun-like star, the transit depth difference between temperate and post-runaway planets is only about few tens of parts-per-million (Fig. 5.3). This is not reachable even with the last generation of instrument such as the James Webb Space Telescope (JWST) but rough estimations of this difference for a Trappist like system may lead to few hundreds parts-per-million (not shown). This is coherent with estimates provided in previous studies (Fauchez et al. 2019 ; Turbet et al. 2023).

Regarding how challenging it is to observe and characterize thin atmospheres around Earth-like planets, more complex techniques could be more appropriated. The very specific dichotomy of the cloud pattern between temperate and post-runaway state induces a very different day-to-night albedo. This could be measured by the next generation of ground based instruments which aim to combine direct imaging with reflected light, such as RISTRETTO@VLT (Lovis et al. 2022) or ANDES@E-ELT (Marconi et al. 2022).

5.4 Long-term evolution of post-runaway states

Post-runaway states are stable from a climate point of view, but they are not necessarily stables on geophysical time-scales. There are two main processes, happening at the surface and at the top of the atmosphere which could modify enough the atmospheric composition to destabilize the climate.

According to Chaverot et al. (2023) and Turbet et al. (2021) which are based on GCM simulations, for water vapor pressures lower than 10 bar, the global surface temperature of planets that have experienced a runaway greenhouse transition cannot exceed $\approx$ 1000 K. However, by using 1D climate models, Turbet et al. (2019) and Boukrouche et al. (2021) show that the relation between the global surface temperature and the available water reservoir is roughly logarithmic. They find a surface temperature equal to 1050 K for 10 bar of vapor, which is consistent with values obtained by Turbet et al. (2021) for a similar atmosphere. Therefore, Boukrouche et al. (2021) expect surface temperature about 1800 K after evaporating the Earth's surface water reservoir (270 bar equivalent). These high temperatures are potentially able to partially melt the surface of the planet, creating a post-runaway magma ocean. The melting surface temperature is a function of the composition of the crust, but assuming an Earth-like planet, the transition between the liquidus and the solidus are at 1400 K and 1950 K, respectively (Andrault et al. 2018). The threshold of 40% of melt required to have a fluid rheology is reached at 1620 K (Salvador & Samuel 2023). This surface melting of post-runaway states is discussed in Selsis et al. (2023) for water dominated atmosphere up to 270 bar. By using a 1D time-marching model, they found that the melting temperature for the Earth is reached for 7 times the current Earth insolation. These extremely high fluxes tend to make this scenario unreachable - at least for an Earth-twin - but it challenges previous studies and

pushes to explore more in detail extreme worlds with high irradiation.

From a global perspective, there is no consensus so far to know if post-runaway states are hot enough to melt the surface, and under which conditions. If such melting happens, this will reactivate the exchanges between the rocky interior and the atmosphere. More precisely, large water vapor quantities could be diluted in the magma ocean (e.g., Dorn & Lichtenberg 2021), thus affecting directly the radiative balance of the planet. If the vapor pressure decreases, the global temperature of the planet decreases as well, potentially leading to a solidification of the post-runaway magma ocean. Such theoretical scenario may "hide" a part of the water content in the rocky interior thanks to a temporary magma ocean phase not predicted by planetary formation models. Therefore, there is a real interest to study the long-term evolution of post-runaway states with direct and strong implications for our understanding of terrestrial planets in general as well as for the past history of Venus.

On the other side, as the highest part of post-runaway atmospheres is water rich, photo-dissociation is more efficient than for temperate planets because of higher X-UV fluxes. If water molecules break under the effect of the stellar radiation, they produce H_2 and O_2 (Luger & Barnes 2015). Then H_2 can escape into space thanks to various processes discussed in Sect. 1.5.2 (see Owen 2019 ; Gronoff et al. 2020). The consequence is that the vapor reservoir decreases, and the atmosphere is enriched in O_2. Under such modification of the atmospheric composition, the radiative balance is strongly affected modifying the equilibrium temperature of the planet. Such scenario of a transient post-runaway state, leading to a water-poor planet through evaporation processes, is one of the two main explanations of the difference of habitability between the Earth and Venus (e.g., Way et al. 2016 ; Way & Del Genio 2020).

These two processes, the potential secondary magma ocean created by a runaway greenhouse transition, and photo-dissociation combined with atmospheric escape, could drastically affect the stability of post-runaway states. By reducing the amount of water vapor in the atmosphere, they could break the climate feedback maintaining this post-runaway state, rising the question of reversibility of the runaway greenhouse. This possibility is discussed in the next section.

5.5 Reversibility of the runaway greenhouse

In Sect. 5.2, I present the transition from temperate to post-runaway states and I show that the climate of these two populations is very different. More precisely, the water vapor enrichment and the drift of the cloud coverage affect drastically the radiative balance of the atmosphere. While clouds tend to cool down the planet at temperate temperatures, they tend to warm it up for post-runaway states. Turbet et al. (2021) studied the potential reversibility of the runaway greenhouse, in other words, the conditions required to condense back the water into a surface ocean. The method is the following: assuming an atmosphere containing 10 bar of water vapor and 1 bar of nitrogen, they reduce step-by-step the insolation to find the tipping point at which the water will condense on the surface. By doing this, they find an insolation threshold much lower than the one required to trigger the runaway greenhouse. This is due to a cloud pattern specific to these hot water-rich atmospheres. For temperate states, a "cloud shield" is formed at the substellar point because of an intense evaporation induced by high temperatures

(Yang et al. 2013 ; Way et al. 2016). When the tipping point of the runaway greenhouse is reached, the continuous evaporation enriches the atmosphere in water vapor (Chaverot et al. 2022), inducing a migration of the cloud coverage toward the upper layers of the atmosphere, where they accumulate on the night side of the planet. When a post-runaway state is reached, the day-side becomes cloud-free, as shown by Turbet et al. (2021). These two different cloud patterns are presented in Fig. 5.4. While the clouds of a temperate planet increase its albedo (panel A), the day-to-night distribution of the clouds for a post-runaway state (panel B) acts like a cover absorbing the thermal emission from the planet, thus preventing the cooling of the planet.

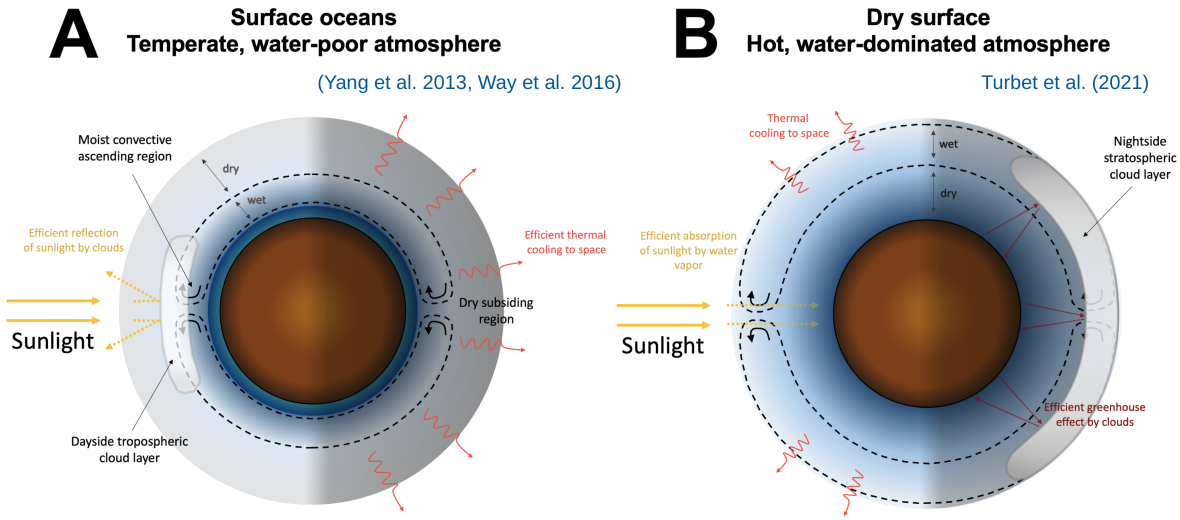


Figure 5.4: Scheme of the cloud distribution around a temperate planet with a surface ocean (*panel A*) and around a steam planet in a post-runaway state (*panel B*). This figure is adapted from Turbet et al. (2021).

As the insolation required to condense back the ocean is lower than the one required to trigger the runway greenhouse, a hysteresis cycle appears. This hysteresis cycle is concomitant with the coexistence of 3 stables states: snowball (Shields et al. 2014), temperate (Leconte et al. 2013) and steam atmosphere (Turbet et al. 2021). While the snowball/temperate bi-stability of the Earth was well known and studied (e.g., Shields et al. 2014 ; Hoffman et al. 2017), no previous works highlighted the specificity of this steam steady state. An important point is that these 3 states exist for the current Earth insolation. This concept of multistability is discussed in detail in Sect. 6.1 (see also Fig. 6.2). Moreover, Turbet et al. (2021) shows that condensation of the Earth ocean was possible thanks to the faint young Sun, highlighting the question of habitability in a new light. Additionally, they show that in their configuration, even with the faint young Sun oceans were never able to condense at the surface of Venus (Fig. 6.2). This alternative scenario challenges the possibility of an ocean on early Venus (Way et al. 2016 ; Way & Del Genio 2020). This makes the future space missions toward Venus, Davinci+, Veritas and EnVision, even more relevant and necessary.

This work and the highlighting of a third steady state for the Earth motivated a reflection, in the context of the CIDER summer school, on the concept of climate multistability of terrestrial planets and led to the article presented in Chapter 6.

Part III

Climate multistability of small terrestrial planets

Chapter 6

Resilience of the snowball state

Contents

6.1 Motivation: The concept of climate multistability 106

6.2 Resilience of the snowball Earth 109

6.3 Implications for exoplanets 127

6.3.1 S-tipping: an inefficient way to deglaciate a planet 127

6.3.2 Toward a more complex definition of the habitable zone 127

6.1 Motivation: The concept of climate multistability

As introduced in Sect. 5.5, there are multiple steady states for Earth-like planets. For a same external forcing (i.e., insolation), a planet can have multiple climate states. A variety of models (from 1-D EBMs to 3-D GCMs) show that there could be three climate regimes existing for the Earth:

- **Snowball**: that is a planet completely covered by ice and snow (Shields et al. 2014 ; Hoffman et al. 2017)
- **Temperate**: that is a planet hosting liquid water on the surface (e.g., Leconte et al. 2013 ; Wolf & Toon 2014, 2015 ; Kopparapu et al. 2016)
- **Steam**: that is a hot planet with a water-rich atmosphere without any liquid surface ocean (Turbet et al. 2021)

As shown by Brunetti et al. (2019), the temperate regime can be made of different steady states induced by the feedback between the ocean and the atmosphere. More precisely, by using the MITgcm in a coupled configuration which includes atmosphere, sea ice and dynamical ocean, they find 4 different steady states in the temperate climate regime (Fig. 6.1). The waterbelt is the coldest and is made of extremely extended polar caps allowing a liquid water ring along the equator. In Brunetti et al. (2019), the albedo of the clouds is prescribed, and they show that the hot state disappears when they assume that it increases near the poles, leaving only three steady states in the temperate regime. Ongoing works at the observatory of Geneva tend to determine how many stable states can exist in the temperate regime for the Earth by using the Generic-PCM (which includes a consistent calculation of the cloud coverage) coupled with a two-layers ocean model including heat and ice transport. These stable states are often found by varying the initial temperature of a planet (see Brunetti et al. 2019), but varying other parameters can also lead to different stable states. For instance, the states will be different for different rotations. Indeed, tidally locked planets can experiment a configuration in which the night-side is completely frozen but where a liquid ocean sustains on the day-side (e.g., Yang et al. 2020).

Climate multistability is an entire field by itself for planetary and exoplanetary sciences. In this chapter, we focus only on the 3 main regimes described above and separating habitable and uninhabitable environments. As introduced in Sect. 5.5, the multistability of Earth-like planets can be discussed in terms of hysteresis cycles. The two hysteresis cycles separating the snowball, temperate and steam regimes are presented in Fig. 6.2. The bi-stability between snowball and temperate states (white and blue dots, respectively, in Fig. 6.2) exists through the large albedo difference between liquid water and ice (0.1 and 0.6, respectively, according to Pierrehumbert 2010). Consequently, liquid water absorbs more energy from the incoming stellar radiation, while ice reflects the majority of the flux (e.g., Shields et al. 2014). A large variation in insolation is thus required to glaciate or deglaciate the planet. On the other side, the hysteresis cycle between steam and temperate (red and blue dots respectively in Fig. 6.2) exists for both the case of the Earth and Venus thanks to the specific cloud pattern described in Sect. 5.5. As shown by Turbet et al. (2021), the high altitude cloud deck on the night side of steam planet prevents its cooling by reducing the albedo of the day-side and increasing the greenhouse effect on the night-side.

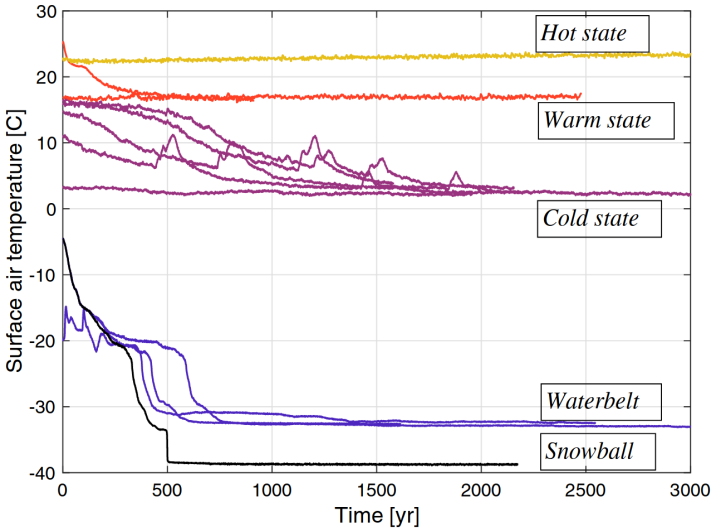


Figure 6.1: Temporal evolution of the global surface temperature for different initial temperatures. The interactions between the ocean and the atmosphere allow for the convergence on different states named: hot, warm, cold, waterbelt and snowball. Figure from Brunetti et al. (2019).

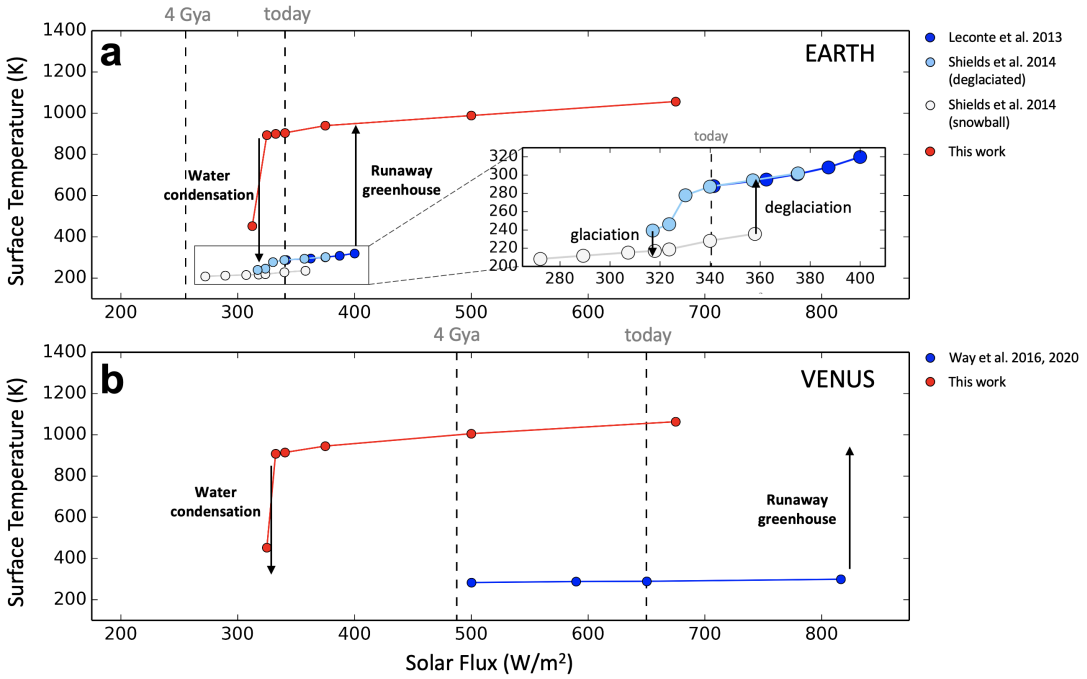


Figure 6.2: Global surface temperature as a function of the insolation reaching the planet. Panel A is for the Earth while panel B is for Venus. Insolation thresholds allowing for a switch from a state to another are indicated by black arrows. Figure from Turbet et al. (2021).

These hysteresis cycles presented in Fig. 6.2 require a large modification of the insolation to go from a state to another, which is only possible over stellar evolution timescales. This is named *bifurcation-induced tipping* (B-tipping, see Fig. 6.3 and Brunetti & Ragon 2023). The question is to know if stochastic events are able to break these feedbacks and tip the climate from a stable state to another without any

strong modification of the insolation, in other words without following the hysteresis. This is a *shock-induced tipping* (S-tipping, see Fig. 6.3 and Brunetti & Ragon 2023). An interesting candidate is a large impactor. Indeed, such dramatic event can erode a significant part of the atmosphere, modifying drastically the atmospheric composition (Schlichting et al. 2015 ; Biersteker & Schlichting 2019 ; Kegerreis et al. 2020 ; Biersteker & Schlichting 2021). If the water vapor quantity is sufficiently reduced, the new stable state could be different from the initial climate of the planet, questioning the survivability of steam steady states for example. For smaller impacts, surface volatiles and aerosols pushed in the stratosphere could also strongly affect the radiative balance of the planet, thus the stability of the climate. Large impacts could also dramatically affect the snowball state. The addition of heat and the melting of the ice crust could also tip the climate from snowball to temperate by breaking the ice-albedo feedback. For this specific transition, volcanoes could be a great candidate as well. One major effect of volcanoes is to release aerosols in the stratosphere which increase the Bond albedo of the planet, thus decreasing the temperature of the planet (e.g., Macdonald & Wordsworth 2017). However, by depositing ash and dust on the ice, they could modify the albedo of the ice, thus potentially modifying the radiative equilibrium (e.g., Abbot & Pierrehumbert 2010).

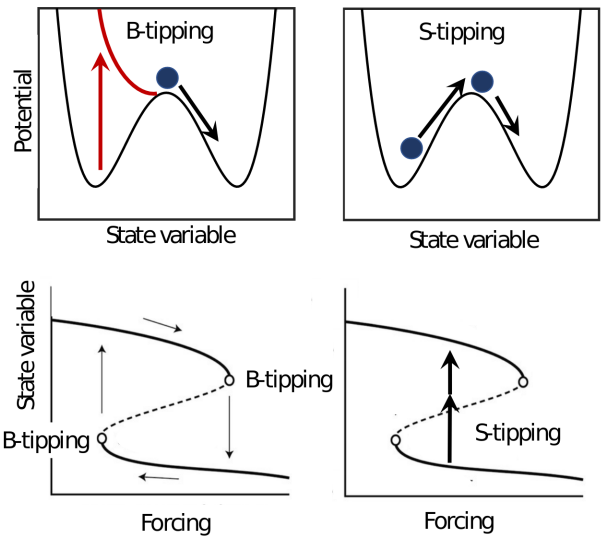


Figure 6.3: Scheme illustrating B-tipping (*left column*) and S-tipping (*right column*) in terms of potential (top row) and hysteresis cycle (bottom row). This figure is adapted from Brunetti & Ragon (2023).

Among all these possible transitions and tipping, we chose in Chaverot et al. (in prep.) (see Sect. 6.2) to focus on the tipping from snowball to temperate. This is motivated by the fact that the Earth lived at least two short snowball events during the Neoprotozoic era (1000-538.8 Ma). We test the possibility of a S-tipping induced by 1) a large impact that adds heat in the atmosphere and modifies the surface albedo by deposing ejecta on the ice, 2) a supervolcanic eruption that modifies the surface albedo by deposing ash on the ice.

6.2 Resilience of the snowball Earth

The following article is the draft version of the work referenced in the manuscript as Chaverot et al. (in prep.)

Resilience of Snowball Earth to stochastic events

Guillaume Chaverot[1,2], Andrea Zorzi[3], Xuesong Ding[4*], Jonathan Itcovitz[5], Bowen Fan[6], Siddharth Bhatnagar[1,2], Aoshuang Ji[7], Tushar Mittal[7]

[1]Observatoire Astronomique de l'Université de Genève, Chemin Pegasi 51, CH-1290 Versoix, Switzerland
[2]Life in the Universe Center, Geneva, Switzerland
[3]Department of Earth and Planetary Sciences, Stanford University, Stanford CA, US
[4]Department of Earth, Planetary, and Space Sciences, University of California, Los Angeles, CA, US
[5]Institute of Astronomy, University of Cambridge, Madingley Road, Cambridge, CB3 0HA, UK
[6]Department of the Geophysical Sciences, University of Chicago, Chicago, IL, USA
[7]Department of Geosciences, Pennsylvania State University, University Park, PA, US

*Now at Bureau of Economic Geology, The University of Texas at Austin, Austin, TX, US

Corresponding author: Guillaume Chaverot, guillaume.chaverot@unige.ch

Abstract

Earth went through at least two periods of global glaciation (i.e., "Snowball Earth" states) during the Neoproterozoic, the shortest of which (the Marinoan) may not have lasted sufficiently long for their terminations to be explained by the volcanic build-up of greenhouse gases in the atmosphere. Large asteroid impacts and supervolanic eruptions have been suggested as stochastic geophysical events that could cause sudden ends to global glaciation via a runaway melting process. Here, we employ an energy balance climate model to simulate the evolution of Snowball Earth's surface temperature after such stochastic events, using impact simulations and estimates of ejecta/ash from both types of events to inform initial conditions. We find that surface albedo, A, is the dominant factor, with changes in A generated by both the initial gap produced in the ice sheet and the covering of ice by far-spreading impact ejecta and volcanic ash. We find that for likely Snowball conditions, impactor diameters of $d \sim 100\,\mathrm{km}$ and the supervolcanic Toba eruption (74 kyr ago), both of which are overestimates of likely event parameters for the Neoproterozoic, are insufficient to terminate a Snowball state. We thus suggest that Earth's Snowball states would have been resilient to termination by stochastic events, and that other mechanisms should be explored to explain Earth's shortest global glaciations.

Plain Language Summary

The terminations of Earth's longest periods of global glaciation are commonly understood to have occurred due to the build-up of greenhouse gases in the atmosphere from volcanism. However, the sudden ends of Earth's shorter global glaciation periods likely cannot be explained by the same mechanisms. Large asteroid impacts and supervolcanic eruptions have been suggested as geophysical phenomena that could cause abrupt ends to global glaciation periods. Here, we model the evolution of the planet's surface temperature in the aftermath of such events. The impacts and eruptions open up gaps in the global ice sheet, and also partially cover the ice in far-spreading dust and ash, both of which increase the amount of solar radiation that is absorbed by the planet when compared to the highly reflective surface of ice and snow. Greater absorption of radiation leads to higher surface temperatures, leading to a larger gap in the ice through melting, generating a feedback loop that can melt the entire planet surface. However, we find that the scales of impact or eruption required to produce global melting are too great to have likely occurred on Earth. Other mechanisms must, therefore, be explored to explain Earth's short glaciation periods.

1 Introduction

The Snowball Earth hypothesis (Kirschvink, 1992; Hoffman et al., 1998) proposes global surface coverage of Earth in a thick ice layer. In contrast, the most recent glacial episode, the Last Glacial Period, witnessed only partial ice coverage extending down from the poles but not all the way to equatorial regions (e.g., Batchelor et al., 2019). Snowball events occurred on at least two occasions during the Neoproterozoic era (1000-538.8 Ma), particularly during the Cryogenian period (720-635 Ma), with other potential Snowball states also suggested (e.g., Chumakov, 2009). Evidence for Snowball Earth's existence comes in many forms, including paleomagnetic data in Australia (Harland, 1964; Hambrey & Harland, 1981), carbonate rock within or above the deposits (Kennedy, 1996), and extreme carbon isotope excursions (Knoll et al., 1986). Geologic measurements have been complemented by modeling efforts (e.g., Caldeira & Kasting, 1992) to understand both the origins and demise of the snowball state.

Under Earth's current insolation, a Snowball state is one of three possible stable climate regimes, along with a temperate state and a hot steam atmosphere state (Shields et al., 2014; Turbet et al., 2021). Different climates can exist under each regime according to climate modeling (e.g., Brunetti et al., 2019). The Snowball state is stable against moderate variations in insolation through the high albedo of ice, which acts to prevent increases in

global temperature (Shields et al., 2014; Hoffman et al., 2017). This creates a bi-stability between the temperate Earth and the snowball Earth through the difference of albedo between ice and liquid water (Ghil, 1994). It is, therefore, impossible to deglaciate without external forcing. One such external forcing that is commonly invoked is the build-up of atmospheric CO_2. Emissions from continental volcanism, coupled with the absence of CO_2 sinks of Earth's temperate-state carbon cycle (e.g., silicate weathering being prevented by the covering of continental landmasses by ice) leads to a strong greenhouse effect that warms the planet, triggering the Snowball termination (Kirschvink, 1992; Caldeira & Kasting, 1992). However, the time required to accumulate sufficient CO_2 to trigger melting (4–30 Myr, Hoffman et al., 1998) is too long to account for the short Marinoan glaciation (Rooney et al., 2015). Suggested alternatives include impact events (Kring, 2003) and massive volcanic eruptions (Lan et al., 2022), hereafter referred to as stochastic events due to their somewhat random and unpredictable nature. However, quantitative estimates on the long-term climate after stochastic events remains relatively unexplored.

Impacts of large asteroids can generate global climatic effects (e.g., Brugger et al., 2017; Pierazzo et al., 1998; Artemieva et al., 2017). Simulations of such impacts have estimated the masses of water vapor injected into the atmosphere by these events, but the climatic effects of this have not been investigated (Koeberl & Ivanov, 2019) or have been inconclusive due to uncertainties on the radiative effect of water (Erickson et al., 2020). Nonetheless, the temporal coincidence between the youngest Paleoproterozoic glacial deposits and the Yarrabubba event has sparked interest in the role of impacts in (long-term) climate evolution (Erickson et al., 2020). Further, given their large kinetic energy, impacts can melt the ice table covering the planet surface and vaporize rocks from the underlying crust. Therefore, among other effects, impacts can (1) increase the planet's surface temperature by hundreds of degrees for large distances from the impact site, and (2) deposit ejecta material onto the icy surface far from the impact site, thus affecting the planet's surface albedo.

Supervolcanic eruptions are also suggested candidates to escape the Snowball Earth state. Such events are defined by either their magnitude ($M \geq 8$, proportional to the erupted mass) or their ejecta volume ($1,000$ km^3, de Silva & Self, 2022), and are thousands of times larger than typical volcanic eruptions (e.g., Hansen et al., 1978). The largest known super-eruption is Toba ($M = 9.1$), which is recorded in the 74,000-year-old Youngest Toba Tuff (YTT, Rose & Chesner, 1990). The ash ejected by the event covered ~ 40 million km^2 of Earth's surface at a depth greater than 5 mm (Costa et al., 2014). Toba-like super-eruptions are expected to happen $1 - 2$ times per million years (Mason et al., 2004). Supervolcanic eruptions have significant global climate effects (e.g., Hansen et al., 1978). First, large volumes of volcanic gases are injected into the atmosphere, such as (1) CO_2, which acts as a classical greenhouse gas, (2) SO_2, which acts as a solar-reflecting coolant, and (3) H_2O, which can act as a greenhouse gas, but can also form solar-reflecting cloud layers. Second, eruptions deposit ash and dust on the icy surface, reducing the albedo in comparison to clean ice and hence increasing the amount of sunlight absorbed by the planet's surface. Although often cited as a possible cause of the onset of global glaciation (Macdonald & Wordsworth, 2017a), there is currently no discovered evidence that any supervolcanic eruption has caused termination of a Snowball state, leaving the question open.

In this study, we quantify the heating effects of stochastic events on a globally glaciated Earth, testing the potential of such events to generate a runaway melting process that would lead to the termination of the Snowball state. Through impact simulations and ash-/ejecta-dispersal modeling (Sects 2.2 and 2.3), we quantify the changes in albedo and surface temperature produced by such events. Using a 1-D Energy Balance Model (EBM; Sect. 2.1), we then analyze the radiative perturbation caused by such temperature and albedo changes, following the evolution of the post-event surface temperature profile and ice coverage. By varying the scale of our stochastic events (e.g., impactor size, magnitude of supervolcanic eruption), we assess the capabilities of such events to trigger global deglaciation, discussing the likelihood of occurrence of our event scales during the Neoproterozoic (Sect. 4).

2 Method

2.1 Climate modeling

Budyko (1969) and Sellers (1969)'s independent seminal works on the Earth's climate established the usefulness and robustness of 1-D EBMs. In an EBM, the prognostic surface temperature is zonally averaged (along a latitude band), thus leaving only the meridional dimension. Still, this is a remarkably good first-order estimate to solving the climate evolution of a planet (North & Coakley Jr, 1979; Spiegel et al., 2008; Dressing et al., 2010). The 1-D nature of the planet is further exemplified by accounting for transport in the atmosphere, parameterized here as temperature-driven diffusion. The bi-stability between the temperate Earth and the snowball Earth is a radiative balance process existing through the difference of albedo between ice and liquid water (Ghil, 1994). Therefore, as the main equation defining an EBM solves the radiative balance of an atmosphere, EBMs are a good model candidate to study the question of the snowball deglaciation. In this work, we use an EBM based on the formulation proposed by Williams et al. (1998); Spiegel et al. (2008) and Dressing et al. (2010), and adapt it to model the climatic aftermath of a stochastic event. As 1-D EBMs are not longitudinally defined, we developed a method to account for spatially-located events, correcting input calculations from impact simulations and estimations of ash-dispersion from eruptions (see Appendix B for more details on the parameterizations used).

For our simulations, we assume a planet following a circular orbit (at 1 AU) around a Sun-like star, with a modern Earth solar constant. We fix the planetary obliquity to 0° and also assume zero eccentricity. Land and oceans are uniformly distributed across the planet such that each latitude cell consists of a 70:30 ocean-to-land ratio (like modern Earth). Heat capacity and albedo parameterizations are taken from Williams and Kasting (1997) and Spiegel et al. (2008). To constrain our study within a simple framework, we neglect the effects of aerosols and ice-melting latent heat: potential caveats from our assumptions are discussed in Sect. 4. Nonetheless, we account for variable relative humidity (RH), cloud forcing (Abbot, 2014) and the potential addition of CO_2 released by volcanic eruptions. We also evaluate the influence of the location of the stochastic event by modeling eruptions and impacts at the equator and at 40° N. The effect of impacts is modeled by modifying the initial temperature distribution as per the hydrocode simulations (see Sect. 2.2). Eruptions do not modify the temperature distribution, but affect the surface albedo due to ash-dispersion.

2.2 Impact simulations

We use the iSALE shock physics code to model asteroidal impacts on a Snowball Earth state and produce 1-D thermal profiles for the surface of the planet in the aftermath of the impact. We additionally analyze the spread of the impact ejecta curtain in order to estimate the reduction in surface albedo associated with covering the ice with ejecta material.

The iSALE shock physics code (Wünnemann et al., 2008) is an extension of the SALE hydrocode (Amsden et al., 1980). Modifications to the original SALE code include an elasto-plastic constitutive model, fragmentation models, various equations of state, and multiple materials (Melosh et al., 1992; Ivanov et al., 1997). More recent improvements include a modified strength model (Collins et al., 2004), a porosity-compaction model (Wünnemann et al., 2006; Collins et al., 2011), and a dilatancy model (Collins, 2014). The thermodynamic behavior of each material is described by equations of state generated by the ANalytic Equation Of State program (ANEOS; Thompson & Lauson, 1974). The detailed properties of each material and the relevant equations of state are detailed in Table A1.

We initialize simulations based on estimates of Snowball Earth's surface state (Hoffman et al., 1998). A 5 km thick global ice sheet thus sits at the surface of the target planet, with a rocky crust, mantle, and iron core sitting below. A surface temperature of 227 K is

prescribed for the pre-impact temperature profile, matching the steady-state temperature found by the EBM in the absence of a stochastic climate forcing event.

Our impactors are sufficiently large that the curvature of the Earth is important. Simulations remain 2-dimensional. Impactors consist entirely of dunite, matching closely the thermodynamic behaviors of the chondritic material that are expected from such impactors (Benz et al., 1989). Impactors vary in diameter between 40 km and 100 km to represent various scenarios. The impact velocity is constant for all impacts at 1.5× mutual escape velocity ($v_{\rm esc}$), representing the most likely impact velocity (Chyba, 1991). We consider only head-on collisions, an approximation accounting for the small mass of the impactors relative to the Earth.

Simulations are ran until the motion in the mantle region excavated by the impact settles out (i.e., the mantle has rebounded and subsequent oscillatory motions have terminated). A 1-D surface temperature profile is then extracted. Due to the difference in resolution between the impact simulations and the EBM, we use cell-centered averaging to extract a temperature profile to initialize the EBM. An albedo profile is similarly extracted, accounting for: 1) the exposure of crustal material after melting of the ice layer, and, 2) the deposition of material from the impact ejecta curtain on top the ice table outside of the impact crater. These are assessed using the fractions of each material that constitute the exposed surface cells in iSALE. The albedo for ejecta-covered areas is set to 0.2, similar to that of cryoconite (Hotaling et al., 2021); then, a step-like transition is assumed between dark ejecta and ice albedo (0.7). The area is converted into latitudinal coverage and input in the EBM.

2.3 Supervolcanic eruptions

We use the formalism from Pyle (1989) to model the variation of volcanic ash thickness (d) with distance from the eruption center. The exponential relationship between d and the isopach area $A_{\rm iso}$ is:

$$d = d_0 e^{-k A_{\rm iso}^{1/2}} \tag{1}$$

where d_0 is the ash maximum thickness (units of m) and k is the rate of ash thinning with isopach area, also in m (Pyle, 1989). We find k using (d, $A_{\rm iso}$) values of volcanic ash fall from Toba, reconstructed through several tens of thickness measurements of the YTT tephra deposit (Costa et al., 2014) and digitized with QGIS.

The ash deposition region is divided into fully- ($d > 0.014$ mm) and partially-covered ($0.002 < d < 0.014$ mm), the latter known as dusty ice (Le Hir et al., 2010). Assuming an elliptical geometry for ash-dispersal, the ash deposition area is converted in latitude and longitude. For Toba, the fully-covered area extends for ±43° in latitude and ±86° in longitude; the dusty ice area spans a wider range between ±50° in latitude and ±100° in longitude. At visible wavelengths, dust has an albedo of 0.18 (Warren, 1982): assuming an ice albedo of 0.7, we let the albedo for dusty ice change linearly between ice and dust albedos (Fig. B2). Those values are consistent with the mean albedo for bare ice measurements (Warren et al., 2002).

3 Results

Figure 1 shows the temporal evolution of the global surface temperature for the supervolcanic eruptions (left column) and for the large impacts (right column). Full lines are the average temperature and dashed lines are the minimum and maximum temperatures. The water melting temperature is indicated by the gray dotted line.

We modeled the effect of a Toba-like eruption (left column in Fig. 1) assuming the Earth's atmosphere with variable water, 1 bar of nitrogen and 400 ppm of CO_2, happening at the equator (top panel) and at 40° N (third panel). We ran also two other simulations including the greenhouse feedback of the clouds (set to 14 W m^{-2}, Abbot, 2014) and assuming

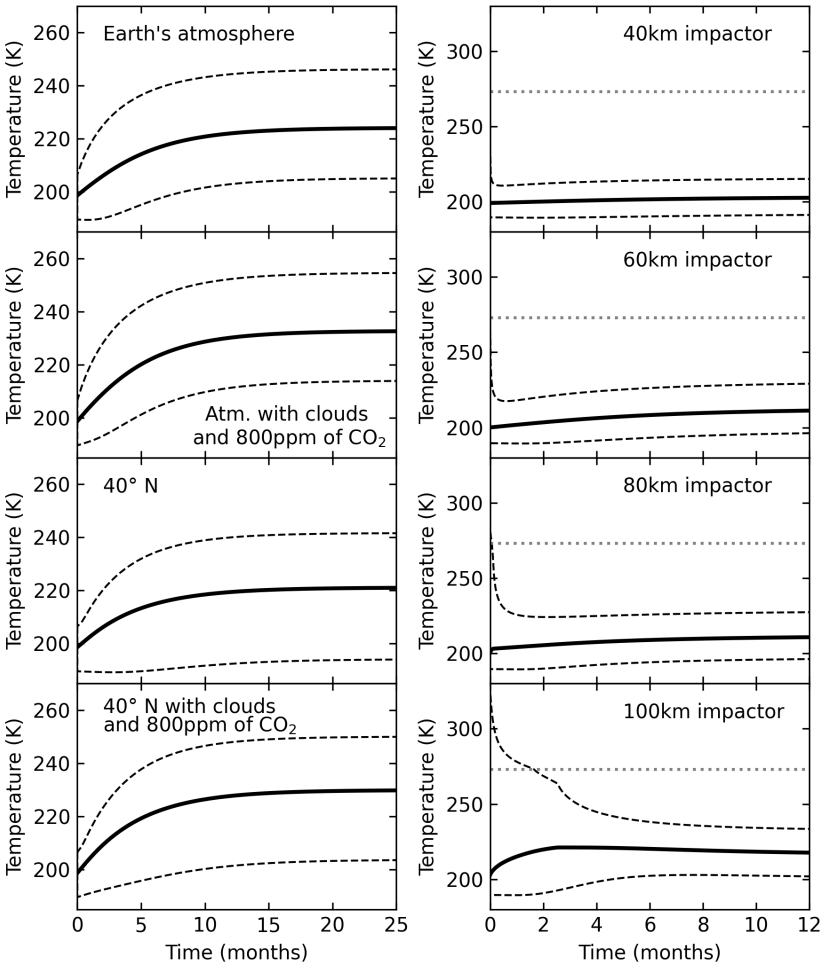


Figure 1. Temporal evolution of the surface temperature after a Toba-like eruption (left column) or after a large impact (right column), where each row correspond to a different setup. The full lines are the average temperature and the dotted lines are the minimum and maximum temperatures.

800 ppm of CO_2, for both volcano locations (second and last panels of Fig. 1, respectively). We show that a Toba-like eruption event does not change the ice albedo in a large enough area to escape the snowball state. In the best-case scenario we model (i.e., accounting for the warming effect of the clouds and with 800 ppm of CO_2), the maximum equatorial temperature after relaxation is 255 K. In addition, we ran different setups to account for other effects: the addition of humidity due to volcanic moisture, lower diffusion coefficient value, different ice albedo value and smaller distance to the Sun (see Appendix B). None of these additional processes lead to deglaciation.

The right column of Fig. 1 shows the temporal evolution of the surface temperature for impactor sizes of 40 km (top panel), 60 km (second panel), 80 km (third panel) and 100 km (last panel). Since we use a 1-D EBM with no longitudinal resolution, the initial temperature at the impact site results from the average of the high-temperature impact site longitudes and the low-temperature unperturbed longitudes: we refer the reader to Appendix B for more details. As a result, the initial temperature in the EBM ($200 - 350$ K) is lower than the temperature at the impact site (1000's of K). This approach tends to slightly overestimate ($< 1\%$) the surface albedo, though facilitating deglaciation. We find

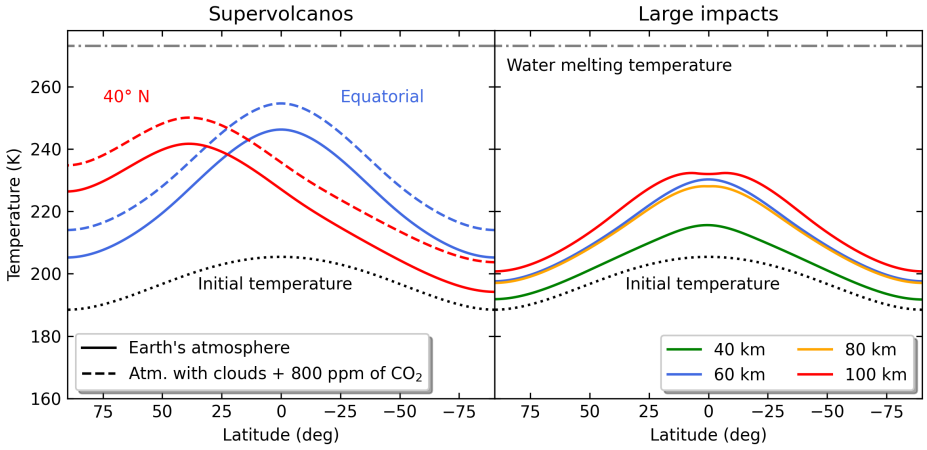


Figure 2. Latitudinal temperature profile after a Toba-like eruption (left panel) or a large impact (right panel). On the left panel, blue and red curves are the temperatures profiles for a super-eruption happening at the equator and at 40° N, respectively. Dashed curves include the cloud forcing and 800ppm of CO_2 in the atmosphere. On the right panel, colored lines correspond to the different impactor sizes (green for 40 km, blue for 60 km, orange for 60 km, and red for 100 km). For both panels, the dotted curve and the dash-dotted curve correspond to the initial temperature profile, and to the water melting temperature, respectively.

that for the biggest impact event considered (100 km), a transient water belt is formed and lasts for around two months. During this time, the surface temperature of the planet decreases due to heat diffusion and thermal emission. This strongly affects the radiative balance of the atmosphere. Once the freezing point is reached, the change of albedo induces a rapid runaway glaciation of the transient waterbelt (right panel in Fig. 1). Evidently, even the 100 km impactor cannot melt a surface large enough to break the ice albedo feedback, which prevents the deglaciation of the planet. Additional heat is distributed in the proximity of the impact site, such that the resulting strong radiative imbalance quickly reduces the surface temperature. Larger impactors will melt more ice and form a bigger impact site, but will also melt part of the planet crust: this is out of the scope of this work, as we are looking for global deglaciation while maintaining a solid surface.

Figure 2 shows the latitudinal temperature profile after a super-volcanic eruption (left panel) and after a large impact (right column). The simulations of the Toba like eruption located at the equator and at 40° N are represented by the solid blue and red curves, respectively. Dashed lines correspond to simulations accounting for the greenhouse effect of the clouds and including 800 ppm of CO_2. The feedback of the clouds and the addition of CO_2 due to the eruption induced a global temperature 10 K hotter, which is not sufficient to deglaciate, even partially, the planet. We note that the results shown here do not account for the ash injected into the stratosphere: its effect is to reduce the bond albedo of the planet, inducing global cooling (e.g., Abbot & Pierrehumbert, 2010). We refer the reader to Sect. 4 for other processes we have neglected and their effect on our conclusions.

The right panel of Fig. 2 shows the latitudinal temperature profile after different large impacts. We find that impactors with a radius ≤ 100 km are not able to initiate deglaciation. Bigger impactors spread ejecta over a larger area, modifying the ice albedo for a significant portion of the planet. We assumed that ejecta reach distances up to $5\times$ the crater radius (e.g., Richardson et al., 2005), corresponding to a distance of 2250 km, 3850 km, 3900 km and 5000 km from the impact site for the 40 km, 60 km, 80 km and 100 km impactors,

respectively. The differing sizes of the ejecta dispersal lead to different global mean surface albedos. Consequently, the four simulations do not converge to the same global temperature: for the 100 km impactor, the final maximum temperature is about 30 K higher than the initial conditions. An interesting point is that there is a small drop of temperature right at the impact site for the 100 km impactor (red curve in the left panel of Fig. 2). This is due to the transient water belt formed after the impact (see Fig. 1). When the planet cools, liquid water freeze at the impact site. Therefore when the climate is stabilized, there is clean ice with a high albedo at the impact site and ice covered by ejecta (thus with a low albedo) all around. This induces a visible pattern on the latitudinal temperature profile.

4 Discussion

4.1 Limitations of the climate model

The variation of humidity and CO_2 partial pressure does not affect the outcome of our study (see Appendix B). H_2O and CO_2 are efficient greenhouse gases and should facilitate the warming and deglaciation of the ice sheet. However, we tested different values for both gases and find that our conclusions hold: in the events we tested, deglaciation is not achieved (see Appendix B). Importantly, we neglected the formation of stratospheric aerosols, but their presence would further prevent deglaciation by acting as a coolant (Macdonald & Wordsworth, 2017b). We also do not account for ice thickness or latent heat released by ice melting to minimize the degrees of freedom in the model. Even accounting for the change of heat capacity between liquid water and ice, the ice thickness could be important to account for the time-scales over which the water belt induced by the 100 km impactor could freeze. In the same way, oceanic circulation will affect the creation of ice in the water belt (e.g., Yang et al., 2020; Brunetti et al., 2019). Those assumptions serve the purpose of finding the minimum size of a stochastic event causing deglaciation.

4.2 Assumptions on impacts and large eruptions

Our simulations suggest that impacts larger than 100 km are necessary, albeit not sufficient, to initiate deglaciation on the planet. However, even such large impacts are expected to occur less than once every billion years from dynamical modeling (Koeberl & Ivanov, 2019). Moreover, we would need more geologic evidence to support this scenario, since a large projectile should have globally spread an ejecta layer analogous to the Chicxulub impact event (Alvarez et al., 1980). So far, no impact signature caused by a $\sim$100 km impactor has been found on Earth (Gyollai et al., 2014; Peucker-Ehrenbrink et al., 2016); as per Allen et al. (2022), the largest impact crater found is caused by a 20-25 km impactor.

The results we present are based on a single impact scenario, comprising of a fixed stratigraphy and an asteroidal projectile hitting the surface at 17 km s^{-1}. We chose an ice thickness of 5 km following Erickson et al. (2020) as a reasonable upper limit for the actual size of glaciers covering the planet. In reality, the ice thickness will depend on the location, as suggested by the geologic record (e.g., McMechan, 2000) and climate modeling (Hyde et al., 2000), ranging from meters to 5 km. Also, we neglected impactors made of materials other than dunite, such as icy bodies. While short-period comets (impact velocity of 30 km s^{-1}, Chyba, 1991) have kinetic energies similar to that of the asteroidal impacts we consider, long-period comets (50 km s^{-1}, Chyba, 1991) might change the impact mechanics, but are less likely to hit the Earth (Weissman, 2006). Finally, we assumed zero porosity as a worst case scenario: for a given size, non-porous material ensures the maximum kinetic energy available to melt ice and vaporize target rocks.

Our conclusions are sensitive to the assumptions made in estimating the dust distribution, namely assuming vertical impacts and no atmosphere present in the impact model. With a 2-D hydrocode, we are unable to reproduce oblique collisions, which affect: 1) the amount of vaporized material, since the shock wave propagates in a larger volume of

ice/crust compared to a vertical impact with the same kinetic energy, and, 2) the shape of ejecta deposits, preferentially distributing in the downrange direction (Collins et al., 2020). Three-dimensional simulations are needed to better understand whether oblique impacts can cause a larger dust coverage. Furthermore, no atmosphere is considered in the impact simulations. Therefore, ejecta follow ballistic trajectories that are not perturbed by atmospheric circulation, so that rock vapor is deposited on the surface without residing in the atmosphere. Consequently, the extension of dust we estimate is a lower limit, since we neglect spreading at further distances due to atmospheric transport (e.g., Kring, 2007).

In modeling volcanic eruptions, results are sensitive to the assumed dust distribution and the absence of lava warming and water vapor. Based on Icelandic dust and ash (Dragosics et al., 2016), a thickness of 15 mm is considered as the threshold for ice to melt due to the decrease in albedo. A thicker layer would thermally insulate the ice below, preventing melting. Increasing such a threshold would expand the dust-covered area subject to melting, favoring deglaciation. Furthermore, the local temperature increase due to erupting lava is disregarded, since its effect is negligible when averaged longitudinally. Similarly, we do not consider a long-term (i.e., multi-year) eruption, which would force a higher temperature around the volcano for a longer time. Finally, as seen for the Hunga Tonga-Hunga Ha'apai eruption (Millán et al., 2022), a substantial amount (up to 10^{11} kg) of water vapor can be injected into the atmosphere. However, the residence time of H_2O in the atmosphere is limited to two weeks before precipitating to the surface (e.g., Gimeno et al., 2021).

4.3 Implications for Earth-like exoplanets

Our findings might not be accurate for Earth-like exoplanets, but nevertheless can provide order-of-magnitude estimates. The modeling in this study is based on Earth-like conditions, which includes target stratigraphy, volcanic dust spreading models, atmospheric chemical composition and thermal structure, geologic record for impact and volcanic events. For instance, the thermo-mechanical response of basalt is different from that of granite (which we assumed to be the material underneath the ice layer), leading to different dust spreading and/or surface temperature profiles. Atmospheric dynamics and structure may affect the transport mechanisms of volcanic ash, so that the scaling laws found for Toba might not apply to planets with a thicker or more turbulent atmosphere. Finally, the limiting factors for Earth do not necessarily apply to other planets. A 100-km projectile is unlikely to hit Earth and no record for an eruption larger than Toba has been found. However, we cannot rule out those events to occur on other Earth-like worlds.

5 Conclusions

We present a framework to evaluate whether stochastic events (impacts and volcanic eruptions) are able to deglaciate Snowball Earth. We model the effects of impacts and supervolcanic eruptions using impact simulations and ash thickness distribution models, respectively. Then, we use an energy balance climate model to assess how the change in surface albedo and temperature perturbs the equilibrium temperature of the planet. We summarize our main conclusions below:

- Even an impactor radius of 100 km is not sufficient to induce deglaciation of Snowball Earth. The warming at the impact site melts ice locally in the short-term, but ice reforms in less than a year, returning the planet to the snowball state. The reduction of albedo due to dark material ejecta deposits drives the warming of the surface. Even if larger impactors could induce deglaciation, it is unlikely to have occurred, based on dynamical modeling and experimental evidence.
- No recorded supervolcanic eruption could have single-handedly deglaciated Earth. The surface temperature increase due to dust deposition from the largest recorded event does not reach the melting temperature of ice. According to previous works

(de Vrese et al., 2021), a change of albedo on a larger area than that of Toba could trigger deglaciation but there is no record of such a massive event on Earth.

- Snowball Earth shows resilience to the stochastic events we tested. However, this does not rule out the possibility of such deglaciation events happening on Earth-like exoplanets.

Our model puts constraints on the magnitude of stochastic events that are capable of triggering Snowball Earth termination. These constraints need to be refined with more comprehensive modeling. For impacts, 3D modeling can better resolve the ejecta distribution and account for oblique impacts. The impact simulations should include the ice erosion effect due to the tsunami created upon impact, which would increase the low-albedo area. For the climate response, 3D GCM modeling is required to include longitudinal and vertical resolutions, as well as to better representations of clouds, atmospheric dynamics, ocean dynamics, and distribution of aerosols ejected by the impactor (e.g., Ashkenazy et al., 2013; Turbet et al., 2020) or released by the volcano.

In this work, we treated impacts and supervolcanos as independent and instantaneous events. Future analyses should investigate the effect of prolonged (e.g., several years) lava eruptions. Also, the combined effect of impacts and eruptions should be considered: impact-induced volcanism has been suggested (e.g., Renne et al., 2015), though still debated (e.g., Bhandari et al., 1995). Those refined analyses can help to better understand the role of stochastic events in transitioning out from a frozen state to another stable climate state.

Appendix A Impact simulation setup

The parameters used for impact simulations using the iSALE shock physics code are resumed in Table A1.

Appendix B EBM parameterization

We investigate the climate of the model planets using a 1-D time-dependent EBM introduced in Williams et al. (1998), Spiegel et al. (2008) and further explored by Dressing et al. (2010). The equation governing the temporal evolution of the surface temperature T is given by:

$$C\frac{\partial T[x,t]}{\partial t} - \frac{\partial}{\partial x}\left(D(1-x^2)\frac{\partial T[x,t]}{\partial x}\right) + I[T,t] = S(1-A[T,t]), \tag{B1}$$

where $x = \sin\lambda$ gives the location of the grid point of latitude λ, t is the time, C is the effective heat capacity of the atmosphere over this grid point, $D = 0.5394$ W m^{-2} K^{-1} is the diffusion coefficient which determines the efficiency of the latitudinal redistribution of heat, $I(T,t)$ is the temperature-dependent infrared emission, S is the incoming stellar radiation and $A(T,t)$ is the temperature-dependent albedo of the grid point. The net radiative energy flux at a grid point is determined by the relationship between the irradiation arriving on the planet (S in Eq. (B1)) and the energy lost via infrared emission (I in Eq. (B1)).

Following Spiegel et al. (2008) and Dressing et al. (2010), we compute the absorbed stellar radiation (ASR) as a function of the surface albedo A and do not account for the atmospheric dependency. The albedo varies from 0.28 for water (+land) to 0.77 for ice following Eq. (B2):

$$A = 0.525 - 0.245\tanh\left(\frac{T-268}{5}\right) \tag{B2}$$

We adapt Eq. (B2) to compare our simulations with Pierrehumbert et al. (2011), which assumes 0.5 for the albedo of the ice. The albedo of "liquid water" is fixed to 0.28 to account for continents (Dressing et al., 2010). The equation giving the insolation as a function of

Table A1. Material parameters used within simulations for the impactors and targets. All parameters used are standard to iSALE or M-ANEOS, and details can be found in the respective manuals (iSALE: `https://github.com/isale-code/isale-wiki`; M-ANEOS: `https://github.com/isale-code/M-ANEOS`).

Parameter	Dunite	Graphite	Calcite	H_2O Ice
EOSNAME	dunite_	granite	calcite	ice___
No. density nodes	240	240	240	240
No. thermal nodes	120	120	240	240
Low density weakening	POLY	POLY	POLY	POLY
Poisson ratio	2.5×10^{-1}	3.0×10^{-1}	3.0×10^{-1}	3.3×10^{-1}
Strength model	ROCK	ROCK	ROCK	ICE
YINT0	1.0×10^{7}	1.0×10^{7}	5.0×10^{6}	1.0×10^{7}
FRICINT	1.2	2.0	1.0	2.0
YLIMINT	3.5×10^{9}	2.5×10^{9}	5.0×10^{8}	1.1×10^{8}
YDAM0	1.0×10^{4}	1.0×10^{4}	1.0×10^{4}	5.0×10^{5}
FRICDAM	6.0×10^{-1}	6.0×10^{-1}	4.0×10^{-1}	6.0×10^{-1}
YLIMDAM	3.5×10^{9}	2.5×10^{9}	5.0×10^{8}	1.1×10^{8}
Damage model	IVANOV			
IVANOV_A	1.0×10^{-4}			
IVANOV_B	1.0×10^{-11}			
IVANOV_C	3.0×10^{8}			
Thermal softening	OHNAKA	OHNAKA	OHNAKA	OHNAKA
TMELT0	1.373×10^{3}	1.673×10^{3}	1.500×10^{3}	0.272×10^{3}
TFRAC	1.2	1.2	1.2	1.2
ASIMON	1.52×10^{9}	6.0×10^{9}	6.0×10^{9}	6.0×10^{9}
CSIMON	4.05	3.00	3.00	3.00

the latitude with obliquity is taken from Berger (1978) assuming no eccentricity. The heat capacity of the ground depends on the surface type of the grid point and varies for land, ocean, ice and cold ice, following Spiegel et al. (2008) and Dressing et al. (2010).

For the thermal emission we consider two different parameterization made using the 1D radiative-convective model presented in Chaverot et al. (2022), representing the atmosphere of the Earth with 1 bar of nitrogen and 400 ppm or 800 ppm of CO_2. In both cases, the water vapor pressure is a function of the temperature following the pseudo-adiabatic assumption (Kasting, 1988). This original parameterization allow us to account for CO_2 released by volcanic eruptions. The relative humidity (RH) is constant during the simulation and can be equal to 0.45 or 1. As shown by Leconte et al. (2013), RH=0.45 is able to reproduce the infrared emission of a temperate Earth from a Global Climate Model. Higher RH values are used to represent the extra moisture accumulated in the atmosphere after a large eruption. This original parameterization of the thermal emission provides similar results to those obtained using the parameterization from Dressing et al. (2010).

By definition, the EBM is longitudinally-averaged which implies that modifying one grid cell affects all corresponding longitudes. As the considered stochastic events are limited to a particular region in space, we add a correction factor so that not all longitudes are impacted. More specifically, during the initialization of the simulation, we average the values of the albedo and of the temperature after the event with the non-impacted part of the planet at every latitude, accounting for the area of this event. By doing so, the initial maximum

temperature of the EBM is much lower than the maximum temperature after the impact obtained from iSALE.

B1 Sensitivity tests

We perform several sensitivity tests in order to benchmark the original parameterization we introduced in the EBM for the thermal emission and to quantify the intrinsic effect of specific parameters. An exhaustive overview of these tests is presented in Table B1 and an overview of the most important ones is shown in Fig. B1.

First, the temperature profile we obtain using our parameterization of the thermal emission with 400 ppm of CO_2 is consistent with that obtained in Dressing et al. (2010). Second, we tested the impact of several parameters of the EBM. The value of the diffusion factor (D in Eq. (B1)) we used is taken from Dressing et al. (2010), but as mentioned in Pierrehumbert et al. (2011), cold climates have a reduced heat transport efficiency. Therefore we tested $D = 0.25$ W m^{-2} K^{-1} as per Pierrehumbert et al. (2011) (see orange curve in Fig. B1). The modification of the heat transport increases the temperature contrast between the equator and poles by a few K. We also added a cloud forcing equal to 14 W m^{-2} to account for their warming effect, according to Abbot (2014). This increases the global temperature by 10 K (difference between blue and red curves in Fig. B1).

Figure Fig. B1 also shows that by considering 800 ppm of CO_2 instead of 400 ppm, the temperature increases by less than 1 K. Likewise, increasing RH up to 1 does not significantly change the temperature from the point of view of deglaciation point. This is coherent regarding the low water vapor content of a cold atmosphere.

Due to our longitudinal correction, we overestimate the albedo by less than 1% depending on the albedo difference and on the temperature gradient along the longitude.

Table B1. Overview of the simulation setups

Simulation	CO_2 pressure	RH	Extra param.
No stochastic event	400 ppm	0.45	
No stochastic event	400 ppm	0.45	Ice albedo = 0.5 (Pierrehumbert et al., 2011)
No stochastic event	400 ppm	0.45	$d = 0.94$ AU
No stochastic event	400 ppm	0.45	$D = 0.25$ W m^{-2} K^{-1}
No stochastic event	400 ppm	0.45	obliquity $\phi = 23°$
No stochastic event	400 ppm	0.45	cloud forcing = 14 W.m^{-2} (Abbot, 2014)
No stochastic event	400 ppm	1	
No stochastic event	800 ppm	0.45	
Toba at the equator	400 ppm	0.45	
Toba at the equator	800 ppm	0.45	
Toba at the equator	400 ppm	0.45	cloud forcing = 14 W.m^{-2} (Abbot, 2014)
Toba at the equator	800 ppm	0.45	cloud forcing = 14 W.m^{-2} (Abbot, 2014)
Toba at 40° N	400 ppm	0.45	
Toba at 40° N	800 ppm	0.45	
Toba at 40° N	400 ppm	1	
40 km impactor	400 ppm	0.45	
60 km impactor	400 ppm	0.45	
80 km impactor	400 ppm	0.45	
100 km impactor	400 ppm	0.45	
100 km impactor	400 ppm	1	
100 km impactor	800 ppm	0.45	
100 km impactor at 40° N	400 ppm	0.45	

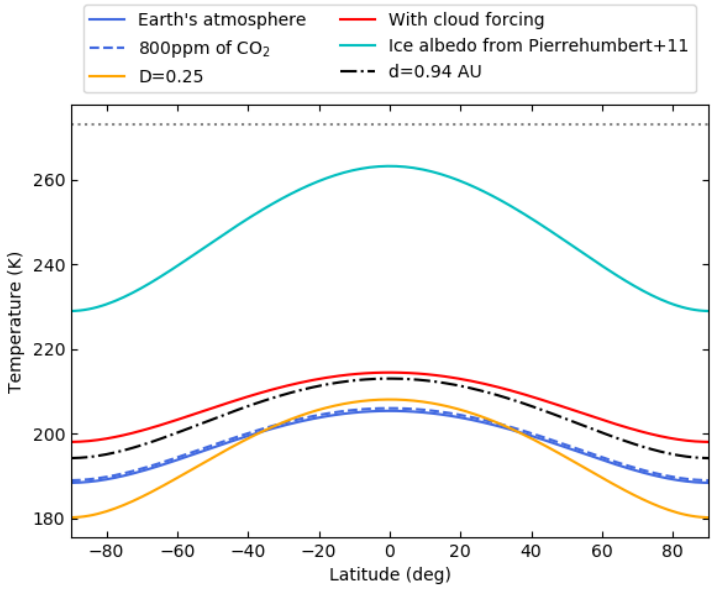


Figure B1. Latitudinal temperature without stochastic events for different parameterizations. Solid curves are for the reference thermal emission corresponding to the Earth's atmosphere including 400 ppm of CO_2. The dashed curve corresponds to simulations with 800 ppm of CO_2. Red, orange and cyan curves are for simulations with cloud forcing, with a diffusion factor $D = 0.25\,\mathrm{Wm^{-2}K^{-1}}$ and an ice albedo from Pierrehumbert et al. (2011) respectively. The black dash-dotted curve is for the Earth located at 0.94 AU from the Sun.

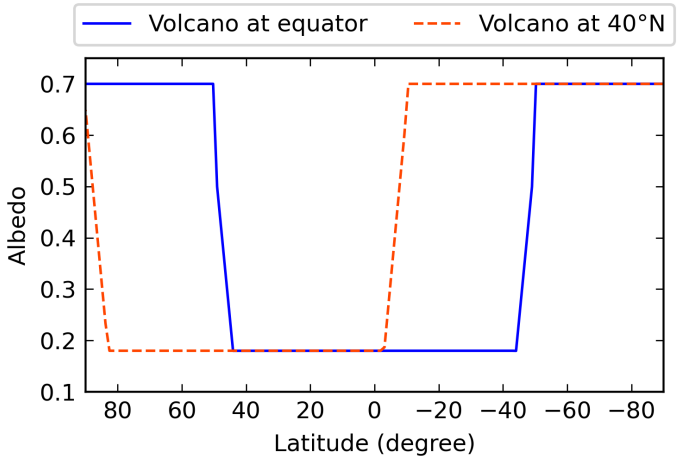


Figure B2. Latitudinal albedo parameterized for Toba-like supervolcanic eruptions with the eruption center at the equator (solid curve) and at 40°N (dashed curve). The albedo values of ice (0.7), dusty ice (0.18-0.7) and dust (0.18) are based on Le Hir et al. (2010) and Warren (1982).

Open Research

At present, the iSALE code is not fully open-source. It is distributed via a private GitHub repository on a case-by-case basis to academic users in the impact community, strictly for non-commercial use. Scientists interested in using or developing iSALE should refer to `http://www.isale-code.de` for a description of application requirements.

Acknowledgments
The project was made possible by the 2022 Cooperative Institute for Dynamic Earth Research (CIDER) workshop in UC Berkeley, funded by the NSF. This work has been carried out within the framework of the NCCR PlanetS supported by the Swiss National Science Foundation under grants 51NF40_182901 and 51NF40_205606. GC acknowledges the financial support of the SNSF (grant number: 200021_197176 and 200020_215760) Authors declare that they have no competing interests.

References

Abbot, D. S. (2014). Resolved Snowball Earth Clouds. *Journal of Climate*, *27*(12), 4391–4402. doi: https://doi.org/10.1175/JCLI-D-13-00738.1

Abbot, D. S., & Pierrehumbert, R. T. (2010). Mudball: Surface dust and Snowball Earth deglaciation. *Journal of Geophysical Research: Atmospheres*, *115*(D3). doi: https://doi.org/10.1029/2009JD012007

Allen, N. H., Nakajima, M., Wünnemann, K., Helhoski, S., & Trail, D. (2022). A revision of the formation conditions of the vredefort crater. *Journal of Geophysical Research: Planets*, *127*(8), e2022JE007186. doi: https://doi.org/10.1029/2022JE007186

Alvarez, L. W., Alvarez, W., Asaro, F., & Michel, H. V. (1980). Extraterrestrial Cause for the Cretaceous-Tertiary Extinction. *Science*, *208*(4448), 1095-1108. doi: https://doi.org/10.1126/science.208.4448.1095

Amsden, A. A., Ruppel, H. M., & Hirt, C. W. (1980). *SALE: a simplified ALE computer program for fluid flow at all speeds* (Tech. Rep.). Los Alamos Scientific Laboratories. doi: https://doi.org/10.2172/5176006

Artemieva, N., Morgan, J., & Party, E. . S. (2017). Quantifying the release of climate-active gases by large meteorite impacts with a case study of Chicxulub. *Geophysical Research Letters*, *44*(20), 10,180-10,188. doi: https://doi.org/10.1002/2017GL074879

Ashkenazy, Y., Gildor, H., Losch, M., Macdonald, F. A., Schrag, D. P., & Tziperman, E. (2013, March). Dynamics of a Snowball Earth ocean. *Nature*, *495*(7439), 90–93. Retrieved 2023-10-17, from `https://www.nature.com/articles/nature11894` (Number: 7439 Publisher: Nature Publishing Group) doi: 10.1038/nature11894

Batchelor, C. L., Margold, M., Krapp, M., Murton, D. K., Dalton, A. S., Gibbard, P. L., ... Manica, A. (2019). The configuration of northern hemisphere ice sheets through the quaternary. *Nature communications*, *10*(1), 3713. doi: https://doi.org/10.1038/s41467-019-11601-2

Benz, W., Cameron, A. G. W., & Melosh, H. J. (1989). The origin of the Moon and the single-impact hypothesis III. *Icarus*, *81*(1), 113-131. doi: https://doi.org/10.1016/0019-1035(89)90129-2

Berger, A. (1978). Long-Term Variations of Daily Insolation and Quaternary Climatic Changes. *Journal of the Atmospheric Sciences*, *35*(12), 2362–2367. doi: https://doi.org/10.1175/1520-0469(1978)035⟨2362:LTVODI⟩2.0.CO;2

Bhandari, N., Shukla, P. N., Ghevariya, Z. G., & Sundaram, S. M. (1995). Impact did not trigger deccan volcanism: Evidence from anjar k/t boundary intertrappean sediments. *Geophysical Research Letters*, *22*(4), 433-436. doi: https://doi.org/10.1029/94GL03271

Brugger, J., Feulner, G., & Petri, S. (2017). Baby, it's cold outside: Climate model simulations of the effects of the asteroid impact at the end of the Cretaceous. *Geophysical Research Letters*, *44*(1), 419-427. doi: https://doi.org/10.1002/2016GL072241

Brunetti, M., Kasparian, J., & Vérard, C. (2019). Co-existing climate attractors in a coupled aquaplanet. *Climate Dynamics*, *53*(9), 6293–6308. doi: https://doi.org/10.1007/s00382-019-04926-7

Budyko, M. I. (1969). The effect of solar radiation variations on the climate of the earth. *Tellus*, *21*(5), 611–619. doi: https://doi.org/10.1111/j.2153-3490.1969.tb00466.x

Caldeira, K., & Kasting, J. F. (1992). Susceptibility of the early Earth to irreversible glaciation caused by carbon dioxide clouds. *Nature*, *359*(6392), 226-228. doi: https://doi.org/10.1038/359226a0

Chaverot, G., Turbet, M., Bolmont, E., & Leconte, J. (2022). How does the background atmosphere affect the onset of the runaway greenhouse? *Astronomy & Astrophysics*, *658*, A40. doi: https://doi.org/10.1051/0004-6361/202142286

Chumakov, N. (2009). The Baykonurian glaciohorizon of the late Vendian. *Stratigraphy and Geological Correlation*, *17*, 373–381. doi: https://doi.org/10.1134/S0869593809040029

Chyba, C. F. (1991). Terrestrial mantle siderophiles and the lunar impact record. *Icarus*, *92*(2), 217-233. doi: https://doi.org/10.1016/0019-1035(91)90047-W

Collins, G. S. (2014). Numerical simulations of impact crater formation with dilatancy. *Journal of Geophysical Research: Planets*, *119*(12), 2600–2619. doi: https://doi.org/10.1002/2014JE004708

Collins, G. S., Melosh, H. J., & Ivanov, B. A. (2004). Modeling damage and deformation in impact simulations. *Meteoritics & Planetary Science*, *39*(2), 217–231. doi: https://doi.org/10.1111/j.1945-5100.2004.tb00337.x

Collins, G. S., Melosh, H. J., & Wünnemann, K. (2011). Improvements to the $\varepsilon - \alpha$ porous compaction model for simulating impacts into high-porosity solar system objects. *International Journal of Impact Engineering*, *38*(6), 434–439. doi: https://doi.org/10.1016/j.ijimpeng.2010.10.013

Collins, G. S., Patel, N., Davison, T. M., Rae, A. S. P., Morgan, J. V., Gulick, S. P. S., ... Scientists, T.-P. (2020). A steeply-inclined trajectory for the Chicxulub impact. *Nature Communications*, *11*(1), 1480. doi: https://doi.org/10.1038/s41467-020-15269-x

Costa, A., Smith, V. C., Macedonio, G., & Matthews, N. E. (2014). The magnitude and impact of the Youngest Toba Tuff super-eruption. *Frontiers in Earth Science*, *2*. doi: https://doi.org/10.3389/feart.2014.00016

de Silva, S., & Self, S. (2022). Capturing the Extreme in Volcanology: The Case for the Term "Supervolcano". *Frontiers in Earth Science*, *10*. doi: https://doi.org/10.3389/feart.2022.859237

de Vrese, P., Stacke, T., Caves Rugenstein, J., Goodman, J., & Brovkin, V. (2021). Snowfall-albedo feedbacks could have led to deglaciation of snowball Earth starting from mid-latitudes. *Communications Earth & Environment*, *2*(1), 1–9. doi: https://doi.org/10.1038/s43247-021-00160-4

Dragosics, M., Meinander, O., Jónsdóttír, T., Dürig, T., De Leeuw, G., Pálsson, F., ... Thorsteinsson, T. (2016). Insulation effects of icelandic dust and volcanic ash on snow and ice. *Arabian Journal of Geosciences*, *9*(2), 126. doi: https://doi.org/10.1007/s12517-015-2224-6

Dressing, C. D., Spiegel, D. S., Scharf, C. A., Menou, K., & Raymond, S. N. (2010). Habitable Climates: The Influence of Eccentricity. *The Astrophysical Journal*, *721*, 1295–1307. doi: 10.1088/0004-637X/721/2/1295

Erickson, T. M., Kirkland, C. L., Timms, N. E., Cavosie, A. J., & Davison, T. M. (2020). Precise radiometric age establishes Yarrabubba, Western Australia, as Earth's oldest recognised meteorite impact structure. *Nature Communications*, *11*(1), 300. doi: https://doi.org/10.1038/s41467-019-13985-7

Ghil, M. (1994). Cryothermodynamics: The chaotic dynamics of paleoclimate. *Physica D: Nonlinear Phenomena*, *77*(1-3), 130–159. doi: https://doi.org/10.1016/0167-2789(94)90131-7

Gimeno, L., Eiras-Barca, J., Durán-Quesada, A. M., Dominguez, F., van der Ent, R., Sodemann, H., ... Kirchner, J. W. (2021). The residence time of water vapour in

the atmosphere. *Nature Reviews Earth & Environment*, *2*(8), 558-569. doi: https://doi.org/10.1038/s43017-021-00181-9

Gyollai, I., Mader, D., Polgári, M. P., Popp, F., & Koeberl, C. (2014). Lack of evidence for impact signatures in Neoproterozoic postglacial deposits from NW-Namibia. *Austrian Journal of Earth Sciences*, *102*(2), 100–111.

Hambrey, M. J., & Harland, W. B. (1981). *Earth's pre-Pleistocene glacial record*. Cambridge University Press.

Hansen, J. E., Wang, W.-C., & Lacis, A. A. (1978). Mount Agung Eruption Provides Test of a Global Climatic Perturbation. *Science*, *199*(4333), 1065-1068. doi: https://doi.org/10.1126/science.199.4333.1065

Harland, W. B. (1964). Critical evidence for a great infra-Cambrian glaciation. *Geologische Rundschau*, *54*(1), 45-61. doi: https://doi.org/10.1007/BF01821169

Hoffman, P. F., Abbot, D. S., Ashkenazy, Y., Benn, D. I., Brocks, J. J., Cohen, P. A., ... Warren, S. G. (2017). Snowball Earth climate dynamics and Cryogenian geology-geobiology. *Science Advances*, *3*(11), e1600983. doi: https://doi.org/10.1126/sciadv.1600983

Hoffman, P. F., Kaufman, A. J., Halverson, G. P., & Schrag, D. P. (1998). A Neoproterozoic Snowball Earth. *Science*, *281*(5381), 1342-1346. doi: https://doi.org/10.1126/science.281.5381.1342

Hotaling, S., Lutz, S., Dial, R. J., Anesio, A. M., Benning, L. G., Fountain, A. G., ... Hamilton, T. L. (2021). Biological albedo reduction on ice sheets, glaciers, and snowfields. *Earth-Science Reviews*, *220*, 103728. doi: https://doi.org/10.1016/j.earscirev.2021.103728

Hyde, W. T., Crowley, T. J., Baum, S. K., & Peltier, W. R. (2000). Neoproterozoic 'snowball Earth' simulations with a coupled climate/ice-sheet model. *Nature*, *405*(6785), 425-429. doi: https://doi.org/10.1038/35013005

Ivanov, B. A., Deniem, D., & Neukum, G. (1997). Implementation of dynamic strength models into 2D hydrocodes: Applications for atmospheric breakup and impact cratering. *International Journal of Impact Engineering*, *20*(1), 411–430. doi: https://doi.org/10.1016/S0734-743X(97)87511-2

Kasting, J. F. (1988). Runaway and moist greenhouse atmospheres and the evolution of Earth and Venus. *Icarus*, *74*(3), 472–494. doi: https://doi.org/10.1016/0019-1035(88)90116-9

Kennedy, M. J. (1996). Stratigraphy, sedimentology, and isotopic geochemistry of Australian Neoproterozoic postglacial cap dolostones; deglaciation, delta 13 C excursions, and carbonate precipitation. *Journal of sedimentary Research*, *66*(6), 1050–1064. doi: https://doi.org/10.2110/jsr.66.1050

Kirschvink, J. L. (1992). Late Proterozoic Low-Latitude Global Glaciation: The Snowball Earth. In J. Schopf & C. Klein (Eds.), *In the Proterozoic Biosphere: A Multidisciplinary Study*. Cambridge, United Kingdom: Cambridge University Press. doi: https://doi.org/10.1017/CBO9780511601064

Knoll, A., Hayes, J., Kaufman, A., Swett, K., & Lambert, I. (1986). Secular variation in carbon isotope ratios from upper Proterozoic successions of Svalbard and east Greenland. *Nature*, *321*(6073), 832–838. doi: https://doi.org/10.1038/321832a0

Koeberl, C., & Ivanov, B. A. (2019). Asteroid impact effects on Snowball Earth. *Meteoritics & Planetary Science*, *54*(10), 2273–2285. doi: https://doi.org/10.1111/maps.13294

Kring, D. A. (2003). Environmental Consequences of Impact Cratering Events as a Function of Ambient Conditions on Earth. *Astrobiology*, *3*(1), 133-152. doi: https://doi.org/10.1089/153110703321632471

Kring, D. A. (2007). The Chicxulub impact event and its environmental consequences at the Cretaceous–Tertiary boundary. *Palaeogeography, Palaeoclimatology, Palaeoecology*, *255*(1), 4-21. doi: https://doi.org/10.1016/j.palaeo.2007.02.037

Lan, Z., Huyskens, M. H., Le Hir, G., Mitchell, R. N., Yin, Q.-Z., Zhang, G., & Li, X.-H. (2022). Massive Volcanism May Have Foreshortened the Marinoan Snowball Earth. *Geophysical Research Letters*, *49*(6), e2021GL097156. doi: https://doi.org/10.1029/

2021GL097156

Leconte, J., Forget, F., Charnay, B., Wordsworth, R., & Pottier, A. (2013). Increased insolation threshold for runaway greenhouse processes on Earth like planets. *Nature*, *504*(7479), 268–271. doi: https://doi.org/10.1038/nature12827

Le Hir, G., Donnadieu, Y., Krinner, G., & Ramstein, G. (2010). Toward the snowball earth deglaciation.... *Climate dynamics*, *35*, 285–297. doi: https://doi.org/10.1007/s00382-010-0748-8

Macdonald, F. A., & Wordsworth, R. (2017a). Initiation of Snowball Earth with volcanic sulfur aerosol emissions. *Geophysical Research Letters*, *44*(4), 1938–1946. doi: https://doi.org/10.1002/2016GL072335

Macdonald, F. A., & Wordsworth, R. (2017b). Initiation of Snowball Earth with volcanic sulfur aerosol emissions. *Geophysical Research Letters*, *44*(4), 1938–1946. doi: https://doi.org/10.1002/2016GL072335

Mason, B. G., Pyle, D. M., & Oppenheimer, C. (2004). The size and frequency of the largest explosive eruptions on Earth. *Bulletin of Volcanology*, *66*(8), 735-748. doi: https://doi.org/10.1007/s00445-004-0355-9

McMechan, M. (2000). Vreeland Diamictites – Neoproterozoic glaciogenic slope deposits, Rocky Mountains, northeast British Columbia. *Bulletin of Canadian Petroleum Geology*, *48*(3), 246-261. doi: https://doi.org/10.2113/48.3.246

Melosh, H. J., Ryan, E. V., & Asphaug, E. (1992). Dynamic fragmentation in impacts: Hydrocode simulation of laboratory impacts. *Journal of Geophysical Research: Planets*, *97*(E9), 14735–14759. doi: https://doi.org/10.1029/92JE01632

Millán, L., Santee, M. L., Lambert, A., Livesey, N. J., Werner, F., Schwartz, M. J., ... Froidevaux, L. (2022). The hunga tonga-hunga ha'apai hydration of the stratosphere. *Geophysical Research Letters*, *49*(13), e2022GL099381. doi: https://doi.org/10.1029/2022GL099381

North, G. R., & Coakley Jr, J. A. (1979). Differences between seasonal and mean annual energy balance model calculations of climate and climate sensitivity. *Journal of Atmospheric Sciences*, *36*(7), 1189–1204. doi: https://doi.org/10.1175/1520-0469(1979)036⟨1189:DBSAMA⟩2.0.CO;2

Peucker-Ehrenbrink, B., Waters, C. A., Kurz, M. D., & Hoffman, P. F. (2016). No evidence of extraterrestrial noble metal and helium anomalies at Marinoan glacial termination. *Earth and Planetary Science Letters*, *437*, 76-88. doi: https://doi.org/10.1016/j.epsl.2015.12.040

Pierazzo, E., Kring, D. A., & Melosh, H. J. (1998). Hydrocode simulation of the Chicxulub impact event and the production of climatically active gases. *Journal of Geophysical Research: Planets*, *103*(E12), 28607-28625. doi: https://doi.org/10.1029/98JE02496

Pierrehumbert, R. T., Abbot, D. S., Voigt, A., & Koll, D. (2011). Climate of the Neoproterozoic. *Annual Review of Earth and Planetary Sciences*, *39*, 417–460. doi: https://doi.org/10.1146/annurev-earth-040809-152447

Pyle, D. M. (1989). The thickness, volume and grainsize of tephra fall deposits. *Bulletin of volcanology*, *51*, 1–15. doi: https://doi.org/10.1007/BF01086757

Renne, P. R., Sprain, C. J., Richards, M. A., Self, S., Vanderkluysen, L., & Pande, K. (2015). State shift in Deccan volcanism at the Cretaceous-Paleogene boundary, possibly induced by impact. *Science*, *350*(6256), 76-78. doi: https://doi.org/10.1126/science.aac7549

Richardson, J. E., Melosh, H. J., Greenberg, R. J., & O'Brien, D. P. (2005). The global effects of impact-induced seismic activity on fractured asteroid surface morphology. *Icarus*, *179*(2), 325-349. doi: https://doi.org/10.1016/j.icarus.2005.07.005

Rooney, A. D., Strauss, J. V., Brandon, A. D., & Macdonald, F. A. (2015). A Cryogenian chronology: Two long-lasting synchronous Neoproterozoic glaciations. *Geology*, *43*(5), 459-462. doi: https://doi.org/10.1130/G36511.1

Rose, W. I., & Chesner, C. A. (1990). Worldwide dispersal of ash and gases from earth's largest known eruption: Toba, Sumatra, 75 ka. *Palaeogeography, Palaeoclimatology, Palaeoecology*, *89*(3), 269-275. doi: https://doi.org/10.1016/0921-8181(90)90023-6

6.3 Implications for exoplanets

6.3.1 S-tipping: an inefficient way to deglaciate a planet

As shown in Chaverot et al. (in prep.), the snowball state is very resilient to any temperature forcing coming from a large impact. A modification of the ice albedo through ash deposits affects more efficiently the global temperature, but even Toba (the biggest event that happened on Earth) is not sufficient to deglaciate. Additionally, there is no geologic record of a bigger eruption on the Earth.

These result tends toward a high stability of steady states to S-tipping and difficulties to tip from a climate regime to another. Moreover, EBMs are simple models, and they neglect complex processes such as interactions between the ice, the ocean, and the atmosphere, 3-D atmospheric circulation or variability of the cloud coverage. Some works (e.g., Lucarini et al. 2022) include an internal variability term to mimic the complexity of these different climate feedback. However, even if the scenarios explored in Chaverot et al. (in prep.) tend to exclude any deglaciation on Earth by that way, more extreme events could happen on exoplanets. The tipping from the steam regime to the temperate one is not discussed in detail but could be of a great interest as well. With current techniques, we probe essentially planets close to their host star, that means planets potentially more irradiated than the inner edge of the HZ. This motivates an effort to understand both the B-tipping (bifurcation induced tipping) transition between temperate and steam regimes but also possibilities of a S-tipping (shock-induced tipping). Moreover, these close-in planets are usually tidally locked because of huge tidal interactions with the host star. As written at the beginning of this chapter, it affects strongly the climate and resulting steady states. The resilience of such particular climates should be investigated as well.

From a general point of view, there is a strong interest to improve our knowledge on climate multistability to know what are the most probable climate regimes as well as the number of planetary candidates we can expect as target to search for life. This could also help to constrain the characteristics of the targets (planetary systems or planets) we select in the quest of extra-terrestrial life inside and outside the solar system.

6.3.2 Toward a more complex definition of the habitable zone

The definition of the HZ as presented in Sect. 1.2.2 implies a range of distance for which the planet can sustain surface liquid water, and other distances for which it cannot. Regarding the discussions in this chapter, this definition seems really too simplistic. Converted in terms of distance to the star, the hysteresis cycles presented in Fig. 6.2 induce a distance to the star for which the planet (here the Earth) can be snowball, temperate or steam depending on its initial global temperature. This adds an extra parameter in the definition of the HZ that is the initial condition (i.e., initial temperature) of the planet. Knowing this, it is not possible to study habitability without a time dependent analysis. The perfect example is the definition of the Water Condensation Zone (WCZ, see Sect. 1.2.3 and Turbet et al. 2023). As shown in Turbet et al. (2023), the cloud pattern of post-runaway planets highlighted by Turbet et al. (2021) requires a low insolation to let an ocean condense at the surface. This means that the inner HZ

limit for condensation is located much farther out than the HZ limit for evaporation (e.g., Way et al. 2016). Therefore, there is a large distance range for which a planet will be - or not - in the HZ depending on its initial temperature. An overview of the inner limits of the HZ computed with different models and different setups is presented in Fig. 6.4. The multistability range of distance is shown by the gray area. Consequently, for a case-to-case study, it is key to know the dynamical history of the planetary system. For planets formed in-situ in the multistability region (gray area in Fig. 6.4), the water vapor degassed by the primary magma ocean (Lebrun et al. 2013 ; Hamano et al. 2013 ; Dorn et al. 2018 ; Lichtenberg et al. 2022 ; Salvador & Samuel 2023) creates a post-runaway climate. Without any evolution of the planetary orbit (and without any event inducing a S-tipping), the ocean will never condense, and the planet can be considered outside the HZ. On the other-side, a planet formed far-away from the star (beyond the WCZ) will be able to condense an ocean. If a late inward migration occurs subsequently through the effect of dynamical forces, the runaway greenhouse will happen at the usual HZ inner edge (Kopparapu et al. 2017). Therefore, such planet will be temperate in the multistability region (gray area). There are few known dynamical processes which can induce a late migration, such as the Kozai-Lidov effect (three body tidal interactions inducing inward migration of a planet, see e.g., Kozai 1962 ; Beust et al. 2012 ; Attia et al. 2021), or a coplanar high-eccentricity migration (e.g., Petrovich 2015).

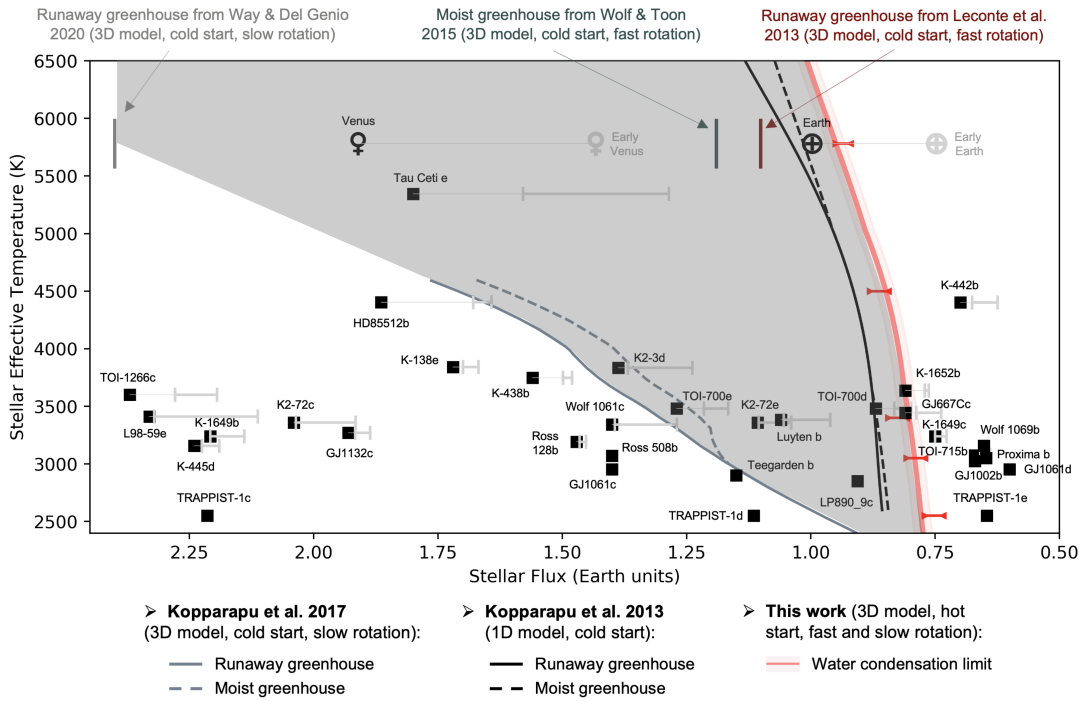


Figure 6.4: Overview of the inner limit of the HZ computed with 1-D (Kopparapu et al. 2013) and 3-D climate models (Leconte et al. 2013 ; Wolf & Toon 2015 ; Kopparapu et al. 2017 ; Way & Del Genio 2020). Dashed and solid lines correspond to the moist and the runaway greenhouse, respectively. The red line and brackets are the calculation of the WCZ from Turbet et al. (2023). All the currently known exoplanets (with a mass $\leq 5\,M_\oplus$ and/or a radius $\leq 1.6\,R_\oplus$) are indicated with black squares. The gray brackets are the insolations estimated at the beginning of the main sequence of the star. The white area on the left of the figure corresponds to planets too hot (i.e., too close to their host star) to sustain liquid water at their surface. The white area on the right of the figure corresponds to planets which are in the HZ. The gray area illustrates the difference of the inner edge of the HZ for a planet initially hot or initially cold. The figure is adapted from Turbet et al. (2023).

For the main results presented in Fig. 6.4 the atmosphere is assumed to be the one of the Earth (or closely similar), which a strong assumption. Various atmospheric compositions will complexify even more the problem. Considering the multistability property of the climate is another argument to say that the "Habitable zone" is an extremely useful concept for statistical study, but should be used carefully to avoid any unfortunate wrong conclusions in a case-by-case approach.

Part IV

Conclusions and prospects

Chapter 7

Conclusions

Contents

7.1 Conclusions 134

7.2 Prospects 135

7.1 Conclusions

In this manuscript, I discuss the three main topics I studied during my PhD. Motivated by the large differences in the literature on the estimation of the OTR of the onset of the runaway greenhouse, I deeply investigated the radiative transfer processes of 1-D radiative-convective models to be able to explain these differences. In Chaverot et al. (2022) (see Sect. 4.2), we show that inter-molecular collisions strongly affect the opacity of the atmosphere, thus the whole radiative transfer calculation. These subtle spectroscopic effects need to be accounted for when the composition changes drastically, as it is the case for the onset of the runaway greenhouse. We also discuss the similarities between the different equations existing in the literature to compute an adiabatic thermal profile. All this work can be used by the community to know which models, approximations or thermal profiles are the most accurate ones to study the runaway greenhouse. The work done in Chaverot et al. (2022) led to the writing of a numerical tool named SpeCT to compute high-resolution absorption spectra for different gas mixtures (H_2O+N_2, H_2O+CO_2 and CO_2+N_2), and accounting for the aforementioned spectroscopic subtleties (see Chapters 2 and 3). The high accuracy of these spectra is driven by the multiple correction factors included in the code, and coming from spectroscopy laboratory experiments. The goal is to use the spectra computed by SpeCT to produce accurate correlated-k tables usable by the climate modeling community. I aim to make this tool open-source as soon as possible to allow other groups to implement the mixtures they need for their own projects. SpeCT could be complementary with other existing libraries and/or databases, more flexible in terms of gas mixtures but which do not always account correctly for the inter-molecular collisions (e.g., ExoMol[1], Helios-K see Grimm et al. 2021). Thanks to recent development of SpeCT, I expand Chaverot et al. (2022) in this manuscript by calculating the thermal emission and the absorbed fluxes of atmospheres made of H_2O and CO_2 instead of H_2O and N_2 (see Sects 4.3 and 4.4). The aim is to propose an updated estimation of the inner edge of the HZ from Kopparapu et al. (2013) with various atmospheric compositions.

In a second time, I studied the runaway greenhouse with the Generic-PCM in order to link two major works estimating the climate of temperate and post-runaway planets with the same model (Leconte et al. 2013 ; Turbet et al. 2021). We show in Chaverot et al. (2023) that the transition between these two very different populations of planets is made of two phases: 1) an evaporation phase, characteristic of the runaway greenhouse for which both the vapor content and the cloud coverage increase rapidly, 2) a dry transition phase, happening when the ocean is totally evaporated, for which the radiative imbalance skyrockets inducing a fast increase of the temperature and then a stabilizing of the climate on a post-runaway state (Sect. 5.2). We describe in detail the evolution of the climate during this transition, in order to have a better idea of a possible evolution of the terrestrial planets we observe. Following this work, I discuss in Sect. 5.3 the possible observation of key steps along this transition.

Finally, motivated by the third stability state of the Earth highlighted by Turbet et al. (2021) and thanks to collaborators met during the CIDER summer school, I worked on the concept of climate multistability (Chapter 6). Knowing that, as a result of numerical simulations of different complexity, there

[1] `https://exomol.com/`

are three stables regimes for the Earth: snowball, temperate and steam, an interesting question is to know how easy it is to tip from a state to another. This question is especially relevant in the context of the search of habitable environment and potential extra-solar traces of life. In this collaboration, we specifically study the transition from snowball to temperate triggered by 1) a large impact providing mainly energy as heat into the atmosphere, 3) a large volcanic eruption depositing ash on the ice, thus modifying the radiative balance of the planet. Using a 1-D EBM, we show in Chaverot et al. (in prep.) that the snowball Earth seems very resilient to these two stochastic events (see Sect. 6.2). We conclude that even if larger events than what we consider in our work could happen on exoplanets, there is no geological record of this on Earth. This conclusion is in favor of the main scenario explaining the deglaciation of the young Earth, thanks to high CO_2 content (e.g. Pierrehumbert 2004 ; Pierrehumbert et al. 2011).

7.2 Prospects

The anthropological global warming happening on Earth motivated the development of numerical climate models. Regarding the dramatic consequences of the climate change we - humanity - initiated, an international scientific consortium, named IPCC (Intergovernmental Panel on Climate Change), was created in 1988, by the World Meteorological Organization (WMO) and United Nations (UN), to provide policymakers with regular assessments of the scientific basis of climate change, its impacts and future risks. Earth climate models improved rapidly to become extremely accurate and precise, including among other processes the ocean circulation, vegetation, subtle micro-physics effects of cloud formation. The negative point is that such extremely models, fine-tuned to the Earth conditions, are not versatile. From my point of view, there is a real interest to adapt the generic tools we use and develop to the study of exoplanets in the context of Earth's climate change. This work has been initiated by Leconte et al. (2013) adapting the water cycle (and more precisely the micro-physics parameterizations) to the case of the Earth. Indeed, IPPC models are not able to simulate a climate too far from current Earth conditions, thus generic models can be a valuable resource. Numerous questions on the long term impact of global warming cannot be studied by Earth's focused models, while Generic GCMs can. For example, what could be the climate beyond year 2200 by following the 8.5 IPCC scenario ? This question could be studied with the Generic-PCM but require some numerical development to get closer to the specific case of the Earth, with a sufficient accuracy to quantify the impact of hundreds of part-per-million of gas.

As written in the introduction of this manuscript, the runaway greenhouse was initially studied in the context of the Earth and Venus. As shown as well, the composition of the atmosphere is of major importance to estimate the onset of the runaway greenhouse and at the same time the inner edge of the HZ. Therefore, in the context of climate change, a burning question is to known if high quantities of CO2 can trigger a runaway greenhouse on Earth. Several works studied this point with GCMs (e.g., Popp et al. 2016 ; Wolf et al. 2018) but there is no consensus so far on the required CO_2 pressure. Popp et al. (2016) argue that 1520 ppm of CO_2 are sufficient to initiate a moist greenhouse state. On the other side, Wolf et al. (2018) conclude that a few bars of CO_2 are needed to trigger a runaway greenhouse. A deep investigating work is needed to understand the differences between the models

and highlight the processes explaining these different results[2]. There is no more consensus by using simpler 1D radiative-convective models. For example, Goldblatt et al. (2013) show that a runaway can be triggered by CO_2 while Ramirez et al. (2014) do not. Therefore, there is a real need to revisit these works, with spectroscopic corrections from the most recent experimental values existing for CO_2 to try to reconcile the literature. By increasing significantly the CO_2 content, some subtle spectroscopic effects which are negligible when CO_2 is a minor constituent (thus often neglected by Earth focused models) needs to be taken into account. Moreover, several works studied the effect of CO_2 on the inner edge of the HZ (e.g., Goldblatt et al. 2013 ; Ramirez et al. 2014) or CH_4 on the outer edge (e.g., Ramirez & Kaltenegger 2018), but as far as I know there is no work studying the combined effect of CO_2 and CH_4 on triggering a runaway greenhouse. Regarding the intense potential warming effect of CH_4, a new estimation of the onset of the runaway greenhouse with an effort done on the accuracy of the spectroscopic data could drastically change our very long term vision of the anthropological Earth warming. Thanks to a SNSF *Postdoc.Mobility*, I will work in this direction during the next two years to propose to the community updated opacity data based on CO_2 and CH_4, and to try to understand a bit more the potential long term effects of our impact on the Earth's climate by performing GCM simulations using the Generic-PCM. This will also have implications on our understanding of the possible evolution of terrestrial exoplanets by revisiting the boundaries of the HZ with updated spectroscopic data.

[2]Such model comparison is the aim of the CUISINES (Climates Using Interactive Suites of Intercomparisons Nested for Exoplanet Studies) consortium (see `https://nexss.info/cuisines/model-intercomparison-projects/`).

Appendix A

Publication list

A.1 Peer-reviewed research articles

6. **Chaverot, G.**, Bolmont, E., Turbet, M. (2023) *First exploration of the runaway greenhouse transition with a GCM*. Astronomy & Astrophysics, Volume 680, id.A103, 15 pp.

5. Turbet, M., Fauchez, T., Leconte, J., ... **Chaverot, G.** ... et al. (2023) *Water Condensation Zones around Main Sequence Stars*. Astronomy & Astrophysics, Volume 679, id.A126, 36 pp.

4. Selsis, F., Leconte, J., Turbet, M., **Chaverot, G.**, Bolmont, E. (2023) *A cool runaway greenhouse without surface magma ocean*. Nature, Volume 620, Issue 7973, p.287-291

3. **Chaverot, G.**, Turbet, M., Bolmont, E., Leconte, J. (2022) *How does the background atmosphere affect the onset of the runaway greenhouse ?* Astronomy & Astrophysics, Volume 658, id.A40, 20 pp.

2. Turbet, M., Bolmont, E., **Chaverot, G.**, Ehrenreich, D., Leconte, J., Marcq, E. (2021) *Day–night cloud asymmetry prevents early oceans on Venus but not on Earth*. Nature, Volume 598, Issue 7880, p.276-280

1. Fauchez, T., Turbet, M., Sergeev, D., ... **Chaverot, G.** ... et al. (2021) *TRAPPIST Habitable Atmosphere Intercomparison (THAI) workshop report*. The Planetary Science Journal, Volume 2, Issue 3, id.106, 28 pp.

- **Chaverot, G.**, Zorzi A., Ding, X., et al. (in prep.) *Resilience of Snowball Earth to stochastic events*. AGU Journal

- Mignon, L., Bonfils, X., Meunier, N., ... **Chaverot, G.** ... et al. (in prep.) *RV homogeneous analysis of an H.A.R.P.S sample of M-Dwarfs. II. Detection limits and planetary occurrence statistic*. Astronomy & Astrophysics

- Ji, A., Tomazzeli, O., Palancar, G., **Chaverot, G.**, et al. (in prep.) *A Correlated-k Parameterization for O2 Photolysis in the Schumann-Runge Bands*

- Forget, F., Turbet, M., Wordsworth, R., ... **Chaverot, G.** ... et al. (in prep.) *The Generic Planetary Climate Model (Generic PCM): A model to simulate the environment on any present or past planet and exoplanets*

A.2 Peer-reviewed contributions through on-site and remote observations

5. Barbato, D., Ségransan, D., Udry, S., ... **Chaverot, G.** ... et al. (2023) *The CORALIE survey for southern extrasolar planets XIX. Brown dwarfs and stellar companions unveiled by radial velocity and astrometry*. Astronomy & Astrophysics, Volume 674, id.A114, 34 pp.

4. Brahm, R., Ulmer-Moll, S., Hobson, M., ... **Chaverot, G.** ... et al. (2023) *Three long period transiting giant planets from TESS*. The Astronomical Journal, Volume 165, Issue 6, id.227, 17 pp.

3. Zhang, Y., Snellen, I., Wyttenbach, A., ... **Chaverot, G.** ... et al. (2022) *Transmission spectroscopy of the ultra-hot Jupiter MASCARA-4 b Disentangling the hydrostatic and exospheric regimes of ultra-hot Jupiters*. Astronomy & Astrophysics, Volume 666, id.A47, 13 pp.

2. Ulmer-Moll, S., Lendl, M., Gill, S., ... **Chaverot, G.** ... et al. (2022) *Two long-period transiting exoplanets on eccentric orbits:NGTS-20 b (TOI-5152b) and TOI-5153 b*. Astronomy & Astrophysics, Volume 666, id.A46, 17 pp.

1. Rodriguez, J., Quinn, S., Zhou, G., ... **Chaverot, G.** ... et al. (2021) *TESS Delivers Five New Hot Giant Planets Orbiting Bright Stars from the Full Frame Images*. The Astronomical Journal, Volume 161, Issue 4, id.194, 25 pp.

- Grieves, N., Bouchy, F., Amstrong, D. J., ... **Chaverot, G.** ... et al. (submitted) *Refining the WASP-132 multi-planetary system: discovery of a cold giant planet and mass measurement of a hot super-Earth*. Astronomy & Astrophysics

A.3 Other contributions

- **Chaverot, G.** (2021). Adiabatic Processes. In: Gargaud, M., et al. Encyclopedia of Astrobiology. Springer, Berlin, Heidelberg. `https://doi.org/10.1007/978-3-642-27833-4_5504-1`

Bibliography

Abbot, D. S. & Pierrehumbert, R. T. (2010). Mudball: Surface dust and Snowball Earth deglaciation, *Journal of Geophysical Research: Atmospheres*, 115 (Cited on page 108.)

Abe, Y., Abe-Ouchi, A., Sleep, N. H., & Zahnle, K. J. (2011). Habitable Zone Limits for Dry Planets, *Astrobiology*, 11, 443 (Cited on page 9.)

Ahrer, E.-M., Alderson, L., Batalha, N. M., et al. (2023). Identification of carbon dioxide in an exoplanet atmosphere, *Nature*, 614, 649 (Cited on page 38.)

Amundsen, D. S., Tremblin, P., Manners, J., Baraffe, I., & Mayne, N. J. (2017). Treatment of overlapping gaseous absorption with the correlated- k method in hot Jupiter and brown dwarf atmosphere models, *Astronomy & Astrophysics*, 598, A97 (Cited on page 35.)

Andrault, D., Pesce, G., Manthilake, G., et al. (2018). Deep and persistent melt layer in the Archaean mantle, *Nature Geoscience*, 11, 139 (Cited on page 100.)

Attia, O., Bourrier, V., Eggenberger, P., et al. (2021). The JADE code: Coupling secular exoplanetary dynamics and photo-evaporation, *Astronomy and Astrophysics*, 647, A40 (Cited on pages 21 and 128.)

Baglin, A., Auvergne, M., Boisnard, L., et al. (2006). CoRoT: a high precision photometer for stellar ecolution and exoplanet finding, 36, 3749 (Cited on page 4.)

Baranov, Y. I. (2018). Collision-induced absorption in the region of the $\nu 2 + \nu 3$ band of carbon dioxide, *Journal of Molecular Spectroscopy*, 345, 11 (Cited on page 41.)

Baranov, Y. I., Lafferty, W. J., & Fraser, G. T. (2004). Infrared spectrum of the continuum and dimer absorption in the vicinity of the O2 vibrational fundamental in O2/CO2 mixtures, *Journal of Molecular Spectroscopy*, 228, 432 (Cited on pages 31 and 41.)

Baranov, Y. I., Lafferty, W. J., & Fraser, G. T. (2005). Investigation of collision-induced absorption in the vibrational fundamental bands of O2 and N2 at elevated temperatures, *Journal of Molecular Spectroscopy*, 233, 160 (Cited on page 41.)

Baranov, Y. I., Lafferty, W. J., Fraser, G. T., & Vigasin, A. A. (2003). On the origin of the band structure observed in the collision-induced absorption bands of CO2, *Journal of Molecular Spectroscopy*, 218, 260 (Cited on page 41.)

Baranov, Y. I. & Vigasin, A. A. (1999). Collision-Induced Absorption by CO2in the Region of $\nu 1$, $2\nu 2$, *Journal of Molecular Spectroscopy*, 193, 319 (Cited on page 41.)

Barnes, R., Mullins, K., Goldblatt, C., et al. (2013). Tidal Venuses: Triggering a Climate Catastrophe via Tidal Heating, *Astrobiology*, 13, 225 (Cited on page 9.)

Barr, A. C., Dobos, V., & Kiss, L. L. (2018). Interior structures and tidal heating in the TRAPPIST-1 planets, *Astronomy and Astrophysics*, 613, A37 (Cited on pages 20 and 78.)

Benz, W., Broeg, C., Fortier, A., et al. (2021). The CHEOPS mission, *Experimental Astronomy*, 51, 109 (Cited on page 5.)

Bergsten, G. J., Pascucci, I., Mulders, G. D., Fernandes, R. B., & Koskinen, T. T. (2022). The Demographics of Kepler's Earths and Super-Earths into the Habitable Zone, *The Astronomical Journal*, 164, 190 (Cited on page 10.)

Beust, H., Bonfils, X., Montagnier, G., Delfosse, X., & Forveille, T. (2012). Dynamical evolution of the Gliese 436 planetary system. Kozai migration as a potential source for Gliese 436b's eccentricity, *Astronomy and Astrophysics*, 545, A88 (Cited on page 128.)

Biersteker, J. B. & Schlichting, H. E. (2019). Atmospheric mass-loss due to giant impacts: the importance of the thermal component for hydrogen–helium envelopes, *Monthly Notices of the Royal Astronomical Society*, 485, 4454 (Cited on page 108.)

Biersteker, J. B. & Schlichting, H. E. (2021). Losing oceans: The effects of composition on the thermal component of impact-driven atmospheric loss, *Monthly Notices of the Royal Astronomical Society*, 501, 587 (Cited on page 108.)

Birkmann, S. M., Ferruit, P., Giardino, G., et al. (2022). The Near-Infrared Spectrograph (NIRSpec) on the James Webb Space Telescope. IV. Capabilities and predicted performance for exoplanet characterization, *Astronomy and Astrophysics*, 661, A83 (Cited on page 5.)

Bolmont, E. 2018, in Handbook of Exoplanets, ed. H. J. Deeg & J. A. Belmonte (Cham: Springer International Publishing), 3069–3090 (Cited on page 9.)

Bolmont, E., Breton, S. N., Tobie, G., et al. (2020). Solid tidal friction in multi-layer planets: Application to Earth, Venus, a Super Earth and the TRAPPIST-1 planets. Potential approximation of a multi-layer planet as a homogeneous body, *Astronomy & Astrophysics*, 644, A165 (Cited on pages 20 and 78.)

Bolmont, E., Selsis, F., Owen, J. E., et al. (2017). Water loss from terrestrial planets orbiting ultracool dwarfs: implications for the planets of TRAPPIST-1, *Monthly Notices of the Royal Astronomical Society*, 464, 3728 (Cited on page 21.)

Bond, I. A., Udalski, A., Jaroszyński, M., et al. (2004). OGLE 2003-BLG-235/MOA 2003-BLG-53: A Planetary Microlensing Event, *The Astrophysical Journal*, 606, L155 (Cited on page 3.)

Borucki, W. J., Koch, D., Basri, G., et al. (2010). Kepler Planet-Detection Mission: Introduction and First Results, *Science*, 327, 977 (Cited on page 4.)

Boukrouche, R., Lichtenberg, T., & Pierrehumbert, R. T. (2021). Beyond Runaway: Initiation of the Post-runaway Greenhouse State on Rocky Exoplanets, *The Astrophysical Journal*, 919, 130 (Cited on pages 13, 14, 77, and 100.)

Bourrier, V., de Wit, J., Bolmont, E., et al. (2017). Temporal Evolution of the High-energy Irradiation and Water Content of TRAPPIST-1 Exoplanets, *The Astronomical Journal*, 154, 121 (Cited on page 21.)

Bower, D. J., Kitzmann, D., Wolf, A. S., et al. (2019). Linking the evolution of terrestrial interiors and an early outgassed atmosphere to astrophysical observations, *Astronomy & Astrophysics*, 631, A103 (Cited on page 20.)

Brown, L. R., Humphrey, C. M., & Gamache, R. R. (2007). CO2-broadened water in the pure rotation and $\nu 2$ fundamental regions, *Journal of Molecular Spectroscopy*, 246, 1 (Cited on page 42.)

Brunetti, M., Kasparian, J., & Vérard, C. (2019). Co-existing climate attractors in a coupled aquaplanet, *Climate Dynamics*, 53, 6293 (Cited on pages 106 and 107.)

Brunetti, M. & Ragon, C. (2023). Attractors and bifurcation diagrams in complex climate models, *Physical Review E*, 107, 054214 (Cited on pages 107 and 108.)

Bryson, S., Kunimoto, M., Kopparapu, R. K., et al. (2021). The Occurrence of Rocky Habitable-zone Planets around Solar-like Stars from Kepler Data, *The Astronomical Journal*, 161, 36 (Cited on page 10.)

Caldas, A., Leconte, J., Selsis, F., et al. (2019). Effects of a fully 3D atmospheric structure on exoplanet transmission spectra: retrieval biases due to day-night temperature gradients, *Astronomy and Astrophysics*, 623, A161 (Cited on page 97.)

Charbonneau, D., Brown, T. M., Latham, D. W., & Mayor, M. (2000). Detection of Planetary Transits Across a Sun-like Star, *The Astrophysical Journal*, 529, L45 (Cited on page 4.)

Charnay, B., Forget, F., Wordsworth, R., et al. (2013). Exploring the faint young Sun problem and the possible climates of the Archean Earth with a 3-D GCM, *Journal of Geophysical Research: Atmospheres*, 118, 10,414 (Cited on page 19.)

Chaverot, G., Bolmont, E., & Turbet, M. (2023). First exploration of the runaway greenhouse transition with a 3D General Circulation Model, *Astronomy & Astrophysics*, 680, A103 (Cited on pages 10, 80, 81, 97, 98, 99, 100, and 134.)

Chaverot, G., Turbet, M., Bolmont, E., & Leconte, J. (2022). How does the background atmosphere affect the onset of the runaway greenhouse ?, *Astronomy & Astrophysics*, 658, A40 (Cited on pages 14, 32, 35, 38, 48, 49, 51, 72, 74, 76, 77, 80, 102, and 134.)

Chaverot, G., Zorzi, A., Ding, X., et al. (in prep.). Resilience of Snowball Earth to stochastic events, *Geophysical Research Letters* (Cited on pages 108, 109, 127, and 135.)

Chen, R. E., Jiang, J. H., Rosen, P. E., Fahy, K. A., & Chen, Y. 2023, Exoplanets Around Red Giants: Distribution and Habitability, arXiv:2307.04975 [astro-ph] (Cited on page 10.)

Chistikov, D. N., Finenko, A. A., Lokshtanov, S. E., Petrov, S. V., & Vigasin, A. A. (2019). Simulation of collision-induced absorption spectra based on classical trajectories and ab initio potential and induced dipole surfaces. I. Case study of N2–N2 rototranslational band, *The Journal of Chemical Physics*, 151, 194106 (Cited on page 41.)

Codron, F. (2012). Ekman heat transport for slab oceans, *Climate Dynamics*, 38, 379 (Cited on page 19.)

Cohen, O., Ma, Y., Drake, J. J., et al. (2015). The Interaction of Venus-like, M-dwarf Planets with the Stellar Wind of Their Host Star, *The Astrophysical Journal*, 806, 41 (Cited on page 21.)

Dorn, C. & Lichtenberg, T. (2021). Hidden Water in Magma Ocean Exoplanets, *The Astrophysical Journal*, 922, L4 (Cited on pages 78 and 101.)

Dorn, C., Noack, L., & Rozel, A. B. (2018). Outgassing on stagnant-lid super-Earths, *Astronomy and Astrophysics*, 614, A18 (Cited on pages 20 and 128.)

Dressing, C. D. & Charbonneau, D. (2015). The Occurrence of Potentially Habitable Planets Orbiting M Dwarfs Estimated from the Full Kepler Dataset and an Empirical Measurement of the Detection Sensitivity, *The Astrophysical Journal*, 807, 45 (Cited on page 10.)

Dressing, C. D., Spiegel, D. S., Scharf, C. A., Menou, K., & Raymond, S. N. (2010). Habitable Climates: The Influence of Eccentricity, *The Astrophysical Journal*, 721, 1295 (Cited on page 16.)

Dubos, T., Dubey, S., Tort, M., et al. (2015). DYNAMICO-1.0, an icosahedral hydrostatic dynamical core designed for consistency and versatility, *Geoscientific Model Development*, 8, 3131 (Cited on page 18.)

Ercolano, B. & Clarke, C. J. (2010). Metallicity, planet formation and disc lifetimes, *Monthly Notices of the Royal Astronomical Society*, 402, 2735 (Cited on page 21.)

Falco, A., Zingales, T., Pluriel, W., & Leconte, J. (2022). Toward a multidimensional analysis of transmission spectroscopy. I. Computation of transmission spectra using a 1D, 2D, or 3D atmosphere structure, *Astronomy and Astrophysics*, 658, A41 (Cited on page 97.)

Fauchez, T. J., Turbet, M., Villanueva, G. L., et al. (2019). Impact of Clouds and Hazes on the Simulated JWST Transmission Spectra of Habitable Zone Planets in the TRAPPIST-1 System, *The Astrophysical Journal*, 887, 194 (Cited on pages 5 and 100.)

Fauchez, T. J., Villanueva, G. L., Sergeev, D. E., et al. (2022). The TRAPPIST-1 Habitable Atmosphere Intercomparison (THAI). III. Simulated Observables—the Return of the Spectrum, *The Planetary Science Journal*, 3, 213 (Cited on page 99.)

Fleurbaey, H., Campargue, A., Carreira Mendès Da Silva, Y., et al. (2022). Characterization of the H2O+CO2 continuum within the infrared transparency windows, *Journal of Quantitative Spectroscopy and Radiative Transfer*, 282, 108119 (Cited on pages 41 and 42.)

Forget, F., Hourdin, F., Fournier, R., et al. (1999). Improved general circulation models of the Martian atmosphere from the surface to above 80 km, *Journal of Geophysical Research: Planets*, 104, 24155 (Cited on page 18.)

Forget, F. & Leconte, J. (2014). Possible climates on terrestrial exoplanets, *Philosophical Transactions of the Royal Society of London Series A*, 372, 20130084 (Cited on page 75.)

Forget, F., Turbet, M., Wordsworth, R., & et al. (in prep.). The Generic Planetary Climate Model (Generic PCM):1 A model to simulate the environment on any present or2 past planet and exoplanets, *Journal of Geophysical Research* (Cited on page 17.)

Frommhold, L. (1994). Collision-induced Absorption in Gases (Cambridge University Press) (Cited on page 31.)

Fu, Q. & Liou, K. N. (1992). On the correlated k-distribution method for radiative transfer in nonhomogeneous atmospheres, *Journal of Atmospheric Sciences*, 49, 2139 (Cited on pages 34 and 35.)

Fujii, Y., Del Genio, A. D., & Amundsen, D. S. (2017). NIR-driven Moist Upper Atmospheres of Synchronously Rotating Temperate Terrestrial Exoplanets, *The Astrophysical Journal*, 848, 100 (Cited on page 99.)

Fulton, B. J., Petigura, E. A., Howard, A. W., et al. (2017). The California-Kepler Survey. III. A Gap in the Radius Distribution of Small Planets, *The Astronomical Journal*, 154, 109 (Cited on page 21.)

Gao, P., Wakeford, H. R., Moran, S. E., & Parmentier, V. (2021). Aerosols in Exoplanet Atmospheres, *Journal of Geophysical Research (Planets)*, 126, e06655 (Cited on page 97.)

Garland, R. & Irwin, P. G. J. (2019). Effectively Calculating Gaseous Absorption in Radiative Transfer Models of Exoplanetary and Brown Dwarf Atmospheres (Cited on pages 34, 35, and 36.)

Goldblatt, C. (2015). Habitability of waterworlds: runaway greenhouses, atmospheric expansion and multiple climate states of pure water atmospheres, *Astrobiology*, 15, 362 (Cited on page 19.)

Goldblatt, C., Robinson, T. D., Zahnle, K. J., & Crisp, D. (2013). Low simulated radiation limit for runaway greenhouse climates, *Nature Geoscience*, 6, 661 (Cited on pages 9, 13, 14, 43, 48, 75, and 136.)

Goldblatt, C. & Watson, A. J. (2012). The runaway greenhouse: implications for future climate change, geoengineering and planetary atmospheres, *Philosophical Transactions of the Royal Society A: Mathematical, Physical and Engineering Sciences*, 370, 4197 (Cited on pages 10 and 13.)

Gonzalez, G., Brownlee, D., & Ward, P. (2001). The Galactic Habitable Zone: Galactic Chemical Evolution, *Icarus*, 152, 185 (Cited on page 13.)

Gordon, I. E., Rothman, L. S., Hargreaves, R. J., et al. (2021). The HITRAN2020 molecular spectroscopic database, *Journal of Quantitative Spectroscopy and Radiative Transfer*, 107949 (Cited on pages 27, 43, and 75.)

Gordon, I. E., Rothman, L. S., Hill, C., et al. (2017). The HITRAN2016 molecular spectroscopic database, *Journal of Quantitative Spectroscopy and Radiative Transfer*, 203, 3 (Cited on page 27.)

Grasset, O., Dougherty, M. K., Coustenis, A., et al. (2013). JUpiter ICy moons Explorer (JUICE): An ESA mission to orbit Ganymede and to characterise the Jupiter system, *Planetary and Space Science*, 78, 1 (Cited on page 7.)

Greene, T. P., Bell, T. J., Ducrot, E., et al. (2023). Thermal Emission from the Earth-sized Exoplanet TRAPPIST-1 b using JWST, *Nature*, 1 (Cited on page 6.)

Grenfell, J. L., Leconte, J., Forget, F., et al. (2020). Possible Atmospheric Diversity of Low Mass Exoplanets - Some Central Aspects, *Space Science Reviews*, 216, 98 (Cited on page 75.)

Grimm, S. L., Malik, M., Kitzmann, D., et al. (2021). HELIOS-K 2.0 Opacity Calculator and Open-source Opacity Database for Exoplanetary Atmospheres, *The Astrophysical Journal Supplement Series*, 253, 30 (Cited on page 134.)

Gronoff, G., Arras, P., Baraka, S., et al. (2020). Atmospheric Escape Processes and Planetary Atmospheric Evolution, *Journal of Geophysical Research (Space Physics)*, 125, e27639 (Cited on pages 21 and 101.)

Gruszka, M. & Borysow, A. (1997). Roto-Translational Collision-Induced Absorption of CO2for the Atmosphere of Venus at Frequencies from 0 to 250 cm-1, at Temperatures from 200 to 800 K, *Icarus*, 129, 172 (Cited on page 41.)

Guillot, T., Fletcher, L. N., Helled, R., et al. (2022). Giant Planets from the Inside-Out (Cited on page 75.)

Hall, C., Stancil, P. C., Terry, J. P., & Ellison, C. K. (2023). A New Definition of Exoplanet Habitability: Introducing the Photosynthetic Habitable Zone, *The Astrophysical Journal*, 948, L26 (Cited on page 12.)

Hamano, K., Abe, Y., & Genda, H. (2013). Emergence of two types of terrestrial planet on solidification of magma ocean, *Nature*, 497, 607 (Cited on pages 14, 20, and 128.)

Hara, N. C. & Ford, E. B. (2023). Statistical Methods for Exoplanet Detection with Radial Velocities, *Annual Review of Statistics and Its Application*, 10, 623 (Cited on page 4.)

Hart, M. H. (1978). The evolution of the atmosphere of the earth, *Icarus*, 33, 23 (Cited on pages 8 and 13.)

Hartmann, J., Boulet, C., & Robert, D. (2021). Collisional Effects on Molecular Spectra: Laboratory Experiments and Models, Consequences for Applications (Cited on page 30.)

Hartmann, J.-M., Boulet, C., & Toon, G. C. (2017). Collision-induced absorption by N2 near 2.16 μm: Calculations, model, and consequences for atmospheric remote sensing, *Journal of Geophysical Research: Atmospheres*, 122, 2419 (Cited on page 41.)

Hartmann, J.-M., Boulet, C., Tran, D. D., Tran, H., & Baranov, Y. (2018). Effect of humidity on the absorption continua of CO2 and N2 near 4 μm: Calculations, comparisons with measurements, and consequences for atmospheric spectra, *The Journal of Chemical Physics*, 148, 054304 (Cited on page 41.)

Hill, M. L., Bott, K., Dalba, P. A., et al. (2022). A Catalog of Habitable Zone Exoplanets, 2687, 3046 (Cited on pages 10 and 75.)

Hoffman, P. F., Abbot, D. S., Ashkenazy, Y., et al. (2017). Snowball Earth climate dynamics and Cryogenian geology-geobiology, *Science Advances*, 3, e1600983 (Cited on pages 102 and 106.)

Hourdin, F., Van, P. L., Forget, F., & Talagrand, O. (1993). Meteorological Variability and the Annual Surface Pressure Cycle on Mars, *Journal of the Atmospheric Sciences*, 50, 3625 (Cited on page 17.)

Howell, S. M. & Pappalardo, R. T. (2020). NASA's Europa Clipper—a mission to a potentially habitable ocean world, *Nature Communications*, 11, 1311 (Cited on page 7.)

Huang, S.-S. (1959). Occurrence of Life in the Universe, *American Scientist*, 47, 397 (Cited on page 8.)

Ingersoll, A. P. (1969). The Runaway Greenhouse: A History of Water on Venus, *Journal of the Atmospheric Sciences*, 26, 1191 (Cited on pages 10, 13, 33, and 48.)

Innes, H., Tsai, S.-M., & Pierrehumbert, R. T. 2023, The Runaway Greenhouse Effect on Hycean Worlds, publication Title: arXiv e-prints ADS Bibcode: 2023arXiv230402698I (Cited on page 78.)

Ishiwatari, M., Takehiro, S.-i., Nakajima, K., & Hayashi, Y.-Y. (2002). A Numerical Study on Appearance of the Runaway Greenhouse State of a Three-Dimensional Gray Atmosphere, *Journal of the Atmospheric Sciences*, 59, 3223 (Cited on page 33.)

Johnstone, C. P. (2020). Hydrodynamic Escape of Water Vapor Atmospheres near Very Active Stars, *The Astrophysical Journal*, 890, 79 (Cited on page 21.)

Kadoya, S. & Tajika, E. (2019). Outer Limits of the Habitable Zones in Terms of Climate Mode and Climate Evolution of Earth-like Planets, *The Astrophysical Journal*, 875, 7 (Cited on page 12.)

Kane, S. R., Ceja, A. Y., Way, M. J., & Quintana, E. V. (2018). Climate Modeling of a Potential ExoVenus, *The Astrophysical Journal*, 869, 46 (Cited on page 80.)

Karman, T., Gordon, I. E., van der Avoird, A., et al. (2019). Update of the HITRAN collision-induced absorption section, *Icarus*, 328, 160 (Cited on pages 31 and 40.)

Karman, T., Koenis, M. A. J., Banerjee, A., et al. (2018). O2-O2 and O2-N2 collision-induced absorption mechanisms unravelled, *Nature Chemistry*, 10, 549 (Cited on page 31.)

Kasting, J. F. (1988). Runaway and moist greenhouse atmospheres and the evolution of Earth and Venus, *Icarus*, 74, 472 (Cited on pages 10, 11, 13, 15, 48, and 49.)

Kasting, J. F., Whitmire, D. P., & Reynolds, R. T. (1993). Habitable Zones around Main Sequence Stars, *Icarus*, 101, 108 (Cited on pages 10, 14, and 48.)

Kegerreis, J. A., Eke, V. R., Massey, R. J., & Teodoro, L. F. A. (2020). Atmospheric Erosion by Giant Impacts onto Terrestrial Planets, *The Astrophysical Journal*, 897, 161 (Cited on page 108.)

Kempton, E. M.-R., Lessard, M., Malik, M., et al. 2023, Where are the Water Worlds ?: Self-Consistent Models of Water-Rich Exoplanet Atmospheres, arXiv:2307.06508 [astro-ph] (Cited on page 78.)

Koll, D. D. B. & Cronin, T. W. (2018). Earth's outgoing longwave radiation linear due to H $_2$ O greenhouse effect, *Proceedings of the National Academy of Sciences*, 115, 10293 (Cited on page 48.)

Koll, D. D. B. & Cronin, T. W. (2019). Hot Hydrogen Climates Near the Inner Edge of the Habitable Zone, *The Astrophysical Journal*, 881, 120 (Cited on pages 9, 14, 33, and 48.)

Komabayasi, M. (1967). Discrete Equilibrium Temperatures of a Hypothetical Planet with the Atmosphere and the Hydrosphere of One Component-Two Phase System under Constant Solar Radiation, *Journal of the Meteorological Society of Japan. Ser. II*, 45, 137 (Cited on page 13.)

Kopparapu, R. K., Ramirez, R., Kasting, J. F., et al. (2013). Habitable Zones around Main-sequence Stars: New Estimates, *The Astrophysical Journal*, 765, 131 (Cited on pages 9, 10, 11, 12, 13, 14, 43, 74, 75, 77, 128, and 134.)

Kopparapu, R. K., Ramirez, R. M., SchottelKotte, J., et al. (2014). Habitable Zones around Main-sequence Stars: Dependence on Planetary Mass, *The Astrophysical Journal*, 787, L29 (Cited on pages 9, 10, 14, 48, and 77.)

Kopparapu, R. k., Wolf, E. T., Arney, G., et al. (2017). Habitable Moist Atmospheres on Terrestrial Planets near the Inner Edge of the Habitable Zone around M Dwarfs, *The Astrophysical Journal*, 845, 5 (Cited on pages 9, 11, 14, 80, and 128.)

Kopparapu, R. k., Wolf, E. T., Haqq-Misra, J., et al. (2016). The inner edge of the habitable zone for synchronously rotating planets around low-mass stars using general circualtion models, *The Astrophysical Journal*, 819, 84 (Cited on pages 11, 14, 80, and 106.)

Kozai, Y. (1962). Secular perturbations of asteroids with high inclination and eccentricity, *The Astronomical Journal*, 67, 591 (Cited on page 128.)

Krissansen-Totton, J. & Fortney, J. J. (2022). Predictions for Observable Atmospheres of Trappist-1 Planets from a Fully Coupled Atmosphere-Interior Evolution Model (Cited on page 20.)

Lacis, A. A. & Oinas, V. (1991). A description of the correlated-k distribution method for modelling nongray gaseous absorption, thermal emission, and multiple scattering in vertically inhomogeneous atmospheres, *Journal of Geophysical Research*, 96, 9027 (Cited on page 34.)

Lafferty, W. J., Solodov, A. M., Weber, A., Olson, W. B., & Hartmann, J.-M. (1996). Infrared collision-induced absorption by N_2 near 4.3 μm for atmospheric applications: measurements and empirical modeling, *Applied Optics*, 35, 5911 (Cited on pages 31 and 41.)

Lainey, V., Arlot, J.-E., Karatekin, Ö., & Van Hoolst, T. (2009). Strong tidal dissipation in Io and Jupiter from astrometric observations, *Nature*, 459, 957 (Cited on page 20.)

Lebrun, T., Massol, H., ChassefièRe, E., et al. (2013). Thermal evolution of an early magma ocean in interaction with the atmosphere, *Journal of Geophysical Research (Planets)*, 118, 1155 (Cited on pages 20 and 128.)

Lecavelier Des Etangs, A. (2007). A diagram to determine the evaporation status of extrasolar planets, *Astronomy and Astrophysics*, 461, 1185 (Cited on page 21.)

Leconte, J. (2021). Spectral binning of precomputed correlated-k coefficients, *Astronomy and Astrophysics*, 645, A20 (Cited on pages 35, 36, and 38.)

Leconte, J., Forget, F., Charnay, B., Wordsworth, R., & Pottier, A. (2013). Increased insolation threshold for runaway greenhouse processes on Earth-like planets, *Nature*, 504, 268 (Cited on pages 10, 11, 14, 19, 80, 102, 106, 128, 134, and 135.)

Lefèvre, M., Turbet, M., & Pierrehumbert, R. (2021). 3D Convection-resolving Model of Temperate, Tidally Locked Exoplanets, *The Astrophysical Journal*, 913, 101 (Cited on page 19.)

Lichtenberg, T., Bower, D. J., Hammond, M., et al. (2021). Vertically resolved magma ocean-protoatmosphere evolution: H2, H2O, CO2, CH4, CO, O2, and N2 as primary absorbers, *Journal of Geophysical Research: Planets* (Cited on page 20.)

Lichtenberg, T., Schaefer, L. K., Nakajima, M., & Fischer, R. A. (2022). Geophysical Evolution During Rocky Planet Formation (Cited on pages 20 and 128.)

Lineweaver, C. H., Fenner, Y., & Gibson, B. K. (2004). The Galactic Habitable Zone and the Age Distribution of Complex Life in the Milky Way, *Science*, 303, 59 (Cited on page 13.)

Liou, K. N. (1980). An introduction to atmospheric radiation. (Cited on page 34.)

Lopez, E. D. (2017). Born dry in the photoevaporation desert: Kepler's ultra-short-period planets formed water-poor, *Monthly Notices of the Royal Astronomical Society*, 472, 245 (Cited on page 21.)

Lopez, E. D., Fortney, J. J., & Miller, N. (2012). How Thermal Evolution and Mass-loss Sculpt Populations of Super-Earths and Sub-Neptunes: Application to the Kepler-11 System and Beyond, *The Astrophysical Journal*, 761, 59 (Cited on page 21.)

Lovis, C., Blind, N., Chazelas, B., et al. (2022). RISTRETTO: high-resolution spectroscopy at the diffraction limit of the VLT, 12184, 121841Q (Cited on pages 6 and 100.)

Lucarini, V., Serdukova, L., & Margazoglou, G. (2022). Lévy noise versus Gaussian-noise-induced transitions in the Ghil–Sellers energy balance model, *Nonlinear Processes in Geophysics*, 29, 183 (Cited on page 127.)

Luger, R. & Barnes, R. (2015). Extreme Water Loss and Abiotic O2Buildup on Planets Throughout the Habitable Zones of M Dwarfs, *Astrobiology*, 15, 119 (Cited on page 101.)

Luque, R. & Pallé, E. (2022). Density, not radius, separates rocky and water-rich small planets orbiting M dwarf stars, *Science*, 377, 1211 (Cited on page 78.)

Lustig-Yaeger, J., Meadows, V. S., & Lincowski, A. P. (2019). The Detectability and Characterization of the TRAPPIST-1 Exoplanet Atmospheres with JWST, *The Astronomical Journal*, 158, 27 (Cited on page 5.)

Macdonald, F. A. & Wordsworth, R. (2017). Initiation of Snowball Earth with volcanic sulfur aerosol emissions, *Geophysical Research Letters*, 44, 1938 (Cited on page 108.)

Madeleine, J.-B. (2011). Nuages et poussières de l'atmosphère martienne: télédétection, modélisation des rétroactions climatiques et application aux paléoclimats, phdthesis, Université Pierre et Marie Curie - Paris VI (Cited on page 18.)

Makarov, V. V., Berghea, C. T., & Efroimsky, M. (2018). Spin-orbital Tidal Dynamics and Tidal Heating in the TRAPPIST-1 Multiplanet System, *The Astrophysical Journal*, 857, 142 (Cited on pages 20 and 78.)

Manabe, S. & Wetherald, R. T. (1967). Thermal Equilibrium of the Atmosphere with a Given Distribution of Relative Humidity, *Journal of the Atmospheric Sciences*, 24, 241 (Cited on page 15.)

Marconi, A., Abreu, M., Adibekyan, V., et al. (2022). ANDES, the high resolution spectrograph for the ELT: science case, baseline design and path to construction, 12184, 1218424 (Cited on pages 6 and 100.)

Marcq, E., Salvador, A., Massol, H., & Davaille, A. (2017). Thermal radiation of magma ocean planets using a 1-D radiative-convective model of H2O-CO2 atmospheres, *Journal of Geophysical Research (Planets)*, 122, 1539 (Cited on page 48.)

Marois, C., Zuckerman, B., Konopacky, Q. M., Macintosh, B., & Barman, T. (2010). Images of a fourth planet orbiting HR 8799, *Nature*, 468, 1080 (Cited on page 3.)

May, E. M., Taylor, J., Komacek, T. D., Line, M. R., & Parmentier, V. (2021). Water Ice Cloud Variability and Multi-epoch Transmission Spectra of TRAPPIST-1e, *The Astrophysical Journal Letters*, 911, L30 (Cited on page 99.)

Mayor, M. & Queloz, D. (1995). A Jupiter-mass companion to a solar-type star, *Nature*, 378, 355 (Cited on pages 2, 3, and 4.)

Meador, W. E. & Weaver, W. R. (1980). Two-Stream Approximations to Radiative Transfer in Planetary Atmospheres: A Unified Description of Existing Methods and a New Improvement, *Journal of the Atmospheric Sciences*, 37, 630 (Cited on page 18.)

Mlawer, E. J., Payne, V. H., Moncet, J.-L., et al. (2012). Development and recent evaluation of the MT_CKD model of continuum absorption, *Philosophical Transactions of the Royal Society of London Series A*, 370, 2520 (Cited on pages 31, 40, and 41.)

Mlawer, E. J., Turner, D. D., Paine, S. N., et al. (2019). Analysis of Water Vapor Absorption in the Far-Infrared and Submillimeter Regions Using Surface Radiometric Measurements From Extremely Dry Locations, *Journal of Geophysical Research: Atmospheres*, 124, 8134 (Cited on pages 31 and 40.)

Modirrousta-Galian, D. & Korenaga, J. (2023). The Three Regimes of Atmospheric Evaporation for Super-Earths and Sub-Neptunes, *The Astrophysical Journal*, 943, 11 (Cited on page 21.)

Morley, C. V., Kreidberg, L., Rustamkulov, Z., Robinson, T., & Fortney, J. J. (2017). Observing the Atmospheres of Known Temperate Earth-sized Planets with JWST, *The Astrophysical Journal*, 850, 121 (Cited on page 5.)

Nakajima, S., Hayashi, Y.-Y., & Abe, Y. (1992). A Study on the "Runaway Greenhouse Effect" with a One-Dimensional Radiative–Convective Equilibrium Model, *Journal of the Atmospheric Sciences*, 49, 2256 (Cited on pages 13, 33, and 48.)

Nakayama, A., Ikoma, M., & Terada, N. (2022). Survival of Terrestrial N2-O2 Atmospheres in Violent XUV Environments through Efficient Atomic Line Radiative Cooling, *The Astrophysical Journal*, 937, 72 (Cited on page 21.)

Otegi, J. F., Dorn, C., Helled, R., et al. (2020). Impact of the measured parameters of exoplanets on the inferred internal structure, *Astronomy and Astrophysics*, 640, A135 (Cited on page 78.)

Owen, J. E. (2019). Atmospheric Escape and the Evolution of Close-In Exoplanets, *Annual Review of Earth and Planetary Sciences*, 47, 67 (Cited on pages 20, 21, and 101.)

Perrin, M. Y. & Hartmann, J. M. (1989). Temperature-dependent measurements and modeling of absorption by CO2-N2 mixtures in the far line-wings of the 4.3 μm CO2 band., *Journal of Quantitative Spectroscopy and Radiative Transfer*, 42, 311 (Cited on pages 40 and 41.)

Peterson, M. S., Benneke, B., Collins, K., et al. (2023). A temperate Earth-sized planet with tidal heating transiting an M6 star, *Nature*, 617, 701 (Cited on page 20.)

Petrovich, C. (2015). Hot Jupiters from Coplanar High-eccentricity Migration, *The Astrophysical Journal*, 805, 75 (Cited on page 128.)

Pierrehumbert, R. & Gaidos, E. (2011). Hydrogen Greenhouse Planets Beyond the Habitable Zone, *The Astrophysical Journal*, 734, L13 (Cited on page 12.)

Pierrehumbert, R. T. (2004). High levels of atmospheric carbon dioxide necessary for the termination of global glaciation, *Nature*, 429, 646 (Cited on page 135.)

Pierrehumbert, R. T. (2010). Principles of planetary climate (Cambridge ; New York: Cambridge University Press) (Cited on pages 49, 50, 51, 74, and 106.)

Pierrehumbert, R. T. (2023). The Runaway Greenhouse on Sub-Neptune Waterworlds, *The Astrophysical Journal*, 944, 20 (Cited on page 78.)

Pierrehumbert, R. T., Abbot, D. S., Voigt, A., & Koll, D. (2011). Climate of the Neoproterozoic, *Annual Review of Earth and Planetary Sciences*, 39, 417 (Cited on pages 9, 16, and 135.)

Popp, M., Schmidt, H., & Marotzke, J. (2015). Initiation of a Runaway Greenhouse in a Cloudy Column, *Journal of Atmospheric Sciences*, 72, 452 (Cited on page 11.)

Popp, M., Schmidt, H., & Marotzke, J. (2016). Transition to a Moist Greenhouse with CO 2 and solar forcing, *Nature Communications*, 7, 10627 (Cited on pages 11, 14, 80, and 135.)

Pörtner, H. O., Roberts, D. C., Tignor, M., et al. (2022). Climate Change 2022: Impacts, Adaptation and Vulnerability, ed. H. O. Pörtner, D. C. Roberts, M. Tignor, E. S. Poloczanska, K. Mintenbeck, A. Alegría, M. Craig, S. Langsdorf, S. Löschke, V. Möller, A. Okem, & B. Rama (Cambridge, UK and New York, USA: Cambridge University Press) (Cited on page 9.)

Quanz, S. (2019). The LIFE mission: a space mission designed to characterize terrestrial exoplanet atmospheres, 13, EPSC (Cited on page 6.)

Rackham, B. V., Apai, D., & Giampapa, M. S. (2018). The Transit Light Source Effect: False Spectral Features and Incorrect Densities for M-dwarf Transiting Planets, *The Astrophysical Journal*, 853, 122 (Cited on page 5.)

Ramirez, R. (2014). Terrestrial Planets Under Extreme Radiative Forcings: Applications to Habitable Zones, Early Mars, and a High-Carbon Dioxide Earth, PhD thesis (Cited on page 43.)

Ramirez, R. M. (2018). A More Comprehensive Habitable Zone for Finding Life on Other Planets, *Geosciences*, 8, 280 (Cited on pages 9 and 10.)

Ramirez, R. M. (2020). The effect of high nitrogen pressures on the habitable zone and an appraisal of greenhouse states, *Monthly Notices of the Royal Astronomical Society*, 494, 259 (Cited on page 9.)

Ramirez, R. M. & Kaltenegger, L. (2017). A Volcanic Hydrogen Habitable Zone, *The Astrophysical Journal*, 837, L4 (Cited on page 12.)

Ramirez, R. M. & Kaltenegger, L. (2018). A Methane Extension to the Classical Habitable Zone, *The Astrophysical Journal*, 858, 72 (Cited on pages 12 and 136.)

Ramirez, R. M., Kopparapu, R. K., Lindner, V., & Kasting, J. F. (2014). Can Increased Atmospheric CO $_2$ Levels Trigger a Runaway Greenhouse ?, *Astrobiology*, 14, 714 (Cited on pages 14, 75, 76, and 136.)

Rieke, G. H., Wright, G. S., Böker, T., et al. (2015). The Mid-Infrared Instrument for the James Webb Space Telescope, I: Introduction, *Publications of the Astronomical Society of the Pacific*, 127, 584 (Cited on page 5.)

Rosseland, S. (1924). Note on the absorption of radiation within a star, *Monthly Notices of the Royal Astronomical Society*, 84, 525 (Cited on page 33.)

Rothman, L. S., Gordon, I. E., Babikov, Y., et al. (2013). The HITRAN2012 molecular spectroscopic database, *Journal of Quantitative Spectroscopy and Radiative Transfer*, 130, 4 (Cited on pages 27 and 75.)

Rothman, L. S., Gordon, I. E., Barber, R. J., et al. (2010). HITEMP, the high-temperature molecular spectroscopic database, *Journal of Quantitative Spectroscopy and Radiative Transfer*, 111, 2139 (Cited on page 43.)

Rothman, L. S., Jacquemart, D., Barbe, A., et al. (2005). The HITRAN 2004 molecular spectroscopic database, *Journal of Quantitative Spectroscopy and Radiative Transfer*, 96, 139 (Cited on pages 26, 27, and 40.)

Rustamkulov, Z., Sing, D. K., Mukherjee, S., et al. (2023). Early Release Science of the exoplanet WASP-39b with JWST NIRSpec PRISM, *Nature*, 614, 659 (Cited on page 38.)

Salvador, A. & Samuel, H. (2023). Convective outgassing efficiency in planetary magma oceans: Insights from computational fluid dynamics, *Icarus*, 390, 115265 (Cited on pages 20, 100, and 128.)

Schlichting, H. E., Sari, R., & Yalinewich, A. (2015). Atmospheric mass loss during planet formation: The importance of planetesimal impacts, *Icarus*, 247, 81 (Cited on page 108.)

Selsis, F., Kasting, J. F., Levrard, B., et al. (2007). Habitable planets around the star Gliese 581 ?, *Astronomy and Astrophysics*, 476, 1373 (Cited on page 10.)

Selsis, F., Leconte, J., Turbet, M., Chaverot, G., & Bolmont, É. (2023). A cool runaway greenhouse without surface magma ocean, *Nature*, 620, 287 (Cited on pages 14, 77, 78, and 100.)

Sergeev, D. E., Fauchez, T. J., Turbet, M., et al. (2021). The TRAPPIST-1 Habitable Atmosphere Intercomparison (THAI). Part II: Moist Cases – The Two Waterworlds (Cited on page 19.)

Shematovich, V. I., Ionov, D. E., & Lammer, H. (2014). Heating efficiency in hydrogen-dominated upper atmospheres, *Astronomy and Astrophysics*, 571, A94 (Cited on page 21.)

Shields, A. L., Bitz, C. M., Meadows, V. S., Joshi, M. M., & Robinson, T. D. (2014). Spectrum-driven Planetary Deglaciation due to Increases in Stellar Luminosity, *The Astrophysical Journal*, 785, L9 (Cited on pages 9, 102, and 106.)

Simpson, G. C. (1929). Some Studies in Terrestrial Radiation, *Quarterly Journal of the Royal Meteorological Society*, 55, 73 (Cited on pages 13 and 48.)

Sing, D. K., Fortney, J. J., Nikolov, N., et al. (2016). A continuum from clear to cloudy hot-Jupiter exoplanets without primordial water depletion, *Nature*, 529, 59 (Cited on page 5.)

Spaargaren, R. J., Ballmer, M. D., Bower, D. J., Dorn, C., & Tackley, P. J. (2020). The influence of bulk composition on the long-term interior-atmosphere evolution of terrestrial exoplanets, *Astronomy and Astrophysics*, 643, A44 (Cited on page 20.)

Spiegel, D. S., Menou, K., & Scharf, C. A. (2008). Habitable Climates, *The Astrophysical Journal*, 681, 1609 (Cited on page 16.)

Stamnes, K., Tsay, S. C., Jayaweera, K., & Wiscombe, W. (1988). Numerically stable algorithm for discrete-ordinate-method radiative transfer in multiple scattering and emitting layered media, *Applied Optics*, 27, 2502 (Cited on page 74.)

Stamnes, K., Tsay, S. C., Jayaweera, K., et al. (2017). DISORT: DIScrete Ordinate Radiative Transfer, *Astrophysics Source Code Library*, ascl:1708.006 (Cited on page 74.)

Stefani, S., Snels, M., Piccioni, G., Grassi, D., & Adriani, A. (2018). Temperature dependence of collisional induced absorption (CIA) bands of CO2 with implications for Venus' atmosphere, *Journal of Quantitative Spectroscopy and Radiative Transfer*, 204, 242 (Cited on page 41.)

Tian, F., Güdel, M., Johnstone, C. P., et al. (2018). Water Loss from Young Planets, *Space Science Reviews*, 214, 65 (Cited on page 21.)

Toon, O. B., McKay, C. P., Ackerman, T. P., & Santhanam, K. (1989). Rapid calculation of radiative heating rates and photodissociation rates in inhomogeneous multiple scattering atmospheres, *Journal of Geophysical Research*, 94, 16287 (Cited on page 18.)

Tort, M. (2015). Dynamique et Modélisation des Atmosphères Profondes, phdthesis, Ecole Polytechnique (Cited on page 19.)

Tran, H., Boulet, C., Stefani, S., Snels, M., & Piccioni, G. (2011). Measurements and modelling of high pressure pure CO2 spectra from 750 to 8500cm-1. I—central and wing regions of the allowed vibrational bands, *Journal of Quantitative Spectroscopy and Radiative Transfer*, 112, 925 (Cited on page 41.)

Tran, H., Turbet, M., Chelin, P., & Landsheere, X. (2018). Measurements and modeling of absorption by CO2 + H2O mixtures in the spectral region beyond the CO2 ν3-band head, *Icarus*, 306, 116 (Cited on pages 29, 40, and 41.)

Tran, H., Turbet, M., Hanoufa, S., et al. (2019). The CO2–broadened H2O continuum in the 100–1500 cm-1 region: Measurements, predictions and empirical model, *Journal of Quantitative Spectroscopy and Radiative Transfer*, 230, 75 (Cited on pages 40 and 41.)

Turbet, M. (2018). Habitability of planets using numerical climate models. Application to extrasolar planets and early Mars, phdthesis, Sorbonne Université (Cited on page 28.)

Turbet, M., Bolmont, E., Chaverot, G., et al. (2021). Day-night cloud asymmetry prevents early oceans on Venus but not on Earth, *Nature*, 598, 276 (Cited on pages 9, 13, 14, 80, 98, 99, 100, 101, 102, 106, 107, 127, and 134.)

Turbet, M., Bolmont, E., Leconte, J., et al. (2018). Modeling climate diversity, tidal dynamics and the fate of volatiles on TRAPPIST-1 planets, *Astronomy and Astrophysics*, 612, A86 (Cited on pages 20 and 78.)

Turbet, M., Ehrenreich, D., Lovis, C., Bolmont, E., & Fauchez, T. (2019). The runaway greenhouse radius inflation effect. An observational diagnostic to probe water on Earth-sized planets and test the habitable zone concept, *Astronomy and Astrophysics*, 628, A12 (Cited on pages 13, 14, 99, and 100.)

Turbet, M., Fauchez, T. J., Leconte, J., et al. (2023). Water condensation zones around main sequence stars, *Astronomy and Astrophysics*, 679, A126 (Cited on pages 13, 100, 127, and 128.)

Turbet, M., Forget, F., Leconte, J., Charnay, B., & Tobie, G. (2017). CO2 condensation is a serious limit to the deglaciation of Earth-like planets, *Earth and Planetary Science Letters*, 476, 11 (Cited on page 12.)

Turcotte, D. L. & Schubert, G. (2002). Geodynamics - 2nd Edition (Cited on page 20.)

Underwood, D. R., Jones, B. W., & Sleep, P. N. (2003). The evolution of habitable zones during stellar lifetimes and its implications on the search for extraterrestrial life, *International Journal of Astrobiology*, 2, 289 (Cited on page 13.)

Veeder, G. J., Matson, D. L., Johnson, T. V., Blaney, D. L., & Goguen, J. D. (1994). Io's heat flow from infrared radiometry: 1983–1993, *Journal of Geophysical Research: Planets*, 99, 17095 (Cited on page 20.)

Wang, H. S., Lineweaver, C. H., Quanz, S. P., et al. (2022). A Model Earth-sized Planet in the Habitable Zone of α Centauri A/B, *The Astrophysical Journal*, 927, 134 (Cited on pages 4 and 20.)

Way, M. J. & Del Genio, A. D. (2020). Venusian Habitable Climate Scenarios: Modeling Venus Through Time and Applications to Slowly Rotating Venus-Like Exoplanets, *Journal of Geophysical Research (Planets)*, 125, e06276 (Cited on pages 101, 102, and 128.)

Way, M. J., Del Genio, A. D., Kiang, N. Y., et al. (2016). Was Venus the first habitable world of our solar system ?, *Geophysical Research Letters*, 43, 8376 (Cited on pages 11, 80, 101, 102, and 128.)

Williams, D. M. & Kasting, J. F. (1997). Habitable Planets with High Obliquities, *Icarus*, 129, 254 (Cited on page 16.)

Wolf, E. T., Haqq-Misra, J., & Toon, O. B. (2018). Evaluating Climate Sensitivity to CO2 Across Earth's History, *Journal of Geophysical Research (Atmospheres)*, 123, 11,861 (Cited on page 135.)

Wolf, E. T. & Toon, O. B. (2014). Delayed onset of runaway and moist greenhouse climates for Earth, *Geophysical Research Letters*, 41, 167 (Cited on pages 9, 14, and 106.)

Wolf, E. T. & Toon, O. B. (2015). The evolution of habitable climates under the brightening Sun, *Journal of Geophysical Research (Atmospheres)*, 120, 5775 (Cited on pages 11, 14, 19, 80, 106, and 128.)

Wolszczan, A. & Frail, D. A. (1992). A planetary system around the millisecond pulsar PSR1257 + 12, *Nature*, 355, 145 (Cited on page 2.)

Wordsworth, R., Forget, F., & Eymet, V. (2010). Infrared collision-induced and far-line absorption in dense CO 2 atmospheres, *Icarus*, 210, 992 (Cited on page 31.)

Wright, S. O. M., Waldmann, I., & Yurchenko, S. N. (2022). Non-local thermal equilibrium spectra of atmospheric molecules for exoplanets, *Monthly Notices of the Royal Astronomical Society*, 512, 2911 (Cited on page 28.)

Wunderlich, F., Godolt, M., Grenfell, J. L., et al. (2019). Detectability of atmospheric features of Earth-like planets in the habitable zone around M dwarfs, *Astronomy & Astrophysics*, 624, A49 (Cited on page 5.)

Yang, J., Boué, G., Fabrycky, D. C., & Abbot, D. S. (2014). Strong Dependence of the Inner Edge of the Habitable Zone on Planetary Rotation Rate, *The Astrophysical Journal*, 787, L2 (Cited on pages 9, 11, and 80.)

Yang, J., Cowan, N. B., & Abbot, D. S. (2013). Stabilizing Cloud Feedback Dramatically Expands the Habitable Zone of Tidally Locked Planets, *The Astrophysical Journal*, 771, L45 (Cited on pages 11, 14, 80, and 102.)

Yang, J., Ji, W., & Zeng, Y. (2020). Transition from eyeball to snowball driven by sea-ice drift on tidally locked terrestrial planets, *Nature Astronomy*, 4, 58 (Cited on page 106.)

Yang, J., Leconte, J., Wolf, E. T., et al. (2016). Differences in water vapor radiative transfer among 1D models can significantly affect the inner edge of the habitable zone, *The Astrophysical Journal*, 826, 222 (Cited on pages 12 and 14.)

Yang, J., Leconte, J., Wolf, E. T., et al. (2019). Simulations of Water Vapor and Clouds on Rapidly Rotating and Tidally Locked Planets: A 3D Model Intercomparison, *The Astrophysical Journal*, 875, 46 (Cited on pages 11, 19, and 80.)

Zhang, Y. & Yang, J. (2020). How Does Background Air Pressure Influence the Inner Edge of the Habitable Zone for Tidally Locked Planets in a 3D View ?, *The Astrophysical Journal*, 901, L36 (Cited on page 48.)

Zieba, S., Kreidberg, L., Ducrot, E., et al. (2023). No thick carbon dioxide atmosphere on the rocky exoplanet TRAPPIST-1 c, *Nature*, 1 (Cited on page 6.)